UNIVERSIDADE DE LISBOA
INSTITUTO SUPERIOR TÉCNICO

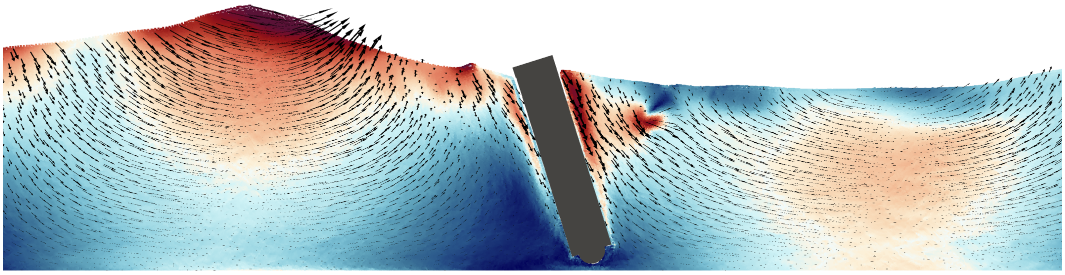

Numerical modeling and experimental testing of an oscillating wave surge converter

Moisés Gonçalves de Brito

Supervisor:	**Doctor Rui Miguel Lage Ferreira**
Co-Supervisors:	**Doctor Maria da Graça Reis e Silva de Oliveira Neves** **Doctor Luis Carlos Teixeira Gurbindo**

Thesis approved in public session to obtain the PhD Degree in

Civil Engineering

Jury final classification: Pass with Distinction

2018

TÉCNICO
LISBOA

UNIVERSIDADE DE LISBOA
INSTITUTO SUPERIOR TÉCNICO

Numerical modeling and experimental testing of an oscillating wave surge converter

Moisés Gonçalves de Brito

Supervisor:	**Doctor Rui Miguel Lage Ferreira**
Co-Supervisors:	**Doctor Maria da Graça Reis e Silva de Oliveira Neves** **Doctor Luis Carlos Teixeira Gurbindo**

Thesis approved in public session to obtain the PhD Degree in

Civil Engineering

Jury final classification: Pass with Distinction

Jury

Chairperson: Doctor António Heleno Cardoso, Instituto Superior Técnico, Universidade de Lisboa

Members of the Committee:

Doctor Luis Carlos Teixeira Gurbindo, Facultad de Ingeniería, Universidad de la República, Uruguay

Doctor Luís Manuel de Carvalho Gato, Instituto Superior Técnico, Universidade de Lisboa

Doctor António Alexandre Trigo Teixeira, Instituto Superior Técnico, Universidade de Lisboa

Doctor Alejandro Jacobo Cabrera Crespo, Facultad de Ciencias de Ourense, Universidade de Vigo, Spain

Doctor Luís Miguel Chagas da Costa Gil, Faculdade de Ciências e Tecnologia, Universidade Nova de Lisboa

Doctor Ricardo Jorge Fonseca Birjukovs Canelas, Instituto Superior Técnico, Universidade de Lisboa

Funding Institution

Fundação para a Ciência e a Tecnologia (FCT) - Portugal, grant PD/BD/705970/2014

2018

Everything should be made as simple as possible but no simpler.

Albert Einstein

Acknowledgments

First and foremost, I would like to acknowledge my supervisor Professor Rui Ferreira and my co-supervisors Professor Maria da Graça Neves and Professor Luis Teixeira, for their expert guidance and constructive criticism during the development of this research work. I want to give a very special thanks for their invaluable support and permanent involvement and commitment and I wish to share with them the credits and success achieved in this work.

This research was financially supported by the Portuguese Foundation for Science and Technology (FCT), through the Grant No. PD/BD/705970/2014, whose funding is greatly acknowledged. I wish to acknowledge the Instituto de Mecánica de los Fluidos e Ingeniería Ambiental (IMFIA), Universidad de la República, Uruguay, for allowing the access to wave flume to carry out the physical model tests. I wish to acknowledge the Environmental Physics Laboratory (EPHYSLAB), Universidade de Vigo, Ourense, Spain, for facilitating the development of the numerical model.

I am grateful to those who contributed to the improvement of my knowledge about the SPH modeling, which was a new subject for me. In particular, I want to thank to Dr. Ricardo Canelas, Dr. Alejandro Crespo, Dr. José Domínguez and Orlando García-Feal for their interest in this work and for help in the numerical implementation.

I want also to thank to Professor Luís Gil for his advice and guidance in multiple decisions made during this research work.

I would like to thank my colleagues at Instituto Superior Técnico (IST) and Laboratório Nacional de Engenharia Civil (LNEC) for their support, attention and friendship.

I would like to tank my parents for their endless support and my friends for their continuous

presence, friendship, support and motivation for the completion of this thesis.

To Nila, my wife, very special thanks for her everlasting patience, continuous support, understanding and love. To Gerson, my son, special thanks for his unconditional love.

Abstract

Oscillating wave surge converters (OWSCs) are an important class of oscillating bodies wave energy converter (WEC) devices, especially designed to operate in the near-shore region. These devices are especially composed by a bottom-hinged buoyant flap and by a hydraulic power take-off (PTO) system. The energy conversion process is based on the complex interactions between wave and flap, and between flap and mechanical constraints, i.e., PTO system, revolute joints and frictional contacts among components. Hence, mechanical constraints cannot be neglected while designing OWSCs. However, most of the previous studies has overlooked the joint (non-linear) effect of these constraints with wave interaction.

In this context, the objectives of this thesis are: i) to develop a numerical tool that is able to simulate the complex fluid-structure interactions and hydrodynamic behavior of the OWSC with mechanical constraints; and ii) to validate the numerical tool with closely controlled laboratory tests. To develop the numerical tool it is necessary to understand the main features of the flow, to understand the dynamic behavior of the hydraulic PTO system, and to recognize and validate existing numerical approaches. The validation then requires independent tests on the dynamic and hydrodynamic behaviors of the OWSC with mechanical constraints.

To attain these objectives, two sets of physical model tests of an OWSC at 1:10 scale model was carried out at the Instituto de Mecánica de los Fluidos e Ingeniería Ambiental (IMFIA), Universidad de la República, Uruguay. In the first set of tests, the hydrodynamic behaviors of the OWSC were characterized. In these tests, the free-surface elevation, pressure in the PTO system, rotation angle and velocity field in the vicinity of the flap are measured and analyzed. A large discrepancy was observed between the experimental data and linear analytical solutions, caused by the non-linear behaviors of wave-OWSC interaction that govern the turbulent field and the boundary layer instead of the inviscid and irrotational flow. The non-linear effects have an important role on the capture width ratio (CWR) and, therefore, analytical models are not accurate to describe the complex hydrodynamics of the OWSC with mechanical constraints. In fact, the measured signals present important linear and also non-linear harmonics components. To predict the CWR, the non-linear output frequency response functions are considered as the extension of the response amplitude operator (RAO). It is observed that the PTO system has a significant influence on the CWR and RAO. The RAO does not exhibit a well-defined peak as from the linear theory, showing a limited variation in a broad frequency band. Furthermore, a weak correlation between CWR and RAO was found, i.e., the maximum CWR does not occur for the maximum value of RAO.

In the second set of tests, the dynamic behaviors of the hydraulic PTO system were characterized. The experimental results show clearly a strong non-linear behaviors, including hysteretic and stochastic behaviors, and cavitation phenomena for large amplitude of motion. To capture and implement these behaviors, a mathematical model was proposed. The systematic comparison between measured and calculated results demonstrates that the proposed model can predict, with a satisfactory accuracy, the dynamic behaviors of the hydraulic PTO system.

The developed numerical tool is based on the implementation of the multi-body solver of Project Chrono under the Smoothed Particle Hydrodynamics (SPH) model of DualSPHysics, where the SPH solver resolves the interaction between wave and flap and the multi-body solver resolves the interaction between flap and mechanical constraints. The coupling procedure consists on the integration of part of the Project Chrono library and the adaptation of several source codes that compose mainly floating bodies in DualSPHysics.

The validation of the numerical tool is performed for both regular and irregular waves. The comparison between numerical results and experimental data shows that the numerical tool properly predicts the dynamics of the OWSC. Furthermore the computed and observed free-surface elevation and mean flow field show reasonable agreement.

Once properly validated, the numerical tool is then applied to study the influence of several parameters of the PTO system and flap configurations on the hydrodynamics of the OWSC. The variation of the friction force shows a gain of about 200% on the OWSC efficiency, while the variation of the pressure force shows a gain of about 50%. The flap inertia also shows an important effect on the OWSC efficiency, with maximum gain of bout 160%. These results show the usefulness of the developed simulation tool as an aid to design OWSCs.

Keywords

Wave energy, Oscillating wave surge converter (OWSC), Experimental modeling, Numerical modeling, Smooth Particle Hydrodynamics (SPH), Mechanical constraint, Hydraulic power take-off (PTO) system, DualSPHysics, Project Chrono

Resumo

Os *oscillating wave surge converters* (OWSCs) são dispositivos de conversão de energia das ondas (WEC) do tipo corpo oscilante que funcionam nas zonas próximas à costa. Estes dispositivos são compostos essencialmente por uma placa oscilante e um sistema hidráulico de extração de energia (PTO). A conversão de energia dos OWSCs caracteriza-se por um conjunto de interações complexas da onda com a placa oscilante e da placa oscilante com as restrições mecânicas, i.e., as restrições impostas pelo sistema PTO e pelos mecanismos de ligação entre os diversos componentes. Assim, estas restrições não devem ser desprezadas no dimensionamento dos OWSCs. No entanto, grande parte dos estudos anteriores foram feitos desprezando os efeitos (não-lineares) combinados destas restrições com a interação da onda.

Os objetivos desta tese são: i) desenvolver uma ferramenta numérica que permita simular interações complexas onda-estrutura e o comportamento hidrodinâmico dos OWSCs com restrições mecânicas; e ii) validar a ferramenta numérica com base em dados laboratoriais. Para desenvolver a ferramenta numérica é necessário compreender as principais características do escoamento e o comportamento dinâmico do sistema PTO, e ainda identificar e validar as metodologias numéricas existentes. A validação requer, por sua vez, testes independentes em modelo físico do comportamento dinâmico e hidrodinâmico do OWSC com restrições mecânicas.

Para atingir estes objetivos, foram realizados dois grupos de ensaios experimentais em modelo físico de um OWSC à escala 1:10 no Instituto de Mecánica de los Fluidos e Ingeniería Ambiental (IMFIA), Universidad de la República, Uruguai. O primeiro grupo de ensaios centra-se na caracterização do comportamento hidrodinâmico do OWSC. Nestes ensaios foram medidos a elevação da superfície livre, a pressão no interior do sistema PTO, o movimento do OWSC e o campo de velocidade na vizinhança da placa oscilante. A comparação entre os dados experimentais e as soluções analíticas lineares apresenta uma grande discrepância, causada pelos efeitos não-lineares da interação onda-OWSC que governam o escoamento turbulento e a camada limite em vez do escoamento invíscido e irrotacional. Efetivamente, os efeitos não-lineares têm uma importância significativa na eficiência (CWR) do OWSC, logo os modelos analíticos lineares não são adequados para descrever com precisão a hidrodinâmica dos OWSCs com restrições mecânicas. Os sinais medidos apresentam forte componentes harmónicas lineares e também não-lineares. Neste contexto, a CWR é estimada considerando as contribuições das componentes harmónicas não-lineares como sendo uma extensão do operador de amplitude de resposta (RAO). O sistema PTO apresenta feitos relevantes no CWR e no RAO. O RAO não apresenta o pico de ressonância, mostrando claramente o efeito do amortecimento do sistema PTO. Adicionalmente, foi observado uma fraca correlação entre CWR e RAO, i.e., o valor máximo do CWR não ocorrer para o máximo do RAO.

O segundo grupo de ensaios centra-se na caracterização do comportamento dinâmico do sistema PTO. Os resultados experimentais mostram um forte comportamento não-linear do sistema PTO (incluindo o comportamento histerético e estocástico, e ainda o fenómeno de cavitação para grande amplitude de movimento). De modo a implementar estes efeitos não-lineares na ferramenta numérica foi desenvolvido um modelo matemático do sistema PTO hidráulico. A exaustiva comparação entre os resultados experimental e os estimados mostra que o modelo desenvolvido prevê com boa aproximação o comportamento dinâmico do sistema PTO.

A ferramenta numérica desenvolvida baseia-se no acoplamento do *solver* multicorpo do Project Chrono e do *solver* Smoothed Particle Hydrodynamics (SPH) do código DualSPHysics. Nesta ferramenta o *solver* SPH calcula a interação onda-placa oscilante e o *solver* multicorpo calcula a interação placa oscilante-restrições mecânicas. O método de acoplamento baseia-se na integração da biblioteca do Project Chrono e na adaptação dos códigos fontes do DualSPHysics que contém a implementação dos corpos flutuantes.

A validação desta ferramenta numérica é feita para condições de agitação regular e irregular. A comparação entre os resultados numéricos e e os dados experimentais mostra que o modelo numérico desenvolvido permite simular com precisão a dinâmica do OWSC. Além disso, os resultados numéricos da elevação da superfície livre e do campo de velocidades médio apresentam boa concordância com os dados experimentais.

O modelo numérico validado é aplicado para estudar a influência de vários parâmetros do sistema PTO e geométricos da placa oscilante. A variação da força de atrito apresenta um ganho na eficiência de aproximadamente 200%, enquanto que a variação da força de pressão apresenta um ganho de aproximadamente 50%. A inércia da placa oscilante também mostra importantes efeitos na eficiência, com um ganho máximo de 160%. Estes resultados mostram claramente a utilidade da ferramenta numérica desenvolvida como ferramenta eficaz no apoio a projectos dos OWSCs. Esta ferramenta permite também simular qualquer tipo de WEC com restrições mecânicas complexas.

Palavras Chave

Energia das ondas, *Oscillating wave surge converter* (OWSC), Modelação física, Modelação numérica, *Smooth Particle Hydrodynamics* (SPH), Restrição mecânica, Sistema hidráulico de extração de energia (PTO), DualSPHysics, Project Chrono

Contents

List of Figures

List of Tables

Acronyms and abbreviations

2D Bidimensional

3D Tridimensional

API Application Programming Interface

CFD Computational Fluid Dynamics

CFL Courant-Friedrich-Levy condition

CPU Central Processing Unit

CUDA Compute Unified Device Architecture

CWR Capture Width Ratio

DVI Differential Variational Inequality

GPU Graphics Processing Unit

JONSWAP Joint North Sea Wave Project

MPI Message Passing Interface

ODE Ordinary Differential Equation

OpenMP Open Multi-Processing

OWSC Oscillating Wave Surge Converter

PCI Peripheral Component Interconnect

PPR Pulses per Revolution

PTO Power Take-Off

PVC Polyvinyl Chloride

RAO Response Amplitude Operator

RO Rated Output

SPH Smooth Particle Hydrodynamics

UVP Ultrasonic Velocity Profiler

VOF Volume-of-Fluid

VTK Visualization ToolKit

WCSPH Weakly Compressible Smooth Particle Hydrodynamics

WEC Wave Energy Converter

XML Extensible Markup Language

List of Symbols

Symbol	Description	Dimensions
A	cross-section area of the cylinder chamber	(L^2)
a	flap thickness	(L)
$\mathcal{A}_i$	fluid particles domain	(–)
$\mathcal{A}_k$	boundary particles domain	(–)
α	angle of UVP probes	(–)
α_ν	empirical coefficient of viscosity term	(–)
$\alpha_{(2p)n}$	complex solutions of the kinematic condition on the flap	(–)
B	bulk modulus	(–)
b	wave flume width	(L)
B_0	friction torque on the revolute joint between flap and bearings	($\mathrm{M\ L^2\ T^{-2}}$)
β	angle between flap and hydraulic cylinder	(–)
$\beta_{(2p)0}$	complex solutions of the no-flux condition on the flap	(–)
C	damper coefficient	($\mathrm{M\ L^2\ T^{-1}}$)
c	speed of sound	($\mathrm{L\ T^{-1}}$)
c_g	wave group velocity	($\mathrm{L\ T^{-1}}$)
$\mathbf{D}$	tangent space generator vector	($\mathrm{M\ L\ T^{-2}}$)
d	still water depth	(L)
δ	Dirac delta function	(–)
e	flap width	(L)
η	free-surface elevation	(L)
f	wave frequency	($\mathrm{T^{-1}}$)
f_p	wave peak frequency	($\mathrm{T^{-1}}$)

$\mathbf{f}$	particle force vector	(M L T^{-2})
$\mathbf{F}_a$	applied force vector	(M L T^{-2})
F_c	Coulomb friction force	(M L T^{-2})
F_{exc}	excitation force	(M L T^{-2})
F_f	friction force	(M L T^{-2})
F_p	pressure force	(M L T^{-2})
F_{PTO}	PTO force	(M L T^{-2})
F_s	maximum static friction force	(M L T^{-2})
G	non-linear output frequency response function	(L^{-1} T^{-1})
g	gravitational acceleration	(L T^{-2})
$\mathbf{g}$	gravitational acceleration vector	(L T^{-2})
g_s	Stribeck function	(–)
γ	peak enhancement factor	(–)
γ_p	polytropic constant	(–)
Γ	Lagrange multiplier	(–)
$\mathcal{H}$	Heaviside step function	(–)
$\mathcal{H}_1^{(1)}$	Hankel function of the first kind and first order	(–)
h	smoothing length	(L)
H	wave height	(L)
h_{ss}	dimensionless steady-state lubricant film thickness	(–)
h_l	dimensionless unsteady-state lubricant film thickness	(–)
H_m	mean wave height	(L)
H_s	significant wave height	(L)
I	moment of inertia	(M L^{2})
$\mathbf{I}$	moment of inertia tensor	(M L^{2})
I_p	fluid inertia coefficient	(M L^{-2} or M L^{-1})
K	constant stiffness coefficient	(M L^{2} T^{-2})
k	wavenumber	(L^{-1})
K_f	proportional constant for lubricant film thickness	(T$^{2/3}$ L$^{-2/3}$)
K_p	pressure loss coefficient	(M L^{-3} or M L^{-1})
K_{PTO}	constant elastic coefficient	(M L^{2} T^{-2})

$\mathbf{L}$	Jacobian matrix	(–)
l	flap height	(L)
λ	wavelength	(L)
M , m	mass	(M)
$\mathbf{M}$	mass matrix	(M)
μ	dynamic viscosity	(M L^{-1} T^{-1})
μ_a	added inertia	(M L^{2})
μ_{PTO}	coefficient of inertia	(M L^{2})
n_s	exponent of Stribeck curve	(–)
ν_{PTO}	coefficient of damping	(M L^{2} T^{-1})
ν_a	radiation damping	(M L^{2} T^{-1})
Ω	domain or solution space	(–)
$\boldsymbol{\Omega}$	rigid body angular velocity vector	(T^{-1})
ω	angular frequency	(T^{-1})
P	pressure	(M L^{-1} T^{-2})
P_{atm}	atmosphere pressure	(M L^{-1} T^{-2})
P_c	minimum static pressure	(M L^{-1} T^{-2})
P_{int}	pressure in the cylinder chamber	(M L^{-1} T^{-2})
P_s	maximum static pressure	(M L^{-1} T^{-2})
P_v	vapor pressure of water	(M L^{-1} T^{-2})
$\boldsymbol{\Phi}$	velocity potential	(L^{2} T^{-1})
ϕ	complex amplitude of velocity potential	(L^{2} T^{-1})
ϕ^D	velocity potential of the diffracted wave	(L^{2} T^{-1})
ϕ^I	velocity potential of the incident wave	(L^{2} T^{-1})
ϕ^R	velocity potential of the radiation wave	(L^{2} T^{-1})
ϕ^S	velocity potential of the scattering wave	(L^{2} T^{-1})
$\mathit{\Pi}$	viscosity term of momentum equation	(M^{-1} L^{5} T^{-2})
$\mathbf{q}$	generalized coordinates	(L)
Q	flow rate in the hydraulic circuit	(L^{3} T^{-1})
$\mathbf{R}$, $\mathbf{r}$	global position vector	(L)
$\mathbf{R}_0$	rigid body center of mass position	(L)

ρ	density	(M L^{-3})
ρ_0	reference density	(M L^{-3})
S	power spectrum	(L^2 T)
σ	Thoma coefficient	(–)
σ_0	stiffness of the elastic bristles	(M T^{-2})
σ_1	micro-viscous friction coefficient for bristles	(M T^{-1})
σ_2	viscous friction coefficient	(M T^{-1})
σ_c	critical cavitation coefficient	(–)
σ_f	standard deviation of the friction force fluctuation	(M L T^{-2})
σ_p	standard deviation of the pressure force fluctuation	(M L T^{-2})
T	wave period	(T)
t	time	(T)
T_p	peak period	(T)
$\mathcal{T}$	complex excitation torque	(M L^2 T^{-2})
$\mathcal{T}_e$	external torque	(M L^2 T^{-2})
$\mathcal{T}_f$	torque of friction force	(M L^2 T^{-2})
$\mathcal{T}_g$	torque due to the gravity	(M L^2 T^{-2})
$\mathcal{T}_p$	torque of pressure force	(M L^2 T^{-2})
$\mathcal{T}_{PTO}$	torque of PTO system	(M L^2 T^{-2})
$\mathcal{T}_h$	hydrodynamic torque	(M L^2 T^{-2})
τ	geometrical scale factor	(–)
τ_h	time constant for lubricant film dynamic	(T)
τ_{h0}	time constant for dwell period	(T)
τ_{hn}	time constant for deceleration period	(T)
τ_{hp}	time constant for acceleration period	(T)
$\boldsymbol{\Theta}$	rotational coordinates	(–)
Θ	complex amplitude of rotation angle of the flap	(–)
θ	rotation angle of the flap	(–)
$\dot{\Theta}$	complex angular velocity of the flap	(T^{-1})
$\dot{\theta}$	angular velocity of the flap	(T^{-1})
$\ddot{\theta}$	angular acceleration of the flap	(T^{-2})

u	longitudinal velocity component	(L T^{-1})
U_{2p}	Chebyshev polynomials of the second kind and order	(–)
U_0	deep-water maximum particle velocity	(L T^{-1})
v	kinematic viscosity	(L^2 T^{-1})
V	volume	(L^3)
$\mathbf{V}$	rigid body linear velocity vector	(L T^{-1})
$\mathbf{v}$	linear velocity vector	(L T^{-1})
v_n	normal component of the boundary velocity	(L T^{-1})
v_r	radial velocity	(L T^{-1})
ε	ratio of the incident and reflected wave power	(–)
φ	function of dynamic pressure coefficient	(–)
W	kernel function	(–)
w	vertical velocity component	(L T^{-1})
W_i	incident wave power	(M L^2 T^{-3})
W_{out}	power capture	(M L^2 T^{-3})
W_r	reflected wave power	(M L^2 T^{-3})
x	linear position	(L)
$\dot{x}$	linear velocity	(L T^{-1})
$\dot{x}_b$	velocity where the friction force becomes minimum	(L T^{-1})
$\dot{x}_s$	Stribeck velocity	(L T^{-1})
$\ddot{x}$	linear acceleration	(L T^{-2})
$\mathbf{x}$	cartesian coordinate system	(L)
z_d	mean deflection of the elastic bristles	(L)
Z_n	depth mode	(–)

1

Introduction

Contents

1.1 Motivation

Oscillating wave surge converter (OWSC) devices are in an early stage of development (Gomes et al., 2015). In recent years, a strong development has been registered with the implementation of some devices in a pre-commercial stage, some of them already connected to the electric network, such as Oyster (Whittaker and Folley, 2012) and WaveRoller (Lucas et al., 2012). Full-scale prototypes of Oyster and WaveRoller have been successfully tested with unit rated of 300 kW and 315 kW, respectively.

Based on actual development stage, OWSC devices can be competitive in the near future. In this context, it is necessary to improve the performance and reliability of these devices and thus the competitiveness on the global energy market. For these reasons, further laboratory and field tests are important to insight into phenomena not completed understood and to establish the most efficient OWSC configurations for each local characteristics. However, the time involved in these tests may be high and the associated costs may be relevant, as it may be necessary to design and build several structural solutions.

Numerical modeling tools may constitute a crucial aid to the design of most efficient solutions. These tools are significantly cheaper than physical model tests and it can be applied to characterize the hydrodynamics of the OWSC beforehand to highlight the zones of interest, to find the most suitable places where the measuring devices can be placed, to anticipate problems or even to select the most relevant cases to be tested physically. Given the complexity of the involved phenomena, the numerical modeling can provide a full flow field (e.g., flow separation, turbulence and wave impact), a full description of hydrodynamics of the OWSCs (e.g., excitation, inertial and drag forces) and allow to test large sets of different configurations without the use of additional resources. However, currently, the main disadvantage of these tools is related to the limitations in the modeling of the complex interactions between wave and OWSC with mechanical constraints, such as hydraulic power take-off (PTO) system, frictional contacts, revolute and slider joints among components. Such mechanical constraints have a non-negligible influence in the dynamics of the OWSCs (Whittaker and Folley, 2012). However, most computational fluid dynamic (CFD) codes, model these devices in simplified way, neglecting the description of its complex non-linear mechanical constraints.

In the literature, only a few works present the modeling of OWSCs with mechanical constraints, including only the effects of the PTO system (Gomes et al., 2015; Lucas et al., 2012; Schmitt et al., 2016). However, these constraints are often simplified with only one mechanical joint as a rotational linear spring and/or a damper (Babarit et al., 2012). In this context, robust and efficient CFD numerical simulation tools are still needed to aid the design of OWSCs without significant compromises on the description of its mechanical behavior. Developing such tools is a challenging task due to discrete (singular) nature of some mechanical constraints and due to the difference in geometric and time scales, in some cases orders of magnitude apart. It is thus necessary to employ multi-scale methods in order to guarantee the well-posedness of the simulation (Liu and Liu, 2003).

Mesh-based methods were considered less appropriate to develop the simulation tool. They have been widely applied in the modeling of OWSCs, see e.g., Martínez-Ferrer et al. (2018); Schmitt et al. (2016); Schmitt and Elsaesser (2015); Wei et al. (2017, 2016, 2015), but they pose difficulties when trying to incorporate mechanical constraints. Firstly, mesh-based method requires commonly expensive and complicated mesh moving algorithms (Liu and Liu, 2003; Yeylaghi et al., 2016), due to the large motion of the flap. Secondly, solving the mechanical constraints usually requires additional complex mathematical transformation to solve non-linear complementarity problem, singularities, non-uniqueness, non-penetration, inequality constraint and NP-hardness, that can be more expensive than solving the hydrodynamic interaction between wave and flap (Liu and Liu, 2003). Thirdly, some mechanical constraints (e.g. frictional revolute, prismatic and slider joints) are not, in general, continuous and straightforward application of mesh-based method for ordinary differential equations (ODEs) requires mesh size and time step that can be impracticable (Mazhar et al., 2013; Shabana, 2005; Tasora et al., 2016). Additionally, the mesh-based method needs to solve an additional equation, such as Volume-of-Fluid (VOF) method to locate and track the free-surface.

A promising alternative to mesh-based methods are the mesh-free methods. Among mesh-free methods, the Smoothed Particle Hydrodynamics (SPH) has been widely adopted in the study of complex free-surface flows for its merits to easily calculate interactions between flow and driven bodies (Canelas et al., 2016; Gómez-Gesteira et al., 2010; Monaghan, 2012; Verbrugghe et al., 2018) and more recently to modeling OWSCs (Dias et al., 2017; Henry et al., 2014a; Yeylaghi et al., 2016; Zhang et al., 2018). The free-surface is captured in the SPH method without the need for solving additional equations to locate and track the free-surface. Moreover, SPH is considered a versatile method, naturally dealing with unsteady and non-linear flows, extreme deformations and complex topological evolutions, such as a breaking free-surface (Colagrossi and Landrini, 2003; Monaghan, 1994). However, given the dynamic nature of the SPH formulation, some mechanical constraints are also difficult to include in

SPH form, for example lubricated contacts or asperities between driven bodies. Considering the success of SPH method for fluid description and multi-body solvers for mechanical constraints, the coupling between them can provide new simulation possibilities. This thesis is devoted to develop and validate an accurate and reliable CFD tool suitable to describe the dynamics of the OWSCs with mechanical constraints.

1.2 Objectives and Methodology

1.2.1 Structural objectives

The objectives of this thesis are:

i) to develop a numerical tool that is able to simulate the complex fluid-structure interactions and hydrodynamic behaviors of the OWSC with mechanical constraints.

ii) to validate the numerical tool with closely controlled laboratory tests.

The work program of this thesis is inscribed in the second development stage of the "URU-WAVE" project, funded by the Uruguayan National Agency for Research and Innovation. This stage requires extensive numerical and laboratory tests to design the most efficient model configuration, given the local wave characteristics.

The specific objectives of the thesis are as follows:

1. Characterize experimentally the hydrodynamic behaviors of the OWSC. The physical model tests will allow to insight into phenomena not completed understood in the hydrodynamics of the OWSC with mechanical constraints and to validate the numerical tool.
2. Characterize experimentally the capture width ratio (CWR) and response amplitude operator (RAO) of the OWSC for a given Uruguayan wave characteristics.
3. Develop a numerical tool for modeling OWSCs, considering the complex interactions between wave and flap, and between flap and mechanical constraints.
4. Characterize experimentally and implement in the numerical tool the dynamic behaviors of the hydraulic PTO system.

5. Validate the numerical tool with a novel experimental data.
6. Apply the numerical tool to study the influence of several parameters of PTO system and flap configurations on the hydrodynamics of the OWSC.

1.2.2 Methodology

To achieve the proposed objectives, it is necessary to firstly understand the main features of the flow and the dynamic behaviors of the hydraulic PTO system. In this context, two sets of independent physical model tests on the dynamic and hydrodynamic behaviors of an OWSC with mechanical constraints, wave generation and propagation were performed. These tests were carried out at the Instituto de Mecánica de los Fluidos e Ingeniería Ambiental (IMFIA), Universidad de la República, Uruguay, in a horizontal wave flume with approximately 60 m long (wave direction), 1.5 m wide and 1.8 m deep, equipped with a piston-type wavemaker.

An OWSC with hydraulic PTO system was designed and manufactured at 1:10 scale model. Similar to the physical model of Folley et al. (2007, 2004); Henry et al. (2014a,b), the OWSC model was also designed to represent quasi-2D test. The tests were carried out for both unidirectional regular and irregular waves with the highest annual frequency, i.e., major contributors to the mean annual energy, in the Uruguayan oceanic coast (Alonso et al., 2015). The free-surface elevation, pressure in the PTO system and flap motion were measured and analyzed. The longitudinal and vertical velocity components in the vicinity of the flap were measured for regular wave using an Ultrasonic Velocity Profiler (UVP). The velocity field was obtained by repeating the same test and moving the UVP probes across the vertical direction. Part of the experimental data was treated using the phase-averaged, to investigate the velocity field and OWSC dynamics over a wave period. On the topic of CWR and RAO, the harmonic decomposition was performed to identify the relevant non-linearities of the interaction between wave and OWSC with mechanical constraints. To explain the main flow features the experimental results were also compared with linear analytical solutions.

To develop the numerical tool it is necessary to adapt a SPH solver considering the interaction between wave and flap and between flap and mechanical constraints, and to validate the tool with experimental data. Structurally the tool consists on a numerical implementation of the multi-body solver of Project Chrono (Tasora and Anitescu, 2011) under SPH model of DualSPHysics (Crespo et al., 2015) and is specifically designed to support the simulation of complex fluid-structure interaction with any mechanical constraints. Hence, the Dual-

SPHysics code is used to model wave-flap interaction and Project Chrono library is used to model the flap-mechanical constraints interaction. The coupling procedure is mainly split in three steps. In the first step, DualSPHysics resolves the interaction by solving the governing equations in SPH form. The motion of the flap is calculated using the Newton's equations for rigid body dynamics. In the second step, the linear and angular acceleration vector to be applied in the centre of mass of the flap are transferred to the Project Chrono. During that time step, Project Chrono updates the flap motion, considering the given mechanical constraints. The position of the centre of mass, linear and angular velocity vector of the flap are transferred back to the DualSPHysics. In the third step, DualSPHysics updates the position of the particles that form the flap with the information transferred from Project Chrono library. Finally, DualSPHysics updates all variables (e.g., position, velocity, density and pressure) of the fluid and boundary particles in the computational domain at the new time step.

The validation of the numerical tool is mainly performed in three stages. In the first stage, the dynamic behavior of the OWSC with mechanical constraints is validated by describing its motion by a given angular velocity. In the second stage, the wave generation and propagation are validated for a several scaled-wave scenarios in the Uruguayan oceanic coast. In the third stage, the hydrodynamics of the OWSC with mechanical constraints are validated with novel experimental data.

Once properly validated, the numerical tool is then applied to study the influence of several parameters of PTO system and flap configurations on the hydrodynamics of the OWSC.

1.2.3 Innovative aspects

The main contribution of this work is a fully non-linear numerical tool for the design of OSWC with mechanical constraints, properly validated. Other important contributions are: an original experimental and numerical investigation on the hydrodynamics of an OWSC with hydraulic PTO system; a mathematical model to describe the damping of hydraulic PTO system; linear and non-linear analyses of OWSC under unidirectional regular and irregular waves; a new approach for predict the CWR based on the RAO and non-linear output frequency response functions.

1.3 Thesis outline

This thesis is divided into ten chapters. Figure 1.1 shows a schematic diagram of the thesis outline and the link between each chapter.

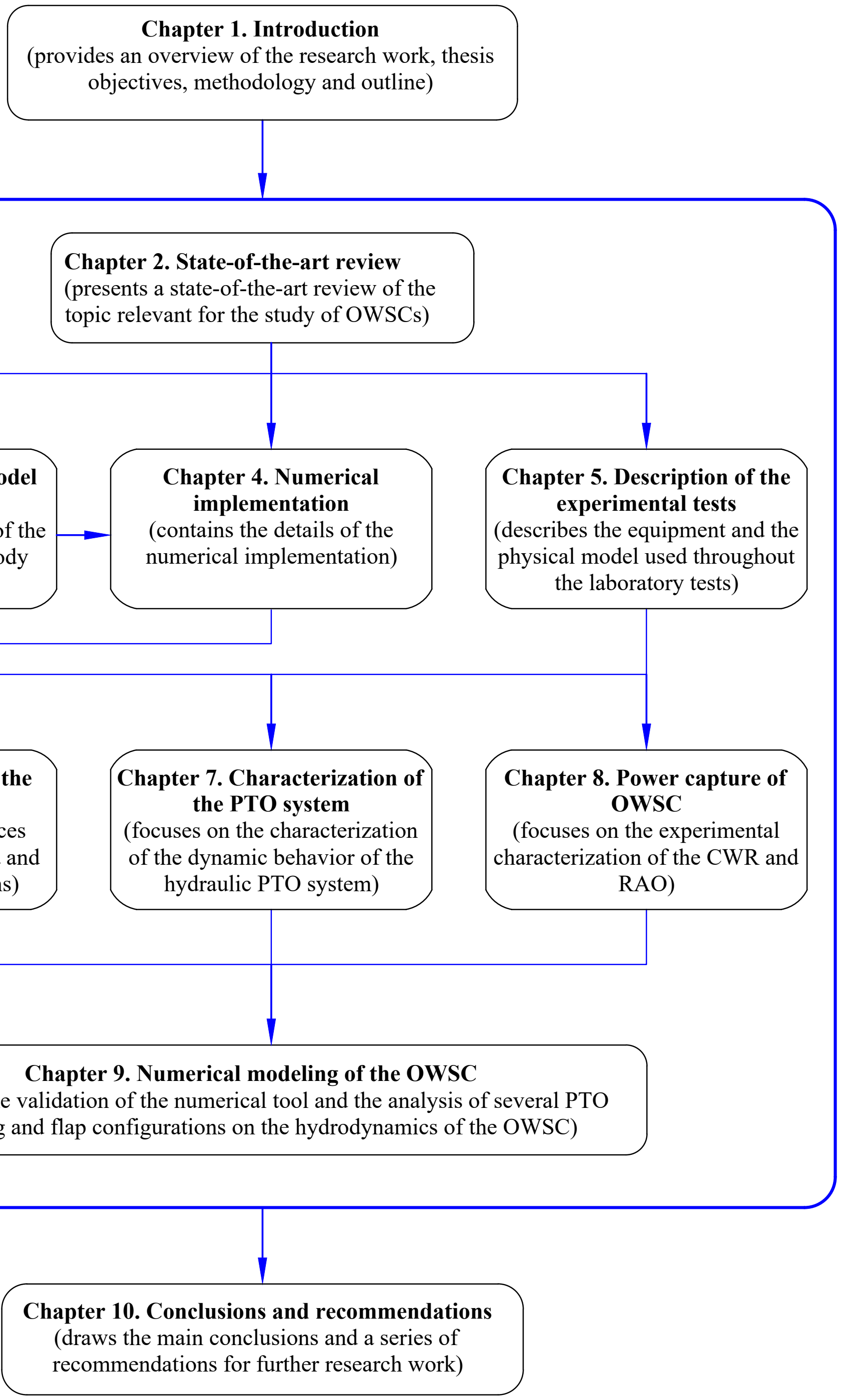
Chapter 1. Introduction
(provides an overview of the research work, thesis objectives, methodology and outline)
Chapter 2. State-of-the-art review
(presents a state-of-the-art review of the topic relevant for the study of OWSCs)
Chapter 3. Numerical model
(describes the detailed mathematical formulation of the SPH method and multi-body dynamics)
Chapter 4. Numerical implementation
(contains the details of the numerical implementation)
Chapter 5. Description of the experimental tests
(describes the equipment and the physical model used throughout the laboratory tests)
Chapter 6. Flow field in the vicinity of OWSC
(investigates the differences between experimental data and linear analytical solutions)
Chapter 7. Characterization of the PTO system
(focuses on the characterization of the dynamic behavior of the hydraulic PTO system)
Chapter 8. Power capture of OWSC
(focuses on the experimental characterization of the CWR and RAO)
Chapter 9. Numerical modeling of the OWSC
(presents the validation of the numerical tool and the analysis of several PTO damping and flap configurations on the hydrodynamics of the OWSC)
Chapter 10. Conclusions and recommendations
(draws the main conclusions and a series of recommendations for further research work)

Figure 1.1: Schematic diagram of the thesis outline and the link between chapters.

Chapter 1 (the current chapter) provides an overview of the research work. The objectives are defined and the methodology followed to complete this research is enunciated. This chapter also presents the innovative aspects and contents of this thesis.

Chapter 2 presents a state-of-the-art review of the topics relevant for the study of OWSCs. First, a literature review focuses on the analytical models of OWSCs is presented. An analytical model of an OWSC in a horizontal wave flume under unidirectional waves is presented and analyzed in detail. The governing equations and boundary conditions of linear water wave theory are reviewed. The solution of the scattering and radiation problems of wave-flap interaction are formulated. Next, the physical model tests and numerical modeling of wave-OWSC interaction were reviewed. Finally, a review focuses on the PTO system models is presented.

Chapter 3 describes the detailed mathematical formulation of the SPH method and multi-body dynamics. The continuous and discrete interpolations and their main properties are firstly introduced and then the most common kernels implemented in DualSPHysics are presented. The governing equations of fluid dynamics (continuity and Navier-Stokes equations) in Lagrangian form are briefly described. The SPH (kernel and particles) approximations are applied to derive the governing equations in SPH form. This discretization leads to a set of ODEs with respect to time. The time integration schemes to compute these ODEs are presented. The following numerical aspects in implementing SPH method are discussed. A set of boundary conditions and algorithms for dealing with particle interactions in the SPH method are presented. Some theoretical and numerical details of multi-body dynamics with equality motion constraints are presented. First, the equations of motion of the corresponding unconstrained system are presented. Next, the formulation is extended to systems with motion constraints. Finally, the time integration scheme for the systems is described.

Chapter 4 contains the details of the numerical implementation of the Project Chrono library under the DualSPHysics code. The principal characteristics of the DualSPHysics and Project Chrono are introduced, focusing in particular to the aspects that are relevant in thesis context. The coupling procedure between DualSPHysics and Project Chrono is presented.

Chapter 5 describes the experimental work and includes the description of the wave flume, OWSC model, equipment and data acquisition system used, together with the methodology used throughout the experimental tests.

Chapter 6 focuses on the experimental characterization of the velocity field in the vicinity of the OWSC, in order to clarify the important differences between experimental data and linear analytical solutions. For this purpose, the free-surface elevation, pressure in the hydraulic PTO system, rotation angle and velocity field are analyzed under regular waves. This work was submitted in an international journal (P.9 in Section 1.4).

Chapter 7 focuses on the experimental characterization of the dynamic behaviors of hydraulic PTO system. The results for regular and irregular motion are presented. The dynamic behaviors of PTO force, which integrates friction and pressure forces, are presented and discussed. The models to describe its dynamic behaviors are presented. The results presented in this chapter were published in an international journal (P.5 in Section 1.4).

Chapter 8 focuses on the experimental characterization of the CWR and RAO of the OWSC under both regular and irregular waves. The effects of PTO system are explicitly taken in consideration. The harmonic decomposition of free-surface elevation, angular velocity of the flap and pressure in the PTO system are analyzed and discussed. A new approach to predict the CWR based on the RAO and non-linear output frequency response functions is presented. This work was submitted in an international journal (P.8 in Section 1.4).

Chapter 9 presents the validation and application of the numerical tool. The validation is mainly performed in three stages. In the first stage, the dynamic behavior of the OWSC with mechanical constraints is validated by describing its motion by a given angular velocity. The dynamic behavior of hydraulic PTO system presented in Chapter 7 is implemented in numerical tool to solve the constraint force of the PTO system. In the second stage, the wave generation and propagation are validated for a several wave scenarios in the Uruguayan oceanic coast. In the third stage, the hydrodynamics of the OWSC with mechanical constraints are validated with novel experimental data. Finally, the validated numerical tool is applied to study the influence of several PTO damping and flap configurations on the hydrodynamics of the OWSC. The numerical tool was published in an international journal (P.7) an submitted in another one (P.10). This work also resulted in several publications in conference proceedings (P.1, P.2, P.3, P.4 and P.6 in Section 1.4).

Chapter 10 draws the main conclusions of this research work and a small series of recommendations for further research. Firstly, a summary of the developed work and the main conclusion of this research are highlighted. Subsequently, the main contributions and impacts of the research developed are outlined. Finally, perspectives and recommendations for future work are provided.

1.4 List of publications

During the development of this research work, several papers have been published and submitted for publication in conference proceedings and international journals:

P.1. **Brito, M.**, García-Feal, O., Domínguez, J. M., Crespo, A. J. C., Canelas, R. B., Ferreira, R. M. L. and Neves, M. G. (2016). 'Coupling between DualSPHysics and Chrono-Engine: towards large scale HPC multi-physics simulations'. *11th SPHERIC International Workshop.*

P.2. **Brito, M.** (2017). 'Development of a numerical tool for modeling wave-structure-structure interactions'. (in Portuguese). *9as Jornadas Portuguesas de Engenharia Costeira e Portuária.*

P.3. **Brito, M.**, Canelas, R. B., Ferreira, R. M. L., García-Feal, O., Domínguez, J. M., Crespo, A. J. C., Teixeira, L. and Neves, M. G. (2017). 'Application, modeling and validation of an OWSC using DualSPHysics'. *12th SPHERIC International Workshop.*

P.4. **Brito, M.**, Pereira, L., Gil, L., Canelas, R. B. and Ferreira, R. M. L. (2017). 'Numerical simulation of an wave energy converter using SPH method'. (in Portuguese). *XIII Congresso Ibero-americano em Engenharia Mecânica - CIBEM.*

P.5. **Brito, M.**, Teixeira, L., Canelas, R. B., Ferreira, R. M. L. and Neves, M. G. (2017). 'Experimental and numerical studies of dynamic behaviors of a hydraulic power take-off cylinder using spectral representation method', *Journal of Tribology* **140**(2): 021102–021102–13.

P.6. Canelas, R. B., **Brito, M.**, Ferreira, R. M. L., García-Feal, O., Domínguez, J. M. and Crespo, A. J. C. (2017). 'DualSPHysics, applications of a HPC multi-physics simulation framework'. *12th SPHERIC International Workshop.*

P.7. Canelas, R. B., **Brito, M.**, García-Feal, O., Domínguez, J. M. and Crespo, A. J. C. (2018). 'Extending DualSPHysics with a Differential Variational Inequality: modeling fluid-mechanism interaction'. *Applied Ocean Research* **76**: 88–97.

P.8. **Brito, M.**, Ferreira, R. M. L., Teixeira, L., Neves, M. G. and Canelas, R. B. (2018). 'Experimental investigation on the power capture of an oscillating wave surge converter in unidirectional waves'. *Renewable Energy* (submitted).

P.9. **Brito, M.**, Teixeira, L., Ferreira, R. M. L., Neves, M. G. and Canelas, R. B. (2018). 'Experimental investigation of the flow field in the vicinity of an oscillating wave surge converter'. *International Journal of Energy Research* (submitted).

P.10. **Brito, M.**, Canelas, R. B., García-Feal, O., Domínguez, J. M., Crespo, A. J. C., Ferreira, R. M. L., Neves, M. G. and Teixeira, L. (2018). 'A numerical tool for modeling oscillating wave surge converter with non-linear mechanical constraints'. *Renewable Energy* (submitted).

2

State-of-the-art review

Contents

2.1 Introduction

Oscillating wave surge converter (OWSC) devices are known to be competitive in the near-shore regions with water depth ranging from 10 to 20 m (Folley et al., 2004; Lucas et al., 2012; Schmitt et al., 2016; Whittaker and Folley, 2012). These devices are especially composed by a buoyant flap and by a hydraulic power take-off (PTO) system. The flap is usually attached to the foundation via bearings, pitching under the action of incoming waves, presenting vertical position in the absence of waves and can be fully or partially submerged (Whittaker et al., 2007). The PTO system is often composed by hydraulic cylinders that pumps fluid inside a closed hydraulic circuit (see the schematic sketch of an OWSC concept in Figure 2.1). The high-pressured fluid drives a hydraulic motor which generates power captured from waves. The electrical output is then connected to the electric grid.

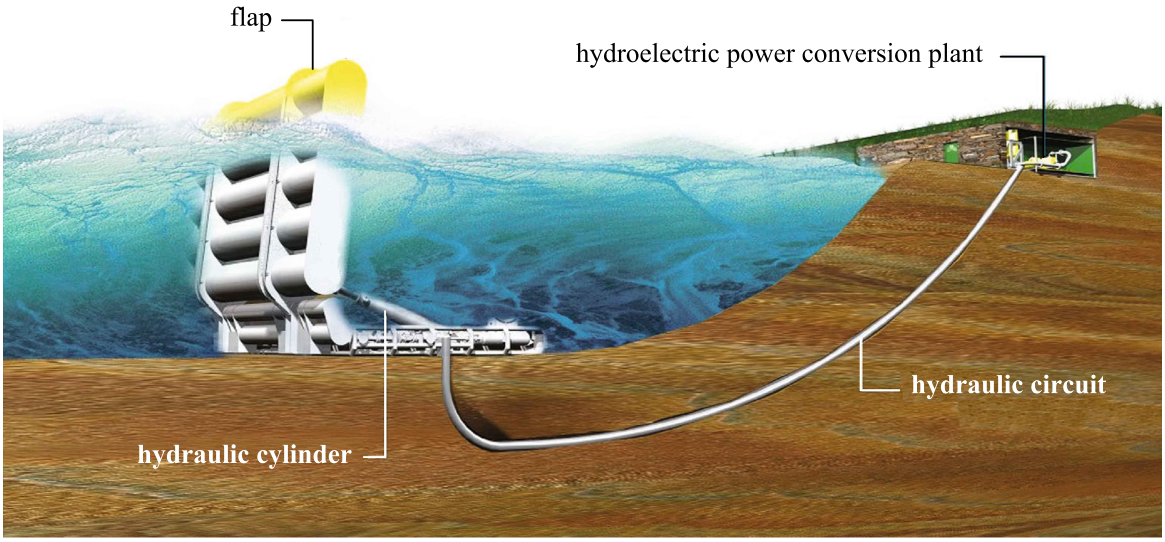

Figure 2.1: Schematic sketch of an OWSC concept (Dias et al., 2017).

The energy conversion process of the OWSCs is based on the complex interactions between wave and flap, and between flap and mechanical constraints, i.e., hydraulic PTO system, revolute joints and frictional contacts among components. Hence, mechanical constraints cannot be neglected while designing OWSCs (Whittaker and Folley, 2012).

This chapter aims to assess the state-of-the-art in the design of OWSCs, to clarify the missing issues in the study of OWSCs with mechanical constraints, and to support the objectives of the current work. The chapter first presents in Section 2.2 the literature review of analytical, experimental and numerical studies of the OWSCs. Next, a review of hydraulic PTO system models is presented in Section 2.3. Finally, the summary and conclusion are presented in Section 2.4.

2.2 Hydrodynamics of the OWSCs

2.2.1 Analytical studies

The hydrodynamics of the OWSCs have been studied analytically by several authors using linear wave theory, see e.g., Evans and Porter (1996); Parsons and Martin (1992, 1994, 1995); Renzi and Dias (2012, 2013*a*,*b*). The mathematical description provided in these studies is based on the assumption that the wave amplitude is small when compared with the wavelength, and then the motion amplitude of the flap is also small. The deduction of linear water wave theory can be found in several reference books in wave mechanics or other related subjects, see e.g., Dean and Dalrymple (1991); Falnes (2002); Newman (1977).

The early studies are often restricted to simple geometries and mainly in 2D. The key parameters that emerge from these studies are the added moment of inertia, radiation damping, wave excitation torque, mean power and CWR. Accordingly, the maximum CWR result in 2D will be close to 0.5. In many cases, the 2D solutions are not accurate to describe the complex hydrodynamics of the OWSCs noticed in the experimental studies (Renzi and Dias, 2012). In the recent years, very few studies have been carried out in 3D. The solutions are obtained based on semi-analytical methods and are often confined to single flap with simplified geometries. The radiation of the waves from a flap is an extension of the widely studied case of a 2D pivoted wavemaker radiating waves from its one side, see e.g., Dean and Dalrymple (1991); Falnes (2002).

Evans and Porter (1996) addressed the hydrodynamic characteristics of a fully-submerged flap, obtaining a semi-analytical solution for the added inertia and radiation damping coefficients for different conditions. The wave diffraction by 3D flap has been addressed by few authors for the study of isolated flap (Renzi and Dias, 2012, 2013*a*).

Renzi and Dias (2012, 2013*a*) developed an analytical model of an OWSC in a horizontal wave flume and in open ocean under unidirectional waves, respectively. Hydrodynamic radiation coefficients for three different flap widths were presented. Renzi and Dias (2013*b*) have made some analytic progress considering infinite periodic arrays of flap as a means of determining interaction effects when a long array of OWSCs are placed in a line. The analytical model developed by Renzi and Dias (2012) consists of a thin flat rectangular flap which is hinged along a horizontal axis above the flume bed in water of constant depth (see Figure 2.1). Parallel-crested waves are incident on the flap and power is taken from the rotation of the flap about the hinge. An overview of this theory is presented here for the sake of completeness as its solutions are used to explain the main experimental flow features.

2.2.1.A Governing equations and boundary conditions

The governing equations of incompressible fluids are adequately described by the following continuity and Navier-Stokes equations, respectively (Mei et al., 2005):

$$\nabla \cdot \mathbf{v} = 0 \tag{2.1}$$

$$\frac{\partial \mathbf{v}}{\partial t} + \mathbf{v} \cdot \nabla \mathbf{u} = -\frac{1}{\rho} \nabla P + \upsilon \nabla^2 \mathbf{v} + \mathbf{g} \tag{2.2}$$

where $\mathbf{v}(\mathbf{x},t)$ is the fluid velocity vector, $\mathbf{x} = (x,y,z)$ is the cartesian coordinate system, t is time, ρ is the density of the fluid, $P(\mathbf{x},t)$ is the pressure, υ is the constant kinematic viscosity, $\mathbf{g} = (0,0,-g)$ is the gravitational acceleration vector, in which g is the gravitational acceleration.

For an inviscid irrotational flow, $\mathbf{v}$ can be represented by the gradient of velocity potential, $\Phi(\mathbf{x},t)$, as:

$$\mathbf{v} = \nabla \Phi \tag{2.3}$$

Combining Equations (2.1) and (2.3) leads to the Laplace equation (Dean and Dalrymple, 1991; Newman, 1977):

$$\nabla^2 \Phi = 0, \qquad \mathbf{x} \in \Omega \tag{2.4}$$

where Ω is the fluid domain. If Φ is known, then the pressure field can be obtained by integrating the Equation (2.2) with respect to the space variables:

$$\frac{\partial \Phi}{\partial t} + \frac{1}{2} \nabla \Phi \cdot \nabla \Phi = -\frac{P}{\rho} - gz \tag{2.5}$$

Equation (2.5) is called the Bernoulli equation. The term gz on the right-hand side of this equation is the hydrostatic contribution, whereas the rest is the hydrodynamic contribution to the total pressure.

The solutions of Laplace and Bernoulli equations require the specification of the problem boundary conditions. It was considered a plane $z = 0$ that coincides with the undisturbed free-surface and the z-axis points upwards (see Figure 2.2). On the free-surface, for a wave propagating in the x-axis positive direction, the free-surface elevation, η, must be followed by the motion of the fluid with $z = \eta(x, y, t)$. This implies that the material derivative of $z - \eta(x, y, t)$ vanishes at the free-surface:

$$\frac{d}{dt}(z - \eta) = 0, \qquad z = \eta \tag{2.6}$$

where $d[\cdot]/dt \equiv \partial[\cdot]/\partial t + \mathbf{v} \cdot \nabla[\cdot]$ denotes material derivative.

The Equation (2.6) can be simplified as:

$$\frac{\partial \eta}{\partial t} + \frac{\partial \Phi}{\partial x}\frac{\partial \eta}{\partial x} + \frac{\partial \Phi}{\partial y}\frac{\partial \eta}{\partial y} = \frac{\partial \Phi}{\partial z}, \qquad z = \eta \tag{2.7}$$

Considering the assumption of small amplitude waves with slope of η to be small (i.e., $\partial \eta / \partial x \ll 1$ and $\partial \eta / \partial y \ll 1$), the kinematic free-surface boundary condition becomes:

$$\frac{\partial \eta}{\partial t} = \frac{\partial \Phi}{\partial z}, \qquad z = \eta \tag{2.8}$$

The dynamic boundary condition assures that P at the free-surface is equal to the atmospheric pressure, P_{atm}, which is assumed to be constant an equal to zero, and Equation (2.5) simplified as:

$$\frac{\partial \Phi}{\partial t} + \frac{1}{2}\nabla\Phi \cdot \nabla\Phi = -gz \tag{2.9}$$

Substituting z for η and neglecting the small second-order term $\nabla\Phi \cdot \nabla\Phi$, the linearized dynamic free-surface condition is given by:

$$\eta = -\frac{1}{g}\frac{\partial \Phi}{\partial t}, \qquad z = 0 \tag{2.10}$$

Combining Equations (2.8) and (2.10), the kinematic-dynamic free-surface boundary condition can be written as:

$$\frac{\partial^2 \Phi}{\partial t^2} + g\frac{\partial \Phi}{\partial z} = 0, \qquad z = 0 \tag{2.11}$$

The no-flux condition on the fixed, solid and impermeable boundaries requires the following kinematic boundary condition:

$$\frac{\partial \Phi}{\partial n} = 0 \tag{2.12}$$

where n is the normal to the boundary surface.

One implication of this condition is the fact that the flow is tangential to these boundaries. In particular, if these boundaries are moving the following kinematic boundary condition is required:

$$\frac{\partial \Phi}{\partial n} = v_n \tag{2.13}$$

where v_n is the normal component of the boundary velocity.

2.2.1.B Solution of the scattering and radiation problems of wave-OWSC interaction

Following Renzi and Dias (2012), the solution of Equation (2.9) for an OWSC in a horizontal wave flume can be derived in the limit of small-amplitude motion of the flap and small-amplitude wave (i.e., the physical scale of the incident wave amplitude $A_i/b \ll 1$, where b is the width of the flume). The schematic sketch of an OWSC in a horizontal wave flume with the key variables and constants is shown in Figure 2.2.

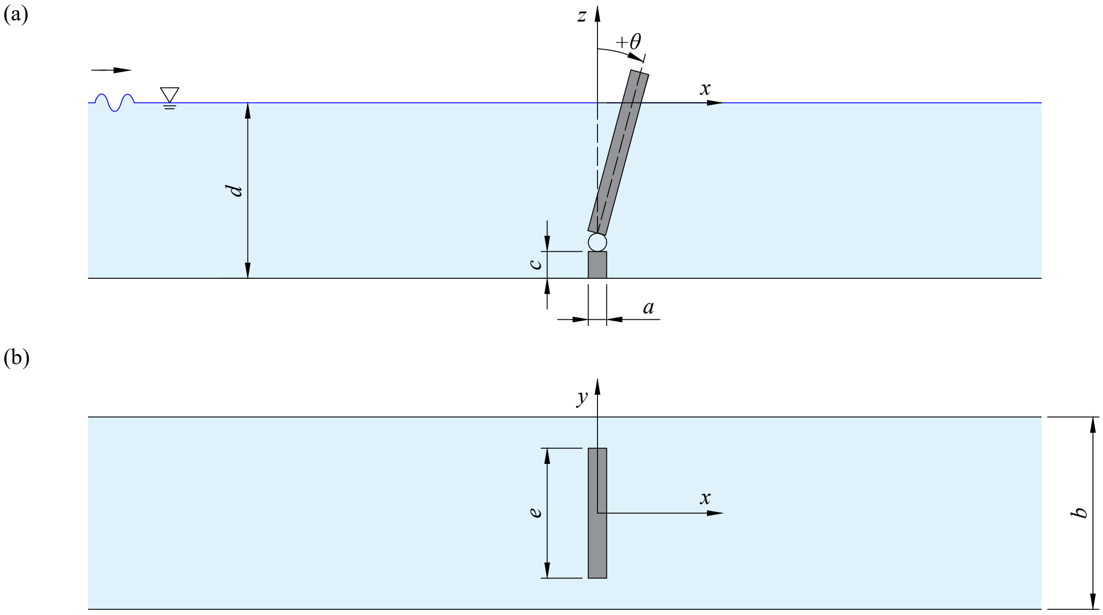

Figure 2.2: Schematic sketch of an OWSC in a horizontal wave flume: (a) side view; (b) plan view. Adapted from Renzi and Dias (2012).

The non-dimensional variables and constants are defined as:

$$\Phi' = \frac{\Phi}{\sqrt{gb}A_i} \tag{2.14}$$

$$(x', y', z', d', a', e', c') = \frac{(x, y, z, d, a, e, c)}{b} \tag{2.15}$$

$$t' = \sqrt{\frac{g}{b}}t \tag{2.16}$$

$$\eta' = \frac{\eta}{A_i} \tag{2.17}$$

$$\theta' = \frac{A_i}{b}\theta \tag{2.18}$$

$$\omega' = \sqrt{\frac{b}{g}}\omega \tag{2.19}$$

where d is the water depth, a and e are the thickness and the width of the flap, η is the free-surface elevation, ω is the angular frequency and θ is the rotation angle of the flap that can be obtained assuming that the flap undergoes simple harmonic oscillations of frequency ω, about its rest position:

$$\theta'(t') = \Re\Big\{\Theta' e^{-\mathrm{i}\omega' t'}\Big\} \tag{2.20}$$

where i is the imaginary unit, $\Re$ is the real part and Θ is the complex amplitude of θ. In this section, the prime indicates a non-dimensional physical quantity.

Equation (2.20) allows to separate the time factor in the time-dependent variables, so that Φ can be rewritten as:

$$\Phi'(\mathbf{x}', t') = \Re\Big\{\phi'(\mathbf{x}') e^{-\mathrm{i}\omega' t'}\Big\} \tag{2.21}$$

where ϕ' is the non-dimensional complex amplitude of Φ'. Due to the linearity of the problem, ϕ' is analyzed by resorting to the classical decomposition (Mei et al., 2005; Renzi and Dias, 2012):

$$\phi' = \phi'^R + \phi'^S \tag{2.22}$$

where ϕ'^R is the solution of the radiation problem, in which the flap is set to oscillate without incoming incident waves, and ϕ'^S is the solution of the scattering problem, where the flap is held fixed in incoming waves, and is given by:

$$\phi'^{S} = \phi'^{I} + \phi'^{D} \tag{2.23}$$

where ϕ'^{I} is the potential of the incident wave and ϕ'^{D} is the potential of the diffracted waves (Mei et al., 2005; Renzi and Dias, 2012). In turn, ϕ' can be decomposed into:

$$\phi' = \phi'^{R} + \phi'^{I} + \phi'^{D} \tag{2.24}$$

In Equation (2.24) each complex amplitude of velocity potential must satisfy the Laplace equation throughout the Ω. Applying the method of separation of variables to ϕ'^{I} and taking into account the bottom boundary condition (Equation (2.12)):

$$\frac{\partial \phi'}{\partial z'} = 0, \qquad z' = -d' \tag{2.25}$$

and the free-surface dynamic boundary condition (Equation (2.11)), after some algebraic manipulation yields to (see e.g., Falnes (2002); Mei et al. (2005)):

$$\phi'^{I}(\mathbf{x}') = -\frac{\mathrm{i}A'_i e^{-\mathrm{i}k'x'}}{\omega' \cosh k'd'} \cosh k'(z'+d') \tag{2.26}$$

where k' is the non-dimensional incident wavenumber.

In Renzi and Dias (2012), after some algebraic manipulation, the radiation and diffraction potential are given, respectively, by:

$$\begin{aligned}\phi'^{R}(\mathbf{x}') = -\frac{\mathrm{i}e'\dot{\Theta}'}{8} \sum_{n=0}^{\infty} \kappa_n x' Z_n(z') \sum_{p=0}^{M} \alpha_{(2p)n} \sum_{m=-\infty}^{+\infty} \int_{-1}^{1} \sqrt{1-u^2}\, U_{2p}(u) \\ \times \frac{\mathcal{H}_1^{(1)}\left(\kappa_n \sqrt{x'^2 + (y' - e'u'/2 - m)^2}\right)}{\sqrt{x'^2 + (y' - e'u'/2 - m)^2}} du\end{aligned} \tag{2.27}$$

$$\phi'^D(\mathbf{x}') = -\frac{\mathrm{i}e'\dot{\Theta}'}{8}k'x'Z_0(z')\sum_{p=0}^{M}\beta_{(2p)0}\sum_{m=-\infty}^{+\infty}\int_{-1}^{1}\sqrt{1-u^2}U_{2p}(u) \times \frac{\mathcal{H}_1^{(1)}\left(\kappa_n\sqrt{x'^2+(y'-e'u'/2-m)^2}\right)}{\sqrt{x'^2+(y'-e'u'/2-m)^2}}du \quad (2.28)$$

where $\mathcal{H}_1^{(1)}$ is the Hankel function of the first kind and first order, U_{2p} are the Chebyshev polynomials of the second kind and second order $2p$, $\dot{\Theta}' = \mathrm{i}\omega'\Theta'$ is the complex angular velocity of the flap. The subscript p indicates the order of the Chebyshev expansion, m identifies the contribution of each sources arranged periodically along the y-axis and n identifies the contribution of each depth mode:

$$Z_n(z') = \frac{\sqrt{2}\cosh\kappa'_n(z'+d')}{\sqrt{h'+\omega'^{-2}\sinh^2\kappa'_n d'}} \quad (2.29)$$

where $\kappa'_0 = k'$ and $\kappa'_n = \mathrm{i}k'_n$ are the solutions of the dispersion relations:

$$\omega'^2 = k'\tanh k'd' \quad (2.30)$$

and

$$\omega'^2 = -k'_n\tan k'_n d' \quad (2.31)$$

The $\beta_{(2p)0}$ are the complex solutions of the linear system for $n = 0$ ensuring that ϕ'^D satisfies the no-flux condition on the flap. The $\alpha_{(2p)n}$ are the complex solutions of the linear system ensuring that ϕ'^R satisfies the kinematic condition on the flap (Equation (2.13)):

$$\frac{\partial\Phi'}{\partial x'} = -\dot{\theta}'(t')(z'+h'-c')\mathcal{H}(z'+h'-c'), \qquad x' = \pm a'/2, \qquad -e'/2 < y' < e'/2 \quad (2.32)$$

where $\mathcal{H}$ denotes the Heaviside step function and $\dot{\theta}'$ is the non-dimensional angular velocity of the flap. The $\beta_{(2p)0}$ system is solved numerically with a collocation scheme, therefore the solution is partly numerical.

Note that the ϕ'^R in Equation (2.27) is an odd function of x, as suggested by the antisymmetric pitching motion of the flap. Physically, Equation (2.27) represents the sum of outgoing waves within the wave flume imposed by the lateral walls. The inner series in Equation (2.27) represents a sum of disturbances radiated by sources arranged periodically along the y-axis and converges as $m^{-3/2}$ for large m. Numerically, summation from $m=-20$ up to $m=20$ ensures convergence of the series. The central series in Equation (2.27) is truncated at $M<1$ and its coefficients were calculated numerically as described in Renzi and Dias (2012). Numerical investigation showed that $M>4$ was sufficient to ensure convergence with virtually no relative error. The outer series in Equation (2.27) over the vertical eigenmodes was found to converge quickly already for $n=4$. Hence the method of solution adopted, based on the appropriate decomposition of the Green's function, proves to be reliable and computationally efficient.

2.2.1.C Flap dynamics

Assuming that the PTO system is composed by a spring and a damper with linear characteristics, the equation of motion for a constrained flap is given by the following linear differential equation (Falnes, 2002):

$$I'\ddot{\theta}'(t')+C'\dot{\theta}'(t')+K'\theta'(t')=\mathcal{T}_e'(t') \tag{2.33}$$

where $I'=I/(\rho b^5)$ is the non-dimensional moment of inertia of the flap about the bearings, C' and K' are respectively the constant damper and stiffness coefficients, $\mathcal{T}_e'=\mathcal{T}_e/(\rho g b^4)$ is the sum of all external moments applied on the flap, $\ddot{\theta}'$ is the angular acceleration of the flap. In Equation (2.33) an over-dot is used to denote differentiation with respect to time, t'.

Using the kinematic condition on the flap (Equation (2.32)), the Equation (2.33) reads (Renzi and Dias, 2012):

$$\begin{aligned}&I'\ddot{\theta}'(t')+K'\theta'(t')=\\&-\int_{-h'+c'}^{0}\int_{-e'/2}^{e'/2}\left[\frac{\partial\Phi'}{\partial t'}(a'/2,y',z',t')-\frac{\partial\Phi'}{\partial t'}(-a'/2,y',z',t')\right](z'+d'-c')dy'dz'+\mathcal{T}_e'(t')\end{aligned} \tag{2.34}$$

Without loss of generality, $\mathcal{T}_e'$ can be given by (Mei et al., 2005):

$$\mathcal{T}_e'(t') = -\mu_{PTO}'\ddot{\theta}'(t') - \nu_{PTO}'\dot{\theta}'(t') - K_{PTO}'\theta'(t') \tag{2.35}$$

where μ_{PTO}' and K_{PTO}' are respectively the inertial and elastic characteristic of the PTO system, ν_{PTO}' is the energy extraction rate. By using the factorizations in Equations (2.20) and (2.21), employing the (2.35) and applying the solution of velocity potential in (2.26), (2.27) and (2.28), the Equation (2.34) in the frequency domain is given by:

$$\left[-\omega'^2(I' + \mu_a' + \mu_{PTO}') + K' + K_{PTO}' - \mathrm{i}\omega'(\nu_a' + \nu_{PTO}')\right]\Theta' = \mathcal{T}' \tag{2.36}$$

where μ_a' is the non-dimensional added inertia, ν_a' is the radiation damping and $\mathcal{T}'$ is the complex excitation torque, corresponding to the action on the flap as if it was held fixed in incoming waves. These parameters are defined as:

$$\mu_a' = \frac{\pi e'}{4}\Re\left\{\sum_{n=0}^{+\infty}\alpha_{0n}\frac{\sqrt{2}\left[\kappa_n'(d'-c')\sinh\kappa_n'd' + \cosh\kappa_n'c' - \cosh\kappa_n'd'\right]}{\kappa_n'^2\sqrt{d' + \omega'^{-2}\sinh^2\kappa_n'd'}}\right\} \tag{2.37}$$

$$\nu_a' = \frac{\omega'\pi e'}{4}\Im\left\{\sum_{n=0}^{+\infty}\alpha_{0n}\frac{\sqrt{2}\left[\kappa_n'(d'-c')\sinh\kappa_n'd' + \cosh\kappa_n'c' - \cosh\kappa_n d'\right]}{\kappa_n'^2\sqrt{d' + \omega'^{-2}\sinh^2\kappa_n'd'}}\right\} \tag{2.38}$$

$$\mathcal{T}' = -\frac{\mathrm{i}\pi e'\omega' A_i'}{2\sqrt{2}}\beta_{00}\frac{\left[k'(d'-c')\sinh k'd' + \cosh k'c' - \cosh k'd'\right]}{k'^2\sqrt{d' + \omega'^{-2}\sinh^2 k'd'}} \tag{2.39}$$

where $\Im$ is the imaginary part.

The average extracted power from the OWSC over a period wave T', is given by:

$$\overline{W'}_{out} = \frac{1}{T'}\int_0^{T'}\left(\nu_{PTO}'\dot{\theta}'\right)\dot{\theta}'dt' \tag{2.40}$$

$$\overline{W'}_{out} = \frac{1}{2}\frac{\omega'^2\nu_{PTO}'|\mathcal{T}'|^2}{\left[-\omega'^2(I' + \mu' + \mu_{PTO}') + K' + K_{PTO}'\right]^2 + \omega'^2(\nu' + \nu_{PTO}')^2} \tag{2.41}$$

2.2.2 Experimental studies

In what concern to physical model tests, there is a lack of experimental data of the hydrodynamics of OWSCs. In fact, very few experimental studies have been carried out focus on this topic.

Historically, the first experimental characterization of the OWSC hydrodynamics and dynamics was carried out by Folley et al. (2004). In this study, the influence of the geometric parameters of a top-hinged flap at 1:40 scale model was investigated. The OWSC model was designed to represent quasi-2D test. The rotation angle of the flap and the torque on the bearings were measured using a potentiometer and a torque transducer, respectively. A Coulomb dry friction brake on the bearings was used as PTO damping. Their tests have shown that the still water depth has an important effect on the hydrodynamics of the OWSC, and thus on the CWR.

Three years later, Folley et al. (2007) investigated the effect of water depth on the same OWSC model. In this study, a potentiometer and a torquemeter were used to measure rotation angle and braking torque, respectively, and a galvanometer was used to measure angular velocity of the flap. The CWR curve has shown an approximately quadratic relationship with applied damping torque, caused by the effects of the Coulomb dry friction. They demonstrated that both the surge wave force and CWR increase in shallow water. In the same year, Whittaker et al. (2007) studied both top-hinged and bottom-hinged flaps at both 1:40 and 1:20 scale model. These models were also designed to represent quasi-2D test and the effects of hydraulic PTO system were also not taken in consideration. They have observed that the highest CWR mostly occurs with a fully submerged flap.

Henry (2009) has also investigated the hydrodynamics of the OWSC at both 1:40 and 1:20 scale model. He has shown that the incident wave periods cause a marginal increase of CWR and the larger diameter of the freeboard reduces the viscous losses and has a greater influence on the CWR. The water depth and the flap width have shown a strong influence on the magnitude of wave force, and thus on the CWR. However, both parameters have limited effects on the hydrodynamics which reduces the CWR, especially in sea states with short periods. It was also observed that as the width increases the CWR gains, associated with the addition of the freeboard, reduces. The PTO damping used has shown a significant effect on the CWR, with constant damping producing between 20% and 30% less CWR than quadratic damping. Furthermore, it was found that applying a higher level of damping, or a damping bias, the flap pitches towards the beach, increasing the CWR of about 10%.

In recent years, Lin et al. (2012) have tested and analyzed different specifications of the flap (e.g., density, moment of inertia and location of centre of mass) on the CWR of a 1:20 scale OWSC model. Their results have shown that flap inertia was a positive relation with CWR when the wave height decreases and an opposite behavior when the wave height increases. In this study, the CWR was evaluated based on the average flow amount delivered by the hydraulic cylinders in a fixed period of time. Therefore, the instantaneous power output was not measured.

Schmitt et al. (2012) presented a series of experimental tests using a 1:25 scale OWSC model. A large number of wave probes were used to measure the free-surface elevation at different locations in the wave flume and pressure sensors were used to measure the pressure field on the flap surface. More recently, Henry et al. (2014a, 2013, 2014b) investigated the wave impacts on an OWSC in extreme sea states. The physics of the slamming process were identified using a high speed camera, and pressure field on the flap surface was measured using pressure transducers. The studies of Henry et al. (2014a, 2013, 2014b); Schmitt et al. (2012) aimed to characterize the survivability of the OWSC in the large high energetic seas and, therefore, tests were performed for decoupled PTO system.

The mentioned experimental studies on the hydrodynamics of the OWSCs have not explicitly taken into account the description of its complex mechanical constraints and the dynamic behaviors of the PTO system were not measured. Furthermore, the flow field in the vicinity of the flap was not measured and the phase differences between the hydrodynamic force and flow quantities such as velocity or free-surface elevation have not been investigated.

2.2.3 Numerical studies

Numerical modeling can provide a comprehensive flow details and a full description of hydrodynamic behaviors of the OWSCs (e.g., flow field, flap motion, excitation, inertial and drag forces). Numerical methods can take into account non-linear effects naturally (e.g., flow separation, turbulence and wave impact), which may be important for predicting accurately the CWR.

In the literature, numerical modeling of OWSCs are usually performed using CFD codes based on mesh-based methods and more recently based on mesh-free methods. The mesh-based methods have been widely applied in the modeling of OWSCs (Day et al., 2015), and have firstly be applied by Qian et al. (2005), using the AMAZON-SC code. Their results have shown that the numerical model predicts accurately the free-surface elevations. However, the flap motion was not validated. Afterward, Folley et al. (2007) have used the SWAN and WAMIT codes to simulate the effect of water depth on the CWR. They have observed that the highest CWR mostly occurs with a fully submerged flap. However, these results were obtained for linear PTO system, i.e., a rotational linear damper plus a rotational linear spring.

More recently, Lucas et al. (2012) have used the WaveDyn code to study the dynamics of the OWSC. In this code the numerical model of OWSC was constructed by connecting structural, hydrodynamic, PTO system and moorings components. The PTO module allows to define only simple models which are linear or polynomial functions of the velocity. In this context, more complex models have also been implemented to incorporate internal system dynamics and more complex losses model. However, the hydrodynamic module uses a quasi-linear formulation based on data calculated by a boundary-element method of the potential flow solver. Some important effects were included in the model, such as diffraction, radiation and hydrostatic, however non-linear effects, such as viscosity and wave-structure interaction, were neglected.

The boundary-element method was also applied by Gomes et al. (2015) to study the hydrodynamics of the OWSCs under both unidirectional regular and irregular waves. In this study, a compressive parametric analysis of the flap width and height was provided. However, much of this study, was also performed using a linear PTO system. To describe the non-linear characteristics (e.g., quadratic or Coulomb dry friction) of the PTO system, the Cummins equation was used. This equation introduces a memory function that was computed by using the linear frequency-dependent values of the radiation damping. Furthermore, similar to Lucas et al. (2012), Gomes et al. (2015) have used linear hydrodynamics and, therefore, the viscous and non-linear effects were also neglected.

To include the viscous and non-linear effects, Bhinder et al. (2012) employed the Flow3D to obtain drag coefficients for an OWSC, oscillating in translational modes only. The flap was not excited by waves but forced to oscillate. This work highlights the importance of viscosity for these types of devices; they estimated CWR reductions of almost 60% when comparing inviscid and viscous solutions.

Schmitt et al. (2012) compared pressure distributions derived from several numerical tools with experimental data for a fixed OWSC in waves. Results of fully viscous CFD simulations obtained with OpenFOAM showed very good agreement with experimental data. This work also highlights the shortcoming of codes based on the linear theory.

In the recent years, Wei et al. (2016, 2015) have used the ANSYS Fluent code to modeling OWSCs. They have investigated the viscous effects and slamming on the OWSC, and therefore the description of its complex mechanical constraints was not taken into account. The VOF method was used to locate and track the free-surface elevation. The rotation of the flap was computed using a dynamic mesh method. The numerical results have confirmed that the viscous effects play an important role on the flow field in the vicinity of the flap (turbulence, vortex shedding). They have observed that the vortex shedding from the flap is a short-lived periodic phenomenon, and that viscous scaling effects are not an important issue for OWSCs. The pressure distribution on the flap surface demonstrated the slosh feature of the impacts and indicated the location of the strongest pressure on the flap. Wei et al. (2017) have also used ANSYS Fluent to study the hydrodynamics of the OWSC. In this last study, the immersed boundary method was developed to investigate the interaction between wave and a modular OWSC. This approach allows to reduce the computational domain and thus the runtime. However, the effects of the hydraulic PTO system were also not included.

To implement the effects of energy losses in the PTO system, Schmitt et al. (2016); Schmitt and Elsaesser (2015) have used the OpenFOAM code to modeling OWSCs. In both studies the VOF and dynamic mesh methods were also used. In Schmitt and Elsaesser (2015), the results of the flap acceleration have shown a good agreement with experimental data. However, it was obtained for unconstrained flap. The effects of the mechanical constraints was then implemented by Schmitt et al. (2016), using moving dissipation zone. This implementation consisted in imposing a constant dissipation parameter in the body motion solvers. The OpenFOAM results were compared with results obtained with WAMIT and NEMOH codes. This comparison shown that even in normal operating conditions, the ideal damping settings do not scale linearly with wave height as linear theory predicts.

Martínez-Ferrer et al. (2018) have also used OpenFOAM to study the wave slamming on an OWSC under extreme sea states. The simulations were also performed in 2D and using both incompressible and compressible solvers. It was shown that the incompressible solver can capture the dynamic behaviors of the flap. Nevertheless, the compressibility effects can be reproduced only with the aid of a compressible solver, which takes into account the density changes in the air and water phases. Those effects produce small high-frequency oscillations on the seaward side of the flap but do not contribute to further increasing the peak pressure. This study was also carried out neglecting the description of the mechanical constraints.

The mentioned studies have been carried out using the mesh-based methods, but they pose difficulties when trying to incorporate mechanical constraints. Firstly, mesh-based methods require commonly expensive and complicated mesh moving algorithms (Liu and Liu, 2003; Yeylaghi et al., 2016), due to the large motion of the flap. Secondly, solving the mechanical constraints usually requires additional complex mathematical transformation to solve non-linear complementarity problem, singularities, non-uniqueness, non-penetration, inequality constraint and NP-hardness, that can be more expensive than solving the hydrodynamic interaction between wave and flap (Liu and Liu, 2003). Thirdly, some mechanical constraints (e.g. frictional revolute, prismatic and slider joints) are not, in general, continuous and straightforward application of mesh-based methods for ordinary differential equations (ODEs) require mesh size and time step that can be impracticable (Mazhar et al., 2013; Shabana, 2005; Tasora et al., 2016). Additionally, the mesh-based methods need to solve an additional equation, such as volume-of-fluid (VOF) method to locate and track the free-surface.

A promising alternative to mesh-based is the mesh-free methods. These methods are favored for modeling flow with large motion since a mesh is not required when solving the Lagrangian formulation of the Navier-Stokes equations. Among mesh-free methods, SPH has been widely adopted in the study of complex free-surface flows for its merits to easily calculate interactions between flow and driven bodies (Canelas et al., 2016; Gómez-Gesteira et al., 2010; Monaghan, 2012). The free-surface is captured in the SPH method without the need for solving additional equations to locate and track the free-surface. Moreover, SPH is considered a versatile method, naturally dealing with unsteady and non-linear flows, extreme deformations and complex topological evolutions, such as breaking free-surface (Crespo et al., 2017).

The SPH method was recently adopted to modeling OWSCs by Henry et al. (2014a); Yeylaghi et al. (2016); Zhang et al. (2018). These studies were performed to investigate 2D and 3D slamming on the OWSCs. However, given the dynamic nature of the SPH formulation, some mechanical constraints are also difficult to include in SPH form, for example, lubricated contacts or asperities between driven bodies.

The numerical results have demonstrated that the the joint (non-linear) effect of the mechanical constraints with wave interaction cannot be described accurately by using current numerical tools. This interaction has posted great CFD challenges due to the discontinuities of some mechanical constraints and due to the difference in geometric and time scales that can be of many orders of magnitude, requiring multi-scale methods in order to guarantee the well-posedness of the simulation.

2.3 Hydraulic PTO system

Due to the complexity of the hydraulic PTO systems, in practice, modeling of OWSCs are often performed using PTO force models, supposing to represent the action of the external PTO systems (Babarit et al., 2004). These models of hydraulic cylinders are often simplified and the inefficiencies such as pressure drops and frictional losses are not incorporated (Babarit et al., 2009; Falcão, 2007, 2008).

In the literature, at present, there are two ways to describing the friction force, by static and by dynamic models (Wojewoda et al., 2008). The fundamental difference between them is the frictional memory. For the static models, this frictional memory is not take into account, whereas for dynamic models, the memory effect is described with additional dynamics between the friction force and the velocity (Andersson et al., 2007; Armstrong-Hélouvry et al., 1994; de Wit et al., 1995).

In general, static friction models present discontinuity at zero velocity that allow the friction rate to take on an infinite number of possible values. This discontinuity does not reflect the real friction force behavior of hydraulic cylinders and causes errors or even instability in the algorithms used to model OWSCs, subsequently leading to inaccurate values of energy absorption (Babarit et al., 2012). Therefore, in studying of hydraulic cylinders there is a clear necessity of using dynamic friction force models to take into account the observed phenomena, such as pre-sliding displacement, frictional lag, varying break-away force and stick-slip (de Wit et al., 1995).

To capture these phenomena, dynamic friction models introduce often the state variables (or internal states) that determine the friction force, where the time evolution of state variables is given by an additional differential equation (Armstrong-Hélouvry et al., 1994; de Wit et al., 1995; Swevers et al., 2000). Several models for dynamic friction force have been proposed, see e.g., Armstrong-Hélouvry et al. (1994); de Wit et al. (1995); Swevers et al. (2000); Tran et al. (2012); Yanada and Sekikawa (2008). The review of existing friction force models are well documented in Andersson et al. (2007); Armstrong-Hélouvry et al. (1994); Ismaila et al. (2011); Olsson et al. (1998); Wojewoda et al. (2008).

There are normally two different models to describing the pressure force of hydraulic PTO system, namely the linear and non-linear models (Babarit et al., 2012). In linear model, the pressure force is linearly dependent on the velocity, leading to a global solution of the equation of motion in the frequency-domain (Child and Venugopal, 2010; Falnes, 2002; Folley and Whittaker, 2009; Korde, 1999; Yavuz et al., 2006, 2011). In many cases, this model assumes pressure force to be a combination of a spring force (which may exist or not) and a damping force (Falcão, 2010; Falnes, 2002). Moreover, PTO systems are often controlled to yield a linear relationship between PTO force and velocity, and then be modeled as a linear damper (Babarit et al., 2012). Unfortunately, the value of the ideal linear damping coefficient is not necessarily constant with frequency (Salter et al., 2002). Furthermore, the frequency of the waves does not always match the natural frequency of the OWSCs, and consequently would lead to numerical prediction of unrealistically large amplitude of motions, and thereby also energy absorption (Falcão, 2010).

In reality, non-linear effects will affect the CWR of the OWSCs (Babarit et al., 2012). A common way of modeling the non-linear effect is to add a quadratic damping term to PTO force. However, the most sophisticated pressure force model does not fully reflect the pressure characteristics observed experimentally due to the influence of some random factors (e.g., turbulence and vibration of valves) (Falcão, 2010; Falnes, 2002).

In the mentioned studies, the dynamic behavior of PTO force, which integrates friction and pressure forces, is still not fully understand (Babarit et al., 2012; Kamizuru and Murrenho, 2011; Sheng et al., 2014). The inefficiencies and dynamics of the components have not been investigated in detail (Cargo, 2012). However, its dependences with angular velocity of the flap in the time-domain have not been investigated.

2.4 Summary and conclusions

An extensive state-of-the-art review was carried out. This review was twofold. Firstly, it aimed at analytical, experimental and numerical studies on the hydrodynamics of the OWSCs. Secondly, it aimed at a better understanding of the missing and unresolved issues associated with the dynamic behavior of the hydraulic PTO system.

The analytical models of OWSCs lead to important solutions of its hydrodynamic characteristics, such as added moment of inertia, radiation damping, wave excitation torque, capture width, mean power and CWR. However, in many cases, these solutions are not accurate to describe the complex hydrodynamics of the OWSCs. The main limitations of the presented analytical model lie in its being unable to account for energy losses due to real (viscous) fluid effects (large eddy turbulence), not being capable to model accurately large amplitude of motion and joint effect with complex mechanical constraints (non-linear behaviors). Such non-linearities are known to be important on the CWR. For these reasons, in order to insight into phenomena not completed understood and to establish where empirical corrections should be applied, it is important to do physical model tests and to improve the numerical tools used nowadays.

Regarding to experimental studies, there is a lack of experimental data of the hydrodynamics of the OWSCs. In fact, some important quantities such as flow field in the vicinity of the flap was not measured, and the phase differences between the hydrodynamic force and velocity or free-surface elevation have not been investigated. Furthermore, those studies do not take into account the description of its complex mechanical constraints. For these reasons, further physical model tests are necessary to insight into a phenomena not completed understood.

With respect to numerical modeling, there is an absence of a numerical tool for modeling OWSCs with complex mechanical constraints. The interactions wave-flap-mechanical constraints cannot be described accurately by using current numerical methods, due to the discontinuities of some constraints and due to the difference in geometric and time scales that can be of many orders of magnitude, requiring multi-scale methods in order to guarantee the well-posedness of the simulation. Considering the success of SPH method for fluid description and multi-body solvers for mechanical constraints, the coupling between them can provide new simulation possibilities.

To modeling accurately the dynamics of the OWSCs it is necessary to look in more detail at the hydraulic PTO system. Since, due to the complexity of this system, the numerical models are often simplified, and the inefficiencies such as pressure drops and frictional losses are not incorporated. For these reasons, further physical model tests are also necessary to characterize the dynamic behavior of this system.

3

Numerical model

Contents

3.1 Introduction

This chapter first describes the detailed mathematical formulation of the SPH method and next the theoretical and mathematical details of the multi-body dynamic are introduced. This chapter is outlined as follows.

In Section 3.2, the continuous and discrete interpolations and their main properties are firstly introduced and then the most common kernel functions are presented. The governing equations of fluid dynamics (continuity and Navier-Stokes equations) in Lagrangian form are briefly described. The SPH (kernel and particles) approximations are applied to the governing equations to derive the corresponding discrete equations in SPH form. This discretization leads to a set of ODEs with respect to time. The time stepping schemes used to solve these ODEs are presented. The following numerical aspects in implementing the SPH method are discussed. A set of boundary conditions and algorithms for dealing with particle interactions in the SPH method are presented.

In Section 3.3, some theoretical and numerical details of multi-body dynamics with equality motion constraints are presented. The equations of motion of the corresponding unconstrained system are firstly presented. Next, the formulation is extended to systems with motion constraints. The formulation is based on a set of equations of motion, represented by a system of second order ODEs in both the coordinates and the Lagrange multipliers associated to the motion constraints. The time stepping scheme for this system is presented.

3.2 SPH method

Smooth Particle Hydrodynamics (SPH) is a Lagrangian numerical method developed by Gingold and Monaghan (1977); Lucy (1977) to solve astrophysical problems. This method was firstly introduced to model free-surface flow by Monaghan (1994) and then applied to a wide range of CFD problems, see e.g., Adami et al. (2012); Colagrossi et al. (2009); Dalrymple and Knio (2001); Dalrymple and Rogers (2006); Gómez-Gesteira et al. (2005); Gómez-Gesteira and Dalrymple (2004); Gómez-Gesteira et al. (2010); Lind et al. (2012); Marongiu et al. (2010); Marrone et al. (2011); Monaghan (2012, 2005); Monaghan et al. (2003).

In SPH method, the fluid is represented as a series of particles each one carrying out a particular mass. Mathematically, its formulation is often divided into two steps. In the first step, an arbitrary field variable is approximated by the integral interpolation or the so-called kernel approximation (Liu and Liu, 2003). In the second step, the integral interpolation of the field variable is then approximated by summing the values of the nearest neighbor particles, which yields the particle approximation of the field variable at a discrete particle. Much of the basic material mentioned herein was developed in Gingold and Monaghan (1977); Lucy (1977) and can be found in summary in Gómez-Gesteira et al. (2010); Liu and Liu (2003); Monaghan (1992, 2005).

3.2.1 Mathematical formulation

The basic idea of SPH method is to represent a generic field variable A as an interpolation of all the known values of the same variable in the domain of interest, as (Gómez-Gesteira et al., 2010; Liu and Liu, 2003; Monaghan, 2005):

$$A(\mathbf{r}) = \int_{\Omega} A(\mathbf{r}')\delta(\mathbf{r}-\mathbf{r}')d\mathbf{r}' \tag{3.1}$$

where δ is the Dirac delta function, $\mathbf{r}$ is the position where A is valuated by interpolation the known values at position $\mathbf{r}'$ and Ω is the solution space. The fundamental principle of SPH method is to approximate δ by an analytic weight function W, so-called a kernel function (Gingold and Monaghan, 1977; Lucy, 1977). The approximation of A is defined as:

$$A(\mathbf{r}) \approx \int_{\Omega} A(\mathbf{r}')W(\mathbf{r}-\mathbf{r}',h)d\mathbf{r}' \tag{3.2}$$

where h is the smoothing length or width of the kernel W.

The kernel W has the following properties:

$$\int_{\Omega} W(\mathbf{r}-\mathbf{r}',h)d\mathbf{r}' = 1 \tag{3.3a}$$

$$\lim_{h\to 0} W(\mathbf{r}-\mathbf{r}',h) = \delta(\mathbf{r}-\mathbf{r}') \tag{3.3b}$$

$$W(\mathbf{r}-\mathbf{r}',h) = 0 \quad \text{if} \quad |\mathbf{r}-\mathbf{r}'| > h \tag{3.3c}$$

The normalization condition (3.3a) and delta function condition (3.3b) relate to the approximation of δ, and the compactness condition (3.3c) means that the kernel W has compact support so that the contribution of variables out of W can be neglected. This condition saves considerable computation time for neighboring search. From the above conditions (3.3) and assuming W is symmetric, the Taylor expansion of $A(\mathbf{r}')$ about $\mathbf{r}$ gives of second order accuracy, $\mathcal{O}(h^2)$. However, this kernel approximation is not necessarily of $\mathcal{O}(h^2)$ if the W is not an even function, or if the condition (3.3a) is not satisfied, see e.g., Liu and Liu (2003).

As previously introduced, in SPH method the fluid is represented as a finite number of particles, so it is possible to rewrite Equation (3.2) in a discrete form, replacing the integral interpolation by a summation (Gingold and Monaghan, 1977; Lucy, 1977). If $A(\mathbf{r}')$ is known at the neighboring particles j, being $j = 1, 2, ..., N$, in which N is the number of particles, the approximation of $A(\mathbf{r}')$ is given by:

$$A(\mathbf{r}') = \sum_{j=1}^{N} A(\mathbf{r}_j)\delta(\mathbf{r}' - \mathbf{r}_j)\Delta V_j \tag{3.4}$$

where ΔV_j is the finite volume of neighboring particle j, given by:

$$\Delta V_j = \frac{m_j}{\rho_j} \tag{3.5}$$

where m_j and ρ_j are respectively the mass and density of particle j. Replacing Equation (3.4) into (3.2):

$$A(\mathbf{r}) \approx \sum_{j=1}^{N} \int_{\Omega} A(\mathbf{r}_j)\delta(\mathbf{r}' - \mathbf{r}_j)\Delta V_j W(\mathbf{r} - \mathbf{r}', h) d\mathbf{r}' \tag{3.6}$$

Integrating, yields to:

$$A(\mathbf{r}) \approx \sum_{j=1}^{N} \frac{m_j}{\rho_j} A(\mathbf{r}_j) W(\mathbf{r} - \mathbf{r}_j, h) \tag{3.7}$$

The approximation for A at particle i can finally be written as:

$$A(\mathbf{r}_i) \approx \sum_{j=1}^{N} \frac{m_j}{\rho_j} A(\mathbf{r}_j) W(\mathbf{r}_i - \mathbf{r}_j, h) \tag{3.8}$$

Equation (3.8) states that the value of A at particle i is approximated using the average of those values of A at all the particles in the support domain of particle i weighted by the kernel W (Gingold and Monaghan, 1977; Gómez-Gesteira et al., 2010; Liu and Liu, 2003; Lucy, 1977; Monaghan, 2005).

Following the same argument, the particle approximation for the spatial derivative of A is given by (Liu and Liu, 2003):

$$\nabla A(\mathbf{r}_i) \approx \sum_{j=1}^{N} \frac{m_j}{\rho_j} A(\mathbf{r}_j) \nabla_i W(\mathbf{r}_i - \mathbf{r}_j, h) \tag{3.9}$$

The gradient $\nabla_i W$ in Equation (3.9) is taken with respect to the particle i.

For a vector function $\mathbf{A}$, the integral interpolation and divergence can be given in a similar manner:

$$\mathbf{A}(\mathbf{r}_i) \approx \sum_{j=1}^{N} \frac{m_j}{\rho_j} \mathbf{A}(\mathbf{r}_j) W(\mathbf{r}_i - \mathbf{r}_j, h) \tag{3.10}$$

$$\nabla \cdot \mathbf{A}(\mathbf{r}_i) \approx \sum_{j=1}^{N} \frac{m_j}{\rho_j} \mathbf{A}(\mathbf{r}_j) \cdot \nabla_i W(\mathbf{r}_i - \mathbf{r}_j, h) \tag{3.11}$$

It can be seen that the particle approximation in Equations (3.8), (3.9), (3.10) and (3.11) converts the continuous integral interpolations (Equation (3.2)) of A and $\mathbf{A}$ and its derivatives to the discretized summations based on an arbitrary set of particles.

The use of particle summations to approximate the integral in Equation (3.2) is, in fact, a key approximation that makes the SPH method simple without using a background mesh for numerical integration. Note that the particle approximation introduces the mass and density of the particle into the equations. This can be conveniently applied to hydrodynamic problems in which the density is a key field variable. This is probably one of the major reasons for the SPH method being particularly popular for CFD problems. The particle approximation is, however, related to some numerical problems inherent in the SPH method, such as the particle inconsistency and the tensile instability. It may be mentioned here that the number of the sampling points for integration should be more than the field particles. The performance of the SPH method depends heavily on the selection of the kernel W (Crespo et al., 2015). The accuracy of this method increases with the order of the polynomials used to define W.

3.2.2 Kernel functions

In literature there are several kernel functions, see e.g., Liu and Liu (2003); Monaghan (1992, 2005); Monaghan and Lattanzio (1985). The most used kernel functions are: Cubic Spline and Quintic Wendland kernels. The Cubic Spline is an alternate kernel to the Gaussian kernel, with similar shape, however presenting a compact support in order to improve the computational cost (Monaghan, 2005). The Cubic Spline kernel is given by (Monaghan and Lattanzio, 1985):

$$W\left(|\mathbf{r}_i-\mathbf{r}_j|,h\right)=\alpha_D\begin{cases}1-\dfrac{3}{2}\dfrac{|\mathbf{r}_i-\mathbf{r}_j|^2}{h^2}+\dfrac{3}{4}\dfrac{|\mathbf{r}_i-\mathbf{r}_j|^3}{h^3} & \text{if} \quad \dfrac{|\mathbf{r}_i-\mathbf{r}_j|}{h}\leq 1\\[2ex] \dfrac{1}{4}\left(2-\dfrac{|\mathbf{r}_i-\mathbf{r}_j|}{h}\right)^3 & \text{if} \quad 1<\dfrac{|\mathbf{r}_i-\mathbf{r}_j|}{h}\leq 2\\[2ex] 0 & \text{if} \quad \dfrac{|\mathbf{r}_i-\mathbf{r}_j|}{h}>2\end{cases} \tag{3.12}$$

where $\alpha_D=10/(7\pi h^2)$ for 2D and $\alpha_D=1/(\pi h^3)$ for 3D modeling.

Cubic Spline kernel satisfies the requirements, i.e., is even, its first derivative is continuous and has a $2h$ radius compact support. However, it is a known issue that using this kernel may lead to particle clumping and thus the so-called tensile instability in SPH method.

To alleviate the particle clustering and improve the stability of the SPH method, a kernel based on one of the Quintic Wendland kernel suggested by Wendland (1995) has been used. The fifth-order Quintic Wendland kernel is given by:

$$W(|\mathbf{r}_i - \mathbf{r}_j|, h) = \alpha_D \begin{cases} \left(1 - \dfrac{|\mathbf{r}_i - \mathbf{r}_j|}{2h}\right)^4 \left(\dfrac{2|\mathbf{r}_i - \mathbf{r}_j|}{h} + 1\right) & \text{if} \quad \dfrac{|\mathbf{r}_i - \mathbf{r}_j|}{h} \leq 2 \\ 0 & \text{if} \quad \dfrac{|\mathbf{r}_i - \mathbf{r}_j|}{h} > 2 \end{cases} \tag{3.13}$$

where $\alpha_D = 7/(4\pi h^2)$ for 2D and $\alpha_D = 21/(16\pi h^3)$ for 3D modeling.

This kernel results in significantly reduced numerical dissipation and particle clumping (Crespo et al., 2015).

3.3 Governing equations in SPH form

In the previous sections, the essential formulations and the W for the SPH method were provided. It is seen that the SPH (kernel and particle) approximations can be used for discretization of partial differential equations. This section presents the application of the SPH method to CFD problems and the discretization of the governing equations: continuity and Navier-Stokes equations, given respectively by:

$$\frac{d\rho}{dt} + \rho \nabla \cdot \mathbf{v} = 0 \tag{3.14}$$

$$\frac{d\mathbf{v}}{dt} = -\frac{1}{\rho}\nabla P + \frac{1}{\rho}\mu \nabla^2 \mathbf{v} + \frac{1}{3}\mu \nabla(\nabla \cdot \mathbf{v}) + \mathbf{g} \tag{3.15}$$

where μ is the dynamic viscosity of the fluid.

3.3.1 Continuity equation

The fluid in the standard SPH formalism is treated as weakly compressible, which allows the use of an equation of state to determine fluid pressure (see Section 3.3.3), rather than solving another differential equation. However, the compressibility is adjusted to slow the speed of sound so that the time step in the model (based on the speed of sound) is reasonable (Crespo et al., 2015). Using Equation (3.8) it is possible to write the evolution of ρ at a particle i in a simple discrete form:

$$\rho_i = \sum_{j=1}^{N} m_j W(|\mathbf{r}_i - \mathbf{r}_j|, h) \tag{3.16}$$

where N is the number of particles in the support domain of particle i. Then the continuity equation can be directly derived in the SPH form using the following identity:

$$\rho \nabla \cdot \mathbf{v} = \nabla \cdot (\rho \mathbf{v}) - \mathbf{v} \nabla \rho \tag{3.17}$$

Hence,

$$\frac{d\rho}{dt} = -\nabla \cdot (\rho \mathbf{v}) + \mathbf{v} \nabla \rho \tag{3.18}$$

Applying the SPH approximations, meanly Equations (3.8) and (3.11), the Equation (3.18) can be written as:

$$\frac{d\rho_i}{dt} = -\sum_{j=1}^{N} \frac{m_j}{\rho_j} \rho_j \mathbf{v}_j \cdot \nabla_i W(|\mathbf{r}_i - \mathbf{r}_j|, h) + \sum_{j=1}^{N} \frac{m_j}{\rho_j} \rho_j \mathbf{v}_i \cdot \nabla_i W(|\mathbf{r}_i - \mathbf{r}_j|, h) \tag{3.19}$$

In this way it is possible to write the continuity equation in the following form:

$$\frac{d\rho_i}{dt} = \sum_{j=1}^{N} m_j \left(\mathbf{v}_i - \mathbf{v}_j\right) \cdot \nabla_i W \left(|\mathbf{r}_i - \mathbf{r}_j|, h\right) \tag{3.20}$$

In order to remove the spurious numerical high-frequency oscillations in the pressure field due to the density fluctuations, the δ-SPH formulation (Marrone et al., 2011) is also used. The Equation (3.20) is now written as:

$$\frac{d\rho_i}{dt}=\sum_{j=1}^{N}m_j\left(\mathbf{v}_i-\mathbf{v}_j\right)\cdot\nabla_iW\left(|\mathbf{r}_i-\mathbf{r}_j|,h\right)$$
$$+2\delta_\phi hc_0\sum_{j=1}^{N}\left(\rho_j-\rho_i\right)\frac{\left(\mathbf{r}_i-\mathbf{r}_j\right)\cdot\nabla_iW\left(|\mathbf{r}_i-\mathbf{r}_j|,h\right)}{\left(\mathbf{r}_i-\mathbf{r}_j\right)^2}\frac{m_j}{\rho_j} \tag{3.21}$$

where δ_ϕ is the δ-SPH coefficient that control the intensity of the diffusion of density. The use of δ-SPH can be explained as the addition of the Laplacian of the density field to the continuity equation. In Antuono et al. (2012, 2010); Molteni and Colagrossi (2009) this formulation have been careful presented and analyzed. A coefficient $\delta_\phi=0.1$ is recommended for most applications.

3.3.2 Navier-Stokes equations

The Navier-Stokes equations written for a inviscid fluid is the well known Euler equation, and can be written as:

$$\frac{d\mathbf{v}}{dt}=-\frac{1}{\rho}\nabla P+\mathbf{g} \tag{3.22}$$

The pressure gradient can be directly derived in the SPH form using the following identity:

$$\frac{1}{\rho}\nabla P=\nabla\left(\frac{P}{\rho}\right)+\frac{P}{\rho^2}\nabla\rho \tag{3.23}$$

Applying the SPH approximations, Equation (3.8), the first and second terms of right-handed side of the Equation (3.23) can be written respectively as:

$$\nabla\left(\frac{P_i}{\rho_i}\right)=\sum_{j=1}^{N}m_j\frac{P_j}{\rho_j^2}\nabla_iW(|\mathbf{r}_i-\mathbf{r}_j|,h) \tag{3.24}$$

$$\frac{P_i}{\rho_i^2}\nabla\rho_i=\frac{P_i}{\rho_i^2}\sum_{j=1}^{N}m_j\nabla_iW(|\mathbf{r}_i-\mathbf{r}_j|,h) \tag{3.25}$$

Replacing the Equations (3.24) and (3.25) into (3.23) yields to:

$$\frac{1}{\rho_i}\nabla P_i = \sum_{j=1}^{N} m_j \left(\frac{P_j}{\rho_j^2}+\frac{P_i}{\rho_i^2}\right)\nabla_i W(|\mathbf{r}_i-\mathbf{r}_j|,h) \tag{3.26}$$

Thus the Equation (3.22) can be written in SPH form as follows:

$$\frac{d\mathbf{v}_i}{dt} = -\sum_{j=1}^{N} m_j \left(\frac{P_j}{\rho_j^2}+\frac{P_i}{\rho_i^2}\right)\nabla_i W(|\mathbf{r}_i-\mathbf{r}_j|,h)+\mathbf{g} \tag{3.27}$$

The application of SPH approximations to shear stresses in Equation (3.15) is avoided since it is too sensitive to particle disorder and limits the choice of the W. Therefore to include the effect of viscosity different formulations have been used over the years in SPH method. The introduction of a viscous term in the Equation (3.27) is necessary not only to consider viscid fluids and no slip boundary conditions, but also to prevent inter-particle penetration and to improve code stability. The artificial viscosity proposed by Monaghan (1992) has been very often used due to its simplicity (Crespo et al., 2015). In SPH form the Equation (3.15) can be written as:

$$\frac{d\mathbf{v}_i}{dt} = -\sum_{j=1}^{N} m_j \left(\frac{P_j}{\rho_j^2}+\frac{P_i}{\rho_i^2}+\mathit{\Pi}_{ij}\right)\nabla_i W(|\mathbf{r}_i-\mathbf{r}_j|,h)+\mathbf{g} \tag{3.28}$$

where $\mathit{\Pi}_{ij}$ is the viscosity term, given by (Monaghan, 1992):

$$\mathit{\Pi}_{ij} = \begin{cases} \dfrac{-\alpha_\nu\,(c_i+c_j)}{(\rho_i+\rho_j)}\dfrac{h\,(\mathbf{v}_i-\mathbf{v}_j)\,(\mathbf{r}_i-\mathbf{r}_j)}{\left[(\mathbf{r}_i-\mathbf{r}_j)^2+0.01h^2\right]} & \text{if} \quad (\mathbf{v}_i-\mathbf{v}_j)\,(\mathbf{r}_i-\mathbf{r}_j)<0 \\ 0 & \text{if} \quad (\mathbf{v}_i-\mathbf{v}_j)\,(\mathbf{r}_i-\mathbf{r}_j)\geq 0 \end{cases} \tag{3.29}$$

where $\alpha_\nu \in [0.01, 0.1]$ is an empirical coefficient and c is the speed of sound. The coefficient $\alpha_\nu = 0.01$ was widely used to model both wave propagation and wave impact on structure, since it is the minimum value that prevents instability and spurious oscillations in the numerical scheme (Altomare et al., 2017).

3.3.3 Equation of state

In the standard SPH formalism the fluid is treated as Weakly Compressible SPH (WCSPH) and the following equation of state is used to determine fluid pressure based on particle density (Monaghan, 1994, 2005):

$$P_i = B\left[\left(\frac{\rho_i}{\rho_0}\right)^{\gamma_p} - 1\right] \tag{3.30}$$

where $\gamma_p = 7$ is the polytropic constant and $\rho_0 = 1000$ kg/m^3 is the reference density. The parameter B is related to the compressibility of the fluid, to provide a maximal limit for the density, B is defined as:

$$B = \frac{c_0^2 \rho_0}{\gamma_p} \tag{3.31}$$

where c_0 is the speed of sound at ρ_0, defined as:

$$c_0 = c(\rho_0) = \sqrt{\frac{\partial P}{\partial \rho}}\bigg|_{\rho_0} \tag{3.32}$$

The compressibility is adjusted so that the speed of sound can be artificially lowered; this means that the size of time step taken at any one moment (which is determined according to a Courant-Friedrich-Levy (CFL) condition, based on the currently calculated c for all particles) can be maintained at a reasonable value. Such adjustment however, restricts the c to be at least ten times faster than the maximum fluid velocity, keeping density variations to within less than 1%, and therefore not introducing major deviations from an incompressible approach (Crespo et al., 2015).

3.3.4 Boundary conditions

Boundary conditions are a major difficulty in SPH models. There are now several techniques available in the literature, such as using ghost particles, using stationary particles, Dynamic Boundary Condition (DBC), using repulsive forces or particle boundary force. In this work, the DBC was used. In DBC the boundaries are described by a set of particles that satisfy the same equations as the fluid particles (Equations (3.20) and (3.28)). An interesting advantage of these boundary conditions is their computational simplicity, since boundary particles can be calculated inside the same loops as fluid ones. For floating bodies its motion is described by net force on each boundary particle is the sum of the contributions of all surrounding fluid particles, while for boundary domain they remain either fixed in position (e.g. fixed boundaries) or move according to an imposed/assigned motion function (i.e. moving bodies such as gates or wavemakers). This DBC has been widely applied by Crespo et al. (2007, 2008); Dalrymple and Knio (2001); Gómez-Gesteira et al. (2005); Gómez-Gesteira and Dalrymple (2004); Gómez-Gesteira et al. (2010) and has been properly validated in (Altomare et al., 2014; Domínguez et al., 2015).

3.3.5 Interaction between fluid and rigid bodies

In SPH, rigid bodies is also described as a set of discrete particles whose variables are integrated in time with a different set of equations (Canelas et al., 2015; Monaghan et al., 2003). The net force on each boundary particle is the sum of the contributions of all surrounding fluid particles i.e., each body particle experiences a force per unit mass given by:

$$\mathbf{f}_k = \sum_{i \in \mathcal{A}_i} \mathbf{f}_{ki} \tag{3.33}$$

where $\mathcal{A}_i$ stands for fluid particles domain, $\mathbf{f}_{ki}$ is the force vector per unit mass exerted by the fluid particle i on the boundary particle k, which is given by:

$$m_k \mathbf{f}_k = -m_i \mathbf{f}_{ki} \tag{3.34}$$

For the motion of the moving body, the basic equations of rigid body dynamics can then be used:

$$M \frac{d\mathbf{V}}{dt} = \sum_{k \in \mathcal{A}_k} -m_k \mathbf{f}_k \tag{3.35}$$

$$\mathbf{I}\frac{d\mathbf{\Omega}}{dt} = \sum_{k\in\mathcal{A}_k} -m_k\left(\mathbf{r}_k - \mathbf{R}_0\right)\times\mathbf{f}_k \tag{3.36}$$

where $\mathcal{A}_k$ stands for boundary particles domain, M and $\mathbf{I}$ are respectively the mass and inertial tensor of the body, $\mathbf{V}$ is the linear velocity vector of the centre of mass, $\mathbf{\Omega}$ is the angular velocity, $\mathbf{r}_k$ is the position vector of particle k and $\mathbf{R}_0$ is position vector of the centre of mass. Equations (3.35) and (3.36) are integrated in time in order to predict the values of $\mathbf{V}$ and $\mathbf{\Omega}$ at the beginning of the next time step. Each particle within the body has a velocity vector given by:

$$\mathbf{v}_k = \mathbf{V} + \mathbf{\Omega}\times\left(\mathbf{r}_k - \mathbf{R}_0\right) \tag{3.37}$$

Finally, the particles within the rigid body are moved by integrating Equation (3.37) in time. Monaghan (2005); Monaghan et al. (2003) have demonstrated that this technique allows the conservation of both linear and angular momentum. Bouscasse et al. (2013) presented successful validations of non-linear wave interaction with driven bodies. Several tests of this technique are also performed in Canelas et al. (2015) who analyzed the buoyancy-driven motion with solid bodies larger than the smallest flow scales and with various densities.

3.3.6 Time stepping schemes

The physical magnitudes of the flow quantities change every time step, Δt, due to the forces calculated during particle interactions. The time integration scheme to compute the new values of these quantities at the next time step in SPH should be at least of second order to obtain accurate enough results (Crespo et al., 2015). Considering that the Equations (3.20) and (3.28), and the variation of $\mathbf{r}_i$ can be written in the following form:

$$\frac{d\mathbf{v}_i}{dt} = \mathbf{F}_i \tag{3.38}$$

$$\frac{d\rho_i}{dt} = D_i \tag{3.39}$$

$$\frac{d\mathbf{r}_i}{dt} = \mathbf{v}_i \tag{3.40}$$

where $\mathbf{v}_i$ may also include an XSPH correction when these equations are integrated in time using any stable time stepping scheme.

Two examples of time stepping schemes used in SPH codes (Crespo et al., 2015) are Verlet and Symplectic. The Verlet scheme is split into two parts and benefits from providing a low computational overhead compared to some other integration techniques, primarily as it does not require multiple (i.e., predictor and corrector) calculations for each step (Verlet, 1967). The predictor stage calculates the variables according to:

$$\begin{cases} \mathbf{v}_i^{n+1} = \mathbf{v}_i^{n-1} + 2\Delta t \mathbf{F}_i^n \\ \rho_i^{n+1} = \rho_i^{n-1} + 2\Delta t D_i^n \\ \mathbf{r}_i^{n+1} = \mathbf{r}_i^n + \Delta t \mathbf{v}_i^n + \frac{\Delta t^2}{2} \mathbf{F}_i^n \end{cases} \tag{3.41}$$

where the superscript n denotes the present time step.

The corrector stage is used every certain number of steps (normally 50 steps is suggested) to correct the variables according to:

$$\begin{cases} \mathbf{v}_i^{n+1} = \mathbf{v}_i^n + \Delta t \mathbf{F}_i^n \\ \rho_i^{n+1} = \rho_i^n + \Delta t D_i^n \\ \mathbf{r}_i^{n+1} = \mathbf{r}_i^n + \Delta t \mathbf{v}_i^n + \frac{\Delta t^2}{2} \mathbf{F}_i^n \end{cases} \tag{3.42}$$

This corrector stage is designed to stop divergence of integrated values through time as the equations are no longer coupled. In cases where the Verlet scheme is used but it is found that numerical stability is an issue, it may be sensible to increase the frequency at which the second part of this scheme (Equation 3.42) is applied, however if it should be necessary to increase this frequency beyond 10 steps then this could indicate that the scheme is not able to capture the dynamics of the case in hand suitably and the Symplectic scheme should be used instead.

Symplectic scheme is time reversible in the absence of friction or viscous effects (Leimkuhler et al., 1996). This scheme can also preserve geometric features, such as the energy time-reversal symmetry present in the equations of motion, leading to improved resolution of long term solution behavior. The scheme used in this work is an explicit second-order Symplectic scheme with an accuracy in time of $\mathcal{O}(\Delta t^2)$ and involves a predictor and corrector stage. During the predictor stage the values of acceleration and density are estimated at the middle of the time step, according to:

$$\begin{cases} \rho_i^{n+\frac{1}{2}} = \rho_i^n + \frac{\Delta t}{2} D_i^n \\ \mathbf{r}_i^{n+\frac{1}{2}} = \mathbf{r}_i^n + \frac{\Delta t}{2} \mathbf{v}_i^n \end{cases} \tag{3.43}$$

During the corrector stage the acceleration, $(\mathbf{v}_i^{n+1} - \mathbf{v}_i^n)/\Delta t$, is used to calculate the corrected velocity, and therefore position, of the particles at the end of the time step according to:

$$\begin{cases} \mathbf{v}_i^{n+1} = \mathbf{v}_i^{n+\frac{1}{2}} + \frac{\Delta t}{2} \mathbf{F}_i^{n+\frac{1}{2}} \\ \mathbf{r}_i^{n+1} = \mathbf{r}_i^{n+\frac{1}{2}} + \frac{\Delta t}{2} \mathbf{v}_i^{n+1} \end{cases} \tag{3.44}$$

At the end of the time step the variation of density, $(\rho_i^{n+1} - \rho_i^n)/\Delta t$, is calculated using the updated values of $\mathbf{r}_i^{n+1}$ and $\mathbf{v}_i^{n+1}$.

The time step control is dependent on the flow properties, the forcing terms, the CFL condition and the viscous diffusion term. For example, the time step decreases when the fluid collides with fixed boundaries since the forces increase. In general, the time step depends on the force per unit mass and the CFL condition. A variable Δt is calculated according to (Monaghan and Kos, 1999):

$$\Delta t = 0.3 \cdot \min\left(\Delta t_f, \Delta t_{cv}\right) \tag{3.45}$$

where Δt_f is time step calculated based on the force per unit mass, $\mathbf{f}_i$, and Δt_{cv} is the time step that combines the CFL and the viscous time step controls, defined respectevely as:

$$\Delta t_f = \min_i \left(\sqrt{\frac{h}{\mathbf{f}_i}} \right) \tag{3.46}$$

$$\Delta t_{cv} = \min_i \frac{h}{c_0 + \max_j \left| \frac{h\left(\mathbf{v}_i - \mathbf{v}_j\right) \cdot \left(\mathbf{r}_i - \mathbf{r}_j\right)}{\left(\mathbf{r}_i - \mathbf{r}_j\right)^2 + 0.01h^2} \right|} \tag{3.47}$$

3.4 Multi-body mechanics

Unlike particles, rigid bodies have distributed masses. The configuration of a rigid body in space can be identified by using six independent coordinates (Shabana, 2005). Three coordinates describe the body translation and three coordinates define the orientation of the body. Figure 3.1a shows a schematic sketch of a rigid body in 3D space, where $Oxyz$ is a coordinate system that is fixed in time and $\tilde{O}\tilde{x}\tilde{y}\tilde{z}$ is a body coordinate system or body reference whose origin is rigidly attached to a point on the rigid body.

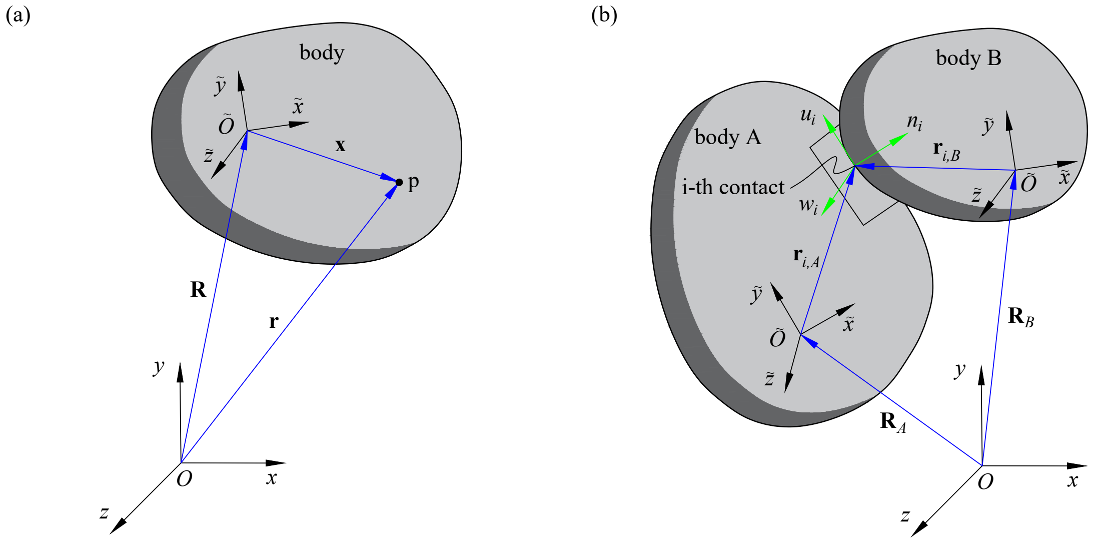

Figure 3.1: Schematic sketch of rigid body dynamics: (a) a rigid body in 3D space; (b) contact i between two bodies A and B.

Considering the global position of an arbitrary point p, the position $\mathbf{r}$ on a body can be defined as (see Figure 3.1a):

$$\mathbf{r} = \mathbf{R}^{\mathrm{T}} + \mathbf{x}^{\mathrm{T}} \tag{3.48}$$

where $\mathbf{R}$ is the global position vector of the origin of the body reference and $\mathbf{x}$ is the position vector of point p with respect to $\tilde{O}$. Since the body is considered rigid, $\mathbf{x}$ remains constant during the motion of the body. The vectors $\mathbf{r}$ and $\mathbf{R}$, however, are defined in the global coordinate system. Therefore, it is important to be able to express the vector $\mathbf{x}$ in terms of its components along the fixed global axes. To this end, one needs to define the orientation of the body coordinate system with respect to the global frame of reference. A transformation between these two coordinate systems can be developed in terms of a set of rotational coordinates. However, this set of rotational coordinates is not unique, and many representations can be found in the literature (Shabana, 2005). The configuration of a rigid multi-body system is described by using six independent coordinates, called generalized coordinates, defined as:

$$\mathbf{q} = [\mathbf{R}^{\mathrm{T}} + \boldsymbol{\Theta}^{\mathrm{T}}]^{\mathrm{T}} \tag{3.49}$$

where $\boldsymbol{\Theta}$ is rotational coordinates that defines the orientation of the body. These coordinates allow to completely define the location and orientation of each body in the system (Shabana, 2005). Once this set of coordinates is identified, the global position of an arbitrary point on the body can be expressed in terms of $\mathbf{q}$.

Equation (3.49) describes the global position of an arbitrary point on the body and implies that the general motion of a rigid body is equivalent to a translation of one point plus a rotation. A rigid body is said to experience pure translation if the displacements of any two points on the body are the same. A rigid body is said to experience a pure rotation about an axis called the axis of rotation, if the particles forming the rigid body move in parallel planes along circles centered on the same axis. A pure rotation can be obtained if one point on the body is fixed, called the base point. This will eliminate the translational degrees of freedom of the body. This is, in fact, Euler's theorem, which states that the general displacements of a rigid body with one point fixed is a rotation about some axis that passes through that point. If no point is fixed, the general motion of a rigid body is given by Chasles' theorem, which states that the most general motion of a rigid body is equivalent to a translation of a point on the body plus a rotation about an axis passing through that point.

3.4.1 Rigid multi-body dynamics

A multi-body system with contact and constraints can be described by Newton-Euler equations. A schematic sketch of the contact between two rigid bodies A and B is shown in Figure 3.1b. Assuming that the body geometries are regular at this point, the contact point along with the shared tangent plane are used to define two local reference frames, one for each body. For body A, the normal $\mathbf{n}_{i,A}$ at contact point i is chosen to be perpendicular on the tangent plane at the shared contact point and to point towards the exterior of body A. Two mutually perpendicular unit vectors $\mathbf{u}_{i,A}$ and $\mathbf{w}_{i,A}$ are chosen to define a right-hand local reference frame associated with contact i on body A. A similar sequence of steps is followed to define a local reference frame for body B based on $\mathbf{n}_{i,B}$, $\mathbf{u}_{i,B}$ and $\mathbf{w}_{i,B}$.

The force associated with contact i can be given by:

$$\mathbf{F}_i = \Gamma_{i,n}\mathbf{n}_i + \Gamma_{i,u}\mathbf{u}_i + \Gamma_{i,w}\mathbf{w}_i \tag{3.50}$$

where $\Gamma_{i,n}$, $\Gamma_{i,u}$ and $\Gamma_{i,w}$ are the Lagrange multipliers, the subscripts n, u and w stand for the orientation of local reference frames at contact point i (Mazhar et al., 2015).

The dynamic equations that govern the motion of rigid bodies can be systematically obtained from the particle equations by assuming that the rigid body consists of a large number of particles. It can be demonstrated that the unconstrained 3D motion of the rigid body can be described using six equations; three equations are associated with the translation of the rigid body, and three equations are associated with the body rotation. If a centroidal body coordinate system is used, the translational equations are called Newton equations, while the rotational equations are called Euler equations. Newton-Euler equations which are expressed in terms of the accelerations and forces acting on the body can be used to describe an arbitrary rigid body motion.

The Newton-Euler equations of a multi-body system with contact and constraints can be written as a system of two differential algebraic equations in the following form (Tasora et al., 2016):

$$\frac{d\mathbf{q}}{dt} = \mathbf{L}(\mathbf{q})\mathbf{V} \tag{3.51}$$

$$\mathbf{M}(\mathbf{q})\frac{d\mathbf{V}}{dt} = \mathbf{F}_a(\mathbf{V},\mathbf{q},t) + \sum_{i\in\mathcal{A}(\mathbf{q},\delta)} (\Gamma_{i,n}\mathbf{D}_{i,n} + \Gamma_{i,u}\mathbf{D}_{i,u} + \Gamma_{i,w}\mathbf{D}_{i,w}) \tag{3.52}$$

where $\mathbf{L}$ is a Jacobian matrix that connects $\mathbf{V}$ to the derivative of $\mathbf{q}$, $\mathbf{M}$ is the mass matrix, $\mathbf{F}_a$ is applied forces and $\mathbf{D}_{i,n}$, $\mathbf{D}_{i,u}$, and $\mathbf{D}_{i,w}$ are tangent space generators.

Equation (3.51) relates the time derivative of $\mathbf{q}$ and $\mathbf{V}$ through a linear transformation defined by $\mathbf{L}$, while (3.52) is the force balance that ties the inertial forces to the applied and constraint forces. The constraint forces are imposed by bilateral constraints that restrict the relative motion of the rigid bodies present in the system. The inclusion states that the frictional contact force lies somewhere inside the friction cone, with a value yet to be determined and controlled by the stick/slip state of the interaction between body and ground (Tasora et al., 2016). In multi-body dynamics the differential inclusion can be posed as a differential variational inequality problem (Stewart, 2000). Specifically, the unilateral constraints define a set of contact complementarity conditions $0 \leq \Psi_i(\mathbf{q}) \perp \Gamma_{i,n} \geq 0$ which make a simple point: for a potential contact i in the active set:

$$i \in \mathcal{A}_q(\mathbf{q},\delta) : \begin{cases} 0 \leq \Psi_i(\mathbf{q}) \perp \Gamma_{i,n} \geq 0 \\ (\Gamma_{i,u},\Gamma_{i,w}) = \underset{\sqrt{y^2+z^2}\leq\mu_i\Gamma_{i,n}}{\operatorname{argmin}} \mathbf{V}^{\mathrm{T}} \cdot (y\mathbf{D}_{i,u} + z\mathbf{D}_{i,w}) \end{cases} \tag{3.53}$$

where Ψ_i is the gap (distance) between two bodies.

Equation (3.53) poses an optimization problem whose first order Karush-Kuhn-Tucker optimality conditions are equivalent to the Coulomb dry friction model. The frictional contact force associated with contact i leads to a set of generalized forces, which are obtained using $\mathbf{D}_{i,n}$, $\mathbf{D}_{i,u}$, and $\mathbf{D}_{i,w}$. The time stepping used in this work is a variant of the well-known implicit Euler method for ODEs (Anitescu, 2006; Anitescu and Hart, 2004; Mazhar et al., 2015; Stewart, 2000).

3.4.2 Time stepping scheme

The numerical solution methodology for the aforementioned Differential Variational Inequality (DVI) problem is built around the following two decisions: i) following the approach proposed in Stewart (2000), a symplectic half-implicit Euler method is used to discretize the dynamics; and ii) a zero gap non-penetration condition between bodies in mutual contact is enforced at the new time step.

The numerical solution at $t^{n+1} = t^n + \Delta t$ is obtained by solving the following numerical problem with complementarity and equilibrium constraints, given as:

$$\mathbf{q}^{n+1} = \mathbf{q}^n + \Delta t \mathbf{L}(\mathbf{q}^n)\mathbf{V}^{n+1} \tag{3.54}$$

$$\begin{aligned}\mathbf{M}(\mathbf{q}^n)\left(\mathbf{V}^{n+1} - \mathbf{V}^n\right) = \Delta t \mathbf{F}_a(\mathbf{V}^n, \mathbf{q}^n, t^n) \\ + \sum_{i \in \mathcal{A}(\mathbf{q}^n, \delta)} \Delta t \left(\Gamma_{i,n}^n \mathbf{D}_{i,n} + \Gamma_{i,u}^n \mathbf{D}_{i,u} + \Gamma_{i,w}^n \mathbf{D}_{i,w}\right)\end{aligned} \tag{3.55}$$

$$i \in \mathcal{A}_q(\mathbf{q}^n, \delta) : \begin{cases} 0 \leq \frac{1}{\Delta t}\Psi_i(\mathbf{q}^n) + \mathbf{D}_{i,n}^T \cdot \mathbf{V}^{n+1} \perp \Gamma_{i,n} \geq 0 \\ (\Gamma_{i,u}, \Gamma_{i,w}) = \underset{\sqrt{y^2+z^2} \leq \mu_i \Gamma_{i,n}}{\operatorname{argmin}} \mathbf{V}^{\mathrm{T}} \cdot (y\mathbf{D}_{i,u} + z\mathbf{D}_{i,w}) \end{cases} \tag{3.56}$$

It should be noted, in Equations (3.55) and (3.56) the superscript n denotes the present time step and subscript n stands for the normal orientation of local reference frames at contact point i (see Figure 3.1b).

In Equation (3.56) the term $\frac{1}{\Delta t}\Psi_i(\mathbf{q}^n)$ achieves the constraint stabilization by eliminating any penetration within one time step Δt. The overall time stepping scheme is summarized as: a multi-body dynamics frictional contact application is formulated as a DVI problem which, based on decisions i) and ii), morphs into an non-linear complementarity problem. Equation (3.55) is then used to expeditiously compute the velocity $\mathbf{V}^{n+1}$. The generalized coordinates $\mathbf{q}^{n+1}$ are recovered using Equation (3.54) and the simulation is advanced at $n+1$.

3.5 Summary and conclusions

This chapter describes the detailed mathematical formulation of the SPH method and the theoretical and mathematical details of the multi-body dynamics.

SPH method has been widely adopted in the study of complex free-surface flows for its merits to easily calculate interactions between flow and driven bodies. The free-surface is captured in the SPH method without the need for solving additional equations to locate and track the free-surface. Moreover, SPH is considered a versatile method, naturally dealing with unsteady and non-linear flows, extreme deformations and complex topological evolutions, such as a breaking free-surface. However, given the dynamic nature of the SPH formulation, some mechanical constraints are also difficult to include in SPH form, for example lubricated contacts or asperities between driven bodies. Considering the success of SPH for fluid descriptions and multi-body solver for mechanical constraints, the coupling between them is expected to provide new simulation possibilities.

4

Numerical implementation

Contents

4.1 Introduction

In order to take into account the interaction between the flap and mechanical constraints it is necessary to implement the Project Chrono library under the DualSPHysics code. This chapter presents the detail of the numerical implementation. The main characteristics of the DualSPHysics and Project Chrono codes are firstly introduced in Sections 4.2 and 4.3, respectively, focusing in particular to the aspects that are relevant in thesis context. In Section 4.4 the coupling procedure between DualSPHysics and Project Chrono is presented.

4.2 Overview of the DualSPHysics

DualSPHysics is an open-source code based on SPH method (`http://dual.sphysics.org`). This code is implemented in C++ and Compute Unified Device Architecture (CUDA), using WCSPH formulation (see Section 3.3.3), and is designed to launch simulations either on multiple Central Processing Units (CPU) using Open Multi-Processing (OpenMP) or on a Graphics Processing Units (GPU). In this context, some files are common for the SPH solver while others are specific to CPU or GPU executions. In order to compile the code for CPU execution, only a C++ compiler is needed with the resultant binary allowing the code to be run on workstations. To run DualSPHysics on GPU, an NVIDIA CUDA-enabled GPU is needed and the GPU driver must be installed. To compile the source code, the GPU programming language CUDA and NVIDIA CUDA compiler driver must also be installed.

The GPU implementation of DualSPHysics allows to simulate millions of particles at a reasonable computation time, allowing to somewhat alleviate the previously expressed concerns about requirements of scale and resolution, since the computations are made up to two orders of magnitude faster than on conventional CPU systems (Domínguez et al., 2013).

The GPU implementation is initially focused on the force computation as this is the most consuming part in terms of runtime. The most efficient technique has been found to be to minimise communication between the CPU and GPU, as the Peripheral Component Interconnect (PCI) Express bus used by current GPU hardware is the slowest point in the computing infrastructure. If the neighbour list and system update are also implemented on the GPU a CPU-GPU memory transfer is only needed at the beginning of the simulation, while relevant data is transferred to the CPU only when saving output data is required. Hence, the three steps were implemented entirely on the GPU to minimise CPU-GPU data transfer.

The GPU and CPU implementations of DualSPHysics are optimised differently to exploit the characteristics of the two architectures. The main difference is the manner in which parallel execution is performed. For example, for all loops regarding particle interactions the GPU model uses one thread of execution to compute the resulting force of one particle as it performs all interactions with its neighbours. In the CPU however symmetry of particle interaction is exploited in order to reduce runtime. This optimisation is not applied in the GPU implementation as there is no efficient solution to avoid typical parallel problems such as memory race conditions arising from using slightly faster but simple approaches of assuming one particle per thread.

The main code has a common core for both the CPU and GPU implementations, with only minor source code differences, implemented for the two devices applying the specific optimisations for CPU and GPU. It is important to note that the CPU and GPU versions of the code may produce results that exhibit minor differences given the same initial condition. These differences are due to the fact that parallel operations may be performed in different orders, which, with floating point arithmetic, can lead to differences in the final few decimal digits. Also the use of different hardware can lead to small differences when IEEE-754 is not fully supported. This effect is common to parallel codes and is an expected phenomenon that should be kept in mind when comparing results obtained using different computing hardware. In Crespo et al. (2015) a diagram that represents the differences between the CPU and GPU implementations and the different steps involved in a complete execution is presented.

Along with the source code, documentation that describes the compilation and execution of the source files, including a set of C++ and CUDA files need to be compiled to generate the DualSPHysics binary, are distributed. In Crespo et al. (2015) all the source files are listed, however each file contains more detailed comments describing the WCSPH formulation and the algorithms.

Different format files for the input and the output data are involved in the DualSPHysics execution, such as .xml, .bi2 and .vtk.

The Extensible Markup Language (XML) is a textual data format that can easily be read or written using any platform and operating system. It is based on a set of labels (tags) that organize the information and can be loaded or written easily using any standard text editor. This format is used as input files for the DualSPHysics code. A XML file contains all the parameters of the system configuration and its execution, such as key variables (i.e., smoothing length, h, reference density, ρ_0, gravitational acceleration vector, $\mathbf{g}$, and speed of sound, c), the number of particles in the system, motion definition of moving boundaries (e.g, wavemaker), properties of moving bodies including mechanical constraints. Different execution parameters can be changed in the XML file: time stepping algorithm (see Section 3.3.6), choice of kernel function (see Section 3.2.2), the value for artificial viscosity, activation of the Shepard density filter and how often it is applied, activation of the δ-SPH correction, the maximum time of simulation and time intervals to save the output data. An example of a XML file is presented in Appendix A.

As DualSPHysics allows simulations to be performed with a large number of particles, a binary file format is used. This format is named BINX2 (.bi2). The files contain only the meaningful information of particle properties. Some variables are removed, e.g., the pressure, P, is not stored since it can be calculated starting from the density using the Equation (3.30) as a pre-processing step. The value of m is constant for fluid and boundary particles and so only two values are used instead of an array. The position of fixed boundary particles is only stored in the first file since they remain unchanged throughout the simulation. Data for particles that leave the limits of the domain are stored in an independent file which leads to an additional saving. Hence, the advantages of BINX2 are the memory storage reduction, fast access, no precision lost and portability (i.e., to different architectures or different operating systems).

VTK (Visualisation ToolKit) files are used for final visualisation of the results and can either be generated as a pre-processing step or output directly by DualSPHysics instead of the standard BINX format (albeit at the expense of computational overhead). VTK not only supports the particle positions, but also physical quantities that are obtained numerically. The VTK file format consists of a header that describes the data and includes any other useful information, the dataset structure with the geometry and topology of the dataset and its attributes. The VTK files of POLYDATA type with legacy-binary format is used.

4.3 Overview of the Project Chrono

Project Chrono is an open-source multi-physics simulation platform (`https://projectchrono.org`). This code is also implemented in C++. A Project Chrono library allows to simulate multi-body and for the straightforward definition of a large number of mechanical constraints, such as joints and sliders, friction and restitution coefficients, restitution forces, and user imposed forces and trajectories with arbitrary degrees of freedom (Mazhar et al., 2013; Tasora and Anitescu, 2011; Tasora et al., 2016). In Project Chrono the configuration of a rigid multi-body system is described by generalized coordinates $\mathbf{q}$ (see Section 3.4). Once this set of coordinates is identified, the global position of an arbitrary point on the body can be expressed in terms of $\mathbf{q}$ (Shabana, 2005).

Project Chrono is organized as a set of modules. These modules are additional libraries that can be optionally used to expand the features of Project Chrono. In this sense, the Project Chrono framework is a modular concept that can be expanded or simplified depending on a user's needs. In this context, Project Chrono does not force the user to have all these prerequisites. Project Chrono can compile and use only the modules that are strictly needed by the user. Splitting the project into smaller components avoids producing a monolithic and huge dll. Further modules could be developed without changing the core library of the project. The Project Chrono module compilation is thus conditional: the user can enable a module compilation. Otherwise, the module is disabled, which keeps the build process clean and simple. A list of the available modules, along with information on how to compile them, can be found in the modules page (`http://api.projectchrono.org/3.0.0/modules.html`). In terms of user support, the API documentation for the main Chrono modules is generated from their annotated C++ sources using Doxygen. All Project Chrono software is configured and built using CMake for a robust cross-platform build experience under Linux, Mac OSX, and Windows.

Project Chrono also allows the GPU computing (as enabled by CUDA), multi-core parallel computing (as enabled by OpenMP), and distributed-memory parallel computing, as enabled by Message Passing Interface (MPI). An Application Programming Interface (API) is in place to define and to perform the operations. User toolkits are also in place to ease the pre- and post-processing. This code allows to investigate the time evolution of systems governed by very large sets of differential-algebraic equations and/or ODEs and/or partial differential equations. Project Chrono can be used to simulate the dynamics of large systems of connected bodies governed by differential-algebraic equations; controls and other first-order dynamic systems governed by ODEs; and to simulate the dynamics of deformable bodies governed by partial differential equations. Project Chrono can handle multi-physics problems in which the solution calls for the mixing of the above dynamics (Mazhar et al., 2013; Tasora and Anitescu, 2011; Tasora et al., 2016).

Project Chrono has five foundational components that provide support for equation formulation, equation solution, proximity computation, parallel computing and post-processing (Tasora et al., 2016). The first foundation component, equation formulation, supports general-purpose modeling for large systems of rigid and flexible bodies. The equation solution, provides the algorithmic support needed to solve the equations of motion. Proximity computation support, provided by the third foundation component, is essential for collision detection and computation of short range interaction forces. The fourth component enables the partitioning and farming out of very large dynamics problems for parallel execution on supercomputer architectures using the MPI paradigm. The fifth component provides pre- and post-processing support. It is compiled into a library subsequently used by third party applications.

4.4 Coupling between DualSPHysics and Project Chrono

As an overview, the source code files that allow the coupling between DualSPHysics and Project Chrono are presented in Figure 4.1.

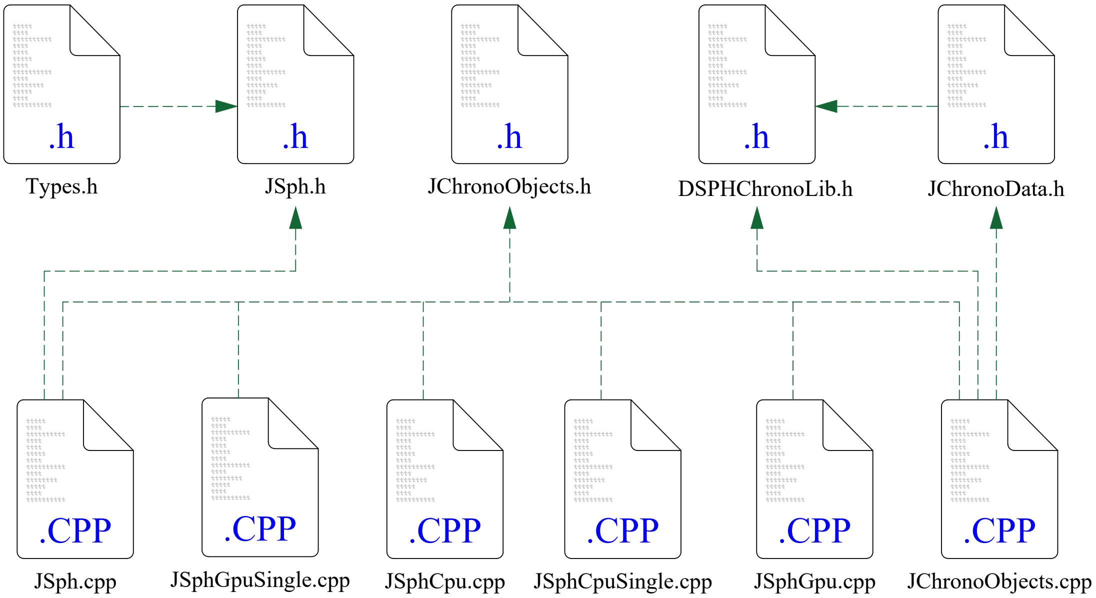

Figure 4.1: Source code files adapted and implemented for coupling between DualSPHysics and Project Chrono.

The coupling was performed using common codes for both CPU and GPU implementations that compose floating bodies and new codes for integration and configuration of Project Chrono library.

The common codes used for the implementation of Project Chrono library are included in the Types.h, JSph.h, JSph.cpp, JSphCpu.cpp, JSphGpu.cpp, JSphCpuSingle.cpp, and JSphGpuSingle.cpp files.

The basic structure of the DualSPHysics is contained in Types.h file, which contains the definition of specific types for the SPH application. The JSph.h and JSph.cpp files contain respectively the declaration and implementation of the class that defines all the attributes and functions that CPU and GPU simulations share. The JSphCpu.cpp and JSphCpuSingle.cpp contain the implementation of the class that defines the attributes and functions used only in CPU simulations and single-CPU, respectively. The JSphGpu.cpp and JSphGpuSingle.cpp contain the implementation of the class that defines the attributes and functions used only in GPU simulations and single-GPU, respectively.

The codes for integration and configuration of Project Chrono library are composed by JChronoObjects.h, JChronoData.h, DSPHChronoLib.h and JChronoObjects.cpp files (see Appendix B). The JChronoObjects.h allows to interface DualSPHysics with dsphchrono.dll library. The JChronoData.h contains the declaration of the class that stores the different body configuration and its integration with Project Chrono. DSPHChronoLib.h contains the declaration of the classes that reads, configures and computes the coupling between DualSPHysics and Project Chrono and JChronoObjects.cpp contains the implementation of those classes.

The numerical implementation of Project Chrono under DualSPHysics starts by adding a new formulation (usechrono) to the structure with the information of the floating body in Types.h file. This structure starts at line 84 in Listing B.1 (see Appendix B), with the usual definition of typedef struct and the usechrono is included at line 94.

The class that manages the information of Project Chrono from the input XML file is declared in JChronoData.h (Listing B.2). This file loads the initial configuration of each floating body including the mechanical constraints among bodies. Several types of mechanical constraints can be load from the input XML file, such as LK_Hinge, LK_Spheric, LK_PointLine and LK_CustomSpring. Within LK_CustomSpring, the user is able to define any constraint force among bodies.

The configuration of each floating body was implemented in JSph.cpp file, from line 543 to 563 in Listing B.3. The inertia tensor of each floating body is calculated some lines below

(Listing B.4). The exportation of this tensor to Project Chrono is performed in line 1234.

After the exportation of the inertia tensor, the Project Chrono physical system is declared in `DSPHChronoLib.h` file (Listing B.5). This file contains the forward declarations to avoid including Project Chrono classes. The simulations can be executed either on the CPU or on the GPU using the function RunChrono implemented in `JSphCpuSingle.cpp` and `JSphGpuSingle.cpp`, respectively (see Listings B.7 and B.8). The RunChrono is then executed according to the classes implemented in `DSPHChronoLib.cpp`. This file contains the configuration of each mechanical constraint, i.e., LK_Hinge, LK_Spheric, LK_PointLine and LK_CustomSpring in Project Chrono. An example of `DSPHChronoLib.cpp` file is presented in Appendix C.

To explain the full coupling procedure, a detailed flow chart is presented in Figure 4.2.

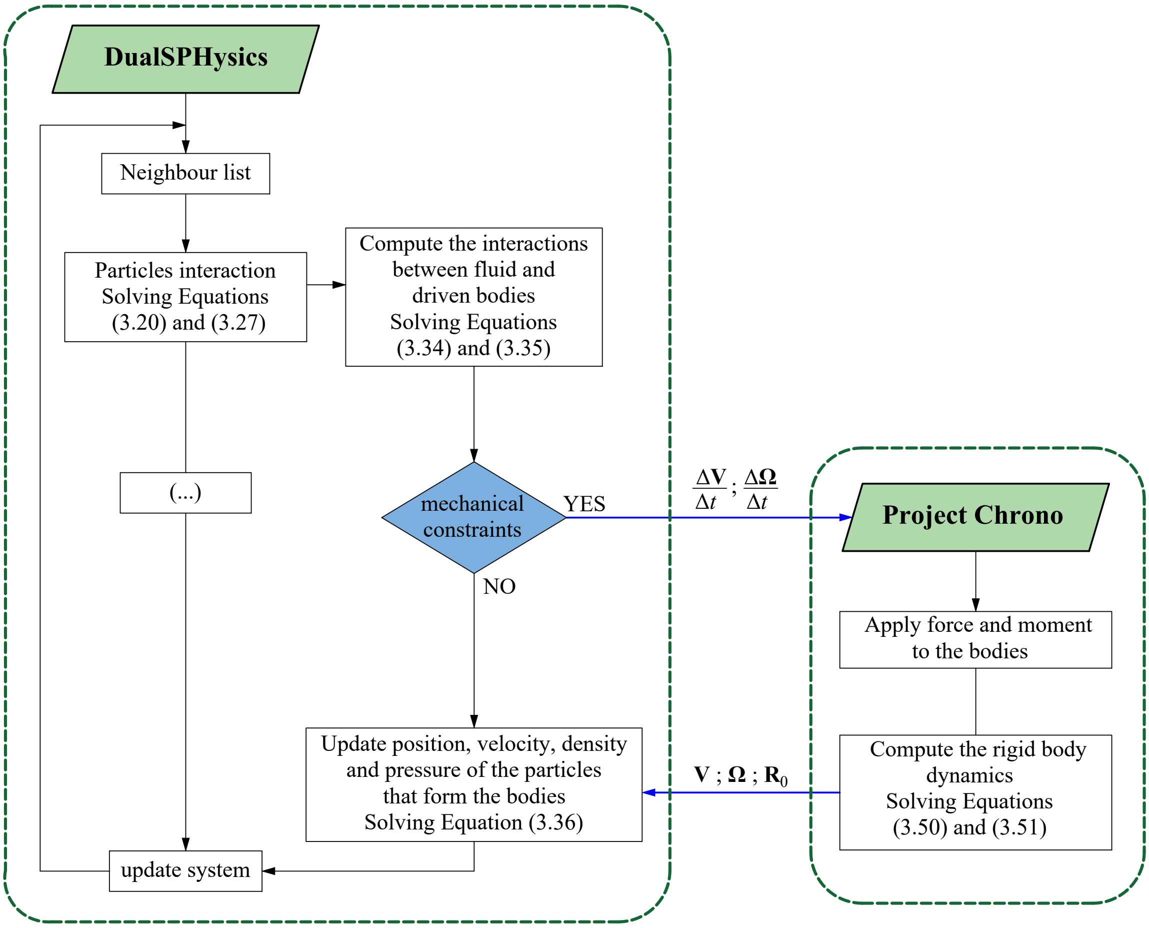
DualSPHysics
Neighbour list
Particles interaction Solving Equations (3.20) and (3.27)
Compute the interactions between fluid and driven bodies Solving Equations (3.34) and (3.35)
(...)
mechanical constraints
YES
NO
$\frac{\Delta \mathbf{V}}{\Delta t}$; $\frac{\Delta \mathbf{\Omega}}{\Delta t}$
Project Chrono
Apply force and moment to the bodies
Compute the rigid body dynamics Solving Equations (3.50) and (3.51)
$\mathbf{V}$; $\mathbf{\Omega}$; $\mathbf{R}_0$
Update position, velocity, density and pressure of the particles that form the bodies Solving Equation (3.36)
update system

Figure 4.2: Flow chart of Project Chrono built under the DualSPHysics numerical implementation, to model wave-structure interaction with mechanical constraints.

In this flow chart, the simulation of the wave-structure interaction (i.e., wave-flap interaction) with mechanical constraints is mainly split in three steps, as follows:

Step 1: DualSPHysics computes the particles interaction by solving the governing equations in SPH form (Equations (3.20) and (3.28)). The motion of a driven body (e.g., flap) is calculated using the Newton's equations for rigid body dynamics (Equations (3.35) and (3.36)).

Step 2: The linear, $d\mathbf{V}/dt$, and angular acceleration vector, $d\mathbf{\Omega}/dt$, to be applied in the centre of mass of the body are transferred to the Project Chrono library. During that time step, Project Chrono computes the rigid body dynamics, considering the given mechanical constraints (Equations (3.51) and (3.52)). The position vector of the centre of mass, $\mathbf{R}_0$, linear, $\mathbf{V}$, and angular velocity vector, $\mathbf{\Omega}$, of the body are transferred back to the DualSPHysics.

Step 3: DualSPHysics updates the position of the particles that form the driven body by Equation (3.37) with the information transferred from Project Chrono library. Finally, DualSPHysics updates all variables (e.g., position vector, $\mathbf{r}$, velocity vector, $\mathbf{v}$, density, ρ, and pressure, P) of all fluid and boundary particles of the computational domain at the new time step.

5

Description of the experimental tests

Contents

5.1 Introduction

To validate the numerical tool and to insight into phenomena, not completed understood, in the hydrodynamics of the OWSC and in the dynamic behaviors of hydraulic PTO system, two set of physical model tests was carried out at the IMFIA. In the first set of tests (Section 5.2), the hydrodynamics of an OWSC at 1:10 scale model in intermediate water depth under both unidirectional regular and irregular waves were investigated. In the second set of tests (Section 5.3), the dynamic behaviors of the hydraulic PTO system under different magnitudes of regular and irregular excitation force, achieved by velocity variation, were characterized. This chapter describes the model tested, the equipment and data acquisition system used, together with the methodology used throughout the experimental tests.

5.2 Hydrodynamics of the OWSC

5.2.1 Wave flume

The wave flume is approximately 60 m long (wave direction), 1.5 m wide and 1.8 m deep, and is equipped with a piston-type wavemaker. A schematic sketch of the side an plan views of experimental setup is shown in Figure 5.1.

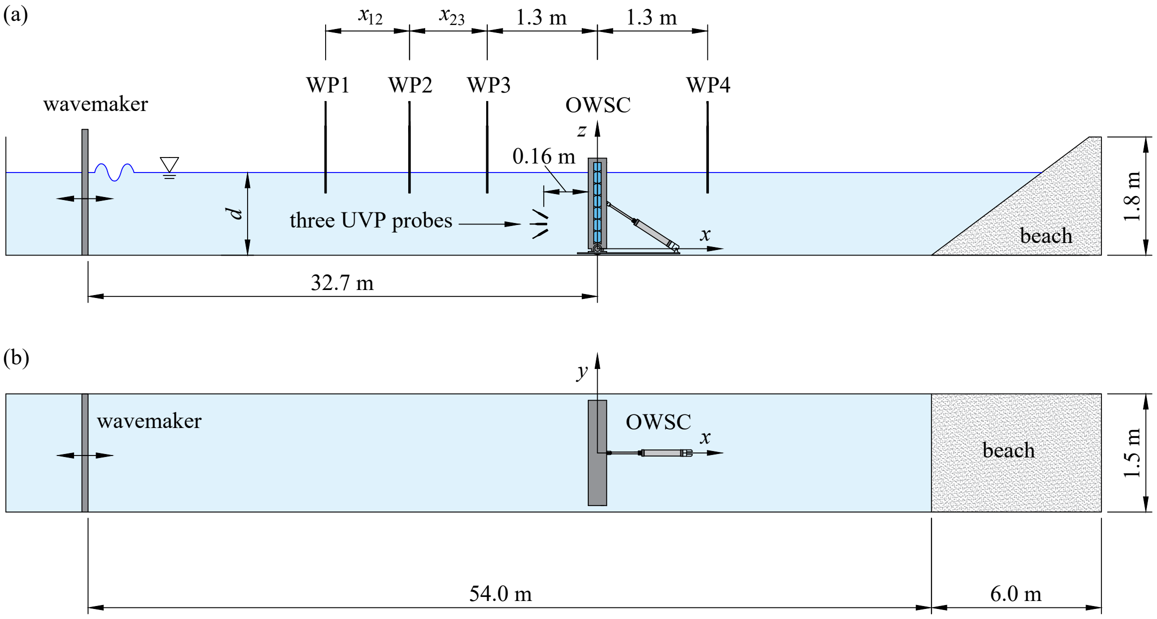

Figure 5.1: Schematic sketch of the wave flume: (a) side view; (b) plan view.

Figure 5.2 shows the full view of the wave flume, measured section, wavemaker and beach.

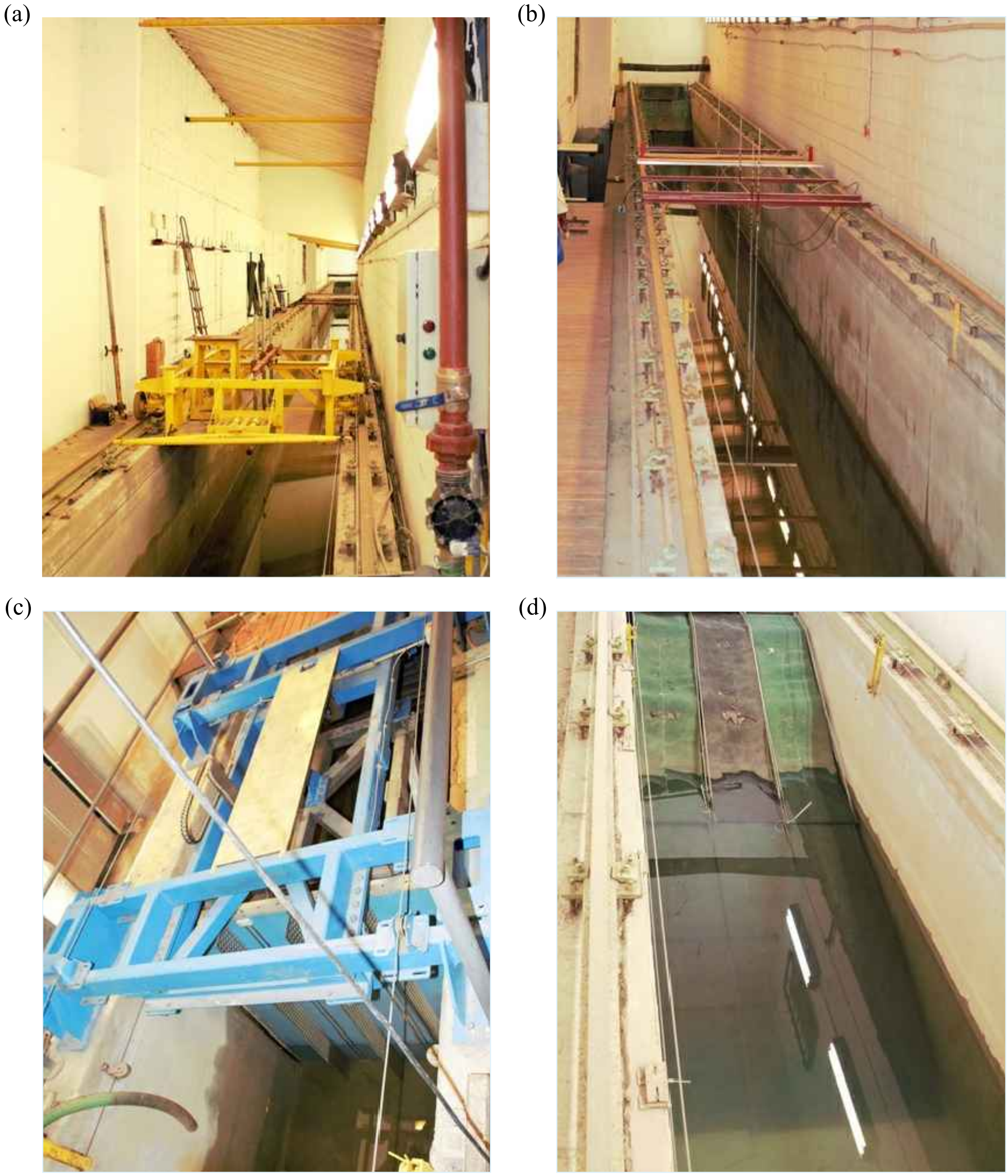

Figure 5.2: Wave flume: (a) full view; (b) measured section; (c) wavemaker; (d) beach.

The wavemaker was driven by an electrical motor through the ball screw with a stroke length of 0.8 m and was controlled by AwaSys 6 (Andersen and Frigaard, 2014). AwaSys 6 allows to generate waves with active wave absorption. At end of the wave flume, there is a passive porous mesh beach with longitudinal slope of 0.3 m/m. The bed and the sidewalls of the wave flume are made of polished concrete.

A cartesian coordinate system is used in which x, y and z refer to the longitudinal (wave direction), lateral and vertical directions, respectively (see Figures 5.1 and 5.4b). The system origin is defined as: $x = 0$ at 32.7 m from the wavemaker; $y = 0$ at centre plane of the flume; and $z = 0$ at 0.1 m from the flume bed in the pivot point of the flap.

5.2.2 OWSC model

The OWSC model is composed by a buoyant flap, a hydraulic PTO system and a foundation. The model was positioned on the central line of the wave flume at 32.7 m from the wavemaker (Figure 5.1). The flap is composed of seven polyvinyl chloride (PVC) tubes, stainless steel frame and bearings with internal diameter of 0.05 m, hinged on y-axis at 0.10 m above the flume bed. Similar to the physical model tests of Folley et al. (2007, 2004); Henry et al. (2014a,b), the OWSC model was designed to represent quasi-2D test. Due to the physical implementation and operation, a total gap of 0.095 m between the flap and the sidewalls of the flume was considered. The details of OWSC model in the wave flume is presented in Figure 5.3.

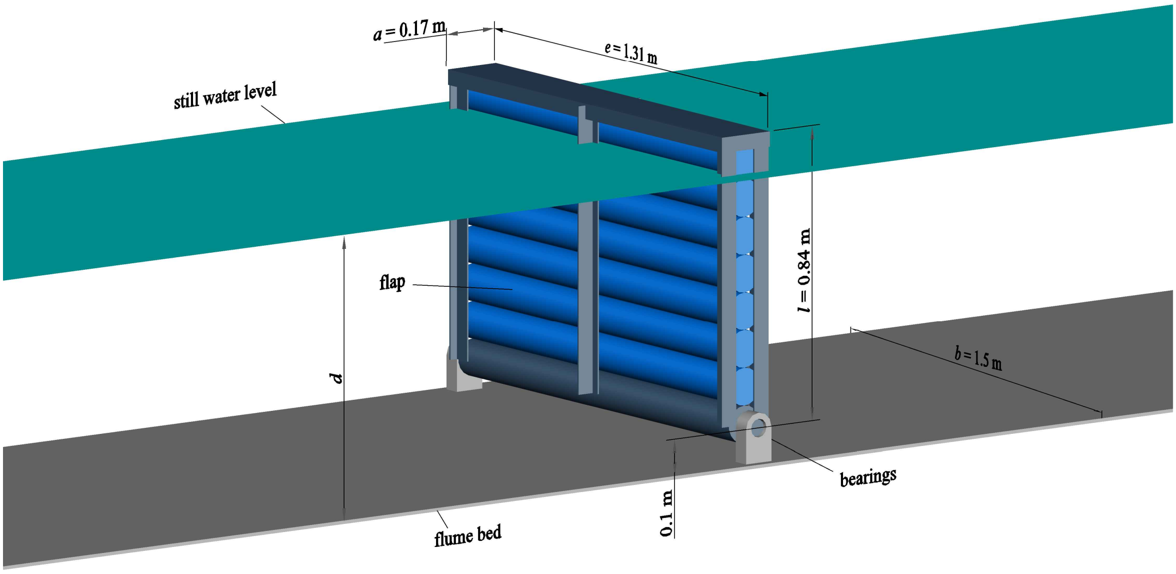

Figure 5.3: Sketch of the OWSC model in the wave flume.

Figure 5.4 shows the flap and the OWSC model in the wave flume.

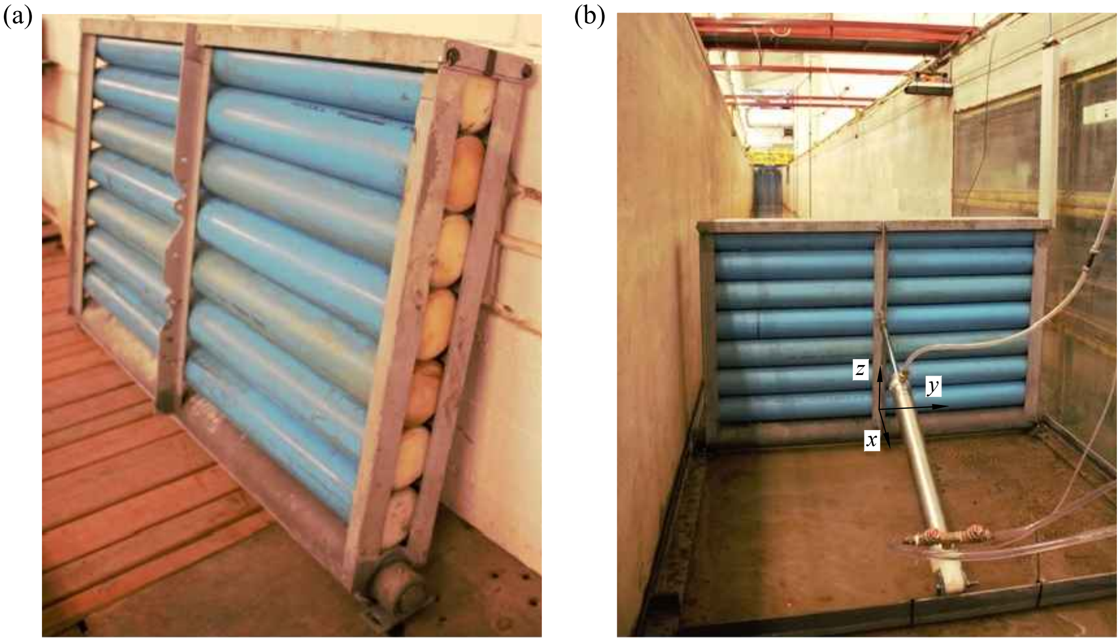

Figure 5.4: Physical model: (a) flap; (b) OWSC model in the wave flume.

The main characteristics of the flap are given in Table 5.1.

Table 5.1: Dimension, mass and moment of inertia (about the bearings) of the flap.

Dimensions	Symbol	Value
Height	l	0.84 m
Width	e	1.31 m
Thickness	a	0.17 m
Mass	m	72.3 kg
Moment of inertia	$(I_{xx}; I_{yy}; I_{zz})$	(27.61; 14.76; 13.11) kg m^2
Centre of mass	$(\overline{x}; \overline{y}; \overline{z})$	(0; 0; 0.33) m

The PTO system is composed by a hydraulic cylinder and by a closed hydraulic circuit, which includes check-valves, globe valves, plastic tubes and reservoir (see the schematic sketch in Figure 5.5). The check-valves prevent the non-return flow and globe valves allow the control of the flow rate and consequently the change of the coefficient of pressure loss (see Chapter 8). In all tests, the hydraulic cylinder was working as a single acting cylinder, with the upper cylinder chamber working at atmosphere pressure, P_{atm}.

5.2.3 Experimental apparatus

The schematic sketch of the side view of OWSC model together with the experimental apparatus are shown in Figure 5.5.

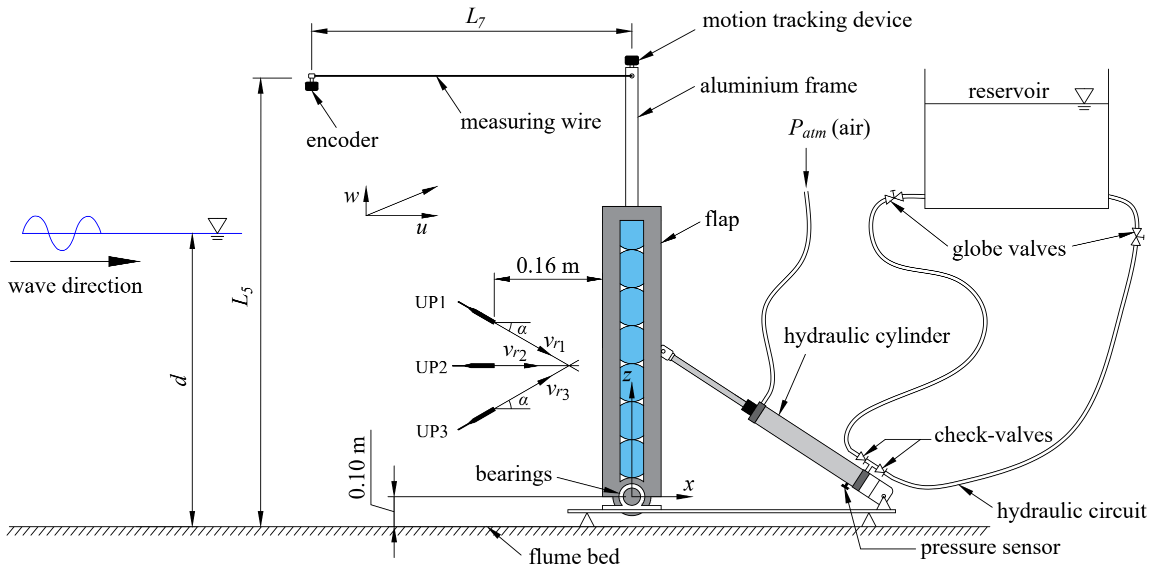

Figure 5.5: Schematic sketch of the side view of OWSC model, illustrating: the position of the experimental apparatus; the configuration of the UVP probes (UP1, UP2 and UP3); and the geometry of the OWSC.

In these tests the rotation angle of the flap, pressure in the cylinder chamber, free-surface elevation and flow velocity in the vicinity of the flap were measured. Figure 5.6 shows the details of the experimental equipment used to measure the rotation angle of the flap and pressure in the cylinder chamber.

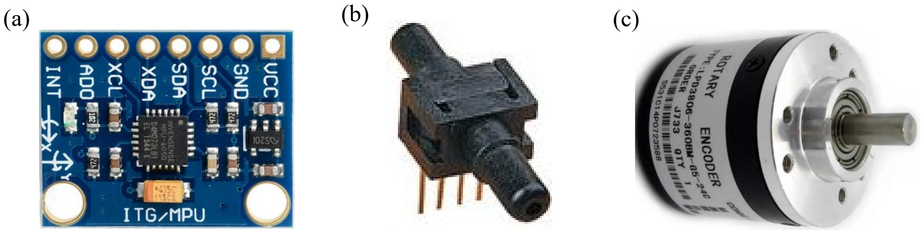

Figure 5.6: Experimental equipment: (a) integrated 6-axis motion tracking device; (b) pressure sensor; (c) encoder.

Figure 5.7 shows the main experimental apparatus, including computer, Ultrasonic Velocity Profiler (UVP), wave probes and encoder.

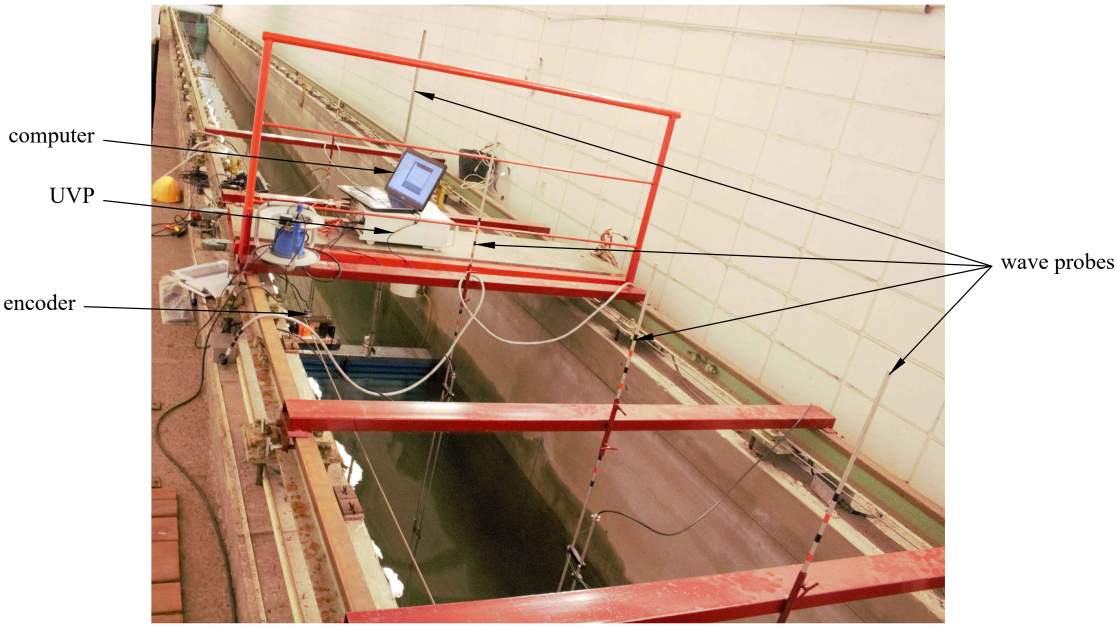

Figure 5.7: Experimental apparatus.

An integrated 6-axis motion tracking device that combines a 3-axis gyroscope and a 3-axis accelerometer (Figure 5.6a), and a linear encoder (Figure 5.6d) with 600 pulses per revolution (PPR) were used to measure the rotation angle of the flap, θ. Due to the scale and functional requirements of the OWSC motion, the sensors have been carefully placed in order to avoid alter the flap inertial characteristics. The encoder was placed at $L_5 = 1.53$ m and $L_7 = 1.48$ m in a vertical aluminium frame fixed to the flap (see also Figure 5.14 for more detail), due to the small rotation of the flap and small PPR.

The water pressure in the cylinder chamber, P_{int}, was measured using a pressure sensor (Figure 5.6c) with an accuracy less than 0.2% rated output (RO).

The pressure sensor and encoder were connected to an Arduino Uno R3. The schematic sketch of the Arduino circuit used to measure the hydrodynamics of the OWSC is presented in Figure 5.8. The Arduino code is included in Listing D.1 (see Appendix D).

The time series of P_{int} obtained from each test were synchronised using the free-surface elevation measured in-line with the bottom hinge. The synchronisation was checked by comparing the signals from wave probes and encoder. The sampling frequency was 100 Hz.

The free-surface elevation η was measured in the centre plane of the wave flume ($y = 0$) by four

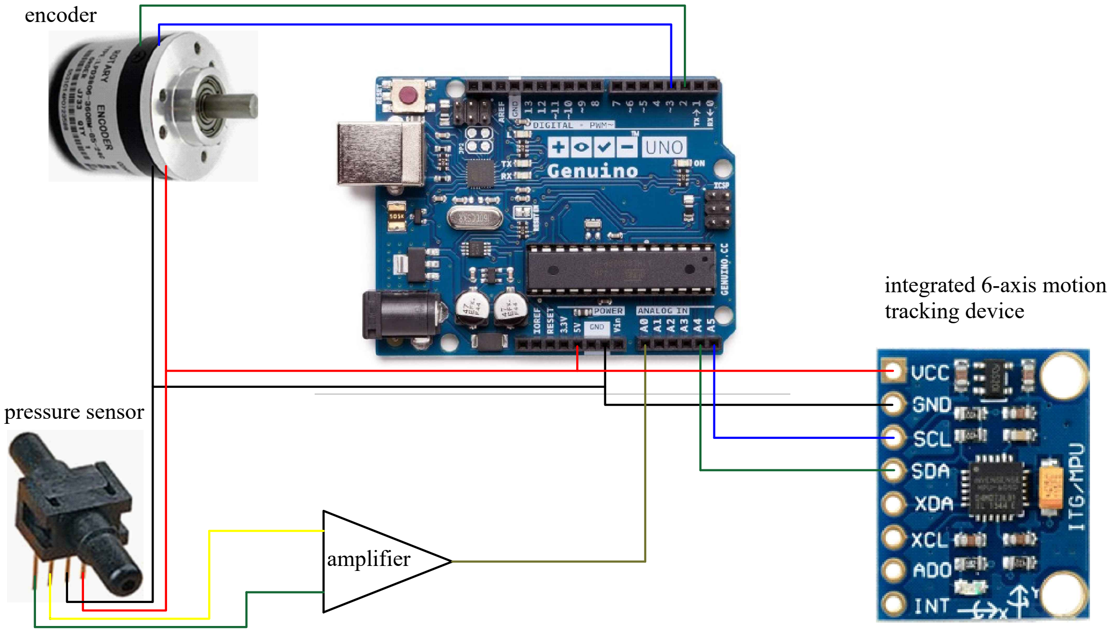

Figure 5.8: Schematic sketch of the Arduino circuit used to measure the hydrodynamics of the OWSC.

standard capacitive wave probes (i.e., WP1, WP2, WP3 and WP4 in Figure 5.1) produced by Akamina Technologies. The distances between wave probes WP1 and WP2, x_{12}, and between WP2 and WP3, x_{23}, were chosen according to the method proposed by Mansard and Funke (1980) in order to make possible to separate the incident and reflected waves. In this study, five equally-spaced water submersions were used for the static calibration of the wave probes. A first-order calibration polynomial relating the output voltages to the η was obtained by a least-square fit procedure (Sarmento, 1992). The sampling frequency of η was 25 Hz.

In order to assess the reflection coefficient of the beach, experimental tests were firstly performed removing the OWSC model from the wave flume. The beach mean reflection coefficient of about 12% have been found.

The flow velocity was measured using an UVP produced by Met-Flow (2002) in the centre plane of the wave flume, $y = 0$ (see Figure 5.9). UVP uses the Doppler shift between the transmitted and the received signal frequencies to compute the velocity of the reflective particles transported in the flow. Then, UVP reports the raw backscatter amplitude, which can be used to estimate the flow velocity (Lemmin and Rolland, 1997; Pedocchi and García, 2012).

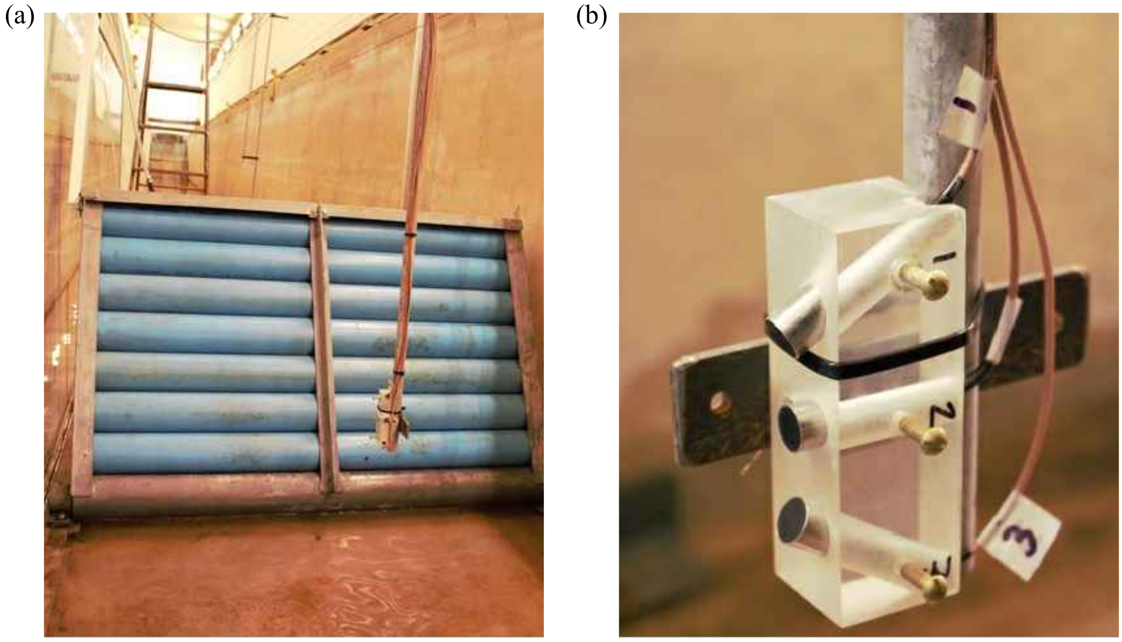

Figure 5.9: UVP detail: (a) position of the UVP probes; (b) configuration of the UVP probes.

A fundamental limitation of the UVP is that the probe measures velocities along one line in space (Lemmin and Rolland, 1997). Therefore, the measurements of longitudinal and vertical velocity components were performed using three UVP probes (UP1, UP2 and UP3) pointing in different directions, as shown in Figures 5.5 and 5.9. The probes were fixed at $x = -0.16 - a/2$ m and an angle $\alpha = 30°$ rad between UP1, UP3 and horizontal (UP2) is considered.

The UVP was operated with a sample frequency of 11.6 Hz and a Doppler frequency of 2 MHz. As UVP measures velocities along one line in space, the velocity field was obtained by repeating the same test 78 times and moving the probes across the vertical direction with step of 2 cm (from $z = 0.20$ to 0.72 m). The velocity field is obtained by phase-averaging the velocity signal over 50 successive waves (Dimas and Galani, 2016; Ting and Kirby, 1994).

5.2.4 Data collection

Two groups of experimental tests were performed, both using Froude's scale, with a geometrical scale factor $\tau = 10$. Therefore, parameters such as wave height and water depth is linearly scaled as τ^{-1}, wave period and velocities as $\tau^{-0.5}$ and power capture as $\tau^{-3.5}$ (Hughes, 1993; Sheng et al., 2014). Using Froude scaling has some limitations, due to neglect the viscous effects. However, the damping due to viscous drag at model scale is expected to be greater than at prototype scale, as the Reynolds number is lower (Flocard and Finnigan, 2012).

The first group of tests was carried out for regular waves with still water depth $d = 0.825$ m. The wave condition considered comprises plane progressive waves of steepnesses ranging from $kH = 0.086$ to 0.385 and water depth ratios varying from $kd = 0.472$ to 1.058, where k and H denote the wavenumber and wave height, respectively. These conditions correspond to the predominant waves (those with the highest annual frequency, i.e., major contributors to the mean annual energy) in the Uruguayan oceanic coast (Alonso et al., 2015) and that corresponds to frequent conditions at the continental Portuguese coast. Table 5.2 shows the wave conditions used for the regular wave tests. Due to the large number of tests requested to obtained the velocity field, the flow velocity was measured only for $T = 3.5$ s and $H = 0.25$ m, as this condition allows almost symmetric motion of the flap (see Chapter 6).

Table 5.2: Wave conditions used for the regular wave tests.

T (s)	kH	kd
2	[0.192; 0.224; 0.256; 0.289; 0.321; 0.353; 0.385]	1.058
2.25	[0.165; 0.193; 0.221; 0.248; 0.276; 0.303; 0.331]	0.910
2.5	[0.145; 0.170; 0.194; 0.218; 0.242; 0.267; 0.291]	0.799
2.75	[0.130; 0.152; 0.173; 0.195; 0.217; 0.238; 0.260]	0.715
3	[0.118; 0.137; 0.157; 0.177; 0.196; 0.216; 0.236]	0.648
3.25	[0.108; 0.126; 0.143; 0.161; 0.179; 0.197; 0.215]	0.591
3.5	[0.099; 0.116; 0.132; 0.149; 0.165; 0.182; 0.198]	0.545
3.75	[0.092; 0.107; 0.127; 0.138; 0.153; 0.167; 0.184]	0.506
4	[0.086; 0.100; 0.114; 0.129; 0.143; 0.157; 0.172]	0.472

The second set of tests was carried out for irregular waves also with $d = 0.825$ m. Four incident wave conditions were considered, generated by different wavemaker input signals (defined by peak period, T_p, significant wave height, H_s, and mean wave height, H_m) were considered (Table 5.3).

Table 5.3: Wave conditions used for the irregular wave tests.

Test	T_p (s)	H_s (m)	H_m (m)
I1	3.6	0.25	0.15
I2	2.5	0.2	0.12
I3	3.6	0.15	0.09
I4	3.6	0.13	0.07

The wavemaker input signal, S_w, of each test is shown in Figure 5.10. Tests I1 and I2 correspond to two standard JONSWAP (Joint North Sea Wave Observation Project) spectrum, both with peak enhancement factor $\gamma = 1.2$ (Figure 5.10a) and tests I3 and I4 correspond to two scaled-field spectrum based on data measured at the Uruguayan oceanic coast (Alonso et al., 2015) (Figure 5.10b).

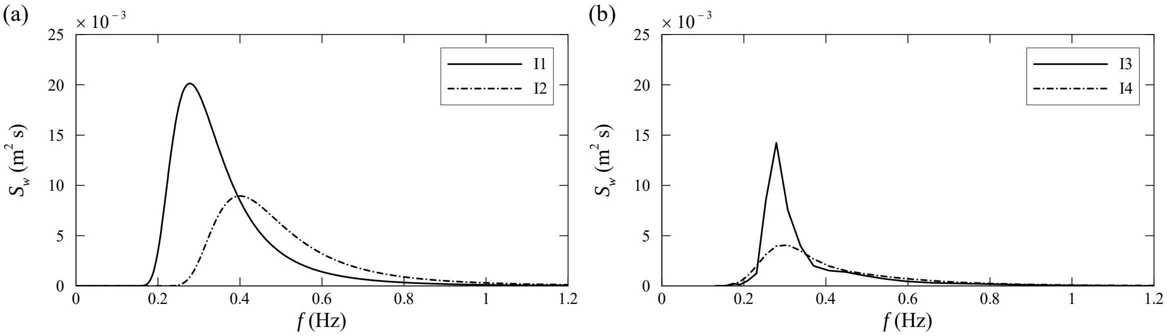

Figure 5.10: Input signals to the wavemaker: (a) JONSWAP spectrum (tests I1 and I2); (b) scaled-field spectrum (tests I3 and I4).

The value of x_{12} and x_{23} used for regular wave and for irregular wave tests are shown in Tables 5.4 and 5.5, respectively.

Table 5.4: Distances between wave probes used for the regular wave tests.

T (s)	x_{12} (m)	x_{23} (m)
2	0.49	1.23
2.25	0.57	1.42
2.5	0.65	1.62
2.75	0.72	1.81
3	0.8	2
3.25	0.88	2.19
3.5	0.95	2.38
3.75	1.02	2.56
4	1.1	2.75

Table 5.5: Distances between wave probes used for the irregular wave tests.

Test	x_{12} (m)	x_{23} (m)
I1	0.62	1.62
I2	0.98	2.45
I3	0.98	2.45
I4	0.98	2.45

The duration of each test is approximately 300 s for regular waves and 3000 s for irregular waves.

5.2.5 Data analysis

The instantaneous power capture of the OWSC, W_{out}, is evaluated as $W_{out}(t) = P_{int}(t)Q(t)$, where Q is the flow rate in the hydraulic circuit, calculated based on the angular velocity of the flap $\dot{\theta}$. The mean power capture, $\overline{W}_{out}$, is determined as:

$$\overline{W}_{out} = \frac{1}{t_{total}} \int_0^{t_{total}} P_{int}(t)Q(t)dt \tag{5.1}$$

where t_{total} is the duration of the test.

According to the linear theory, for regular waves the mean incident power per unit width is defined by:

$$\overline{W}_i = \frac{1}{8}\rho g H^2 c_g \tag{5.2}$$

where c_g is the wave group velocity, and for the intermediate water depth wave conditions studied, c_g is given by:

$$c_g = \frac{\omega}{2k}\left(1 + \frac{2kh}{\sinh 2kh}\right) \tag{5.3}$$

where $\omega = 2\pi f$ is the wave angular frequency, f is the wave frequency and k is given by the dispersion relationship as $\omega^2 = gk\tanh(kh)$.

For unidirectional irregular waves, $\overline{W}_i$ is defined as:

$$\overline{W}_i = \rho g \int_0^{\infty} c_g(f) S_\eta(f) df \tag{5.4}$$

where S_η is the power spectrum of the incident waves.

A common way to indicate the power capture capability of an OWSC is the capture width ratio (CWR), defined as (Falnes, 2002):

$$\mathrm{CWR} = \frac{\overline{W}_{out}}{\overline{W}_i e} \tag{5.5}$$

The ratio of the mean reflected wave power, $\overline{W}_r$, and $\overline{W}_i$ is one of the possible alternatives to estimate the performance of the OWSC, defined as:

$$\varepsilon = \frac{\overline{W}_r}{\overline{W}_i} \tag{5.6}$$

In order to investigate the velocity field over a wave period T, the phase-averaging was carried out (Dimas and Galani, 2016). The phase-averaged velocities were calculated in a quasi-steady condition over 50 wave periods (see Chapter 6). The transient data (approximately 35 waves after the start of wave generation) were removed from the time series, since these could cause large distortions in the statistical quantities (Ting, 2001). The phase-averaged longitudinal, $\langle u \rangle$, and vertical, $\langle w \rangle$, velocities are given, respectively, by:

$$\langle u \rangle (x,z,t) = \frac{1}{N} \sum_{i=1}^{N} u(x,z,t+(i-1)T)\ , \quad 0 \leq t < T \tag{5.7}$$

and

$$\langle w \rangle (x,z,t) = \frac{1}{N} \sum_{i=1}^{N} w(x,z,t+(i-1)T)\ , \quad 0 \leq t < T \tag{5.8}$$

where i is the oscillation cycle number and $N = 50$ is the total number of wave cycles over which averaging was performed (Dimas and Galani, 2016; Monin and Yaglom, 1971; Singh et al., 2016; Umeyama, 2009).

The radial velocity, v_r, measured by each UVP probe, contains information of the instantaneous longitudinal, u, and vertical, w, velocity components (Lemmin and Rolland, 1997), that can be expressed by:

$$v_{r1} = u_1 \cos\alpha - w_1 \sin\alpha \tag{5.9}$$

$$v_{r2} = u_2 \tag{5.10}$$

$$v_{r3} = u_3 \cos\alpha + w_3 \sin\alpha \tag{5.11}$$

where v_{r1}, v_{r2}, and v_{r3} are the instantaneous radial velocities and the subscripts 1, 2 and 3 refer to probes UP1, UP2 and UP3, respectively (see Figures 5.5 and 5.9). Then, $\langle u \rangle$ and $\langle w \rangle$ can be calculated by adding and subtracting Equations (5.9) and (5.11):

$$v_{r1} + v_{r3} = (u_1 + u_3)\cos\alpha + (w_3 - w_1)\sin\alpha \tag{5.12}$$

$$v_{r1} - v_{r3} = (u_1 - u_3)\cos\alpha - (w_1 + w_3)\sin\alpha \tag{5.13}$$

Averaging and assuming that the flow is statistically uniform over the vertical and longitudinal direction (i.e., $\langle u_1 \rangle = \langle u_3 \rangle = \langle u \rangle$ and $\langle w_1 \rangle = \langle w_3 \rangle = \langle w \rangle$), yields to:

$$\langle u \rangle = \frac{\langle v_{r1} \rangle + \langle v_{r3} \rangle}{2\cos\alpha} \tag{5.14}$$

$$\langle w \rangle = \frac{\langle v_{r3} \rangle - \langle v_{r1} \rangle}{2\sin\alpha} \tag{5.15}$$

5.3 Dynamics of the hydraulic PTO system

5.3.1 Regular motion applied to the hydraulic cylinder

The schematic sketch of the experimental setup designed to characterize the hydraulic PTO system under regular motion is shown in Figure 5.11. The mechanical system used to drive the piston is composed mainly by a electrical motor, crank, connecting rod, selector rod and linear bearings (Figure 5.11a).

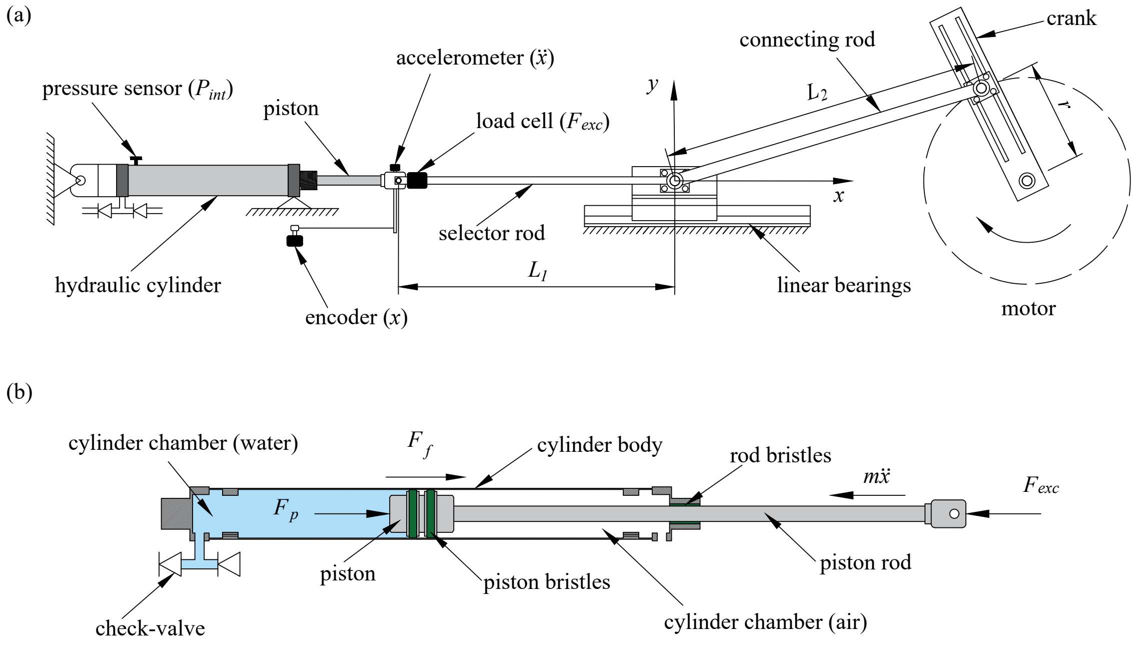

Figure 5.11: Schematic sketch of the side view of hydraulic cylinder: (a) experimental setup, illustrating the position of the experimental apparatus and the geometry of the mechanical system; (b) cylinder details.

The specifications of the hydraulic cylinder and the mechanical components tested are listed in Table 5.6.

Table 5.6: Specifications of the hydraulic cylinder and the mechanical components.

component	dimension (m)	mass (kg)
connecting rod	$L_2 = 0.95$	4.5
selector rod	$L_1 = 0.8$	2.2
crank	$r = 0.07$	8.5
cylinder body	0.063 (bore diameter)	2.65
piston	0.02 (rod diameter), 0.45 (stroke)	2

In this test, an accelerometer (Figure 5.12a) was used to measure the acceleration of the piston, $\ddot{x}$. This accelerometer has an accuracy less than 0.1% RO. The position of the piston, x, was measured by the encoder. The relative velocity of the piston, $\dot{x}$, was calculated by an approximate differentiation of the measured x. The noise in the calculated $\dot{x}$ signal was filtered by an causal low-pass filter with a bandwidth of 2 Hz cut-off frequency (Tran and Yanada, 2013).

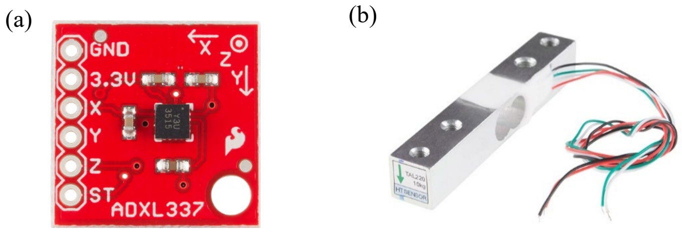

Figure 5.12: Experimental equipment: (a) accelerometer; (b) load cell.

The schematic sketch of the Arduino circuit used to measure the dynamics of the hydraulic PTO system is presented in Figure 5.13. The Arduino code is included in Listing D.2 (see Appendix D).

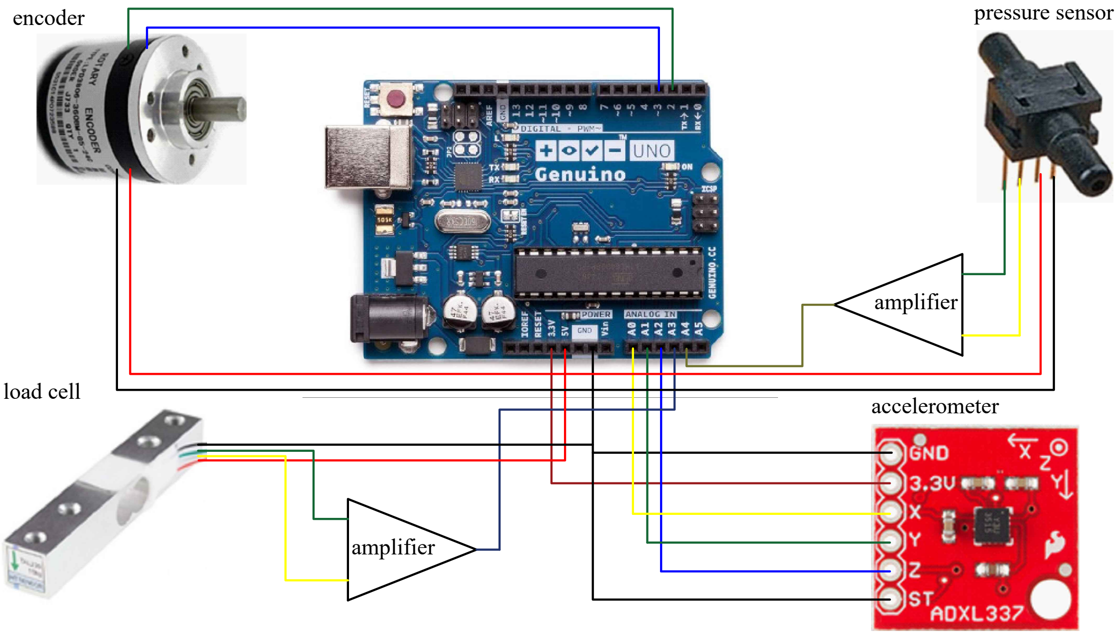

Figure 5.13: Schematic sketch of the Arduino circuit used to measure the dynamics of the hydraulic PTO system.

The excitation force, F_{exc}, applied by the mechanical system was measured by a load cell

(Figure 5.12b), which was set in series between the piston rod and the selector rod (see Figure 5.11a). The load cell has the capacity of 150 N, accuracy less than 0.15% RO and response time of 1.0 ms. The friction force, F_f, between the piston bristles and the cylinder body and between the rod bristles and the piston rod can be calculated based on the equation of motion, using measured values of F_{exc}, P_{int} and $\ddot{x}$ of the piston, as:

$$F_f(t) + F_p(t) = F_{exc}(t) - m\ddot{x}(t) \tag{5.16}$$

where m is the mass of the piston and F_p is the pressure force, given by:

$$F_p(t) = P_{int}(t)A \tag{5.17}$$

where A is the cross-section area of the cylinder chamber.

In this test, x, $\ddot{x}$, P_{int} and F_{exc} were measured for two periodic motion with period $T = 5.1$ and 7.0 s. The discrete time series of x, $\ddot{x}$, P_{int} and F_{exc} were recorded with a sampling frequency of 120 Hz.

5.3.2 Irregular motion applied to the OWSC

In this test, the OWSC with above hydraulic cylinder was excited by irregular force. The hydraulic cylinder is set at $L_4 = 0.47$ m and $L_3 = 1.04$ m (Figure 5.14).

Figure 5.15 shows the experimental setup used to characterize the hydraulic PTO system under irregular motion.

The load cell was placed at $L_6 = 1$ m from the bottom hinge and the integrated 6-axis motion tracking device was placed at $L_5 = 1.53$ m. The encoder was placed at $L_5 = 1.53$ m and $L_7 = 1.48$ m in a vertical aluminium frame fixed to the flap (see Figures 5.14 and 5.15), due to the small rotation of the flap and small PPR.

The rotation angle of the flap θ can be calculated by the following implicit equation:

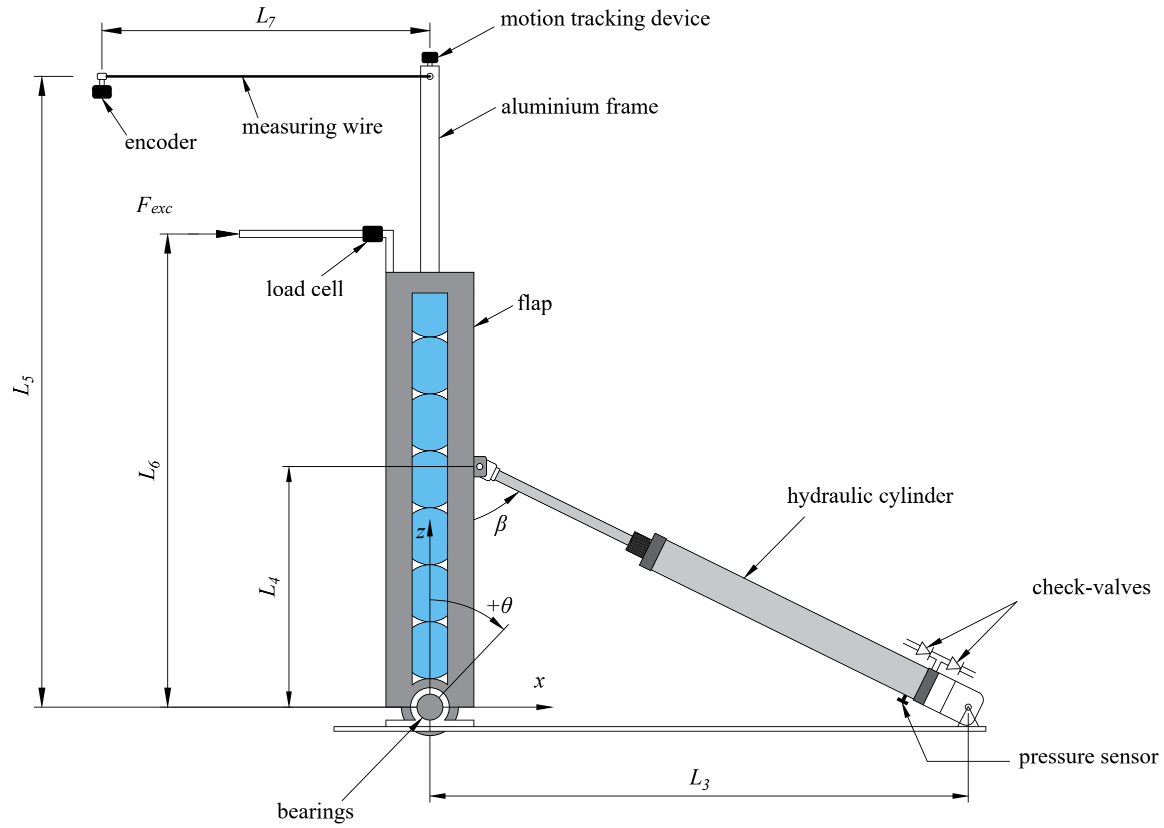

Figure 5.14: Schematic sketch of the side view of the experimental setup used in the irregular motion applied to the OWSC, illustrating the position of the experimental apparatus.

$$[L_7 - \Delta L_7(t)]^2 = L_7^2 + \left[2L_5 \sin\left(\frac{\theta(t)}{2}\right)\right]^2 - 2L_7L_5 \sin(\theta(t)) \tag{5.18}$$

where ΔL_7 is the variation of the length of the measuring wire. The detailed description of the parameters introduced in Equation (5.18) can be found in Figure 5.14. The value of θ obtained by encoder was validated against the integration of angular velocity given by the gyroscope of the integrated 6-axis motion tracking device and video tracker method. The relative error between these three methods was less than 1%. The $\dot{\theta}$ is calculated by an approximate differentiation of the measured θ. The noise in the calculated $\dot{\theta}$ signal was also filtered by a causal low-pass filter with a bandwidth of 2 Hz cut-off frequency.

From the physical model of the OWSC the following mathematical model is formulated:

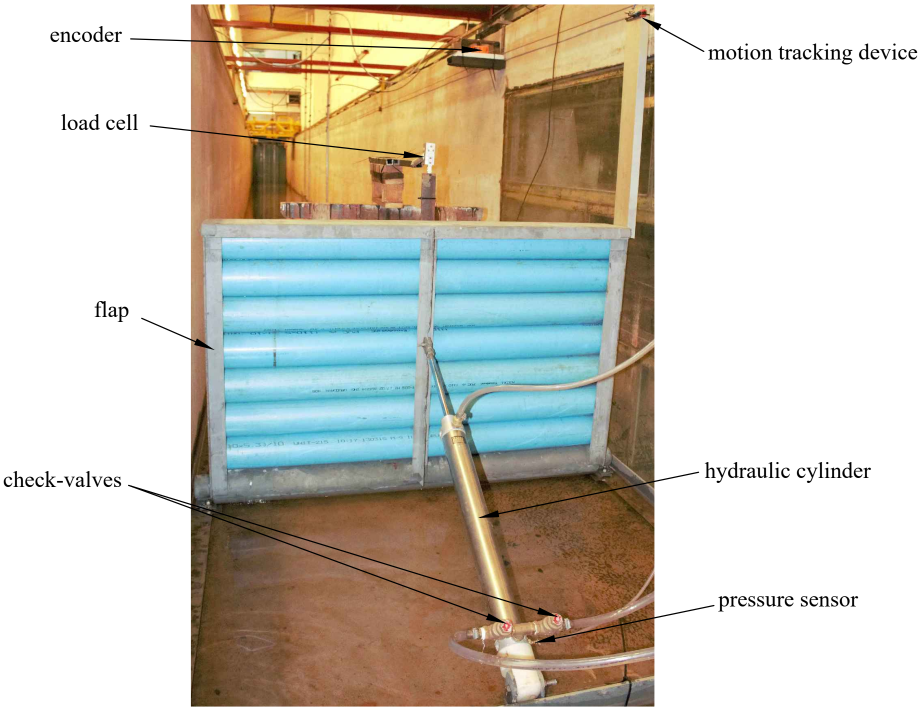

Figure 5.15: Experimental setup used to characterize the hydraulic PTO system under irregular motion.

$$I_{yy}\ddot{\theta}(t) = F_{exc}(t)L_6 - mg\overline{z}\sin(\theta(t)) - F_{PTO}(t)L_4\sin(\beta(t)) - B_0(t) \tag{5.19}$$

where F_{PTO} is the PTO force of the hydraulic cylinder, I_{yy} is the rotational inertia of the flap about the bottom hinge (see Section 5.2.2), $\ddot{\theta}$ is the angular acceleration of the flap and B_0 is the friction torque of the flap about the bottom hinge, β is the angle between the flap and the piston, given by:

$$\beta(t) = \tan^{-1}\left[\frac{1}{\dfrac{L_4}{L_3\cos(\theta(t))} + \tan(\theta(t))}\right] \tag{5.20}$$

Hence, $\dot{x}$ of the piston can be given by:

$$\dot{x}(t) = \cos[\theta(t) + \beta(t)]L_3\dot{\theta}(t) \tag{5.21}$$

The detailed description of the geometric parameters can be found in Figure 5.14.

6

Flow field in the vicinity of the OWSC

The results presented in this chapter has been submitted as Brito, M., Teixeira, L., Ferreira, R. M. L., Neves, M. G. and Canelas, R. B. 'Experimental investigation of the flow field in the vicinity of an oscillating wave surge converter'. *International Journal of Energy Research.*

Contents

6.1 Introduction

In what concern to physical model tests, there is a lack of experimental data on the hydrodynamic of OWSCs. In fact, very few experimental studies have been carried out focus on the hydrodynamics of the OWSCs, see e.g., Folley et al. (2007, 2004); Henry et al. (2014a,b); Lin et al. (2012); Schmitt et al. (2012); Whittaker et al. (2007). In those studies, the flow field in the vicinity of the OWSCs were not measured and the phase differences between the hydrodynamic force and flow quantities such as velocity or free-surface elevation have not been investigated (Schmitt et al., 2016). Furthermore, those studies do not provide the shortcomings of the linear analytical solutions based on the flow field.

This chapter investigates the velocity field in the vicinity of the OWSC under regular wave, in order to understand the flow features and to explain trends of experimental results and to clarify the important differences between experimental data and linear analytical solutions. Although there are several analytical model of hydrodynamic characteristics of OWSCs, this chapter considers the model developed by Renzi and Dias (2012) (see Section 2.2.1). Since this model allows the analysis of OWSC in a wave flume (i.e., takes into account the effect of sidewalls by the diffraction potential).

6.2 Results and discussions

6.2.1 Hydrodynamic characteristics of the OWSC

The variation of amplitude of the hydrodynamic torque, $\mathcal{T}_h$, with wave period, T, for wave height $H = 0.15$, 0.2 and 0.25 m is shown in Figure 6.1. In order to explain trends of $\mathcal{T}_h$, the experimental data are compared with analytical solution of Equation (2.39). In general, due to non-linearity of the wave-OWSC interactions, important discrepancy can be observed between experimental data and analytical solutions. For higher value of H, the experimental variation of $\mathcal{T}_h$ is much larger than obtained from the linear theory. This behavior is caused by the non-linearities of the interaction of wave with the flume bed and by the interaction between wave and the OWSC, that increases with H.

Figure 6.2 shows the variation of the amplitude of rotation angle of the flap, θ, and capture width ratio (CWR) with T for the same conditions presented in Figure 6.1. A large discrepancy is also observed between experimental data and analytical solutions, with experimental variation of θ and CWR much smaller than the analytical one. This large discrepancy can

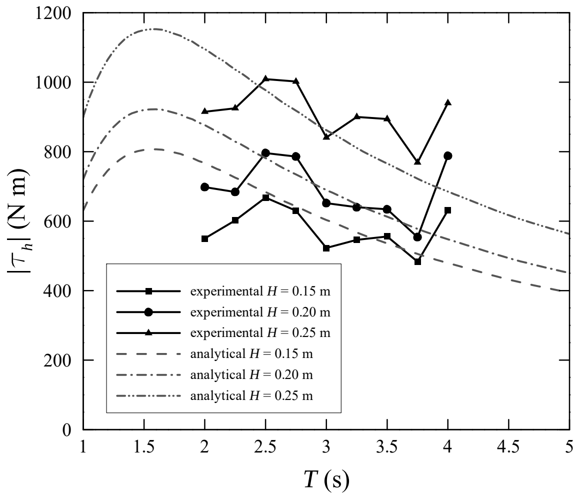

Figure 6.1: Comparison between experimental and analytical variation of the amplitude of hydrodynamic torque with wave period.

be explained by the experimental asymmetry of the OWSC motion, caused by wave-OWSC interactions and by the hydraulic PTO system. Since analytical solutions were obtained for linear PTO damping. In order to clarify the differences between experimental data and analytical solutions the velocity field in the vicinity of OWSC is presented and analyzed.

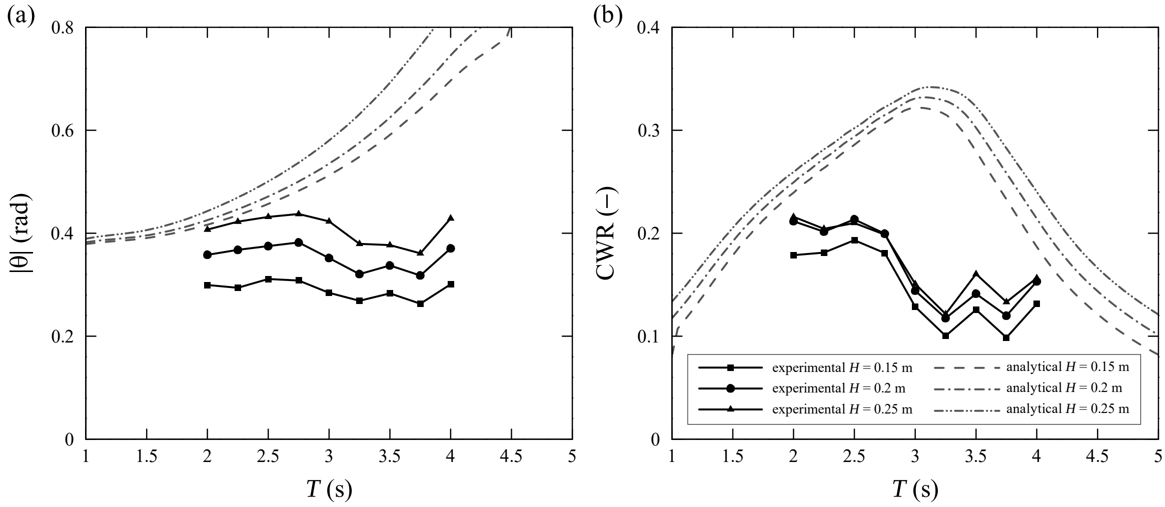

Figure 6.2: Comparison between experimental and analytical variation of: (a) amplitude of rotation angle of the flap; (b) CWR.

6.2.2 Velocity field in the vicinity of the OWSC

As referred in Section 5.2.4, the velocity field was obtained by repeating the same test condition 78 times and, therefore, high degree of repeatability of the tests is essential to ensure the accuracy of data (Dimas and Galani, 2016; Ting and Kirby, 1994). The repeatability of the tests is verified by comparing all measured time series of free-surface elevation, η, and rotation angle of the flap, θ, with its ensemble-averaged, respectively. Figure 6.3 shows the comparison of time series of η measured by WP1 and θ with its ensemble-averaged, respectively, after the quasi-steady condition, for $65 \leq t/T \leq 70$. In Figure 6.3, the red line represents the ensemble-averaged and the gray lines stand for all tests.

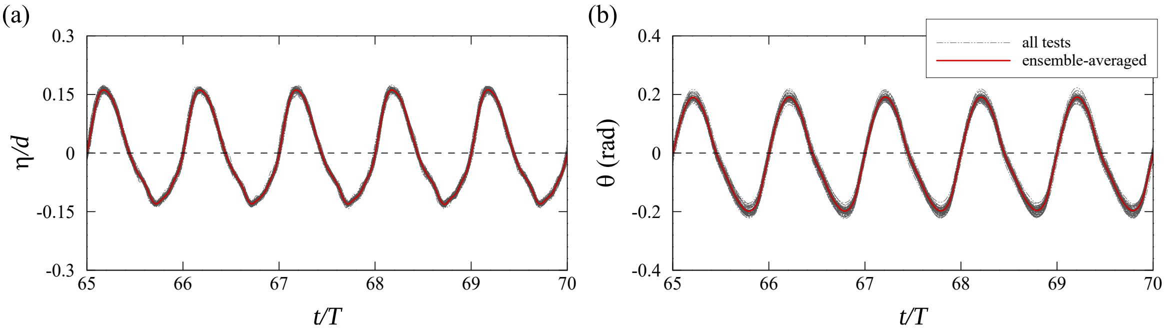

Figure 6.3: Time series: (a) free-surface elevation measured by WP1; (b) rotation angle of the flap. Red line represents the ensemble-averaged and gray lines stand for all tests.

An excellent repeatability of both η and θ was observed, with small differences in the maximum amplitude of θ, which were attributed to slight variations in the experimental tests. The standard deviations of η amplitudes and periods were less than 0.5% and 0.2%, respectively, and of θ amplitudes and periods were less than 2.1% and 0.4%, respectively. Hence, it was reliable to assume that the tests are fully repeatable.

Transient data in the time series can also cause a large distortion in the processing of statistical quantities (Ting, 2001). To estimate accurately these quantities by means of the phase-averaging method the quasi-steady condition of the tests from wave-to-wave must be ensured (Dimas and Galani, 2016; van der A et al., 2011). The full time series of η and θ are shown in Figure 6.4. Similar to Dimas and Galani (2016); Ting (2001), in this study the quasi-steady condition is quantified by comparing the amplitude scale of η and θ (dash-dotted line in Figure 6.4) with its maximum amplitudes in each wave cycle. The quasi-steady condition was considered when relative errors between the amplitude scale and its maximum amplitudes are less than 2%. For both η and θ, the time series reach a quasi-steady condition at $t/T \geq 35$, i.e., approximately 35 waves after the start of wave generation.

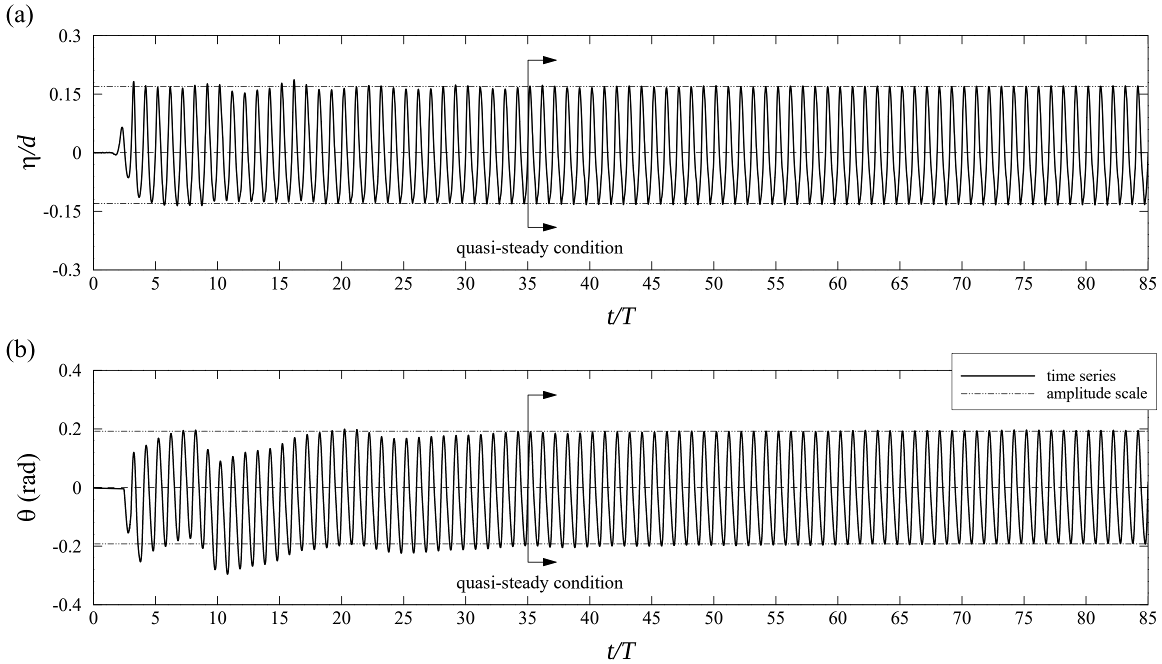

Figure 6.4: Full time series: (a) free-surface elevation; (b) rotation angle of the flap. Dash-dotted line represents the amplitude scales. Vertical line at $t/T = 35$ indicates the beginning of the quasi-steady condition.

Time series of five consecutive wave periods of η, θ, pressure in the hydraulic cylinder P_{int} and angular velocity of the flap $\dot{\theta}$ after the quasi-steady condition, for $65 \leq t/T \leq 70$, are presented in Figure 6.5. This details allow to confirm that the incident wave condition presents a good wave-to-wave repeatability after the quasi-steady condition. The parameters presented in Figure 6.5 are synchronized with θ in order to analyze the difference in phase of different measuring quantities.

The phase-averaged of free-surface elevations, $\langle\eta\rangle$, rotation angle of the flap, $\langle\theta\rangle$, power capture, $\langle W_{out}\rangle$, and angular velocity of the flap, $\langle\dot{\theta}\rangle$, are shown in Figure 6.6. In this figure, η is a sinusoidal function, θ was calculated by Equation (2.36), $\dot{\theta}$ is the derivative of θ and $W_{out} = \nu_{PTO}\dot{\theta}^2$ (see Equation (2.40)).

In terms of wave cycle, at $t/T = 0$ the flap is in the vertical position with $\langle\theta\rangle = 0$. As the wave crest approaches the OWSC, the flap moves toward the beach, $\langle\theta\rangle > 0$, reaching its maximum $\langle\theta\rangle \approx 0.19$ rad, being fully submerged as the wave crest passes over it at $t/T \approx 0.2$. Once the flap is fully submerged, $\langle\dot{\theta}\rangle$ decreases rapidly and the flap stops. As the wave crest

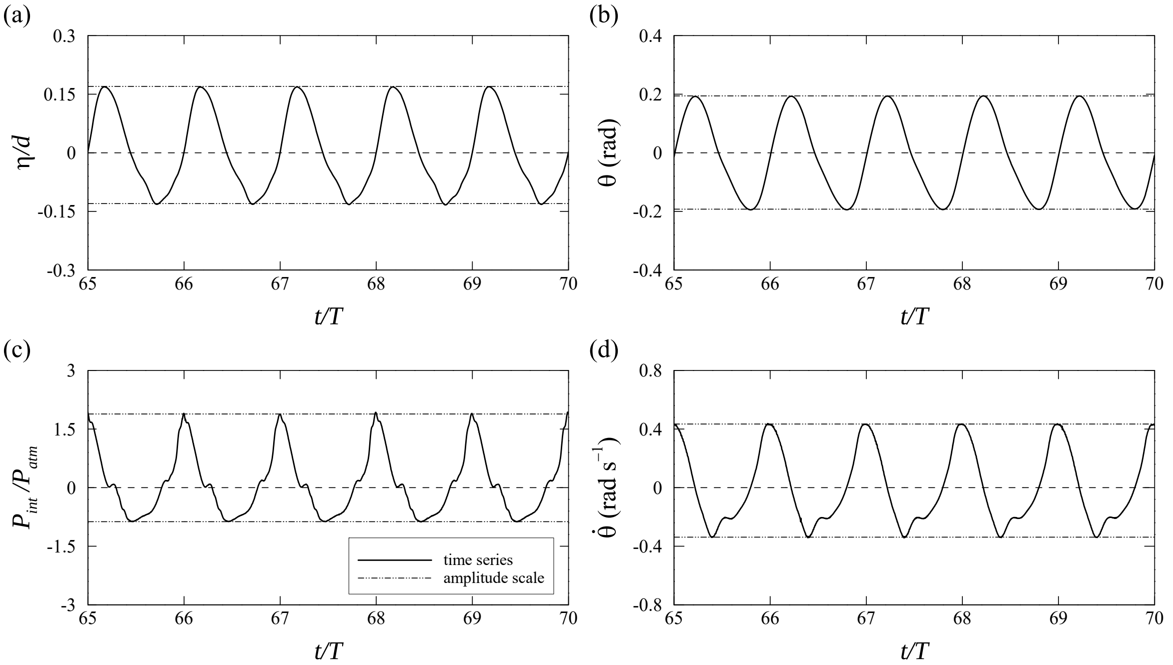

Figure 6.5: Time series for $65 < t/T < 75$: (a) free-surface elevation; (b) rotation angle of the flap; (c) pressure in the cylinder chamber; (d) angular velocity of the flap. Dash-dotted lines represents the amplitude scale.

moves away from the flap, the wave pressure is reduced and the water level begins to drop as the trough approaches. The flap begins to rise up and pierces through the back of the wave crest. As the flap reaches $\langle\theta\rangle = 0$ and as the wave is in the trough phase, it is moving towards the wavemaker with $\langle\theta\rangle < 0$. The water level is low, much of the flap becomes exposed and, therefore, the water provides little resistance to the flap motion. The association between low water level and strong non-linear behavior of the PTO system (see Chapter 7) causes the steep gradient of $\langle\dot{\theta}\rangle$ at $0.4 < t/T < 0.6$ (Figure 6.6d). At $t/T \approx 0.75$, the flap reaches its minimum $\langle\theta\rangle \approx -0.19$ rad. It should be noted that this minimum $\langle\theta\rangle$ occurs after the minimum of $\langle\eta\rangle$ due to the inertia of the system. As the water level increases, the wave pressure increases and the flap starts to move towards the beach and the wave cycle is repeated.

As depicted in Figure 6.6, the experimental data show a strong non-linear behaviors. In general, due to non-linearity of the wave-OWSC interactions, a large discrepancy can be observed between experimental data and analytical solutions. The experimental wave crest occurs at $t/T \approx 0.2$ and the analytical at $t/T = 0.25$. This experimental asymmetry is caused by the interaction of wave with the flume bed and by the interaction between wave and OWSC with mechanical constraints. Such interactions have more influence on the $\langle\theta\rangle$, $\langle W_{out}\rangle$ and $\langle\dot{\theta}\rangle$ than on the $\langle\theta\rangle$. The maximum $\langle\theta\rangle$ is 37% smaller than the analytical one. As for $\langle\eta\rangle$, the

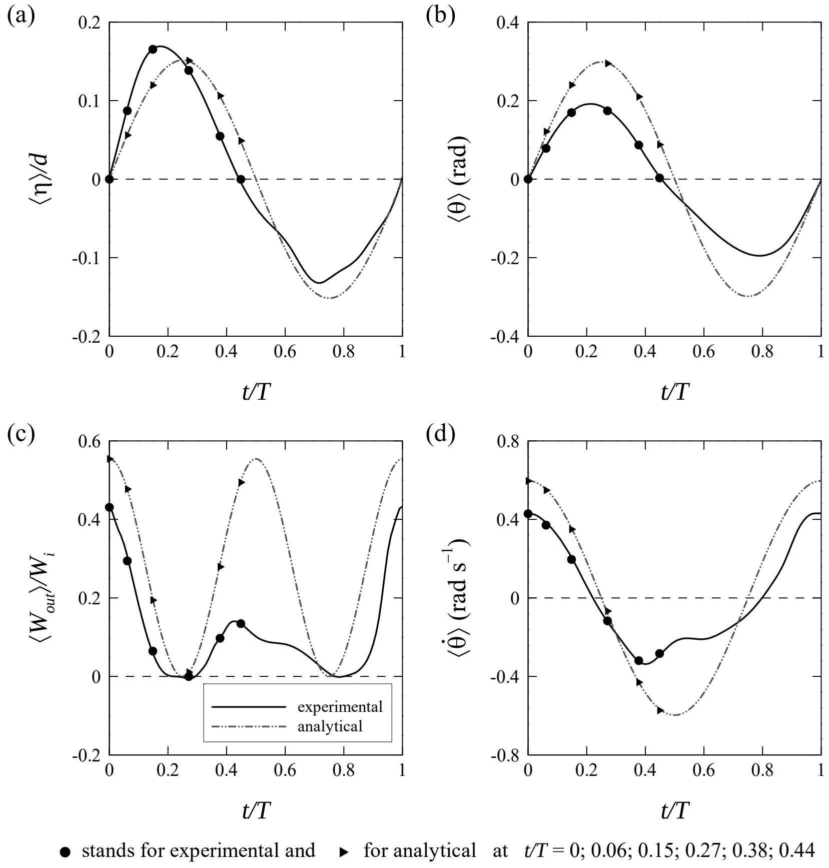

Figure 6.6: Comparison between experimental and analytical phase-averaged: (a) free-surface elevation; (b) rotation angle of the flap; (c) power capture; (d) angular velocity of the flap.

maximum absolute value of experimental $\langle\theta\rangle$ does not match with the phase of maximum analytical $\langle\theta\rangle$. The experimental $\langle W_{out}\rangle$ shows a large discrepancy from the analytical (Figure 6.6c), with CWR = 0.12 and 0.33, respectively. Such discrepancy is generated by the wave overtopping on the flap, non-linear characteristics of the hydraulic PTO system and its brake effects on the flow field. It should be highlighted that the analytical solutions were obtained for linear PTO damping. The interval when $\langle\theta\rangle < 0$ is characterized by steep gradient of $\langle\dot{\theta}\rangle$ due to the PTO system and due to the rapid variations and a complete change in the nature of the flow (see Figure 6.7).

The experimental phase-averaged velocity vector field, $(\langle u\rangle,\langle w\rangle)$, and contour of $\langle u\rangle$ normalized by the deep-water maximum particle velocity, $U_0 = \pi H/T$, in the points presented in Figure 6.6 ($t/T = 0$, 0.06, 0.15, 0.27, 0.38 and 0.44) are shown in Figure 6.7. The considered t/T refers to the half wave cycle with $0 \leq t/T \leq 0.44$. It should be noted that data for $t/T > 0.44$ are not shown as the flap covers most of the experimental mesh.

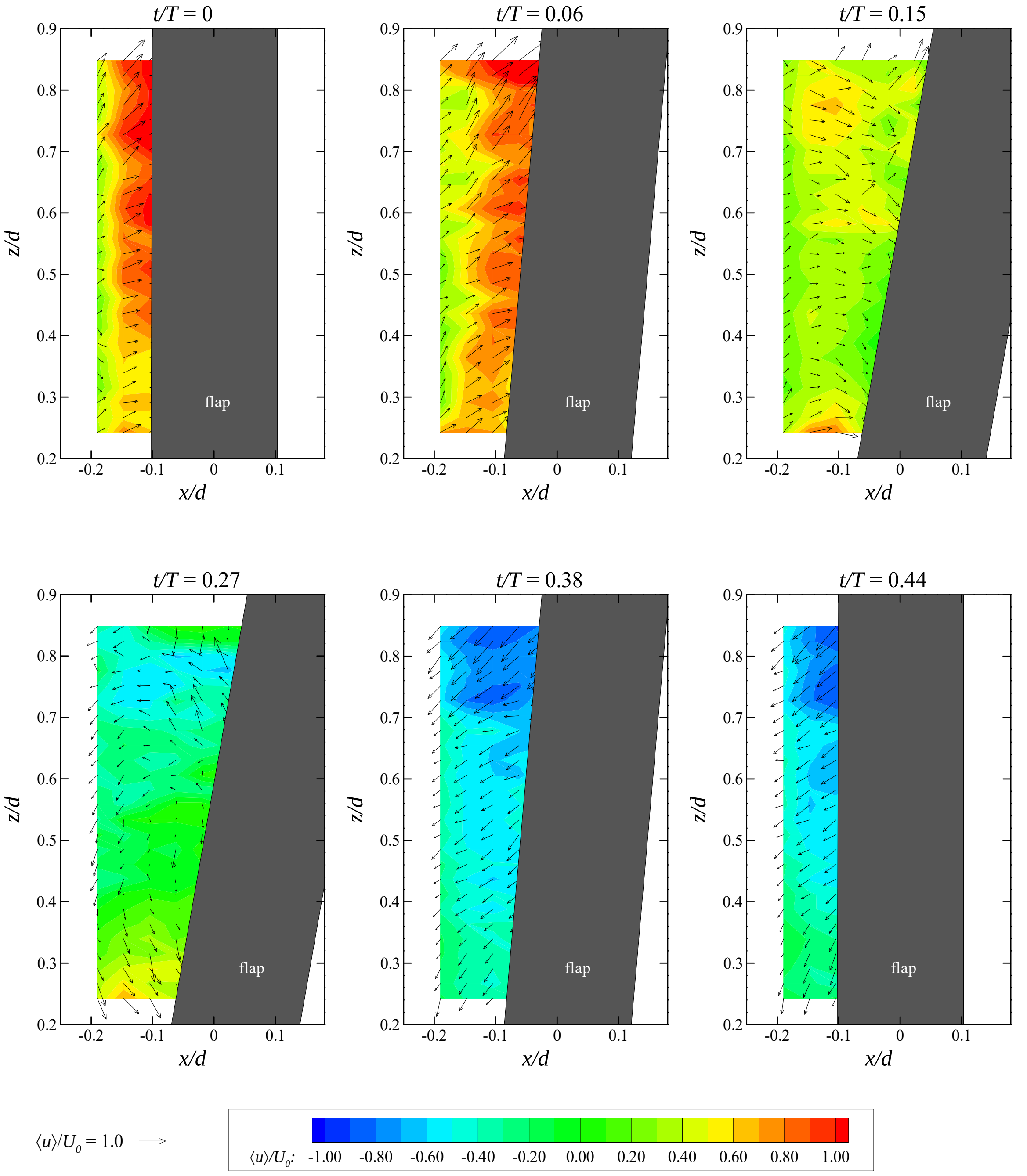

Figure 6.7: Experimental phase-averaged velocity vector field and contour of longitudinal velocity normalized by U_0 at different instants.

In terms of ($\langle u \rangle$,$\langle w \rangle$) field, a difference in the orientation of vectors near the flume bed and near the free-surface are observed at $t/T = 0$. For example, for $z/d < 0.5$ the vectors are nearly horizontal, with $\langle w \rangle < \langle u \rangle/2$, and for $z/d > 0.7$ the vectors present strong $\langle w \rangle$, with $\langle w \rangle \approx \langle u \rangle$. This increased of $\langle w \rangle$ with z is generated by effects of the wave propagation and the ascendant flow which are caused by the approach of the wave crest and the blockage effect of the flap (Count and Evans, 1984). Hence, from $t/T = 0$ to 0.06 the vertical acceleration is mostly larger than the longitudinal one. In fact, the flow presents longitudinal deceleration at $z/d > 0.6$ (see velocity profiles in Figures 6.8a and b). At $t/T = 0.06$ the vectors are markedly oriented towards the free-surface, indicating that practically the entire mass of water passes over the flap.

The interval $0.06 \leq t/T \leq 0.15$ is characterized by rapid variations and a complete change in the nature of the flow. Such large deceleration is not surprising since $\langle \dot{\theta} \rangle$ evolves very rapidly (see Figure 6.6d) and the flow decelerates to compensate the pressure field. Another key feature at $t/T = 0.15$ is the flow rotation generated by the beginning of the deceleration. From $t/T = 0.15$ to 0.27 a largest flow deceleration can be observed, caused by the arrival of the wave crest at $t/T \approx 0.2$ and the change on the orientation of $\mathcal{T}_h$. This can be seen on the large deceleration visible from $t/T = 0.15$ to 0.27, as well as in the velocity profiles (Figure 6.8), which are both irreconcilable with potential flow description, with the difference being due to the presence of flow rotation. For $t/T \geq 0.27$ the vectors were always oriented toward the wavemaker, indicating that the surrounding water are moving with $\langle u \rangle < 0$. However, near the flume bed ($z/d < 0.4$), $\langle u \rangle > 0$, confirming the flow rotation (see Figure 6.8). The fully descendant flow with $\langle w \rangle \approx \langle u \rangle$ is observed at both $t/T = 0.38$ and 0.44, with small deceleration from $t/T = 0.38$ to 0.44. At these instants, similar orientation of $(\langle u \rangle, \langle w \rangle)$ can be explained by the lower variation of $\langle \dot{\theta} \rangle$ (see Figure 6.6).

In terms of $\langle u \rangle$ contours, at $t/T = 0$ the maximum magnitude of $\langle u \rangle$ is located near to the free-surface. The position of this maximum $\langle u \rangle$ is generated by the approach of the wave crest and the maximum $\langle \dot{\theta} \rangle$. From $t/T = 0$ to 0.06 the flow presents longitudinal acceleration near the flume bed, for $z/d < 0.4$, and deceleration near to the free-surface at $z/d > 0.6$. At $t/T = 0.06$, $\langle u \rangle$ shows a longitudinal gradient, due to the differences in the turbulent field, with increases of turbulent kinetic energy near to the free-surface and close to the flap. Naturally, the presence of the thin viscous boundary layer in the flap prevents too extreme accelerations. It was not possible, in any case, to measure very close to the flap boundary. As mentioned above, the flow at $0.15 \leq t/T \leq 0.27$ is characterized by rapid variations and a complete change in its nature. Consequently, the spatial distribution of $\langle u \rangle$ is complex, with the presence of longitudinal and vertical gradients, related to the deceleration of the flow caused by the reversal $\langle \theta \rangle$. At this interval the dominant feature is a nearly constant $\langle u \rangle$ at $z/d < 0.4$ and the association between $\langle u \rangle < 0$ and $\langle u \rangle > 0$, and therefore, $\langle u \rangle$ provide a clear pattern of flow rotation. At $t/T = 0.38$ and 0.44, $\langle u \rangle$ shows lower longitudinal and vertical acceleration and deceleration than those observed at $t/T \leq 0.27$.

The profiles of $\langle u \rangle$ and $\langle w \rangle$ normalized by U_0 at section $x/d = -0.11$ and at $t/T = 0$, 0.06, 0.15, 0.27, 0.38 and 0.44 are presented in Figure 6.8.

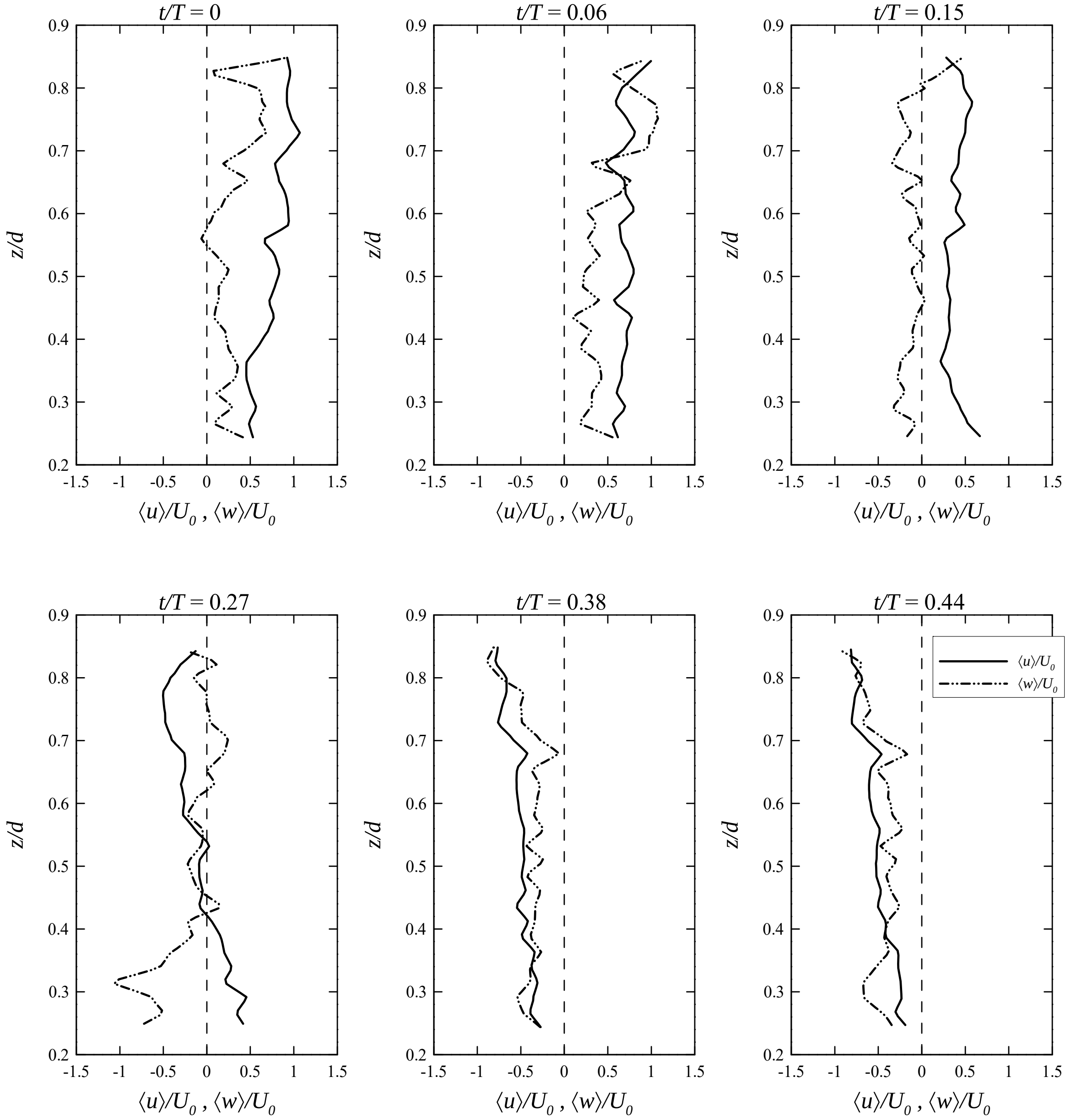

Figure 6.8: Longitudinal and vertical phase-averaged velocity profiles normalized by U_0 at different instants.

The small longitudinal acceleration and deceleration can be observed in Figure 6.8, where $\langle u \rangle$ profile at $t/T = 0.38$ is similar to the one at $t/T = 0.44$. However, $\langle w \rangle$ profile presents some difference near the flume bed ($z/d \approx 0.3$) due to the return flow below the flap occurring to maintain mass conservation in the flume. As expected, the velocity profiles confirm the strong phase variation. At $t/T = 0$ the magnitude of $\langle w \rangle$ is clearly smaller than the magnitude of $\langle u \rangle$, and as the flap moves towards the beach, the variation of $\langle u \rangle$ is much lower than $\langle w \rangle$. This higher variation of $\langle w \rangle$ indicates that the turbulence and the ascendant flow generated by the mass transfer over and below the flap have small influence on $\langle u \rangle$. However, from $t/T = 0.15$ to 0.27, the variation of $\langle u \rangle$ is considerably higher than $\langle w \rangle$, indicating that the deceleration and the acceleration have large influence on $\langle u \rangle$. At $t/T \geq 0.38$, similar shapes of $\langle w \rangle$ and $\langle u \rangle$ were observed.

6.3 Summary and conclusions

The experimental data of free-surface elevation, pressure in the hydraulic PTO system, power capture, rotation angle, angular velocity of the flap and velocity field in the vicinity of the OWSC are presented and analyzed under regular waves.

In order to explain trends of the hydrodynamic characteristics of the OWSC, the experimental data were compared with linear analytical solutions. In general, a large discrepancy was observed between experimental data and analytical solutions, caused by the non-linear behaviors of wave-OWSC interaction that govern the turbulent field and the boundary layer instead of the inviscid and irrotational flow. The velocity field shows a strong ascendant flow, generated by a mass transfer over the flap, due to the approach of the wave crest and the blockage effect of the flap. The velocity vectors are markedly oriented towards the free-surface, indicating that practically the entire mass of water passes over the flap and hence the vertical acceleration is mostly larger than longitudinal one (in fact, the flow presenting longitudinal deceleration). The interval when the flap is in the maximum rotation angle is characterized by rapid variations and a complete change in the nature of the flow. Such large deceleration is not surprising since angular velocity of the flap evolves very rapidly and the flow decelerates to compensate the pressure field.

Another key feature of velocity field is the flow rotation generated by the beginning of the flap deceleration. A largest deceleration of the flow can be observed, caused by the arrival of the wave crest and the change on the orientation of hydrodynamic torque. The flow rotation, generated by wave-OWSC interactions and mass transfer, has an important role on the CWR and, therefore, linear analytical solutions are not accurate to describe the complex hydrodynamics of the OWSC with mechanical constraints observed in the experimental data.

7

Characterization of the hydraulic PTO system

The results presented in this chapter have been published as Brito, M., Teixeira, L., Canelas, R. B., Ferreira, R. M. L. and Neves, M. G. (2017). 'Experimental and numerical studies of dynamic behaviors of a hydraulic power take-off cylinder using spectral representation method'. *Journal of Tribology*.

Contents

7.1 Introduction

The dynamic behaviors of the hydraulic PTO system are often simplified and the inefficiencies such as pressure drops and frictional losses are not incorporated (Babarit et al., 2009; Falcão, 2007, 2008). This chapter aims to understand and to develop a mathematical model of the hydraulic PTO system, that includes the dynamic behaviors of friction and pressure losses.

This chapter presents the results of the physical model tests of the hydraulic PTO system (see Section 5.3). The mathematical model of the PTO system is introduced in Section 7.2 and the results of regular and irregular motions applied to the hydraulic cylinder are presented in Section 7.3.

7.2 Mathematical model of the PTO system

The mathematical model of the hydraulic PTO system is based on the physical model of the hydraulic cylinder presented in Section 5.3, where the PTO force is given by:

$$F_{PTO}(t) = F_f(t) + F_p(t) \tag{7.1}$$

where F_f is the friction force and F_p is the pressure force.

7.2.1 Friction force

Friction between sliding contact surfaces is a result of stochastic interactions between rubbing asperities. The rubbing asperities cause friction by shearing surface materials, lubricants, or surface coatings (Wojewoda et al., 2008). Therefore, F_f is highly stochastic in nature, with significant variations in both amplitude and frequency. However, most friction models do not take these variations into account and instead represent the F_f by a smooth component, F_f^{smooth} (Andersson et al., 2007). The stochastic component, F_f^{sto}, can be represented by adding fluctuation to F_f^{smooth}, and can then be written as:

$$F_f(t) = F_f^{smooth}(t) + F_f^{sto}(t) \tag{7.2}$$

The F_f^{smooth} is modeled by the modified LuGre model presented in Tran et al. (2012); Yanada and Sekikawa (2008). This model is based on the standard LuGre model (de Wit et al., 1995) by incorporating a dimensionless fluid film thickness parameter, h_l, into the Stribeck function, g_s, for modeling the dynamic behavior of F_f^{smooth} in the fluid lubrication regime. Similar to the standard LuGre model, the modified model is based on the bristles deflection, described by:

$$\dot{z}_d(t) = \dot{x}(t) - \frac{\dot{x}(t)}{g_s(\dot{x}(t), h_l(t))} z_d(t) \tag{7.3}$$

and

$$F_f^{smooth}(t) = \sigma_0 z_d(t) + \sigma_1 \dot{z}_d(t) + \sigma_2 \dot{x}(t) \tag{7.4}$$

where z_d is the mean deflection of the elastic bristles, σ_0 and σ_1 are the dynamics coefficients, standing for stiffness and micro-viscous friction coefficient of the bristles, respectively. The static coefficient σ_2 stands for the viscous friction coefficient. The damping term, $\sigma_1 \dot{z}_d$, in Equation (7.4) prevents the model from behaving as a linear spring at small displacements (de Wit et al., 1995). This model takes the Coulomb friction force, F_c, and Stribeck effect in consideration through the g_s, i.e., F_f^{smooth} decreases when increasing $\dot{x}$ at certain low $\dot{x}$ regime (Stribeck, 1902). Stribeck effect is needed to correctly predict initial conditions leading to stick-slip motion. Therefore, g_s curve is a continuous drop of F_f^{smooth} for small $\dot{x}$, which originates from the transition of boundary lubrication to full fluid lubrication through partial fluid lubrication (Yanada and Sekikawa, 2008), and is given by:

$$g(\dot{x}(t), h_l(t)) = \frac{1}{\sigma_0}[(1 - h_l(t))F_c + (Fs - Fc)]e^{-(|\dot{x}(t)|/|\dot{x}_s|)^{n_s}} \tag{7.5}$$

where h_l can be expressed as:

$$\dot{h}_l(t) = \frac{1}{\tau_h}[h_{ss} - h_l(t)] \tag{7.6}$$

with

$$\tau_h = \begin{cases} \tau_{hp} & \{\dot{x} \neq 0, h_l \leq h_{ss}\} \\ \tau_{hn} & \{\dot{x} \neq 0, h_l > h_{ss}\} \\ \tau_{h0} & \{\dot{x} = 0\} \end{cases} \tag{7.7}$$

$$h_{ss} = \begin{cases} K_f |\dot{x}|^{2/3} & \{|\dot{x}| \leq |\dot{x}_b|\} \\ K_f |\dot{x}_b|^{2/3} & \{|\dot{x}| > |\dot{x}_b|\} \end{cases} \tag{7.8}$$

$$K_f = \left(1 - \frac{F_c}{F_s}\right) |\dot{x}_b|^{2/3} \tag{7.9}$$

where h_{ss} is the dimensionless steady-state of h_l, K_f is the proportional constant, $\dot{x}_b$ is the velocity at which the steady-state of F_f^{smooth} becomes minimum, $\dot{x}_s$ is the Stribeck velocity, n_s is the exponent of g_s curve, F_s is the maximum static friction force and τ_{hp}, τ_{hn}, and τ_{h0} are the time constants for acceleration, deceleration, and dwell periods, respectively. In Equation (7.7), $h_l < h_{ss}$ corresponds to the acceleration period, $h_l > h_{ss}$ to the deceleration period. It is assumed by Equation (7.8) that the h_l is increased with $\dot{x}$ only in the negative resistance regime, $|\dot{x}| \leq |\dot{x}_b|$, and is kept at a maximum value outside this regime (Yanada and Sekikawa, 2008).

The F_f^{sto} is expressed using the spectral representation method (Hu and Schiehlen, 1997; Patir and Cheng, 1978; Shinozuka and Deodatis, 1991; Wiercigroch and Cheng, 1997), by the following series:

$$F_f^{sto}(t) = \sigma_f \sum_{i=0}^{M-1} \sqrt{2S(\omega_i)\Delta\omega} \cos(\omega_i t + \varphi_i) \tag{7.10}$$

where σ_f is the standard deviation of the F_f fluctuation, S is the power spectral density function, φ_i is a random phase angle uniformly distributed over $[0, 2\pi]$, $\omega_i = i\Delta\omega$ is a typical frequency, $\Delta\omega$ is the frequency increment, the subscripts $i = 0, 1, 2, ..., M-1$, and M is the sampling number (Shinozuka and Deodatis, 1991; Wiercigroch and Cheng, 1997).

7.2.2 Pressure force

This section aims to formulate a new model for the F_p, that incorporates the stochastic and hysteretic behaviors observed in the experimental tests. Assuming an interval of t when the piston is moving in extending or retracting stroke and one-dimensional flow, the smooth pressure force, F_p^{smooth}, may be written as:

$$F_p^{smooth}(t) = \left[K_p \dot{x}(t)^2 + I_p \ddot{x}(t)\right] A \tag{7.11}$$

where K_p is the coefficient of pressure loss, I_p is the coefficient that takes into account the inertia of the fluid (Falcão, 2007, 2008). The stochastic component, F_p^{sto}, appearing during the piston motion can be represented by adding fluctuation to the F_p^{smooth}, and can then be written as:

$$F_p(t) = F_p^{smooth}(t) + F_p^{sto}(t) \tag{7.12}$$

The F_p^{sto} is also generated using the spectral representation method given by Equation (7.10), with the standard deviation of the F_p fluctuation, σ_p. Due to the dynamic behaviors of $F_p(\dot{x})$ characteristics (see Figures 7.3e and f) an additional condition is added to Equation (7.12). Based on the approach presented in Wojewoda et al. (2008), the mathematical description of the F_p can be generalized to the following form:

$$F_p(t) = \begin{cases} F_p^{smooth}(t) + F_p^{sto}(t) + F_+(t) & \{\text{sign}(\dot{x}\ddot{x}) > 0\} \\ F_p^{smooth}(t) + F_p^{sto}(t) + F_-(t) & \{\text{sign}(\dot{x}\ddot{x}) < 0\} \end{cases} \tag{7.13}$$

Due to the observed non-reversibility of F_p, the dynamic F_p coefficient in acceleration (F_+) and deceleration (F_-) phases, can be approximated by:

$$F_+(t) = P_c \left[1 + \frac{P_s - P_c}{P_c} \psi(\dot{x}(t))\right] A \tag{7.14}$$

$$F_-(t) = P_c \left[1 - \frac{P_s - P_c}{P_c} \psi(\dot{x}(t))\right] A \tag{7.15}$$

where P_s and P_c are the maximum and minimum static pressure (observed at the beginning of piston motion, $\dot{x} \approx 0$), respectively. The general characteristic of Equations (7.14) and (7.15) is allowed an arbitrary form of the function ψ (see Section 7.3.1).

7.3 Results and discussions

7.3.1 Regular motion applied to the hydraulic cylinder

As referred in the Section 5.3.1, two different magnitudes of regular F_{exc}, for $T = 5.1$ and 7.0 s, are applied to the hydraulic cylinder. Figures 7.1 and 7.2 show the time series of the measured x, F_{exc} and F_p and the calculated $\dot{x}$. The experimental results of the dynamic behaviors of F_{PTO}, F_f and F_p are presented in Figure 7.3.

In general, a strong non-linear behavior can be observed in all force-velocity characteristics, i.e., $F_{PTO}(\dot{x})$, $F_f(\dot{x})$ and $F_p(\dot{x})$. The $F_{PTO}(\dot{x})$ characteristics show the hysteretic behavior for extending ($\dot{x} > 0$) and retracting ($\dot{x} < 0$) strokes, for both T. In Figure 7.3 the arrows indicate the direction and the numbers indicate the order of the hysteretic loops. These loops are asymmetric to $\dot{x} = 0$ and its directions are clockwise on the $F_{PTO} - \dot{x}$ plane. Such asymmetrical nature of $F_{PTO}(\dot{x})$ maybe is caused by the asymmetrical characteristic of the hydraulic circuit used. For example, as can be seen from Figure 7.3a, the remarkable vertical expansion for $T = 5.1$ s occurs in retracting stroke for $0 > \dot{x} > -0.025$ m s^{-1} and extending stroke for $0 < \dot{x} < 0.05$ m s^{-1}. For $T = 7.0$ s, the vertical expansion occurs in retracting stroke for $0 > \dot{x} > -0.005$ m s^{-1} and extending stroke for $0 < \dot{x} < 0.035$ m s^{-1}. In addition, the shape and size of the hysteretic loops depend on the rate of increases of $\dot{x}$ (i.e., depends on the $\ddot{x}$). The vertical expansion of the hysteresis loop decreases tightly with decreases of $\ddot{x}$ (i.e., increases of T). This expansion of hysteresis loop is induced by the increases of P_{int} and by the dynamic characteristic of the hydraulic circuit under a varying the $\dot{x}$ condition. For the hysteretic loops, $|F_{PTO}|$ observed during acceleration period is larger than that observed during deceleration period in almost whole $\dot{x}$ range (Figures 7.3a and b). This behavior shows the non-reversibility of F_{PTO} and may be explained by the effect of memory caused by a lag in the F_{PTO}.

A break-away F_{PTO} (points 2 and 5), i.e., the force required to stop sticking and initiate the motion (e.g., from point 1 to point 2) can be observed. Figures 7.3a and b led to the conclusion that the magnitude of break-away force depends on the $\ddot{x}$ during stick, i.e., higher value of $\ddot{x}$

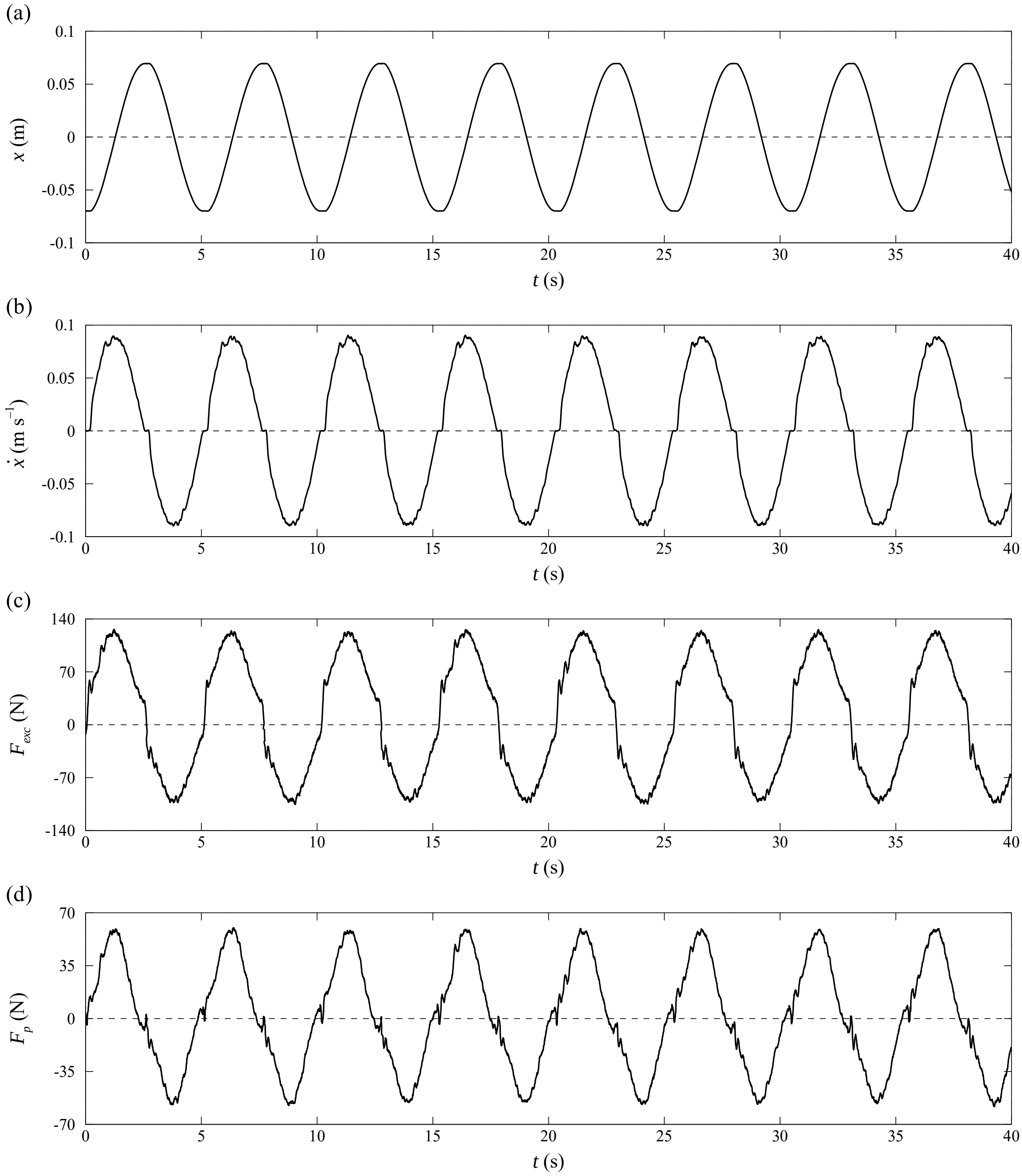

Figure 7.1: Time series measured for $T = 5.1$ s: (a) position; (b) velocity; (c) excitation force; (d) pressure force.

results in higher break-away force. The break-away force for $T = 7.0$ s is 15% smaller than the observed for $T = 5.1$ s. When $|F_{exc}|$ reaches the break-away force the piston starts to slide and $|F_{PTO}|$ decreases rapidly to the minimum $|F_{PTO}|$ in the acceleration period, due to the inertia effect of the hydraulic circuit. The slope of decreasing $|F_{PTO}|$ to the minimum

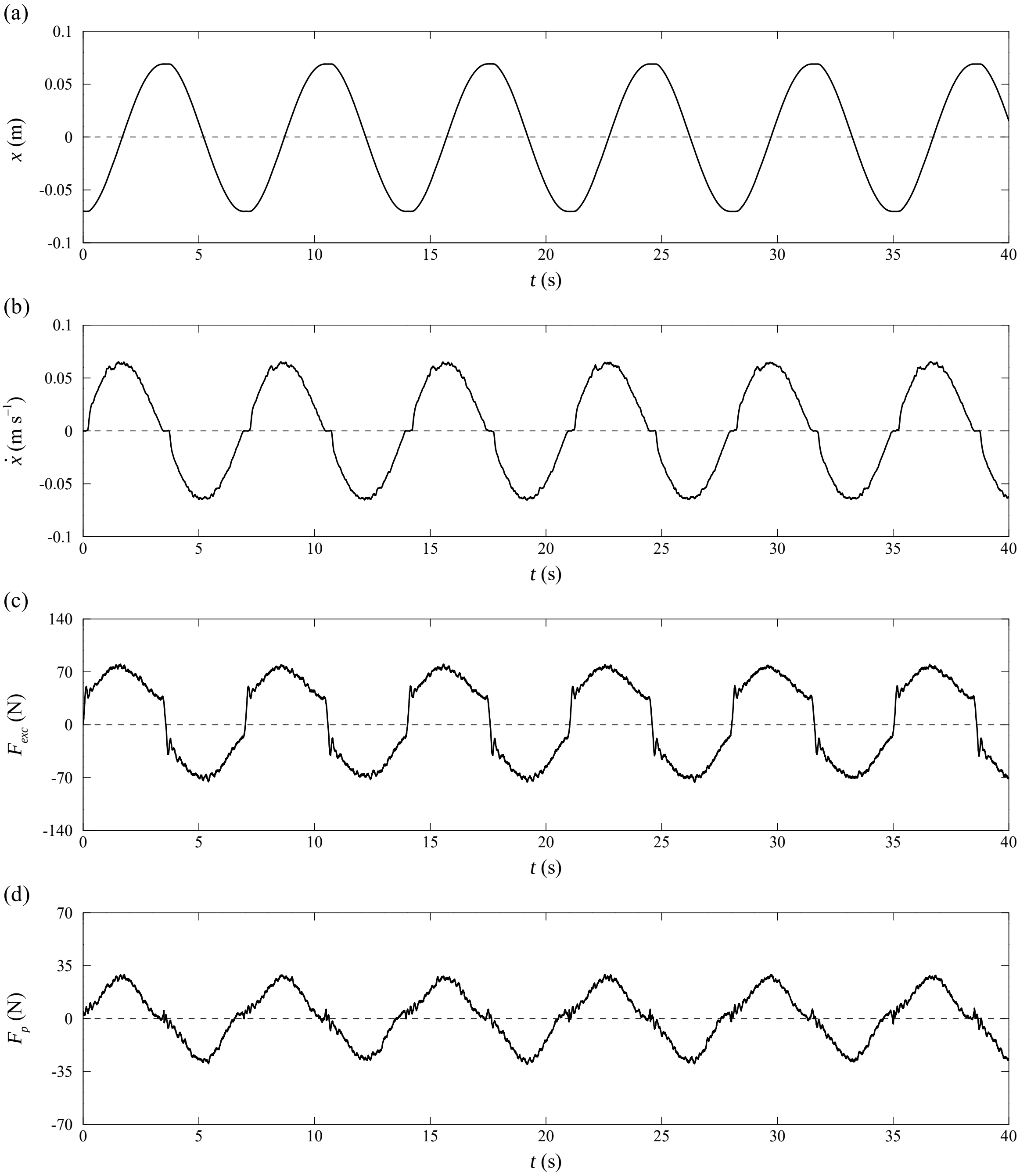

Figure 7.2: Time series measured for $T = 7.0$ s: (a) position; (b) velocity; (c) excitation force; (d) pressure force.

value also depends on the $\ddot{x}$. For small velocities, i.e., $|\dot{x}| < 0.02$ m s^{-1}, it is clearly seen from Figures 7.3a and b that $|F_{PTO}|$ becomes lower than the break-away force during acceleration period. Then, for $-0.025 > \dot{x} > 0.05$ m s^{-1} ($T = 5.1$ s) and for $-0.005 > \dot{x} > 0.035$ m s^{-1} ($T = 7.0$ s), $|F_{PTO}|$ is increased nearly linearly with $|\dot{x}|$ to the maximum magnitude (points

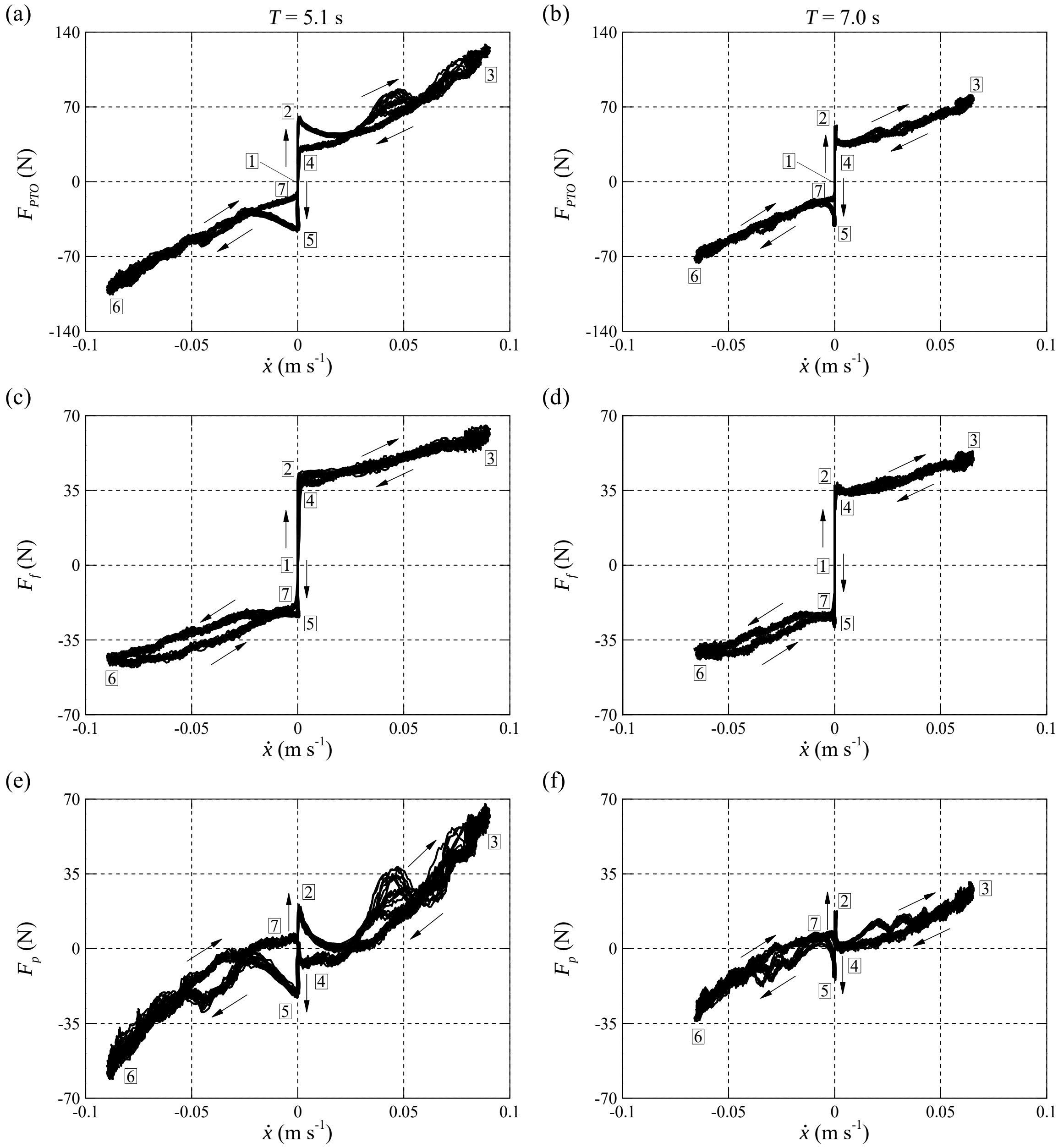

Figure 7.3: Dynamic behavior measured during regular $\dot{x}$ variation for $T = 5.1$ (left column) and 7.0 s (right column): (a,b) PTO force; (c,d) friction force; (e,f) pressure force.

3 and 6). This linearity is caused by the viscous effect and dynamic pressure. During the following deceleration period, the magnitude of $|F_{PTO}|$ decreases almost linearly with $|\dot{x}|$ in the whole $\dot{x}$ range (from point 3 to 4 for $\dot{x} > 0$, and point 6 to 7 for $\dot{x} < 0$). After that, the signal of the F_{PTO} is reversed almost at the same time as the $\dot{x}$ reversal. After this first cycle, the dynamic behavior of F_{PTO} is repeated in the following order: $1 \rightarrow 2 \rightarrow 3 \rightarrow 4 \rightarrow 5 \rightarrow 6 \rightarrow 7$.

As expected, $F_f(\dot{x})$ characteristics also show the stochastic and hysteretic behaviors. Similar results are also obtained by Armstrong-Hélouvry et al. (1994); de Wit et al. (1995); Tran et al. (2012); Tran and Yanada (2013); Yanada and Sekikawa (2008); Yanada et al. (2009). For $\dot{x} > 0$, $|F_f|$ are increased (during acceleration period) and decreased (during deceleration period) nearly linearly with increasing and decreasing $\dot{x}$, respectively, with slope of approximately 300 N s m^{-1}. Furthermore, $|F_f|$ observed during acceleration period for $\dot{x} > 0$ are mostly larger than that observed for deceleration period, and the hysteretic loops is clockwise. However, the stochastic behavior overcome the hysteretic behavior in almost all $\dot{x}$ range. For $\dot{x} < 0$, $|F_f|$ observed during acceleration are smaller than that observed during deceleration period, therefore, the direction of the loops become counter-clockwise. The vertical expansion of the hysteretic loops for $\dot{x} < 0$ are increased when increasing $\ddot{x}$ (Olsson et al., 1998).

As referred in Section 6.2.1, the F_f of the hydraulic cylinder is mainly caused by the bristles made of rubber. The rate-dependent deformation characteristic of the rubber, which results from a viscoelastic nature of rubber, may cause such counter-clockwise behavior (Yanada and Sekikawa, 2008). Additionally, it seems that this behavior is closely related to the large deformation of the bristles caused by P_{int} and by the fact that the hydraulic cylinder was working as a single piston effect and probably the fluid lubrication regime is taken differently for $\dot{x} < 0$ and $\dot{x} > 0$ (see Section 7.3.3).

For $T = 7.0$ s, F_f shows a typical Stribeck curve and the negative resistance regime, clearly seen at $|\dot{x}| < 0.01$ m s^{-1} (Figure 7.3d). However, for $T = 5.1$ s this regime is not clearly seen, as F_f increases almost linearly with $\dot{x}$, only for $\dot{x} > 0$ (Figure 7.3c). This dynamic behavior shows that when $\ddot{x}$ is relatively high, the unsteady-state friction behaves as if there is no Stribeck effect and the F_f can approximately be modeled by $F_f(t) = F_c + \sigma_2\dot{x}(t)$ (Yanada and Sekikawa, 2008). Therefore, the maximum $|F_f|$ is reached when $|\dot{x}|$ is maximum (points 3 and 6). These behaviors of hydraulic cylinder are caused by the viscous friction effects, and its are in agreement with those obtained by Tran and Yanada (2013).

As can be seen in Figures 7.3e and d, $F_p(\dot{x})$ also show the stochastic and hysteretic behaviors in almost whole $\dot{x}$ range, yielding most of hysteretic behaviors observed in $F_{PTO}(\dot{x})$ characteristics. The value of F_p also reaches the break-away force after onset of the motion from the rest. This break-away force are caused by sudden P_{int} gradients (responsible for accelerating and decelerating flows in the hydraulic circuit) and by the variation of flow regime (see Chapter 8). The magnitude of break-away F_p is lower than observed for F_f. Therefore, for both T, the break-away F_{PTO} depends mainly of F_f. On the other hand, the break-away F_p

for $T = 7.0$ s is 20% smaller than the observed for $T = 5.1$ s. After the break-away force is reached, $|F_p|$ decreases when increasing $\dot{x}$ during acceleration period. During the following deceleration period, $|F_p|$ decreases almost linearly with decreasing $\dot{x}^2$ in the whole $\dot{x}$ range (from point 3 to 4 for $\dot{x} > 0$, and point 6 to 7 for $\dot{x} < 0$). After that, the wave form of the F_p becomes almost unchanged, due to the memory effect of the hydraulic circuit.

In this chapter, the numerical modeling of PTO force model, presented in Section 7.2.2, was performed using MatLab and the strategies proposed by Do et al. (2007). The static parameters of F_f were identified experimentally from the steady-state friction characteristics using the least-squares method (Yanada and Sekikawa, 2008). Where for $\dot{x} > 0$: $F_s = 35$ N, $F_c = 32$ N, $\dot{x}_s = 0.003$ m s^{-1}, $\dot{x}_b = 0.1$ m s^{-1}, $n = 0.5$, $\sigma_2 = 300$ N s m^{-1}; and for $\dot{x} < 0$: $F_s = -30$ N, $F_c = -22$ N, $\dot{x}_s = -0.002$ m s^{-1}, $\dot{x}_b = -0.1$ m s^{-1}, $\sigma_2 = 320$ N s m^{-1}, $n = 0.5$. The dynamic parameters, $\sigma_0 = 10^8$ N m^{-1} and $\sigma_1 = 100$ N s m^{-1}, were identified experimentally by the method proposed in Tran et al. (2012); Tran and Yanada (2013); Yanada et al. (2009). The time constant, $\tau_{hp} = 5$ s, $\tau_{hn} = 2$ s, and $\tau_{h0} = 10$ s, were also identified experimentally using the data presented in Figure 7.3.

For the conditions tested the results showed that the values of F_s, F_c and $\dot{x}_s$ varies with the P_{int} while the other static parameters are practically unchanged with P_{int}. Tran and Yanada (2013) obtained that F_s, F_c and $\dot{x}_s$ increases slightly linear with P_{int}, however, in this study they were considered constant. The parameter σ_0 showed a strong influence on the dynamic behavior of F_f. However, here, relatively high values of σ_0 predict well the behavior of F_f for $\dot{x} < 0$ and $\dot{x} > 0$. The parameters $K_p = 2.3 \times 10^6$ kg m^{-3}, $I_p = 1.2 \times 10^4$ kg m^{-2}, $P_s = 2000$ Pa and $P_c = -500$ Pa were identified from the measured F_p. It should be noted that these values depend on the valve-opening (see Chapter 8). The standard deviations, $\sigma_f = 2.2$ N and $\sigma_p = 3.4$ N, were estimated from fluctuation signals of measured F_f and F_p, respectively.

The stochastic components are generated using the spectral representation method given by Equation (7.10), therefore, is necessary estimate S for the fluctuation signals of F_f and F_p. The measured and the fitted (used in the mathematical model) one-sided S are presented in Figure 7.4.

The fitted S can be given by:

$$S(\omega) = \frac{\kappa e^{-\xi\omega}}{1 + (\xi\omega)^{\zeta}} \tag{7.16}$$

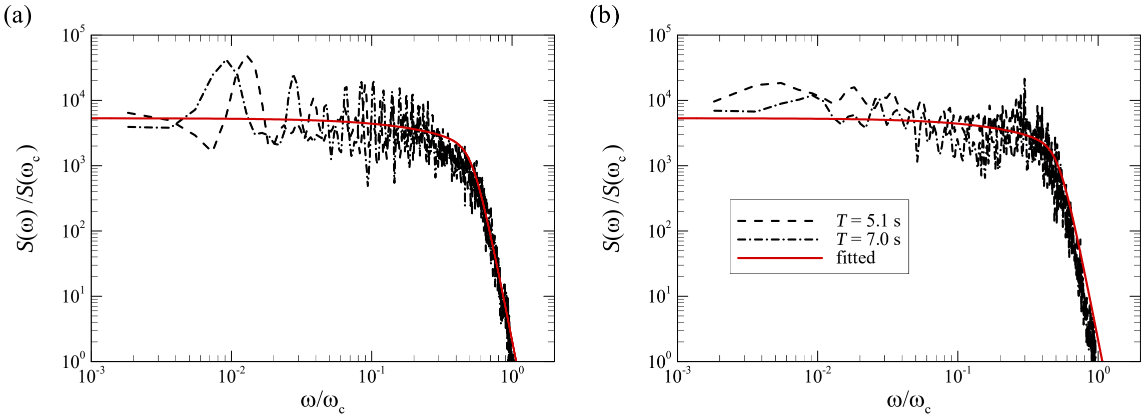

Figure 7.4: Measured and fitted power spectrum density: (a) fluctuation signal of the friction force; (b) fluctuation signal of the pressure force.

where $\kappa = 0.4$ N^2 s, $\zeta = 10$ and $\xi = 0.02$ s are the fitted parameters of S. These values allow to represent the measured characteristics of S with a relatively good accuracy. The upper cut-off frequency, ω_c, of the fitted S is determined from the measured S by:

$$\int_0^{\omega_c} S(\omega)d\omega \cong (1-\epsilon)\int_0^{\infty} S(\omega)d\omega \tag{7.17}$$

and assuming the admissible relative error, $\epsilon = 0.01$ (Shinozuka and Deodatis, 1991). It yields $\omega_c = 96.4$ rad s^{-1}, and the value of the measured $S(\omega_c) = 7.5 \times 10^{-5}$ N^2 s. It turns out that this value is very small and can be neglected (Hu and Schiehlen, 1997). The time step, Δt, is fixed and chosen equal to the experimental tests, i.e., 1/120 s. The function ψ, appearing in Equations (7.14) and (7.15), was applied in the following form:

$$\psi(\dot{x}(t)) = \frac{1}{1+(\dot{x}(t)/\dot{x}_p)^2} \tag{7.18}$$

with $\dot{x}_p = 0.002$ m s^{-1}.

A preliminary evaluation of the accuracy of the mathematical model is performed by comparison the difference between the measured and calculated F_f and F_p obtained with and without stochastic components, i.e., $F_f^{sto} = 0$ in Equation (7.2) and $F_p^{sto} = 0$ in Equation (7.12).

Figure 7.5 presents the scatter diagrams of measured versus calculated F_f and F_p for $T = 5.1$ and 7.0 s. A 1:1 line (black line) is plotted for reference, over this line the measured is equal to calculated F_f or F_p.

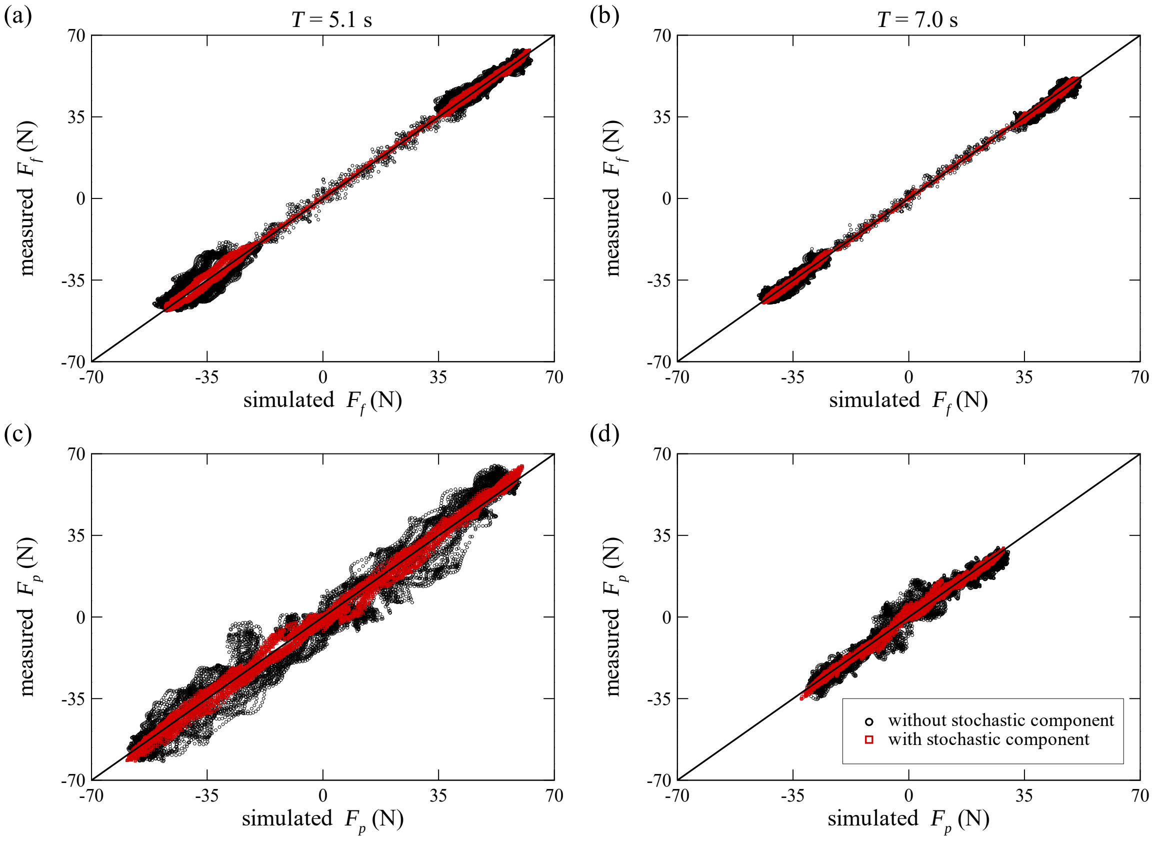

Figure 7.5: Comparison of the scatter diagrams obtained with and without stochastic components for $T = 5.1$ (left column) and 7.0 s (right column): (a,b) friction force; (c,d) pressure force.

Figures 7.5a and b show a strong positive linear correlation between measured and calculated F_f obtained with stochastic component for both T, with almost all data fitted by the 1:1 line. The root-mean-square error is increased for relatively high value of F_f, due to the fact that the direction of the measured loops become counter-clockwise (see Figures 7.3c and d) and the modified LuGre model cannot predict it with good accuracy (see Figures 7.8c and 7.9c).

Figures 7.5c and d also show a positive linear correlation between measured and calculated F_p obtained for both T, however, the root-mean-square error of F_p is larger than F_f one. In general, the scatter diagrams of F_f and F_p obtained with stochastic components show a tight distribution (i.e., smaller root-mean-square error) about the 1:1 line then without stochastic component one. These results demonstrate that the mathematical model can predict with a satisfactory accuracy most of dynamic behaviors of F_f and F_p.

Figures 7.6 and 7.7 confirm the mentioned good agreement between the measured and calculated time series of F_{PTO}, F_f and F_p. The break-away F_{PTO} caused by two stops per cycle (at $t \cong iT/2$, where $i = 1, 2, ..., M - 1$) are clearly visible in the calculated results. For $t \neq iT/2$, the results show a remarkable agreement between the measured and calculated F_{PTO}, with a relative error less than 2%. These results highlight that the fitted S can predict the stochastic behaviors of F_{PTO}.

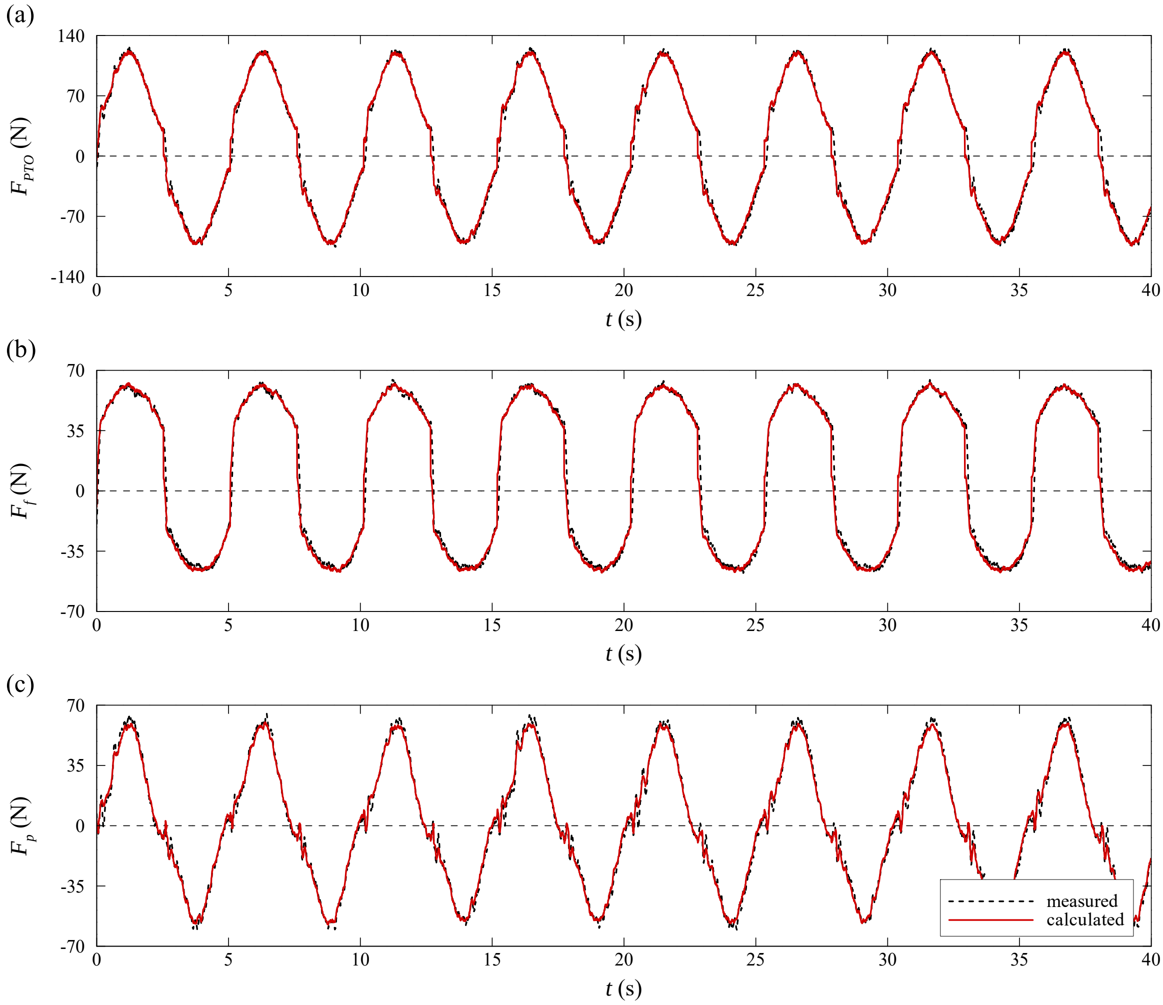

Figure 7.6: Comparison between measured and calculated time series for $T = 5.1$ s: (a) PTO force; (b) friction force; (c) pressure force.

The modified LuGre model can predict accurately the dynamic behaviors of F_f (Figures 7.6b and 7.7b). However, in the pre-sliding regime some discrepancies are observed, due to the dependency on the σ_0 (Yanada and Sekikawa, 2008). This pre-sliding regime occurs at $t \cong iT/2$ and is characterized by a dominant adhesive forces, and thus the F_f appears to be primarily a function of x rather than the $\dot{x}$. The reason for this behavior is that the asperity

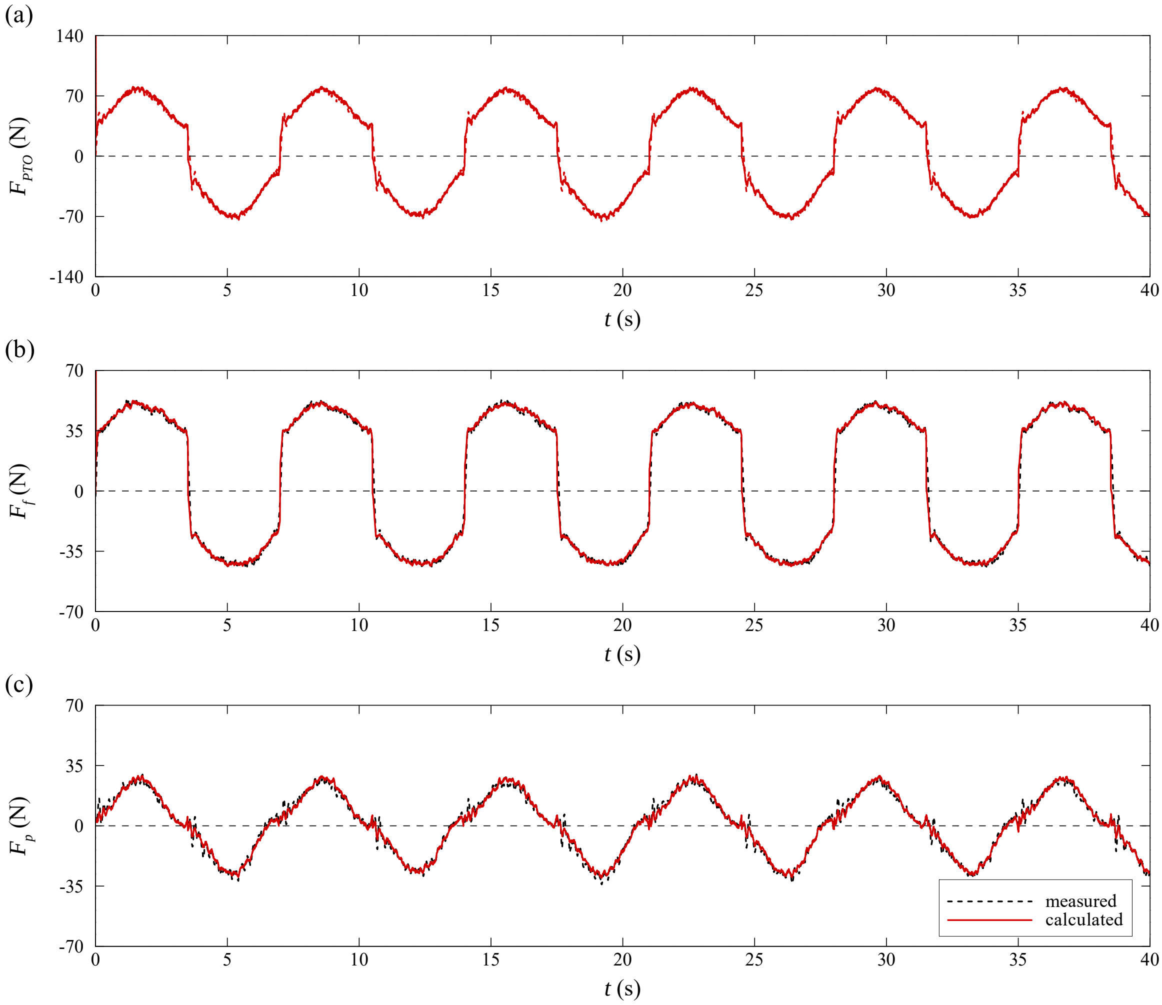

Figure 7.7: Comparison between measured and calculated time series for $T = 7.0$ s: (a) PTO force; (b) friction force; (c) pressure force.

junctions deform elasto-plastically (depending on their individual loading), thus behaving as non-linear hysteretic springs (Swevers et al., 2000). As x increases the junctions will break resulting in the break-away F_f (Armstrong-Hélouvry et al., 1994).

Figures 7.6c and 7.7c show that the F_p can be satisfactory modeled using the proposed model and constant values of K_p and I_p. However for $T = 5.1$ s the maximum F_p was hardly calculated, presenting a relative error of 5%. This difference can be related with dependency of K_p and I_p on the $\dot{x}$. At $t \cong iT/2$ some discrepancies are also observed, due to the asymmetry of hydraulic circuit and dynamic characteristic of check-valves, as vibration and delay time, which exist under a varying $\dot{x}$ condition and was not including in the mathematical model.

The comparison between measured and calculated dynamic behaviors of F_{PTO}, F_f and F_p, for $T = 5.1$ and 7.0 s, are shown in Figures 7.8 and 7.9, respectively.

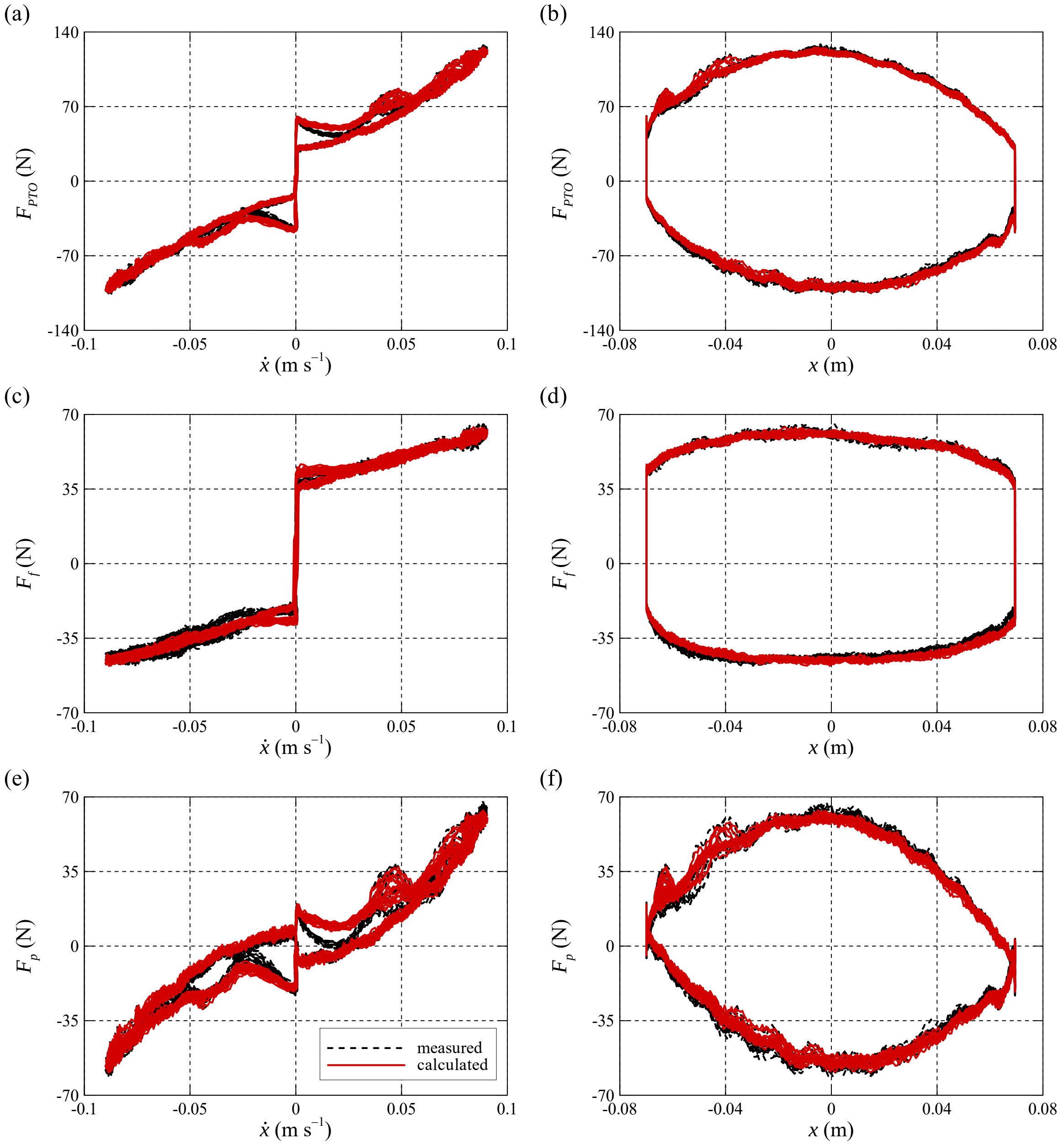

Figure 7.8: Comparison of measured and calculated force-velocity (left column) and force-displacement (right column) characteristics for $T = 5.1$ s: (a,b) PTO force; (c,d) friction force; (e,f) pressure force.

In general, the mathematical model reproduces reasonably the dynamic behaviors of the hydraulic cylinder. The proposed model can predict most of dynamic behaviors of F_p, however, cannot predict with a good accuracy the hysteretic loop, may be due to the effect of some other mechanisms (turbulence, shear stresses, 3D flow) that are not incorporated in this

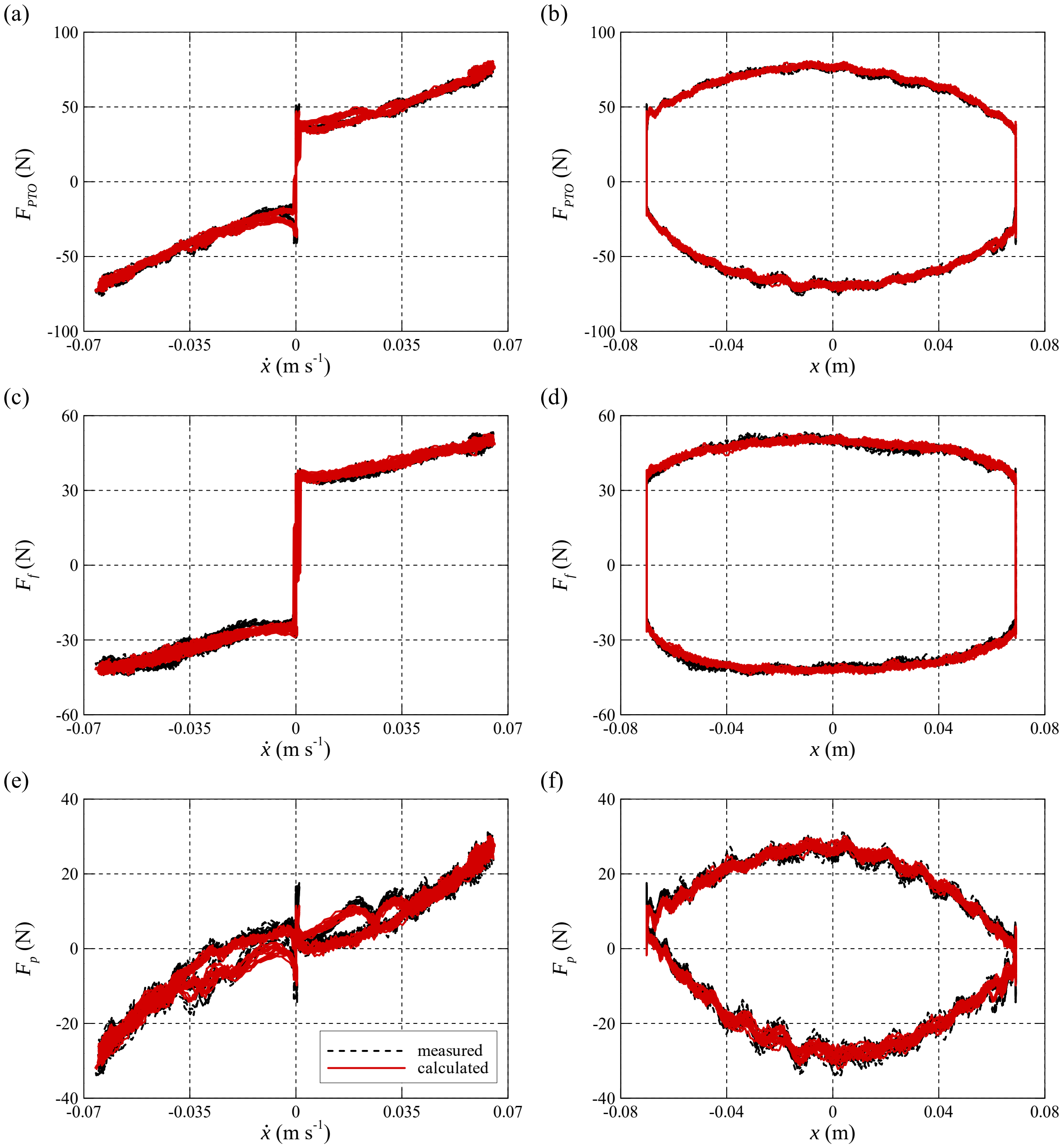

Figure 7.9: Comparison of measured and calculated force-velocity (left column) and force-displacement (right column) characteristics for $T = 7.0$ s: (a,b) PTO force; (c,d) friction force; (e,f) pressure force.

model. For $\dot{x} < 0$, the modified LuGre model predicts a much smaller size of the hysteretic loop than the measured one, for both T (Figures 7.8c and 7.9c). These differences are caused by the fact that the direction of the measured loops become counter-clockwise and, therefore, as referred above, the modified LuGre model cannot predict it.

Another convenient means of representing these results is the force-displacement characteristics (Wiercigroch et al., 1999). This representation can provide useful information regarding the force variation and relating it to motion of the piston, especially to highlight the non-reversibility of the hydraulic circuit. The force-displacement characteristics confirm clearly the non-reversibility of $F_{PTO}(x)$, $F_f(x)$ and $F_p(x)$, i.e., different path for acceleration and deceleration period. For example, if a simple Coulomb model was used, the $F_f(x)$ characteristics would be a plain rectangle.

7.3.2 Irregular motion applied to the OWSC

As the model can predict, with a satisfactory accuracy, most of regular dynamic behaviors of F_{PTO}, in this section, the measured and calculated results of irregular motion applied to the OWSC are presented. The irregular motion was performed for the time series presented in Figure 7.10a.

From a viewpoint of the indirect measurement of B_0, is not straightforward due to a number of unknown parameters in Equation (5.19). Therefore, experimental tests were firstly performed for OWSC motion without the hydraulic cylinder, where the dynamic of the OWSC can be described by the following equation:

$$I_{yy}\ddot{\theta}(t) = F_{exc}(t)L_6 - mg\overline{z}\sin(\theta(t)) - B_0(t) \tag{7.19}$$

The results of these experimental tests show, as for regular motion applied to the hydraulic cylinder, a small hysteretic and stochastic behavior of B_0. Therefore, in this study, B_0 was modeled using the simple approach presented in Wojewoda et al. (2008), using Coulomb friction, with static friction coefficient of 0.16.

As can be seen in Figure 7.10c, the calculated F_p is in good agreement with the measured data. This result confirms that F_p can be satisfactory modeled using constant values of K_p and I_p. However, some discrepancies are observed where the pressure gradients is higher, for example at $28.5 < t < 29$ s. These differences may be caused by the asymmetrical characteristic of the hydraulic circuit. In fact to include all the dynamic effects in a single model is not an easy task, and it is especially difficult to define a mechanism governing the switch between the check-valves. The calculated F_{PTO} also presents a good agreement with the measured data (Figure 7.10d). These results highlight that the mathematical model can predict, with a satisfactory accuracy, most of dynamic behaviors of F_{PTO} in irregular motion.

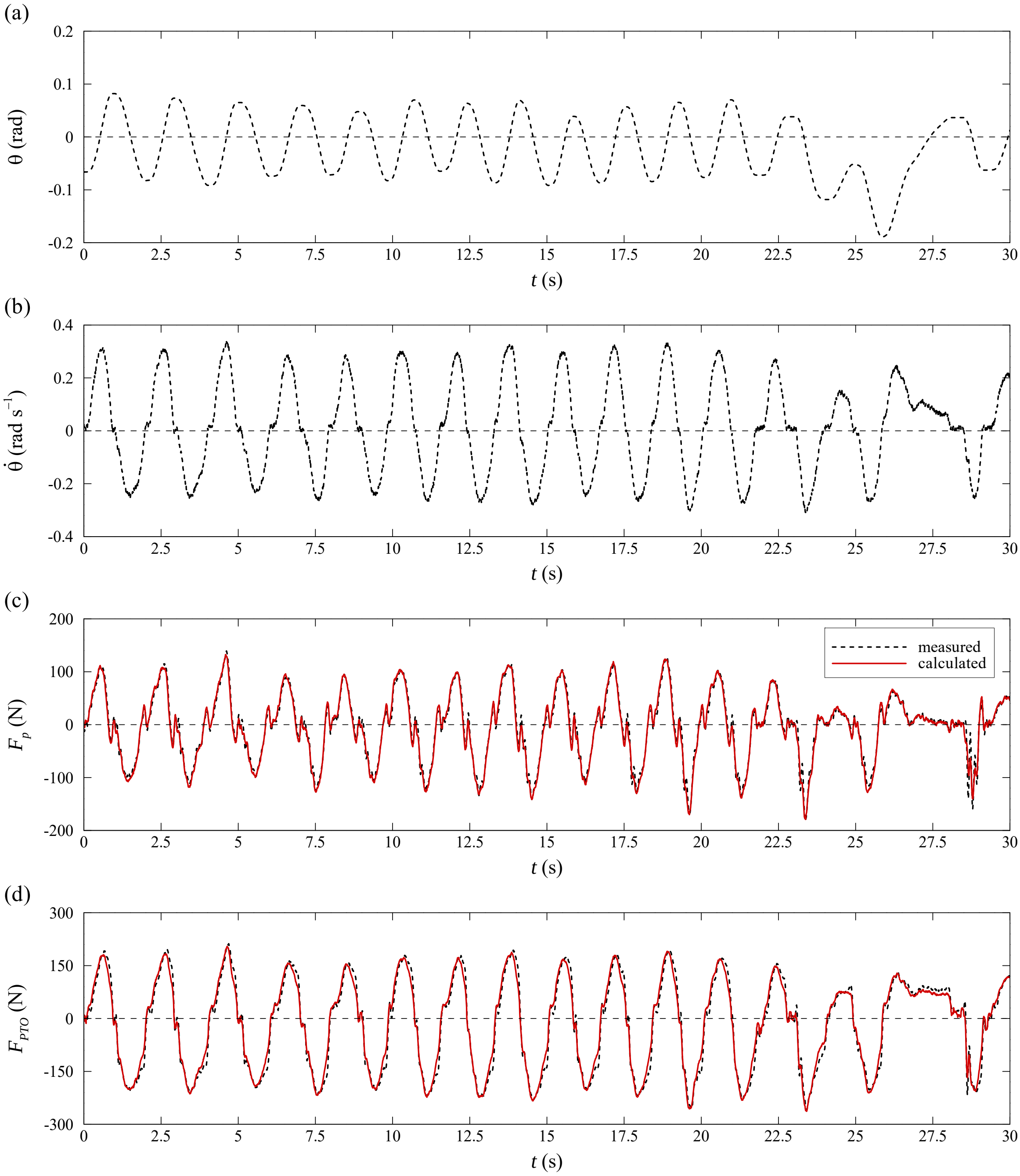

Figure 7.10: Comparison between measured and calculated time series: (a) rotation angle; (b) angular velocity; (c) pressure force; (d) PTO force.

7.3.3 Characteristics of PTO damping under regular wave

The equation of motion of the flap expresses the dynamic equilibrium of the torque about the bearings, and it is given by:

$$\mathcal{T}_h = I\ddot{\theta} + \mathcal{T}_g + \mathcal{T}_{PTO} \tag{7.20}$$

where $\mathcal{T}_h$ is the hydrodynamic torque, $\mathcal{T}_g$ is the torque due to the gravity and $\mathcal{T}_{PTO}$ is the torque exerted on the flap by the PTO system, which is given by:

$$\mathcal{T}_{PTO} = \mathcal{T}_f + \mathcal{T}_p \tag{7.21}$$

Here $\mathcal{T}_f$ and $\mathcal{T}_p$ are respectively the torque due to friction and pressure forces of the hydraulic cylinder, given by $\mathcal{T}_f = F_f L_4 \sin\beta$ and $\mathcal{T}_p = F_p L_4 \sin\beta$, where β is the angle between the piston rod and the flap (see Figure 5.14 for detail), F_f and F_p are calculated according to Sections 7.2.1 and 7.2.2, respectively. However, due to the cavitation phenomena observed in the expansion phase of the hydraulic cylinder, the Equation (7.11) is adapted as:

$$F_p = A \begin{cases} K_p\dot{\theta}^2 + I_p\ddot{\theta} & \text{for } \sigma \geq \sigma_c \text{ (no cavitation)} \\ \\ P_v + I_p\ddot{\theta} & \text{for } \sigma < \sigma_c \text{ (cavitation)} \end{cases} \tag{7.22}$$

where P_v is the vapor pressure of water in the hydraulic circuit, σ_c is the critical cavitation coefficient and σ is the Thoma coefficient that allows to determine the cavitation intensity, defined as:

$$\sigma = \frac{P_{atm} + P_{int} - P_v}{P_{atm}} \tag{7.23}$$

In this work, it was considered $\sigma_c = 0$, and its variation with the pressure is not modeled due to the lack of information concerning its physical characteristics. The comparison between the measured and the fitted $\mathcal{T}_p$ for $T = 3.5$ s and $H = 0.25$ m, and for $T = 2.5$ s and $H = 0.2$ m is shown in Figure 7.11. The fitted $\mathcal{T}_p$ shows a good agreement with measured data with the least squares goodness-of-fit $R^2 = 0.95$. This model predicts the dynamic behaviors of $\mathcal{T}_p$ with a satisfactory accuracy, and therefore allows to estimate $\mathcal{T}_h$ from Equation (7.20).

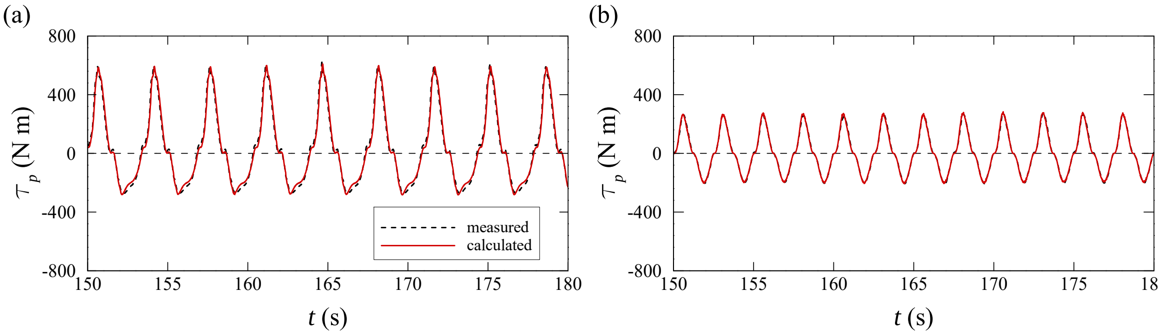

Figure 7.11: Comparison between measured and fitted torque due to pressure force of the hydraulic cylinder for: (a) $T = 3.5$ s and $H = 0.25$ m; (b) $T = 2.5$ s and $H = 0.2$ m.

7.4 Summary and conclusions

The dynamic behaviors of the hydraulic PTO system were investigated under different magnitudes of controlled regular and irregular excitation force.

The experimental results show a strong non-linear behaviors, including hysteretic and stochastic behaviors, of PTO force. The hysteretic loops of the PTO force is expanded to higher velocities and its size increased when the acceleration is increased. Non-reversibility of PTO force, i.e., different paths in the PTO force-velocity characteristics for the acceleration and deceleration phases, are observed.

To capture the hysteretic behavior the modified LuGre model was used for the friction force and a new model was proposed for the pressure force. To model the stochastic behavior of the measured friction force and pressure force the spectral representation method was used. The systematically comparison between measured and calculated results have been demonstrated that the mathematical model can predict, with a satisfactory accuracy, most of dynamic behaviors of PTO force. The modified LuGre model can predict the reduction of the friction force at small velocities with decreasing period. However, this model cannot predict the expansion of the hysteretic loop to higher velocities at decreased period and the counter-clockwise loops. The new model for the pressure force seems appropriated for the problem involving hydraulic cylinders.

The hydraulic PTO system also shows the cavitation phenomena for large amplitude of flap motion. The mathematical model was adapted, and it can predict the dynamic behaviors of the hydraulic PTO system with satisfactory accuracy.

8

Power capture of OWSC

The results presented in this chapter has been submitted as Brito, M., Ferreira, R. M. L., Teixeira, L., Neves, M. G. and Canelas, R. B. ‘Experimental investigation on the power capture of an oscillating wave surge converter in unidirectional waves’. *Renewable Energy*.

Contents

8.1 Introduction

A comprehensive knowledge of the wave-flap and flap-PTO system interactions in the energy conversion process is essential in the design and performance of OWSCs. However, due to the complexity of these interactions, most of previous works on the OWSCs had looked at the design and performance of the flap in laboratory-scale tests without hydraulic PTO system.

At present, few experimental studies have been performed on the hydrodynamics of OWSCs (see e.g., Folley et al. (2007, 2004); Henry (2009); Henry et al. (2014a,b); Lin et al. (2012); Schmitt et al. (2012); Whittaker et al. (2007)). These studies have been often focused on the effects of water depth, wave period and height, density, moment of inertia and location of centre of mass of the flap on the OWSC dynamics. Their results provide useful information but are still limited in what concerns the influence of hydraulic PTO system on the CWR and RAO (Ning et al., 2017).

This chapter first presents the experimental results of the OWSC under regular waves, from which the CWR and RAO are obtained. The effects of PTO system, wave frequency and height on the OWSC dynamics are presented and discussed in Section 8.2. The effects of non-linearity due to large amplitude of flap motion are discussed. The experimental results of OWSC under irregular waves are analyzed in Section 8.3. Due to the non-linearities, the RAO is analyzed by harmonic decomposition. Finally, the non-linear output frequency response functions are considered as the extension of the RAO to the non-linear case to predict the CWR (Section 8.4).

8.2 Experimental results of the OWSC under regular waves

In order to illustrate the experimental results of the OWSC under regular waves, the measured η obtained from WP3 and WP4 together with angular velocity of the flap, $\dot{\theta}$, pressure in the cylinder chamber, P_{int}, and power capture, W_{out}, for $T = 2.5$ s and $H = 0.20$ m (corresponding to $kH = 0.194$ and $kd = 0.799$) and for $T = 3$ s and $H = 0.25$ m (corresponding to $kH = 0.196$ and $kd = 0.648$, see Table 5.2) are presented in Figure 8.1.

From Figures 8.1a and b, it is clear that the free-surface elevation, η, shows a non-linear behavior, caused by the wave interactions with OWSC and flume bed. Such interactions cause differences between incident plus reflected waves (measured by WP3) and transmitted

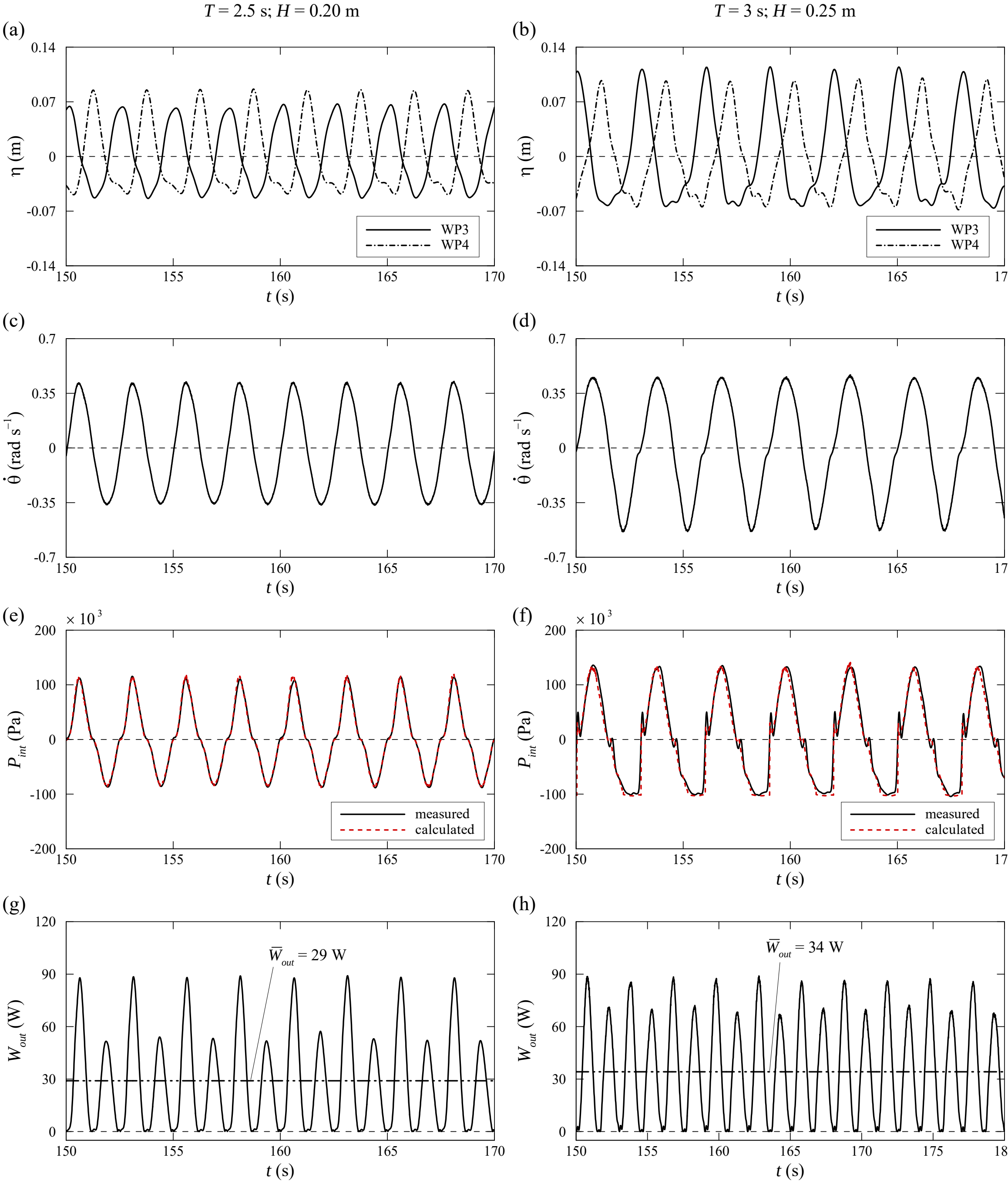

Figure 8.1: Time series of: (a,b) free-surface elevation measured by WP3 and WP4; (c,d) angular velocity of the flap; (e,f) pressure in the cylinder chamber; (g,h) power capture. The left column shows time series for $T = 2.5$ s and $H = 0.20$ m, and the right column for $T = 3$ s and $H = 0.25$ m. In (e,f) the measured pressure in the cylinder chamber is fitted by Equation (7.22). In (g,h) the horizontal dash-dotted line indicates the mean power capture.

waves (measured by WP4) for both cases. It was observed that the wave amplitude decreases close to the flap to approximately 45% for $T = 2.5$ s and $H = 0.20$ m, and to 30% for $T = 3$

s and $H = 0.25$ m, due to the blockage effect of the flap.

In terms of wave cycle, as the wave crest approaches the OWSC, the flap starts to move toward the beach with $\dot{\theta} > 0$ (Figure 8.2a). The flap reaches its maximum $\dot{\theta}$ when the wave crest begins to pass over it (Figure 8.2b). Once the flap is fully submerged, $\dot{\theta}$ decreases rapidly and then the flap stops. As the wave crest moves away from the flap, the wave pressure is reduced and the water level begins to drop as the trough approaches and the flap begins to rise up and pierces through the back of the wave crest (Figure 8.2c). As the wave comes to the trough, the flap is moving towards the wavemaker with $\dot{\theta} < 0$. The water level is low, much of the flap becomes exposed and, therefore, the water provides little resistance and the flap reaches its minimum $\dot{\theta}$ (Figure 8.2d). Then the flap pitches forward into the incoming wave crest, and the wave cycle is repeated. A more detail view of wave-OWSC interaction can be seen in Figure 8.2, where a series of snapshots of the OWSC for $T = 3$ s and $H = 0.25$ m is presented. The direction of wave propagation is from right to left.

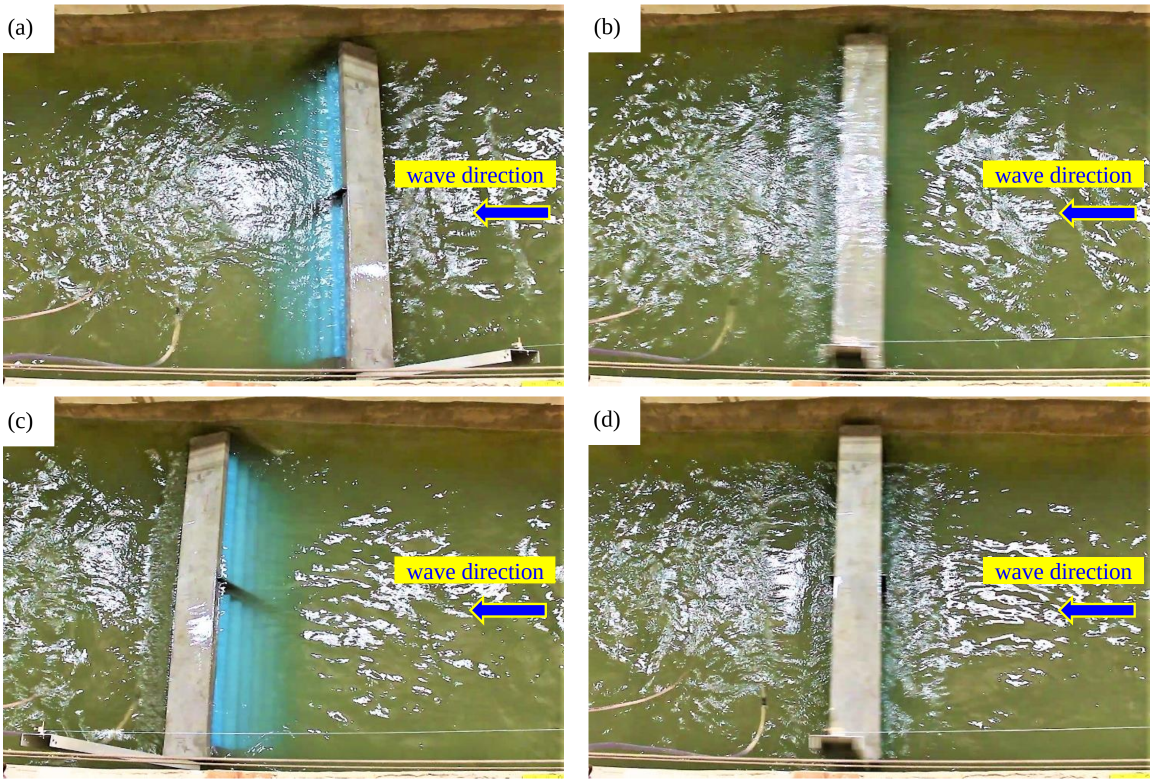

Figure 8.2: Series of snapshots of the OWSC for $T = 3$ s and $H = 0.25$ m when: (a) wave crest approaches the OWSC; (b) wave crest begins to pass over the flap; (c) wave trough approaches the OWSC; (d) wave trough passes through the flap. The direction of wave propagation is from right to left.

Figure 8.2a shows the instant when $\dot{\theta} \approx 0$ and the wave crest approaches the OWSC. Figure 8.2b shows the instant when the wave crest begins to pass over the flap. At this instant, the flap reaches its maximum $\dot{\theta} \approx 0.45$ rad s^{-1}. Figure 8.2c shows the instant when $\dot{\theta} \approx 0$ and the wave trough approaches the OWSC. Figure 8.2d shows the instant when the wave trough passes through the flap. At this instant, the flap reaches its minimum $\dot{\theta} \approx -0.54$ rad s^{-1} (see Figure 8.1d).

In order to investigate the non-linear effects, the non-linear harmonic decompositions by Hilbert Transform of η, $\dot{\theta}$ and P_{int} for the conditions presented in Figure 8.1 are shown in Figure 8.3.

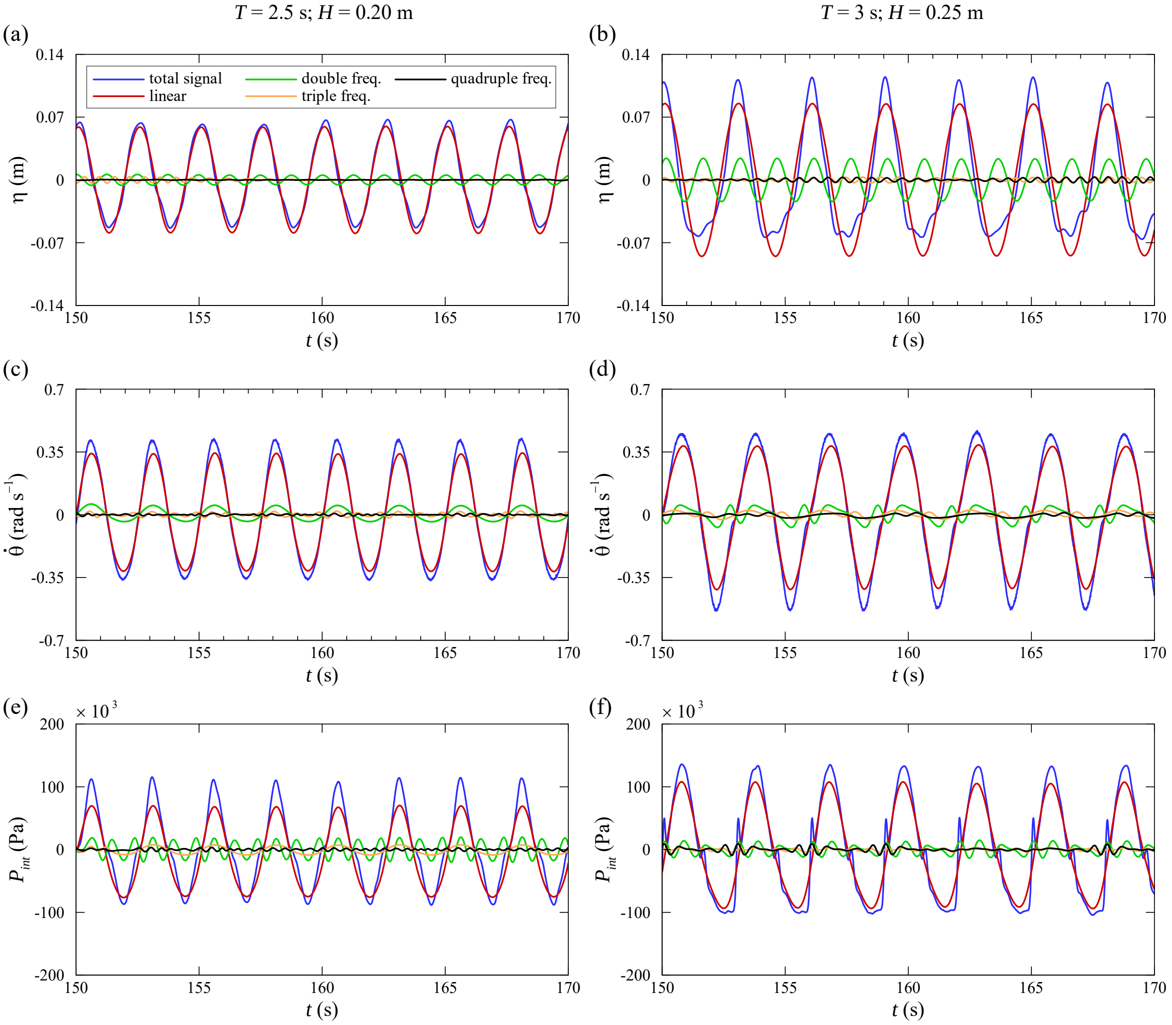

Figure 8.3: Harmonic decomposition of: (a,b) free-surface elevation measured by WP3; (c,d) angular velocity of the flap; (e,f) pressure in the cylinder chamber. The left column shows time series for $T = 2.5$ s and $H = 0.20$ m, and the right column for $T = 3$ s and $H = 0.25$ m.

In the decompositions of η, $\dot{\theta}$ and P_{int} are necessary fourth-order harmonics components (i.e., linear, double, triple and quadruple frequency components) to describe the main wave-OWSC interactions (Henry et al., 2014a). If fact, the effect of local non-linearities such as viscous damping is significant, any contribution from this drag term would produce linear and triple frequency components (Santo et al., 2017). As expected, qualitatively, the structure of the measured time series are dominated by the linear component. However, the signals present some important double and triple frequency components. In general, the quadruple frequency component is slightly smaller than the other components. However, for the P_{int} with $T = 3$ s and $H = 0.25$ m this quadruple frequency component presents a higher value (Figure 8.3f), caused by the cavitation phenomena observed in the expansion phase of the hydraulic cylinder ($\dot{\theta} < 0$). The $P_{int} = F_p/A$ is fitted by the Equation (7.22).

In a perfect PTO system, pressure loss coefficient, K_p, would be constant but this was not the case. The value of K_p is dependent on the flow regime in the hydraulic circuit, and presents different value for compression ($\dot{\theta} > 0$) and for expansion ($\dot{\theta} < 0$) phases of the hydraulic cylinder (see Figure 8.4). As referred in Section 5.3, the value of K_p was controlled by the valve-opening, and was quantified based on the number of rotation of hand-wheel of the globe valves, M. In this work, the experimental tests were performed for six valve-openings ($M = 0$, 1, 2, 3, 4 and 5) for $\dot{\theta} > 0$ and for a full valve-opening ($M = 0$) for $\dot{\theta} < 0$. $M = 5$ corresponds to the maximum pressure range of the hydraulic cylinder used.

An example of the variation of K_p with magnitude of $\dot{\theta}$ for $T = 3$ s and $H = 0.25$ m is shown in Figure 8.4.

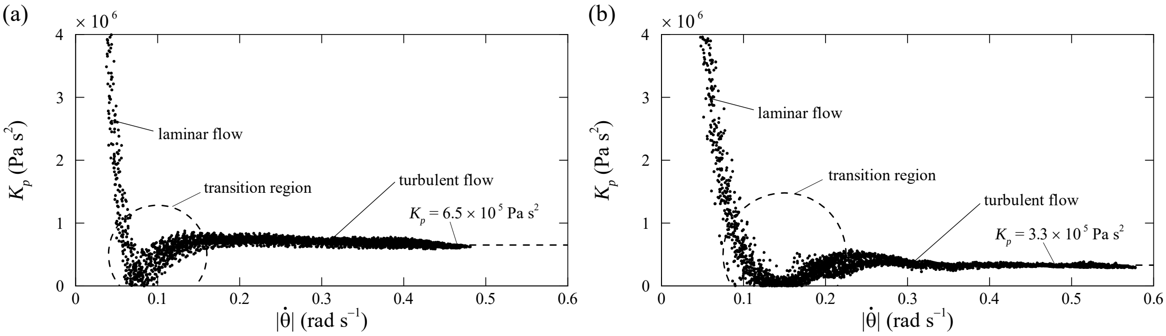

Figure 8.4: Variation of the coefficient of pressure loss with magnitude of angular velocity of the flap for $T = 3$ s and $H = 0.25$ m: (a) compression phase of the hydraulic cylinder ($\dot{\theta} > 0$) for $M = 1$; (b) expansion phase of the hydraulic cylinder ($\dot{\theta} < 0$) for $M = 0$.

As expected for both phases of the hydraulic cylinder, the variation of K_p with $\dot{\theta}$ presents the typical transition region between laminar and turbulent flows. However, in the turbulent flow regime the K_p is almost constant (Figure 8.4). The transition region is characterized by a complex variation of K_p, and due to the lack of information concerning its physical characteristics, the measured P_{int} in Figures 8.1e and f is fitted using a constant value of K_p in the turbulent flow.

The calculated P_{int} shows a good agreement with measured data with the least squares goodness-of-fit $R^2 \approx 0.98$ for $T = 2.5$ s and $H = 0.20$ m (Figure 8.1e). In the Figure 8.1f, for $T = 3$ s and $H = 0.25$ m, some discrepancy is observed for $\dot{\theta} \approx 0$, may be due to the dissolve of cavitation bubbles (see Section 7.3.3). The association between cavitation bubbles and the strong non-linear behavior of wave-OWSC interaction causes the steep gradient of P_{int} (Figure 8.1f). However, the calculated P_{int} shows a good agreement with experimental data with $R^2 \approx 0.95$. Furthermore, this steep gradient of P_{int} is absorbed in the W_{out} (Figure 8.1h), as its occurs for small value of $\dot{\theta}$. The experimental and calculated $\overline{W}_{out}$ presents an relative error of about 2%.

In order to investigate the non-linear behavior of the wave-OWSC interaction the response amplitude operator (RAO) is introduced. As RAO describes the linear relationship between the resultant response and the incident wave amplitude (Santo et al., 2017), in this study, RAO was obtained by evaluating the magnitude of $\dot{\theta}$ and η. Similarly to Flocard and Finnigan (2012), due to the asymmetry of the flap motion (i.e., $|\dot{\theta}_{max}| \neq |\dot{\theta}_{min}|$), the RAO is defined as:

$$\mathrm{RAO} = \frac{\left|\dot{\theta}_{max} - \dot{\theta}_{min}\right|}{H} \tag{8.1}$$

where $\dot{\theta}_{max}$ and $\dot{\theta}_{min}$ are the maximum and minimum of $\dot{\theta}$, respectively. The variation of RAO with wave frequency, f, and with pressure loss coefficient, K_p, for different wave conditions are presented in Figure 8.5. The variation of RAO with f in Figure 8.5a is obtained for $K_p = 6.5 \times 10^5$ Pa s^2 (i.e., $M = 1$) in the compression phase and for $K_p = 3.3 \times 10^5$ Pa s^2 (i.e., $M = 0$) in the expansion phase of the hydraulic cylinder, and for three different $H = 0.2$, 0.25 and 0.3 m. It can be seen that the RAO decreases when increasing H, which may be due to the viscous dissipation caused by vortex shedding and wave non-linearity that increases with H (see Figure 8.3). This effect can be related to the Keulegan-Carpenter number of the upper part of the flap, which increases with H causing the viscous drag damping (Caska and Finnigan, 2008). This phenomenon was also reported by Folley et al. (2007) and can be explained by the relation between wave surge force and f, as shorter waves experience larger horizontal water particle acceleration and thus induce a larger force on the flap.

In Figure 8.5b the variation of RAO with K_p are obtained for $T = 3$ s and $H = 0.2$ and 0.25 m, corresponding respectively to $kH = 0.157$ and 0.196, and $kd = 0.648$ (see Table 5.2). The value of K_p does not appreciably change the RAO for $K_p < 12 \times 10^5$ Pa s^2, however when the K_p increases further a large variation of RAO is observed, due to the increases of latching effect of the hydraulic PTO system where the flap remains stationary for as long as the hydrodynamic forces on its wetted surface are unable to overcome the resisting force introduced by the PTO system.

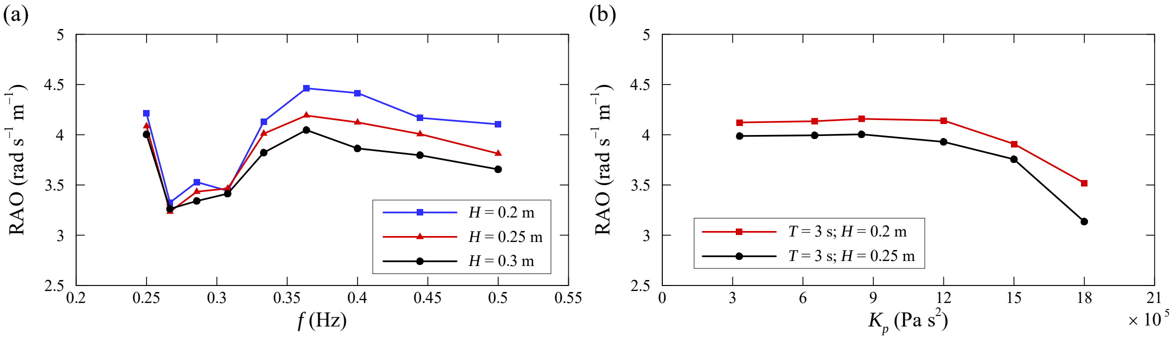

Figure 8.5: Variation of RAO with: (a) wave frequency; (b) coefficient of pressure loss.

Figure 8.6 shows the variation of CWR and ratio of the incident and reflected wave power, ε, with f and with K_p in the same conditions presented in Figure 8.5.

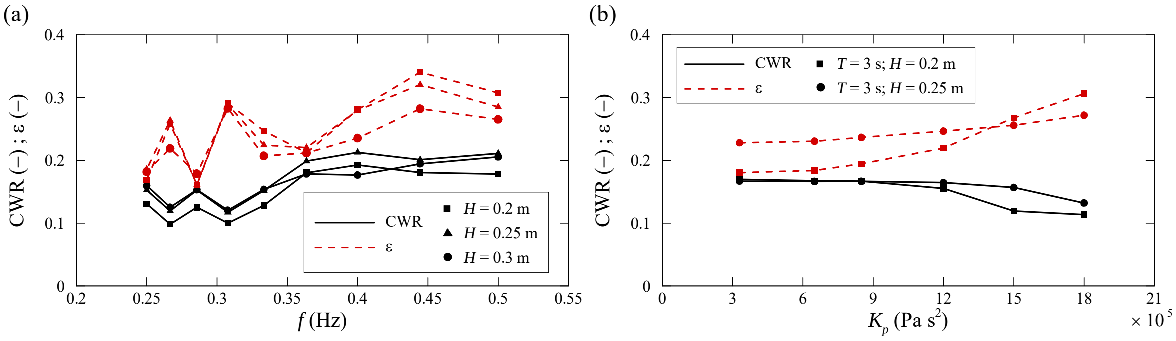

Figure 8.6: Variation of CWR and ratio of the mean reflected wave power with: (a) wave frequency; (b) coefficient of pressure loss.

It can be seen that ε decreases when increasing H, showing almost the same trend of RAO except for the low values of f (see Figures 8.5a and 8.6a). However the CWR does not seem to vary excessively with H and showing a much narrow values. The comparison of

ε and CWR shows that ε is much larger than the CWR, of about 30% (Figure 8.6a). An explanation for this behavior is the increase of reflection due to the PTO brake effects on the flap. This behavior can be confirmed in Figure 8.6b where ε increases as K_p increases. The measurement of ε seems not accuracy to estimate the performance of the OWSC with hydraulic PTO system.

In order to better understand the influence of the H and f in the results, the variation of CWR and RAO with respect to both H and f are plotted in Figure 8.7.

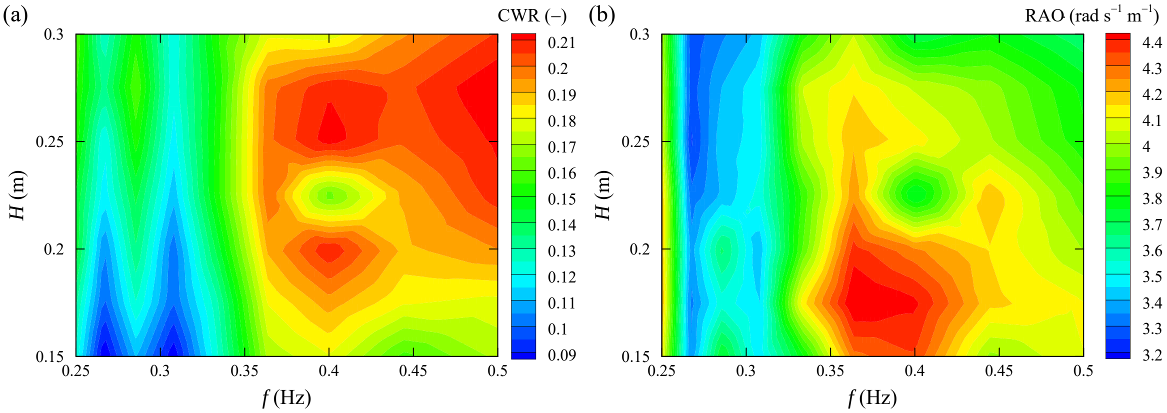

Figure 8.7: Contour plot of CWR and RAO as a function of wave height and frequency: (a) CWR; (b) RAO.

In general, it can be confirmed that the influence of the H is of lesser significance on the CWR than f. However, both f and H have a large effect on RAO, with higher values being obtained for $0.35 \lesssim f \lesssim 0.45$ Hz and for $0.15 \lesssim H \lesssim 0.2$ m. It can be concluded that there is weak correlation between CWR and RAO, i.e., the maximum CWR does not occur for the maximum value of RAO.

8.3 Experimental results of OWSC under irregular waves

In order to illustrate the experimental results of OWSC under irregular waves, an example of the time series of η, $\dot{\theta}$, P_c and W_{out} for test I1 ($T_p = 3.6$ s, $H_s = 0.25$ m and $H_m = 0.15$ m, see Table 5.3) is shown in Figure 8.8. It is clear that the η and $\dot{\theta}$ show a strong non-linear behavior, caused by the wave interactions with OWSC and flume bed. Such interactions cause differences between incident plus reflected waves measured by WP1 and therefore a non-linear dependence between η and $\dot{\theta}$ (Figures 8.8a and b). The calculated P_{int} shows a good agreement with measured data, with typical value of $R^2 \approx 0.92$ (Figure 8.8c). As for regular waves the model captures most of dynamic behaviors of P_{int}, including the cavitation in the hydraulic PTO system. For this test condition $\overline{W}_{out} = 20$ W and CWR = 17% are obtained.

In order to analyze the dynamic behavior of the OWSC under irregular waves the RAO is also used. However, as RAO describes the linear relationship between the resultant response and the incident wave amplitude (Santo et al., 2017), in this study, RAO was obtained by evaluating the magnitude of the linear component of $\dot{\theta}$ and η, as:

$$\mathrm{RAO}(f) = \sqrt{\frac{S_{\dot{\theta}}(f)}{S_{\eta}(f)}} \tag{8.2}$$

where $S_{\dot{\theta}}$ and S_{η} are the power spectrum of the first-harmonic of $\dot{\theta}$ and η, respectively. The incident η is obtained by the separation of incident and reflected waves, using the three-point method proposed by Mansard and Funke (1980).

Figure 8.9 shows the harmonic decompositions of measured η, $\dot{\theta}$ and P_{int} in the same conditions presented in Figure 8.8. Qualitatively, the structure of the signals are dominated by the linear component. However, as for regular waves, the signals contain important double and triple frequency components, especially for higher values of f. In fact, this higher-order components is more significant on the η for smaller f than $\dot{\theta}$ and P_{int}. An explanation for this behavior is the reflected waves and the 3D effects of the flume, that are more noticeable for a large measure time (3000 s).

As the higher-order frequency seems important, the non-linear output frequency response functions, G_n, where $n = 2$, 3 and 4 is the order of harmonic decomposition, are considered as the extension of the RAO to the non-linear case (Lang and Billings, 2005). Figure 8.10 shows the comparison of RAO and G_n for each test condition presented in Table 5.3.

The RAO for all test condition are very similar in shape, except for low values of f where the variation of RAO seems a function of incident waves. Unlike from the linear theory, the RAO curve does not show a well-defined peak, showing a limited variation in a broad f band. In fact, the RAO shows two small relative peaks at about $f = 0.42$ and 0.84 Hz, contaminating the curve to the left and right side of the peaks. The G_n curves also show a limited variation, presenting values of the same order of magnitude than RAO. Each average G_n shows similar

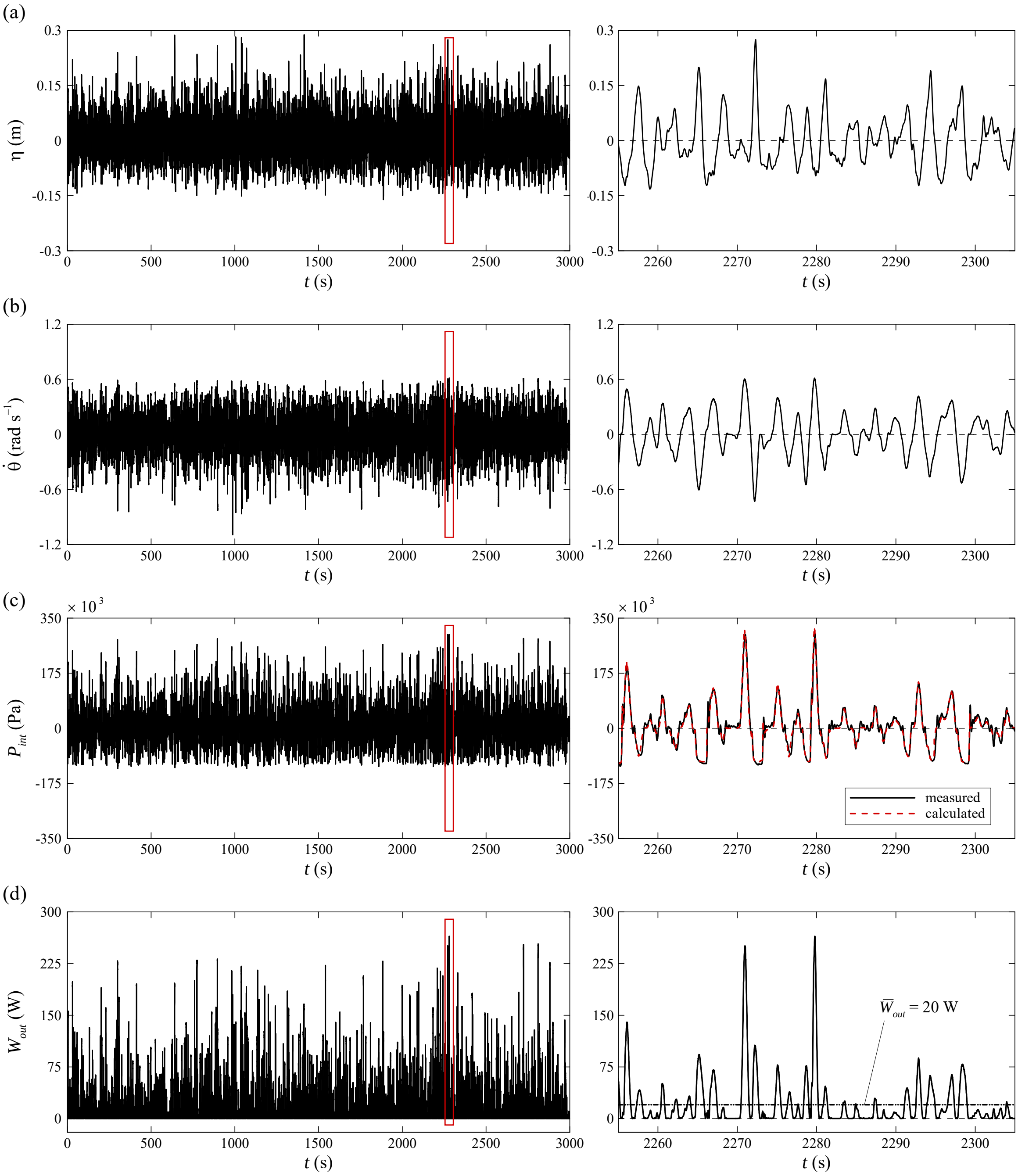

Figure 8.8: Time series of: (a) free-surface elevation measured by WP1; (b) angular velocity of the flap; (c) pressure in the cylinder chamber; (d) power capture. These time series are obtained for test I1 ($T_p = 3.6$ s, $H_s = 0.25$ m and $H_m = 0.15$ m). The right column shows in detail the interval shown in the red box in the left column. In (c) the measured pressure in the cylinder chamber is fitted by Equation (7.22) on the right hand side.

shapes for all test condition, however with more scatter than the RAO, presumably due to the effect of non-homogeneous interactions between G_n and possibly viscous damping for

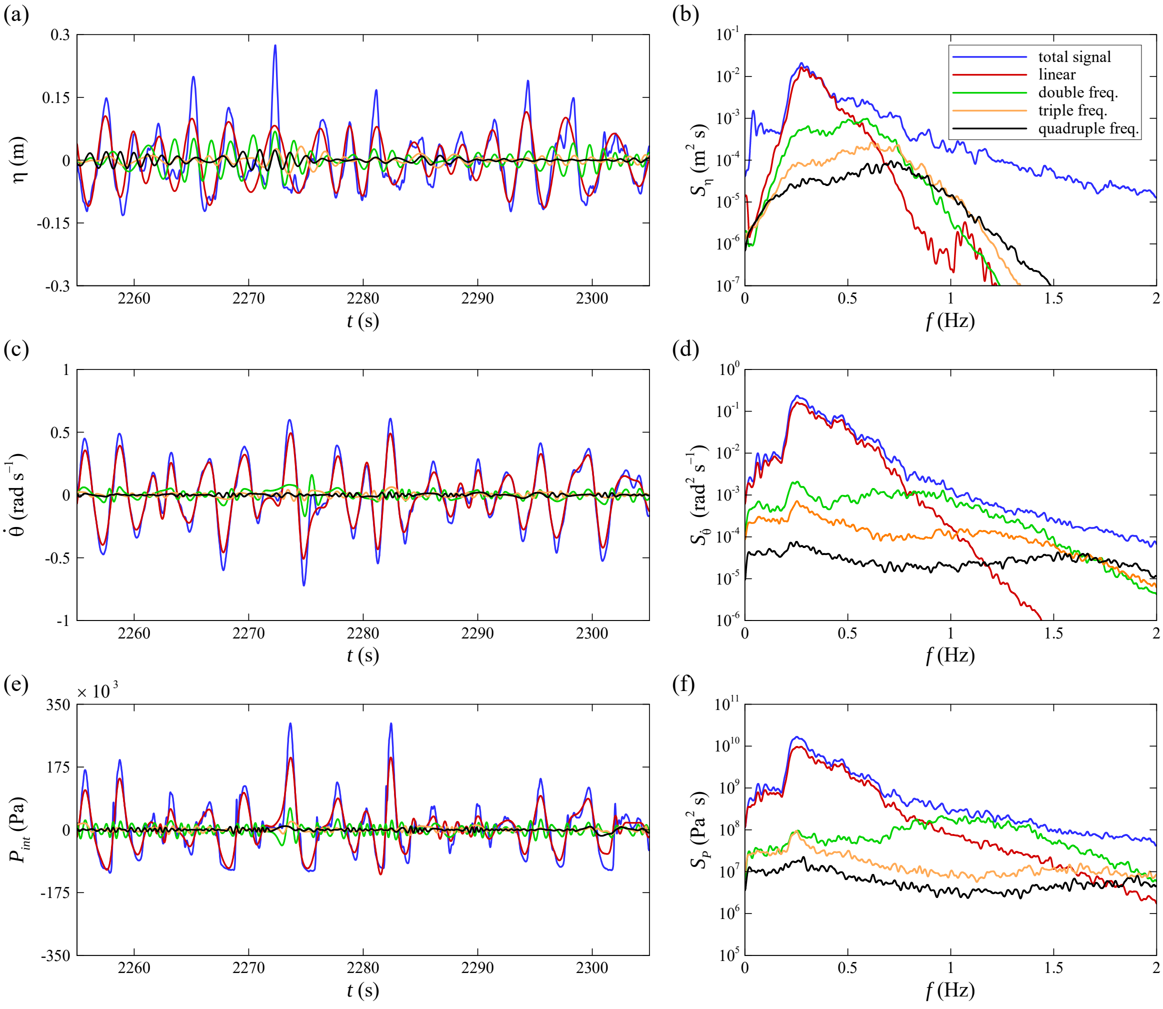

Figure 8.9: Harmonic decomposition of: (a) free-surface elevation measured by WP1; (c) angular velocity of the flap; (e) pressure in the cylinder chamber. Power spectra of: (b) free-surface elevation measured by WP1; (d) angular velocity of the flap; (f) pressure in the cylinder chamber. These data are obtained for test I1 ($T_p = 3.6$ s, $H_s = 0.25$ m and $H_m = 0.15$ m).

very large relative motion, which generally reduces the overall flap motion.

In order to investigate the effects of PTO system, the average RAO and G_n presented in Figure 8.10 are compared with data obtained for $K_p = 12 \times 10^5$ Pa s^2 and without PTO system in Figure 8.11. As for regular waves, the RAO shows a small dependence with variation of K_p from 6.5×10^5 to 12×10^5 Pa s^2. G_2 shows some differences only for $f < 1$ Hz. G_3 shows however a significant difference, with a shape slightly more asymmetric, hence more dependent on the K_p. G_4 seems almost independent on the K_p, with similar values for both K_p tested. Therefore, the effect of K_p produces double and triple frequency components. As expected, the PTO system introduces a large variation on the RAO, as the use of hydraulic PTO system

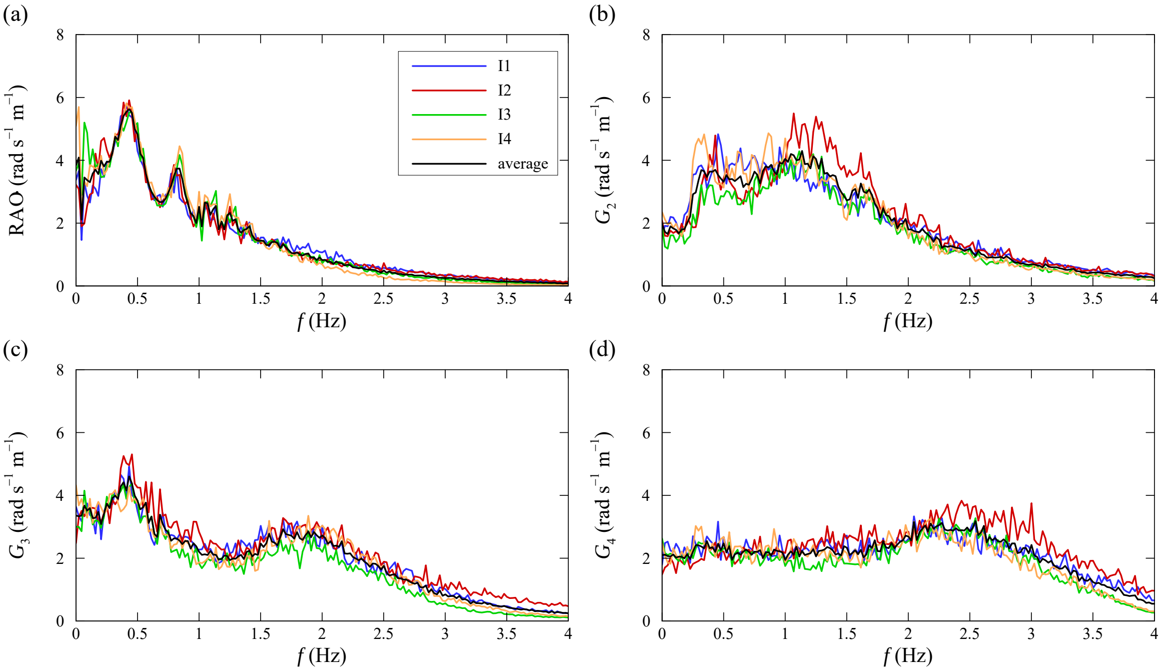

Figure 8.10: Comparison of RAO and non-linear output frequency response functions for each test condition presented in Table 5.3: (a) RAO; (b) second-order; (c) third-order; (d) fourth-order.

provides a natural latching: the flap remains stationary for as long as the hydrodynamic forces on its wetted surface are unable to overcome the resisting force introduced by the PTO system. G_2 also shows a significant difference, hence more dependent on the effect of PTO system. G_3 and G_4 are weakly dependent on the PTO damping.

8.4 Analysis of OWSC under irregular waves

In this section the effects of H_s and peak frequency, f_p, on the CWR are investigated. For a narrow-banded process, it should be possible to approximate the double, triple and quadruple frequency contributions in terms of the linear component as (Santo et al., 2017; Walker et al., 2004):

$$\eta = A_{11}\eta_{11} + A_{22}\eta_{22} + A_{31}\eta_{31} + A_{33}\eta_{33} + A_{42}\eta_{42} + A_{44}\eta_{44} \tag{8.3}$$

and

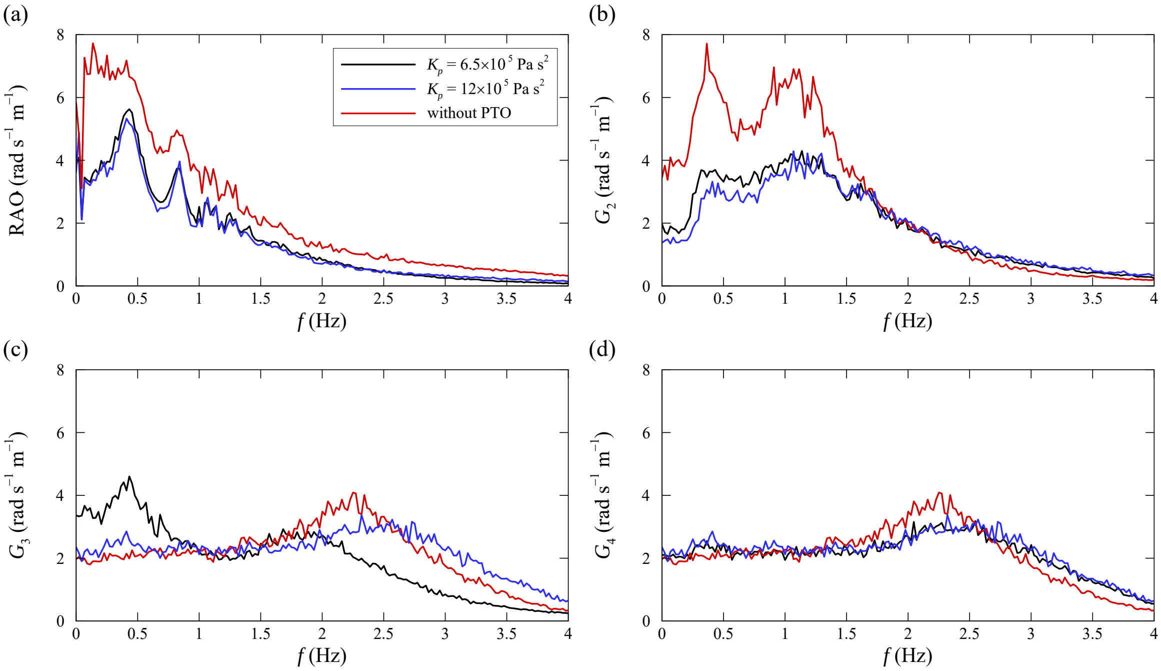

Figure 8.11: Comparison of RAO and non-linear output frequency response functions for $K_p = 6.5\times10^5$, 12×10^5 Pa s^2 and without PTO system: (a) RAO; (b) second-order; (c) third-order; (d) fourth-order.

$$\dot{\theta} = B_{11}\dot{\theta}_{11} + B_{22}\dot{\theta}_{22} + B_{31}\dot{\theta}_{31} + B_{33}\dot{\theta}_{33} + B_{42}\dot{\theta}_{42} + B_{44}\dot{\theta}_{44} \tag{8.4}$$

where A_{ij} and B_{ij} (i, $j = 1$, 2, 3 and 4) are the modified Stokes coefficients, η_{ij} and $\dot{\theta}_{ij}$ are the variables that contain both the amplitude and phase information and are defined in terms of the linear signal record, η_L and $\dot{\theta}_L$, and its Hilbert transform, η_{LH} and $\dot{\theta}_{LH}$, respectively. Being, $\eta_{11} = \eta_L$; $\eta_{22} = \eta_L^2 - \eta_{LH}^2$; $\eta_{31} = \eta_L(\eta_L^2 + \eta_{LH}^2)$; $\eta_{33} = \eta_L(\eta_L^2 - 3\eta_{LH}^2)$; $\eta_{42} = (\eta_L^2 + \eta_{LH}^2)(\eta_L^2 - \eta_{LH}^2)$; $\eta_{44} = (\eta_L^2 - \eta_{LH}^2) - (2\eta_L\eta_{LH})^2$; (Walker et al., 2004) and $\dot{\theta}_{11} = \dot{\theta}_L$; $\dot{\theta}_{22} = \dot{\theta}_L^2 - \dot{\theta}_{LH}^2$; $\dot{\theta}_{31} = \dot{\theta}_L(\dot{\theta}_L^2 + \dot{\theta}_{LH}^2)$; $\dot{\theta}_{33} = \dot{\theta}_L(\dot{\theta}_L^2 - 3\dot{\theta}_{LH}^2)$; $\dot{\theta}_{42} = (\dot{\theta}_L^2 + \dot{\theta}_{LH}^2)(\dot{\theta}_L^2 - \dot{\theta}_{LH}^2)$; $\dot{\theta}_{44} = (\dot{\theta}_L^2 - \dot{\theta}_{LH}^2) - (2\dot{\theta}_L\dot{\theta}_{LH})^2$. In order to investigate the validity of this approximation, the double, triple and quadruple frequency components of η and $\dot{\theta}$ for test I1 are compared in Figure 8.12.

It can be observed that the approximation of double, triple and quadruple frequency contributions in terms of the linear component cannot be used to provide a complete description of the output frequency response of wave-OWSC interaction with hydraulic PTO system (Figure 8.12). A large discrepancy is observed between measured and calculated solution of Equations (8.3) and (8.4), showing that the OWSC higher-order frequency components of η

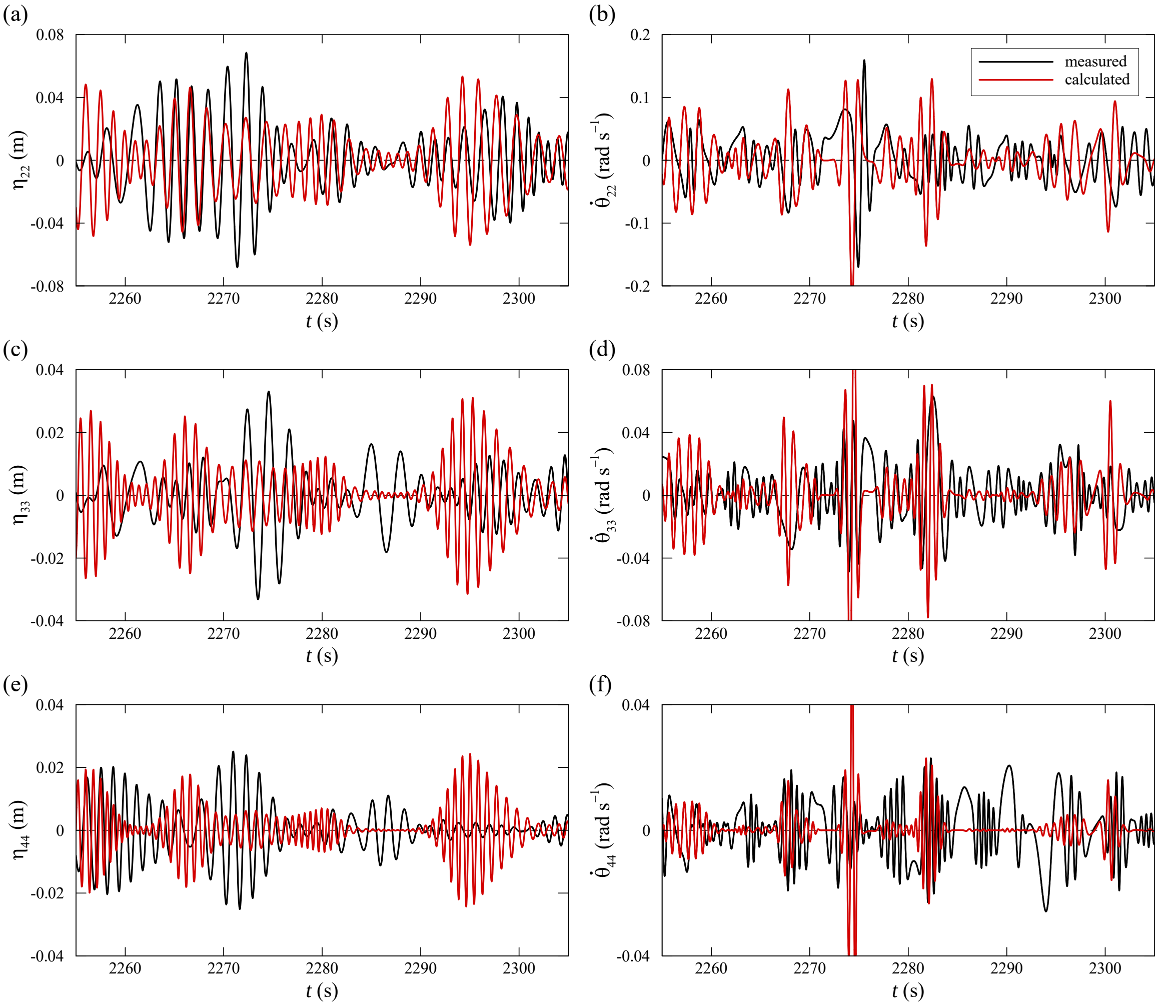

Figure 8.12: Comparison of the higher frequency components of the free-surface elevation and angular velocity of the flap for test I1 ($T_p = 3.6$ s, $H_s = 0.25$ m and $H_m = 0.15$ m): (a,b) double; (c,d) triple; (e,f) quadruple frequency component.

and $\dot{\theta}$ are the effect of a combination of the output frequency responses of the involved homogeneous non-linear systems (Lang and Billings, 2005). Therefore, the higher-order generalized frequency response function are considered as the extension of the RAO to the non-linear case. However, the relationship between the η and $\dot{\theta}$ of non-linear systems is much more complicated than in the linear system case.

A new concept can be regarded as another extension of the linear frequency response function concept to the non-linear case, which is a complement to the RAO, where $\dot{\theta}$ can be given by:

$$\dot{\theta}(f) = \text{RAO}(f)\eta_L(f) + \sum_{n=2}^{4} G_n(f)\eta_n(f) \tag{8.5}$$

To predict the CWR of OWSC under irregular waves this concept is used. The simulation of incident waves was performed using MatLab. Firstly, for each significant wave height, H_s, and wave peak frequency, f_p, the S_η is determined by:

$$S_\eta(f) = \mathcal{C} H_s^2 \frac{f_p^4}{f^5} \exp\left[-\frac{5}{4}\frac{f_p^4}{f^4}\right] \gamma^{\mathcal{B}(f)} \tag{8.6}$$

with

$$\mathcal{C} = \frac{0.0624}{0.23 + 0.0336\gamma - 0.185(1.9+\gamma)^{-1}} \tag{8.7}$$

and

$$\mathcal{B}(f) = \exp\left[-\frac{(f-f_p)^2}{2\sigma_i^2 f_p^2}\right] \tag{8.8}$$

where $\sigma_i = 0.07$ for $f \leq f_p$ and $\sigma_i = 0.09$ for $f > f_p$. Then the following decomposition is applied to simulate the η time series from a S_η:

$$\eta(t) = \sum_{n=1}^{N} A_n \cos(\omega_n t + \mathcal{K}_n) \tag{8.9}$$

where $\mathcal{K} \in [0; 2\pi]$ is the random wave phase and A_n is the wave amplitude of frequency n, given by:

$$A_n = \sqrt{2 S_\eta(f_n)\Delta f} \tag{8.10}$$

Posteriorly, the harmonic decompositions of measured η are performed and $\dot{\theta}$ is calculated according to the Equation (8.5). Finally, P_{int} is calculated according to the Equation (7.22), CWR by Equation (5.5) and $\overline{W}_{out}$ by Equation (5.1).

In order to illustrate the computed results, two examples of the time series of η, $\dot{\theta}$ and W_{out} for $\gamma = 1.2$ and 3.3 are shown in Figure 8.13. These results are obtained for $H_s = 0.3$ m and $f_p = 0.42$ Hz. As RAO and G_n show a limited variation, $\overline{W}_{out}$ is lightly larger for $\gamma = 3.3$ than for $\gamma = 1.2$. Being $\overline{W}_{out} = 37$ W and CWR = 26% for $\gamma = 3.3$ and $\overline{W}_{out} = 31$ W and CWR = 23% for $\gamma = 1.2$.

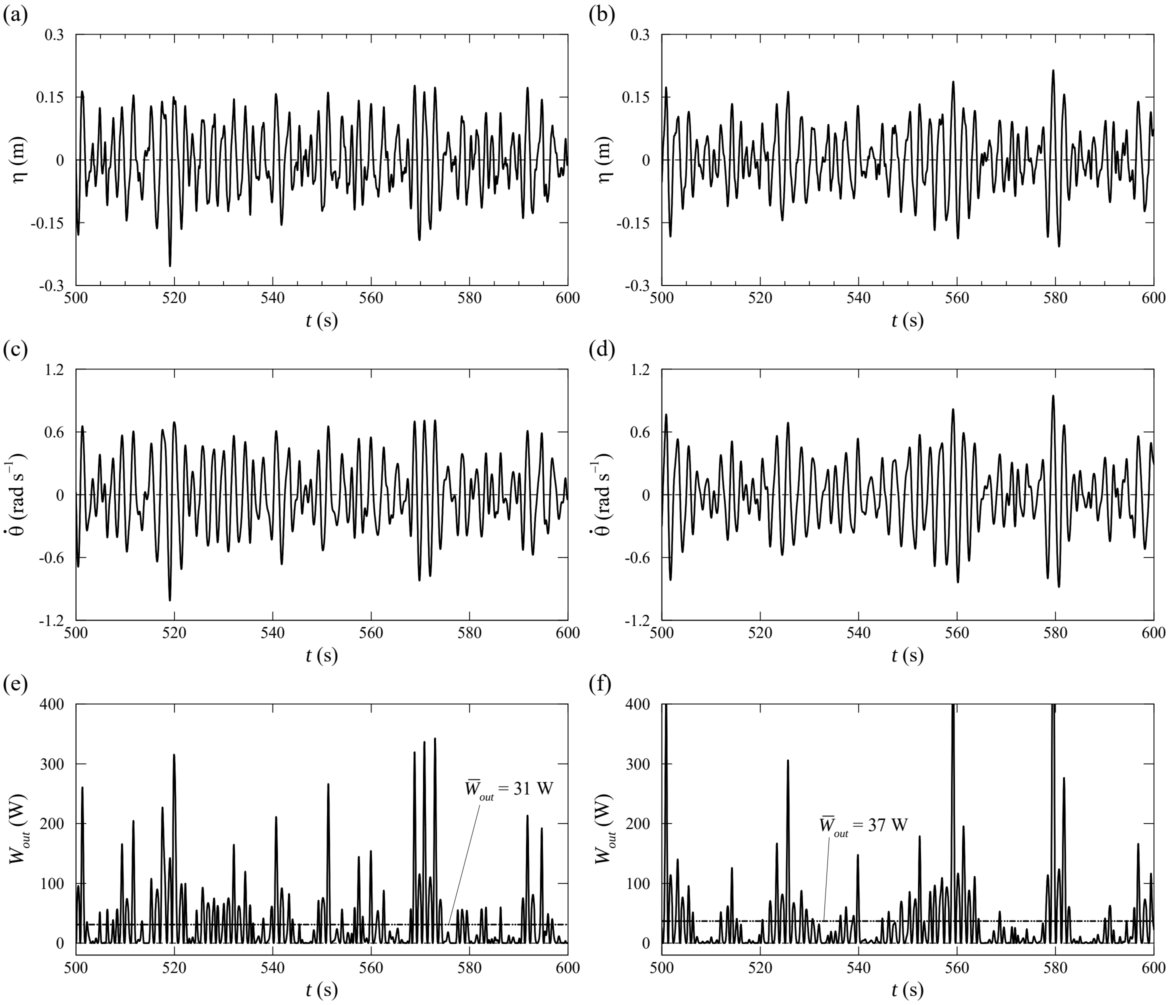

Figure 8.13: Time series of: (a,b) free-surface elevation; (c,d) angular velocity of the flap; (e,f) power capture. The left column shows time series for $\gamma = 1.2$ and the right column for $\gamma = 3.3$.

The contour plot of CWR as a function of both H_s and f_p is shown in Figure 8.14. The white line represents the maximum wave steepness, defined as $s_p = H_s/\lambda_p$, where λ_p is the peak wavelength.

The contours of CWR for both $\gamma = 1.2$ and 3.3 are very similar and, as expected, the CWR increases with H_s. The maximum CWR occurs firstly for $f_p \approx 0.42$ Hz, the same result was

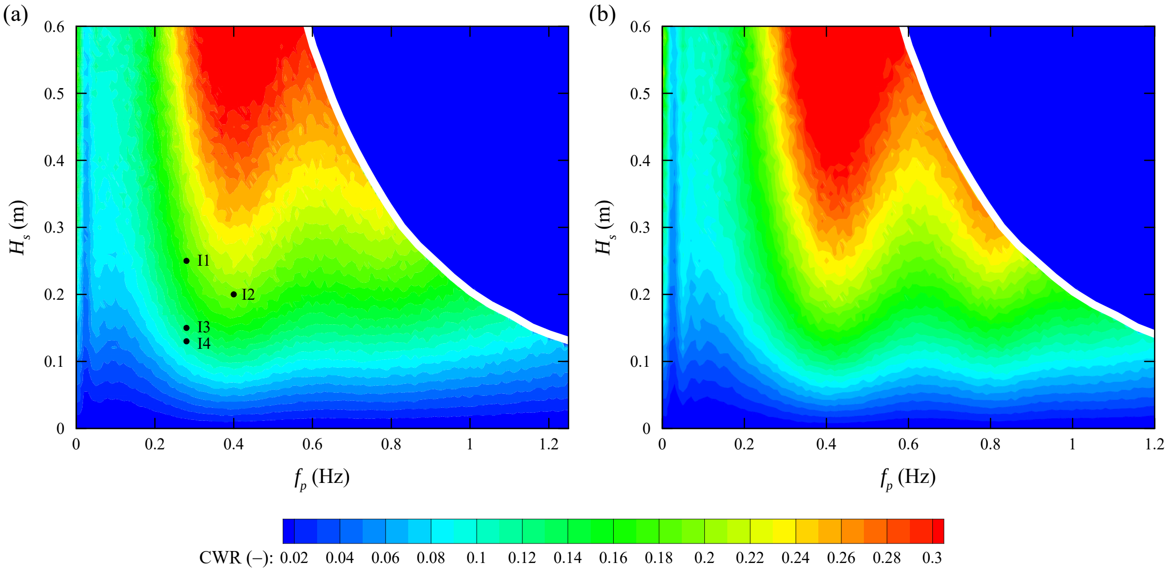

Figure 8.14: Contour plot of CWR as a function of significant wave height and peak frequency for: (a) $\gamma = 1.2$; (b) $\gamma = 3.3$.

also obtained for regular waves (see Figure 8.7a). For both γ, the CWR is greater than 28% across a broad range of f, showing the importance of the non-linearities on the efficiency of the OWSCs.

8.5 Summary and conclusions

The CWR and RAO of the OWSC with hydraulic PTO system are experimentally investigated. The experimental tests were performed for both unidirectional regular and irregular waves. The effects of PTO system and wave condition on the OWSC dynamics were presented.

The preliminary results for regular waves indicate that the PTO system, wave frequency and height have a significant influence on the CWR and RAO. It was observed that the RAO decreases when increasing wave height, which may be due to the viscous dissipation caused by vortex shedding and wave non-linearity that increases with the increasing of wave height. However, the CWR does not seem to vary excessively with wave height and showing a much limited variation. Both CWR and RAO have a strong dependence of wave frequency. In general, a weak correlation between CWR and RAO was observed, i.e., the maximum CWR of about 21% does not occur for the maximum value of RAO.

The RAO does not present a well-defined peak as from the linear theory, showing a limited variation in a broad wave frequency band. It was observed that the RAO is strongly affected by the hydraulic PTO system. The time series of free-surface elevation, angular velocity of the flap and pressure in the PTO system are dominated by the linear component, however, they also present some important higher-order frequency components. Therefore, to predict the variation of CWR with significant wave height and peak frequency, the non-linear output frequency response functions were considered as the extension of the RAO to the non-linear case. These functions also show a limited variation in a broad wave frequency band, presenting values of the same order of magnitude of RAO. It was observed that the CWR is strongly affected by the significant wave height and peak frequency. CWR greater than 28% was found for higher significant have height close to the maximum wave steepness and therefore (for best results) the OWSC should be adjusted to match the sea state.

This chapter shows that the hydraulic PTO system introduces non-linear behaviors that affects the relation between RAO and CWR, namely that the maximum CWR may not be registered at the RAO peak. This result, not observed before, has an important impact on the design of the OWSC and call for further studies of particular flap and hydraulic PTO system pairs.

9

Numerical modeling of OWSC with mechanical constraints

The results presented in this chapter has been submitted as Brito, M., Canelas, R. B., García-Feal, O., Domínguez, J. M., Crespo, A. J. C., Ferreira, R. M. L., Neves, M. G. and Teixeira, L. 'A numerical tool for modeling oscillating wave surge converter with non-linear mechanical constraints'. *Renewable Energy.*

Contents

9.1 Introduction

This chapter presents the validation and application of the developed numerical tool (see Chapter 4), designed to support the simulation of complex fluid-structure interactions and hydrodynamic behaviors of the OWSC with mechanical constraints.

The validation of the numerical tool is mainly performed in three stages (Section 9.2). In the first stage, the dynamic behavior of the OWSC with mechanical constraints is validated by comparing measured and computed OWSC's angular velocities (Section 9.2.1). In the second stage, removing the OWSC model from the wave flume, the wave generation and propagation are validated by comparing the free-surface elevation for both regular and irregular waves (Section 9.2.2). In the third stage, the hydrodynamic of the OWSC with mechanical constraints is validated by comparing numerical and computed flap motion and flow field in the vicinity of the flap (Section 9.2.3).

The numerical analysis of the OWSC for several PTO damping and flap configurations are presented in Section 9.3.

The main conclusions are summarized in Section 9.4.

9.2 Validation of the numerical tool

9.2.1 Dynamics of the OWSC with mechanical constraints

The side view of the OWSC model implemented in Project Chrono with the mechanical joints among components is shown in Figure 9.1.

The constraint of the F_{PTO} on the slider joint between piston rod and cylinder is defined according to the Section 7.2. The friction torque on the revolute joint between flap and bearings, B_0 (see Figure 9.1), is modeled using the Coulomb friction, with static friction coefficient of 0.16 (Brito et al., 2017). The joints revolute joints between flap and piston rod and between cylinder and ground are modeled without friction.

The time series of the angular velocity of the flap, $\dot{\theta}$, during the physical model test (imposed in Project Chrono) and the comparison of the numerical and experimental results of F_{PTO} are shown in Figure 9.2.

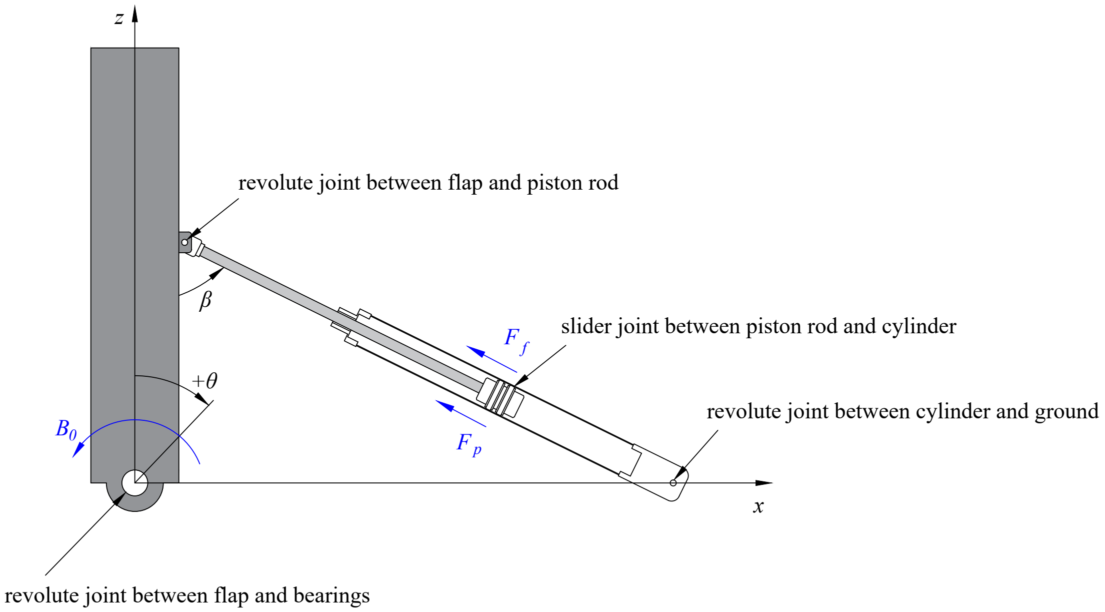
z
revolute joint between flap and piston rod
β
F_f
slider joint between piston rod and cylinder
+θ
B_0
revolute joint between cylinder and ground
F_p
x
revolute joint between flap and bearings

Figure 9.1: Sketch of the OWSC model implemented in Project Chrono, including the mechanical joints among components.

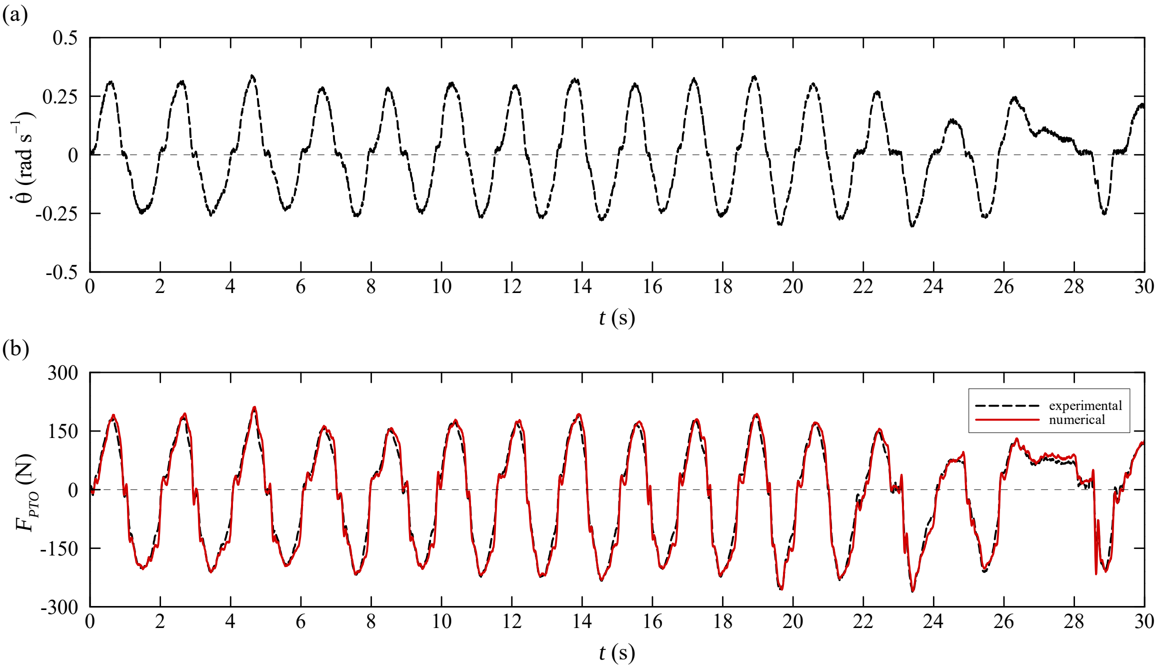

Figure 9.2: Time series: (a) imposed angular velocity of the flap; (b) comparison of numerical and experimental PTO force.

The agreement between numerical and experimental results is quantified considering two statistical parameters: normalized amplitude error, A_χ, and normalized phase error, φ_χ, given respectively by:

$$A_\chi = \sqrt{\frac{\sum_{i=1}^{N} (\chi_i^{num})^2}{\sum_{i=1}^{N} (\chi_i^{exp})^2}} \tag{9.1}$$

and

$$\varphi_\chi = \sqrt{\frac{\sum_{i=1}^{N} (\chi_i^{num} - \chi_i^{exp})^2}{\sum_{i=1}^{N} (\chi_i^{exp})^2}} \tag{9.2}$$

where χ_i is the magnitude of the signal to be analyzed, N is the number of samples, superscripts *num* and *exp* refer to numerical and experimental values, respectively.

A perfect agreement between signals would result in $A_\chi \to 1$ and $\varphi_\chi \to 0$. The agreement of the time series shown in Figure 9.2b is characterized by $A_\chi = 1.05$ and $\varphi_\chi = 0.15$. Note that values of $A_\chi > 1$ means that the numerical results have overestimated the experimental data in amplitude, however here it is close to 1, which means a good agreement. Some discrepancies are observed, may be caused by the asymmetrical characteristic of the experimental hydraulic circuit. In fact, the inclusion of all the dynamic effects in a single model is not an easy task, and it is especially difficult to define a mechanism governing the switch between the check-valves (Brito et al., 2017). On the other hand, lower φ_χ was obtained and therefore the Project Chrono is assumed as capable to predict the dynamic of OWSC, allowing for the full mechanical modeling of flap-mechanical constraints interactions.

9.2.2 Wave generation and propagation

In order to validate the wave generation and propagation and to study the convergence analysis, experimental and numerical tests were performed removing the OWSC model from the wave flume. The validation is firstly carried out for four regular wave conditions presented in Table 5.2, which are summarized in Table 9.1 (λ is the wavelength defined according to the linear theory).

To validate the numerical tool for more realistic application, numerical tests were also carried out for irregular wave conditions I1 and I2 (see Table 5.3).

Table 9.1: Wave conditions considered for the validation of wave generation and propagation in regular waves.

Test	d (m)	T (s)	H (m)	λ (m)
R1	0.825	2.0	0.15	4.90
R2	0.825	2.0	0.25	4.90
R3	0.825	3.0	0.20	8.01
R4	0.825	3.5	0.25	9.51

The convergence analysis has been carried out for test R1 in 2D, where different resolutions (i.e. different initial inter-particle distance, d_p) are used to obtain the free-surface elevations, η. The total number of particles, computational runtime, number of particles per wave height, H, A_χ and φ_χ for each d_p are given in Table 9.2.

Table 9.2: Comparison of the statistical parameters for different resolutions.

d_p (m)	particles	particles/H	runtime (min)	A_χ	φ_χ
0.005	2,217,430	30	14,850	0.99	0.15
0.008	866,737	19	3,920	0.99	0.17
0.01	554,977	15	2,100	0.98	0.18
0.02	138,806	8	340	0.96	0.21
0.04	34,824	4	70	0.86	0.36
0.05	22,290	3	50	0.80	0.42

It can be observed that for $d_p \leq 0.01$ m, $A_\chi \approx 1$ was obtained, which means a good agreement between numerical results and experimental data. In the same way, lower φ_χ is achieved when decreasing d_p (increasing resolution). However, $d_p = 0.01$ m (approximately 15 particles per H) was shown to be accurate enough to simulate η with relative low computational runtime about 2,100 min of 300 s of physical time. Simulations have been executed on a Nvidia GTX 1060. Altomare et al. (2015); Crespo et al. (2017) have shown that more than 10 particles per H allows to model wave propagation with a good accuracy (with $A_\chi \approx 1$ and $\varphi_\chi < 0.25$).

The validation of the wave generation and propagation was also carried out in 2D. The comparison of the experimental and numerical time series of η obtained at $x = 0$ (i.e., 32.7 m from the wavemaker) is shown in Figure 9.3.

In general, a good agreement between numerical and experimental time series of η are obtained for all wave conditions, with $A_\chi \approx 1$ and $\varphi_\chi < 0.25$ (see Table 9.3). The mean reflection coefficient, ϵ, of each numerical test are very similar to the experimental data (see Table 9.3).

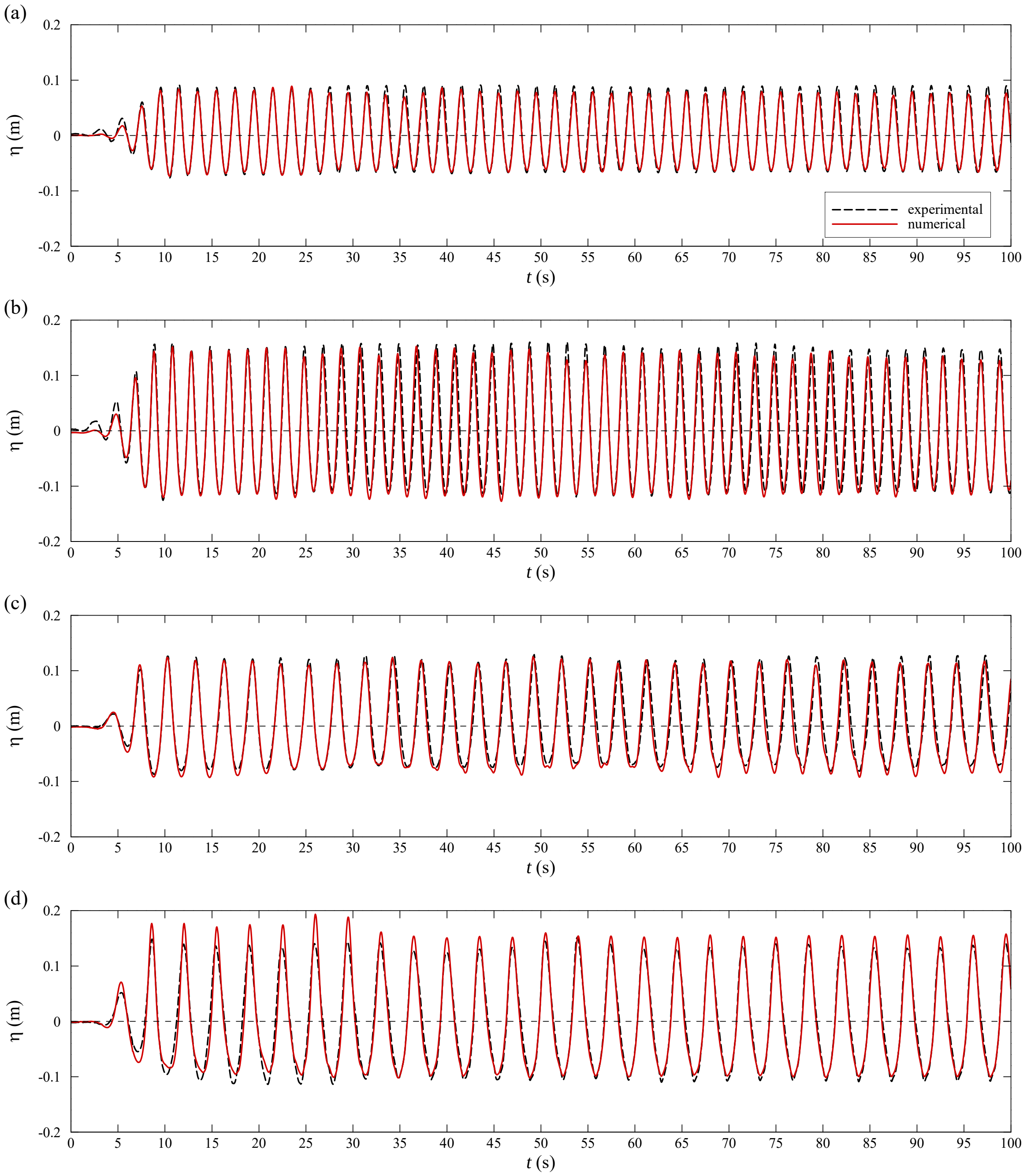

Figure 9.3: Comparison of numerical and experimental time series of free-surface elevation for test: (a) R1; (b) R2; (c) R3; (d) R4.

The separation of incident and reflected waves was obtained using the method proposed by Mansard and Funke (1980). The low relative error between experimental and numerical results of ϵ confirms that the waves are being properly generated and propagated.

Table 9.3: Statistical parameters of wave generation and propagation, and comparison of the mean reflection coefficient in 2D.

Test	A_χ	φ_χ	experimental ϵ	numerical ϵ	relative error of ϵ
R1	0.98	0.18	8.6%	8.1%	5.8%
R2	0.97	0.19	11.8%	12.6%	6.8%
R3	1.02	0.22	13.3%	14%	4.4%
R4	1.04	0.21	12.6%	13.2%	4.8%

Figure 9.4 shows the power spectrum of free-surface elevation, S_η, obtained at $x=0$ (i.e., 32.7 m from the wavemaker) for both irregular tests. To get accurate results, 1000 frequencies have been calculated with wave frequency $f \in [0,3]$ Hz. It can be observed that the irregular waves are also accurately predicted by the numerical tool at $x=0$. Comparing the peak values, a higher relative error of about 4% was found between both tests. For higher frequency, the S_η shows greater difference with a maximum relative error of about 20%. This difference may be attributed to the viscous dissipation effects of SPH method that occurs for higher frequencies.

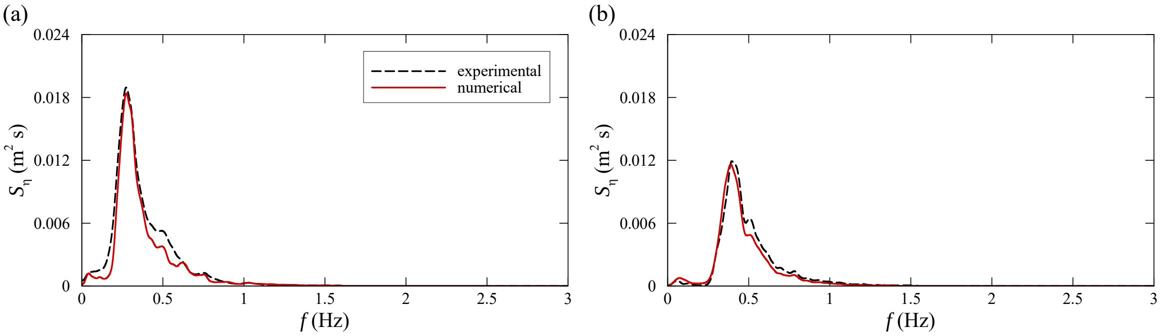

Figure 9.4: Comparison of numerical and experimental power spectrum of free-surface elevation for test: (a) I1; (b) I2.

The full 3D wave flume with approximately 10 particles per H requires approximately 84 millions of particles, making time consumed impracticable, the length of the computational domain was reduced. In this context, 3D modeling was performed for reduced computational domain with approximately 3λ long (about 7 millions of particles). As the reduction of the domain length may cause different reflections at boundaries, leading to unphysical behavior of waves. In order to evaluate the effect of domain length, several tests were also performed in 2D for tests R1 and I1, see Tables 9.1 and 5.3, respectively.

The total number of particles, computational runtime, A_χ and φ_χ for different domain length are given in Table 9.4. The value of A_χ and φ_χ were obtained comparing each domain length with full wave flume.

Table 9.4: Comparison of the parameters for different domain length for test R1 in 2D.

Domain length	particles	runtime (min)	A_χ	φ_χ
full wave flume	554,977	2,100	–	–
6λ	365,882	1,300	1.01	0.04
3λ	174,941	600	1.05	0.06
λ	47,647	160	1.31	0.42

Figure 9.5 shows the S_η for different domain length for test I1 in 2D. It is observed that the computational domains with length larger than 3λ show a good agreement between numerical and experimental power spectrum of incident and reflected waves. A relative error of ϵ less than 10% was found. Similar results were also obtained by Crespo et al. (2017); Zhang et al. (2018). For a longer time simulation and smaller computational domain, special treatment like active wave absorption system in the generation of waves should be considered to avoid unphysical behavior of waves.

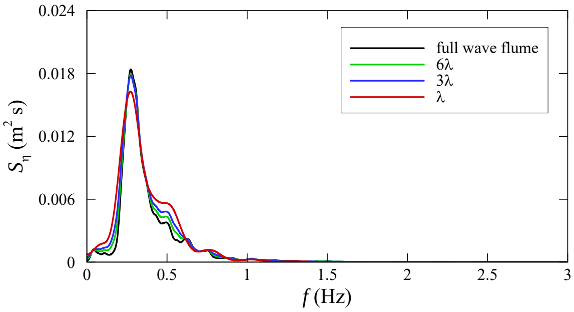

Figure 9.5: Comparison of the power spectrum of free-surface elevation for different domain length for test I1 in 2D.

9.2.3 Dynamics of the OWSC

The dynamics of the OWSC model are validated in full 3D with wave flume length of 3λ, for the wave conditions presented in Tables 9.1 and 5.3. The 3D modeling was performed using approximately 10 particles per H. The choice of this d_p is based on the results from Altomare et al. (2017) where a good compromise between accuracy and computational time is obtained using approximately 10 particles per H. The computational runtime of the 3D modeling was of about 10 days of 100 s of physical time in the same GPU.

Figure 9.6 shows the comparison of the numerical and experimental time series of $\dot{\theta}$, after the quasi-steady condition for $50 \leq t \leq 100$ s.

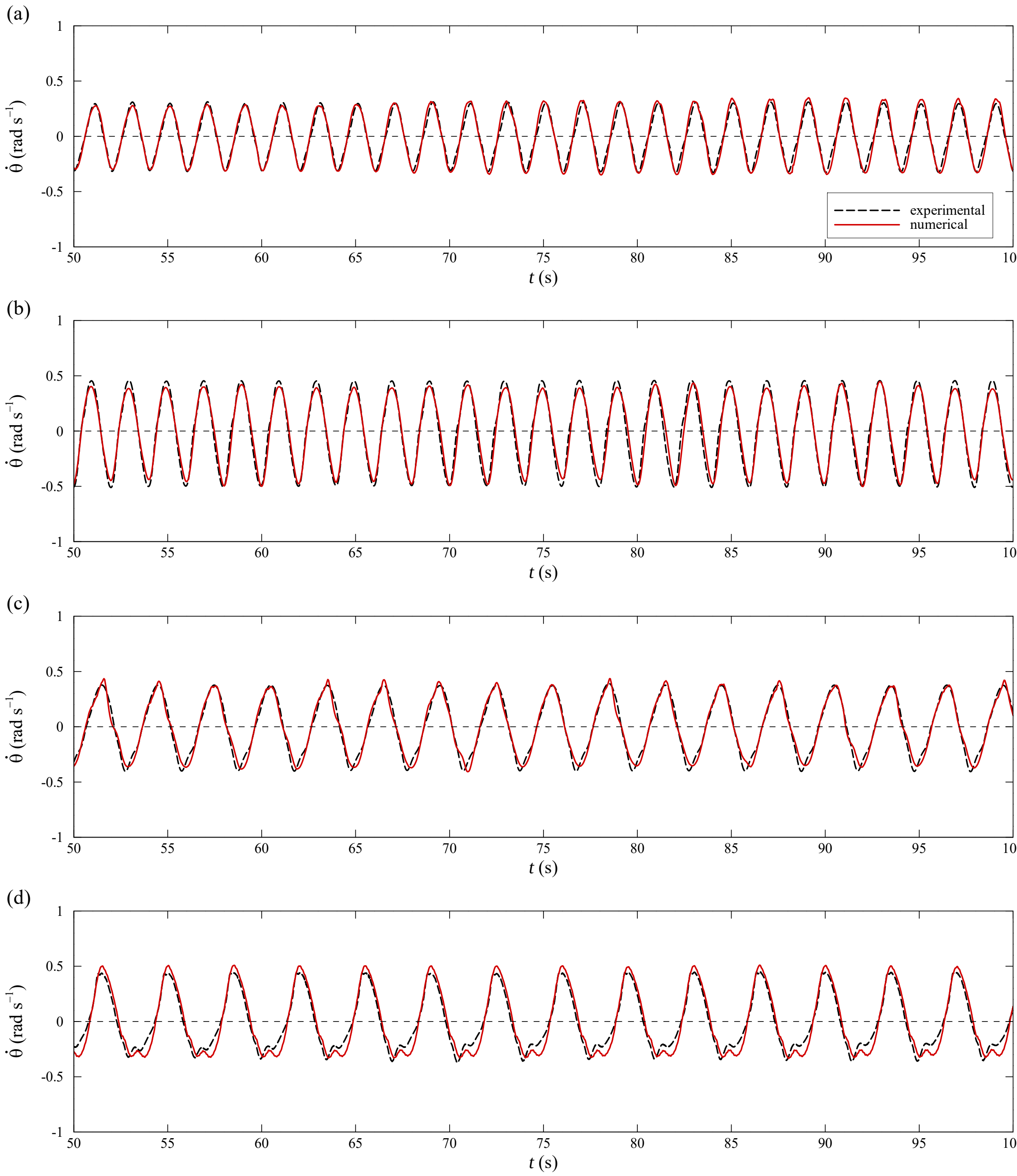

Figure 9.6: Comparison of numerical and experimental time series of angular velocity of the flap for test: (a) R1; (b) R2; (c) R3; (d) R4.

It can be observed that the numerical $\dot{\theta}$ shows a small deviation from the experimental data, which may be caused by the superposition of the reflected and incident waves. However, the numerical tool can predict most of OWSC dynamic with a satisfactory accuracy ($A_\chi \approx 1$ and $\varphi_\chi < 0.25$).

9.2.4 Phase-averaged flow field

The comparison of the experimental and numerical phase-averaged velocity vector field, ($\langle u\rangle$,$\langle w\rangle$), and contour of horizontal component, $\langle u\rangle$, in the plane $x-z$ at the middle of the flume ($y=0$), normalized by the deep-water maximum particle velocity U_0 at different phase when the flap moves toward the beach ($\theta > 0$) is shown in Figures 9.7 and 9.8.

The experimental velocity fields (Figures 9.7 and 9.8) were measured for the half wave cycle with $\theta > 0$ and for the wave condition R4, being $U_0 = 0.22$ m s^{-1}.

In terms of ($\langle u\rangle$,$\langle w\rangle$) field, a small difference in the orientation of vectors near the flume bed and near the free-surface are observed between experimental and numerical results. The experimental ascendant flow, caused by the approach of the wave crest and the blockage effect of the flap, is mostly larger than the numerical one. The experimental $\langle w\rangle$ component is mostly larger than the numerical one near the free-surface. However, the experimental spatial distribution of $\langle u\rangle$ is complex, with the presence of longitudinal and vertical gradients, related to the deceleration of the flow caused by the reversal motion of the flap.

In general, the magnitudes of ($\langle u\rangle$,$\langle w\rangle$) fields were predicted with reasonable accuracy while the contours of $\langle u\rangle$ in the recirculation zones were predicted approximately. It is difficult to identify the vortex caused by the flap deceleration in the experimental data, due to the limited size of the measurement mesh. However, the numerical results provide a full flow field in the vicinity of the flap.

The main limitation of these results is the gap (with a maximum value of about 0.03 m) between fluid and flap near the freeboard. This gap of 0.03 m is related with the resolution of the problem, so that, the increases of the resolution allows to get a smaller gap. However results are good enough now and there is no need to increase the computational time when increasing resolution (reducing d_p, so that reducing the gap).

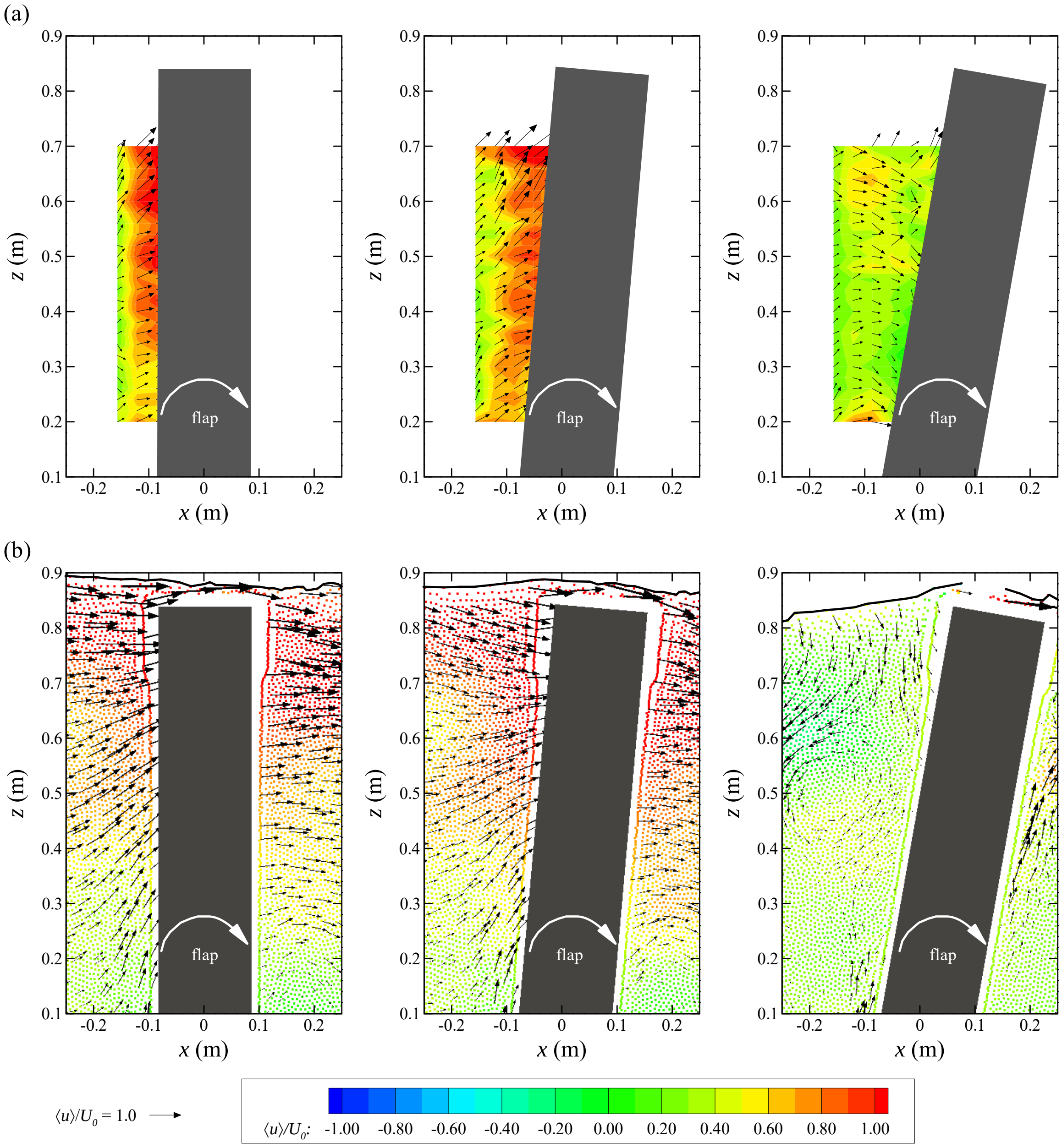

Figure 9.7: Comparison of the velocity field in the vicinity of OWSC for $\dot{\theta} > 0$: (a) experimental; (b) numerical.

The experimental and numerical S_η, obtained in the middle of the flume ($y = 0$) at $x = -3.43$ m, and the power spectrum of angular velocity of the flap, $S_{\dot{\theta}}$, for both irregular wave tests I1 and I2 (see Table 5.3) are compared in Figure 9.9.

Comparing the peak values of S_η, a relative error of about 4% was found between the tests (similar to Figure 9.4). The peak values of $S_{\dot{\theta}}$ for both tests I1 and I2 shows a relative

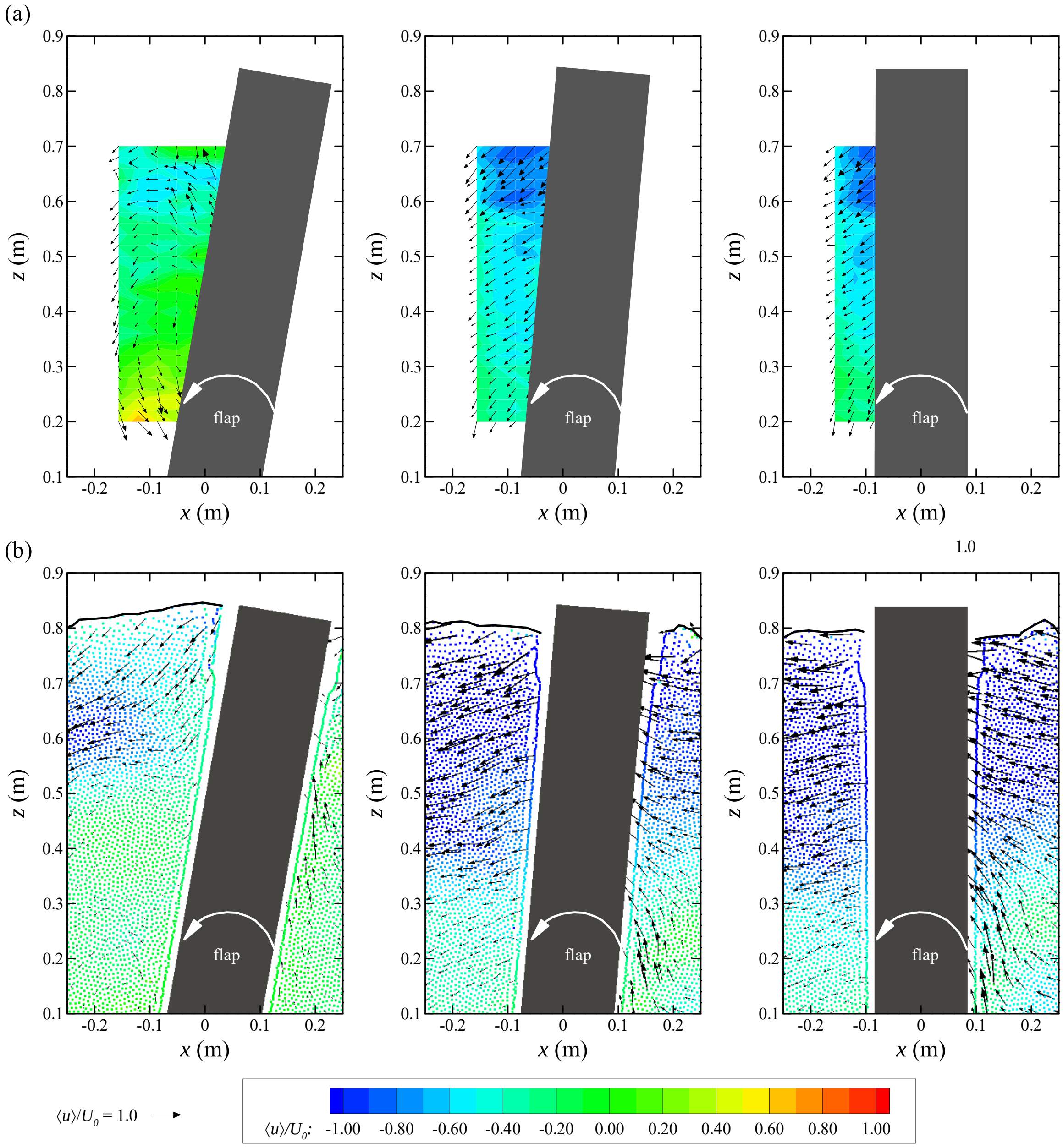

Figure 9.8: Comparison of the velocity field in the vicinity of OWSC for $\dot{\theta} < 0$: (a) experimental; (b) numerical.

error of about 10%. For higher frequencies the S_η shows greater difference with maximum relative error of about 20%. However, in general, it can be observed that both S_η and $S_{\dot{\theta}}$ are accurately predicted by the numerical tool.

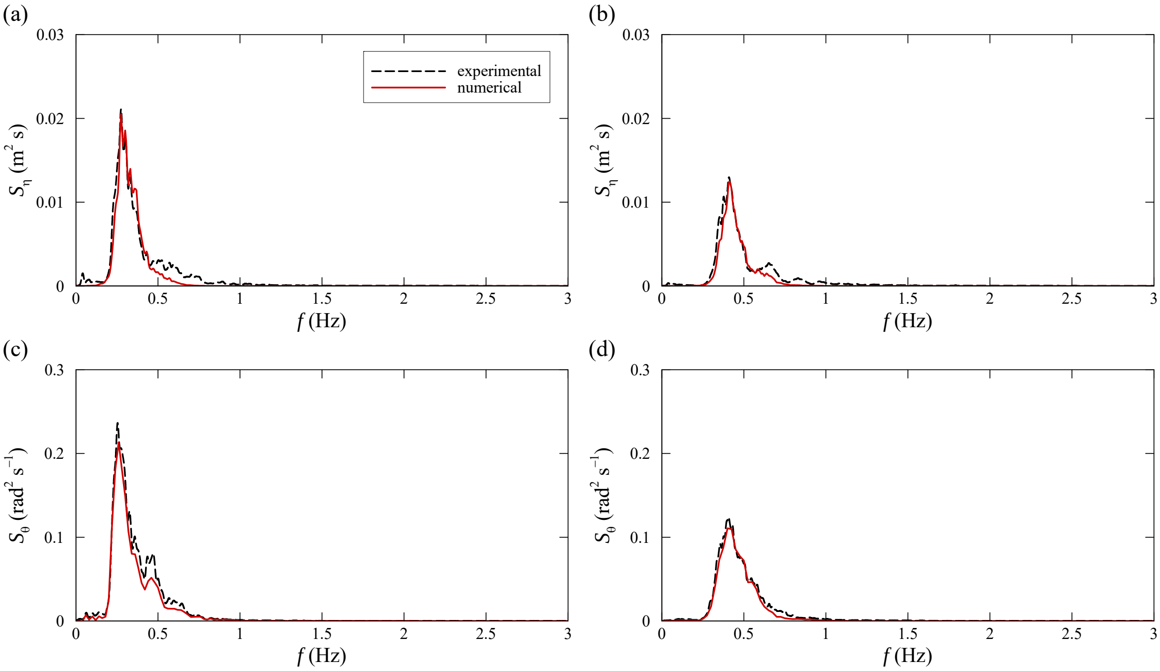

Figure 9.9: Comparison of the numerical and experimental power spectrum of angular velocity of the flap for test: (a) I1; (b) I2.

9.3 Application of the numerical tool

The properly validated numerical tool is here applied to study the influence of the PTO system, flap inertia and geometry on the hydrodynamics of the OWSC under regular waves. This study was performed for the wave test conditions R1 and R2 (see Table 9.1).

9.3.1 Influence of PTO system

The influence of the PTO system on the hydrodynamics of the OWSC is analyzed through the change of the PTO damping coefficients. From the several coefficients of pressure force, F_p, and friction force, F_f, (see Section 7.2), the pressure loss coefficient, K_p, and viscous friction coefficient, σ_2, have shown to be the most relevant on the OWSC's hydrodynamics and power capture.

The value of K_p is directly related with hydraulic circuit that included hydraulic cylinder, check-valves, globe valves, pipes and reservoir, while σ_2 is related with piston and rod bristles (made of rubber) and cylinder body.

The analysis was performed for ten values of K_p ranging from 3.25×10^5 to 16.25×10^5 Pa s^2 and for seven values of σ_2 ranging from 100 to 1000 N s m^{-1}. The analysis of K_p effect was done for constant $\sigma_2 = 300$ N s m^{-1} and the analysis of σ_2 effect was performed for constant $K_p = 6.5 \times 10^5$ Pa s^2. An example of the time series of angular velocity of the flap, $\dot{\theta}$, and the instantaneous power capture, W_{out}, for three different PTO damping coefficients is presented in Figure 9.10.

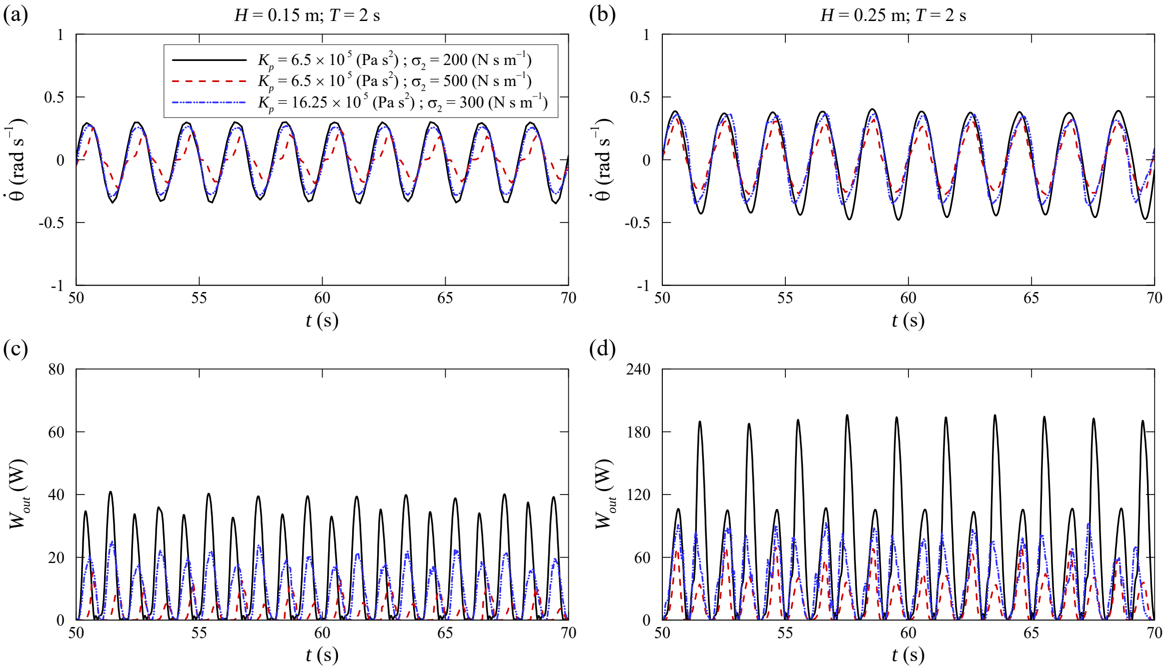

Figure 9.10: Influence of PTO damping coefficients on the: (a,b) angular velocity of the flap; (c,d) instantaneous power capture. The left column shows time series for $H = 0.15$ m and $T = 2$ s, and the right column for $H = 0.25$ m and $T = 2$.

As expected, the PTO system has an important influence on the $\dot{\theta}$ and on the W_{out}. The results highlight that the designer should be worried with rate-dependent deformation characteristics (viscoelastic nature) of the rubber and not with pipe diameter and roughness as the W_{out} varies a lot with σ_2 and not K_p (see Figures 9.10c and d). The main consequence of this result is the large modification of the capture width ratio (CWR) of the OWSC. The variation of CWR with σ_2 and K_p are presented in Figure 9.11.

It can be seen that the variation of both damping coefficients have an important effect on the CWR. However, the influence of σ_2 is more relevant than K_p for the same ratio of variation. In fact, CWR decreases significantly with increasing of σ_2 and a much smaller difference is shown with increasing of K_p: the influence of the σ_2 presents a maximum difference in the

CWR of about 200% for both wave conditions (Figure 9.11a); while the influence of the K_p shows a maximum difference of about 20% for the test R1 and 50% for test R2 (Figure 9.11b). This behavior is caused by the large energy dissipation through the σ_2 and the notable change in the flow field (i.e. available energy) caused by its brake effects.

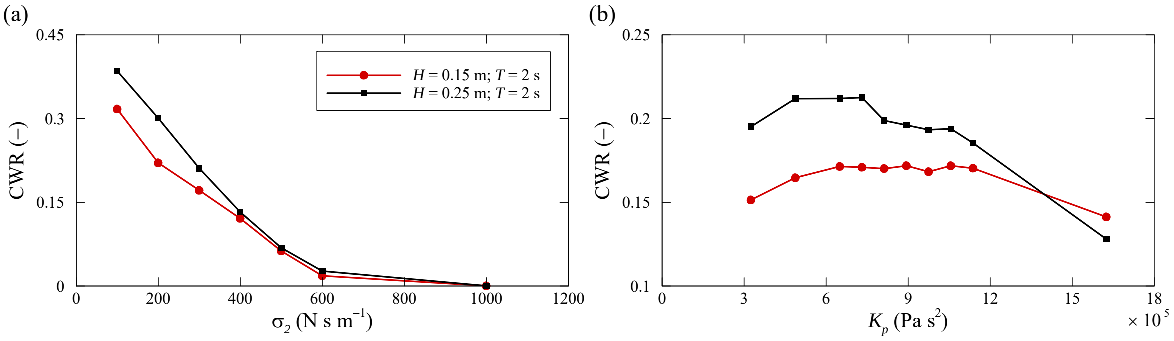

Figure 9.11: Influence, on the CWR, of the: (a) viscous friction coefficient; (b) pressure loss coefficient.

In order to illustrate the influence of these parameters on the flow field, Figures 9.12 to 9.15 show the velocity fields for the three different PTO damping coefficients presented in Figure 9.10 at $t = 52$, 52.5, 53 and 53.5 s.

These velocity fields correspond to wave test condition R2. The different mechanical moment (applied by the PTO system on the flap) causes a large variation on the velocity field, including a strong non-linear behavior. Due to the non-linearity of the wave-OWSC interaction, a large discrepancy can be observed in the free-surface elevation and velocity distributions for different PTO damping coefficients. For example, at $t = 52$ s, when the wave crest starts to approach the flap, different ascendant flows are observed, which are caused by the blockage effect of the flap (Count and Evans, 1984). Hence, the mass of water that passes over the flap at $t = 52.5$ s is different from case to case, indicating that W_{out} is affected by the instantaneous submergence of the flap (see Figure 9.13).

Different wake is also observed at $t = 53$ and 53.5 s, characterized by the flow rotation, which is irreconcilable with potential flow description (see Figures 9.14 and 9.15).

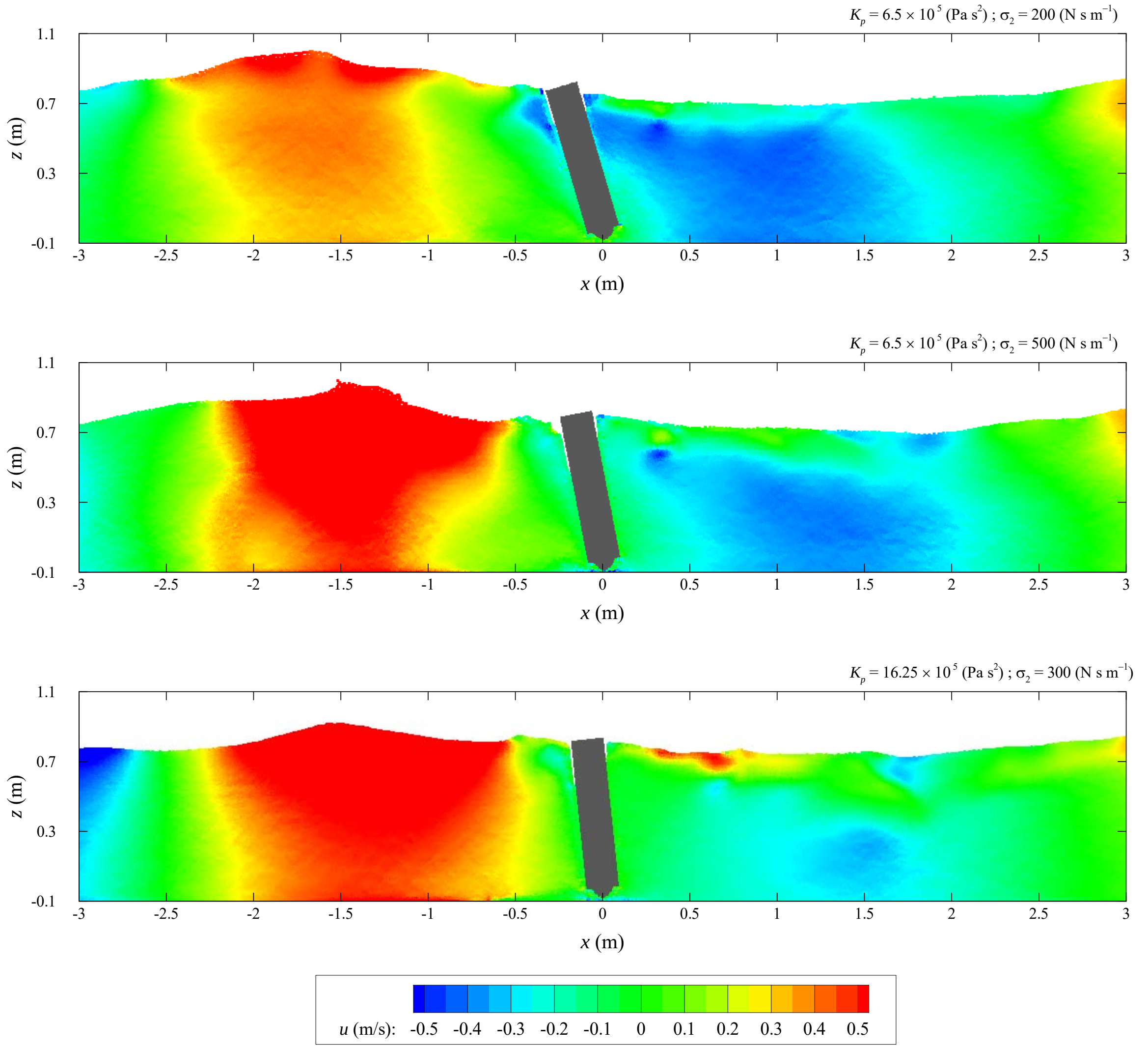

Figure 9.12: Different instants of the velocity field in the vicinity of the flap for different PTO damping coefficients at $t = 52$ s.

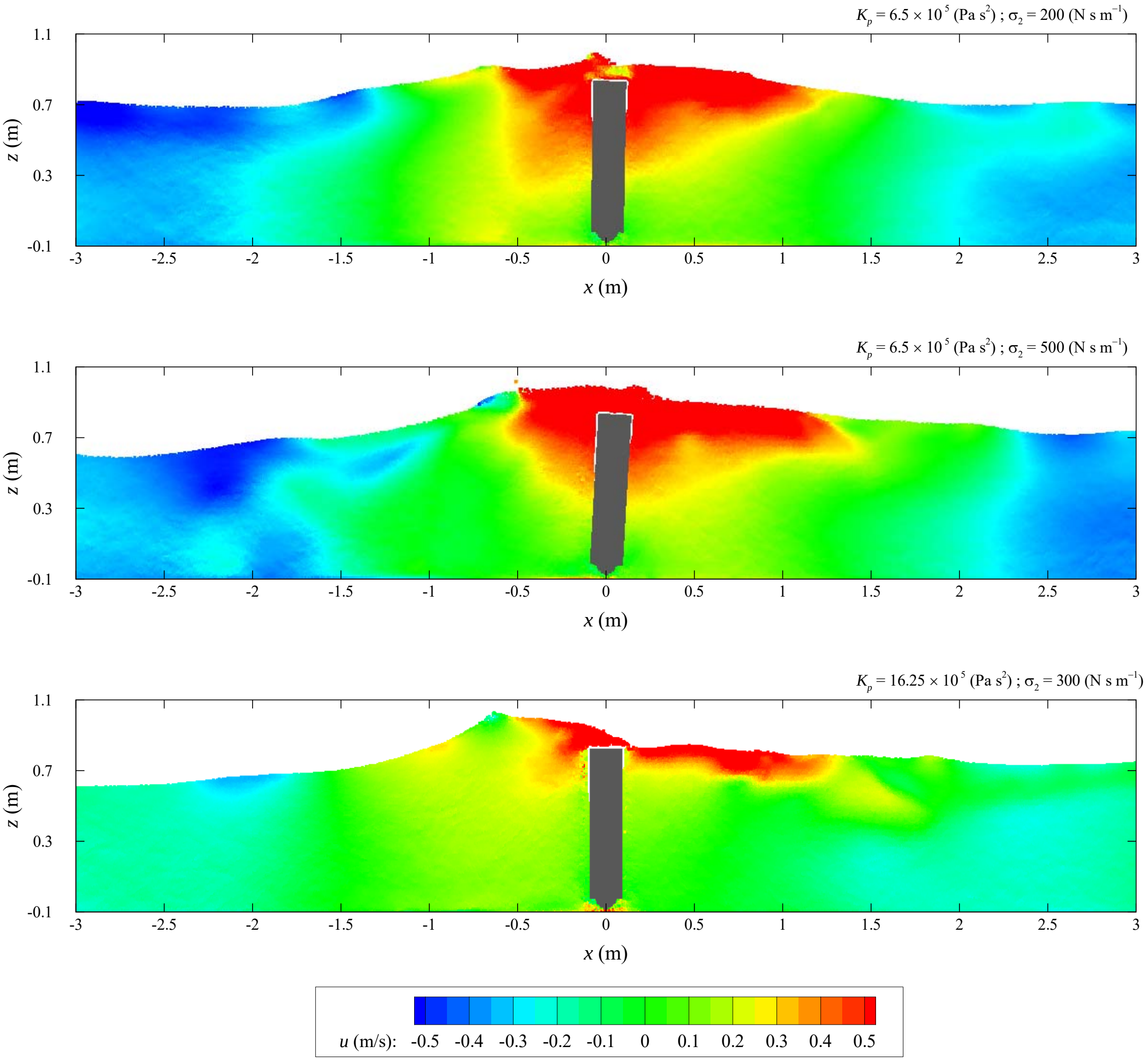

Figure 9.13: Different instants of the velocity field in the vicinity of the flap for different PTO damping coefficients at $t = 52.5$ s.

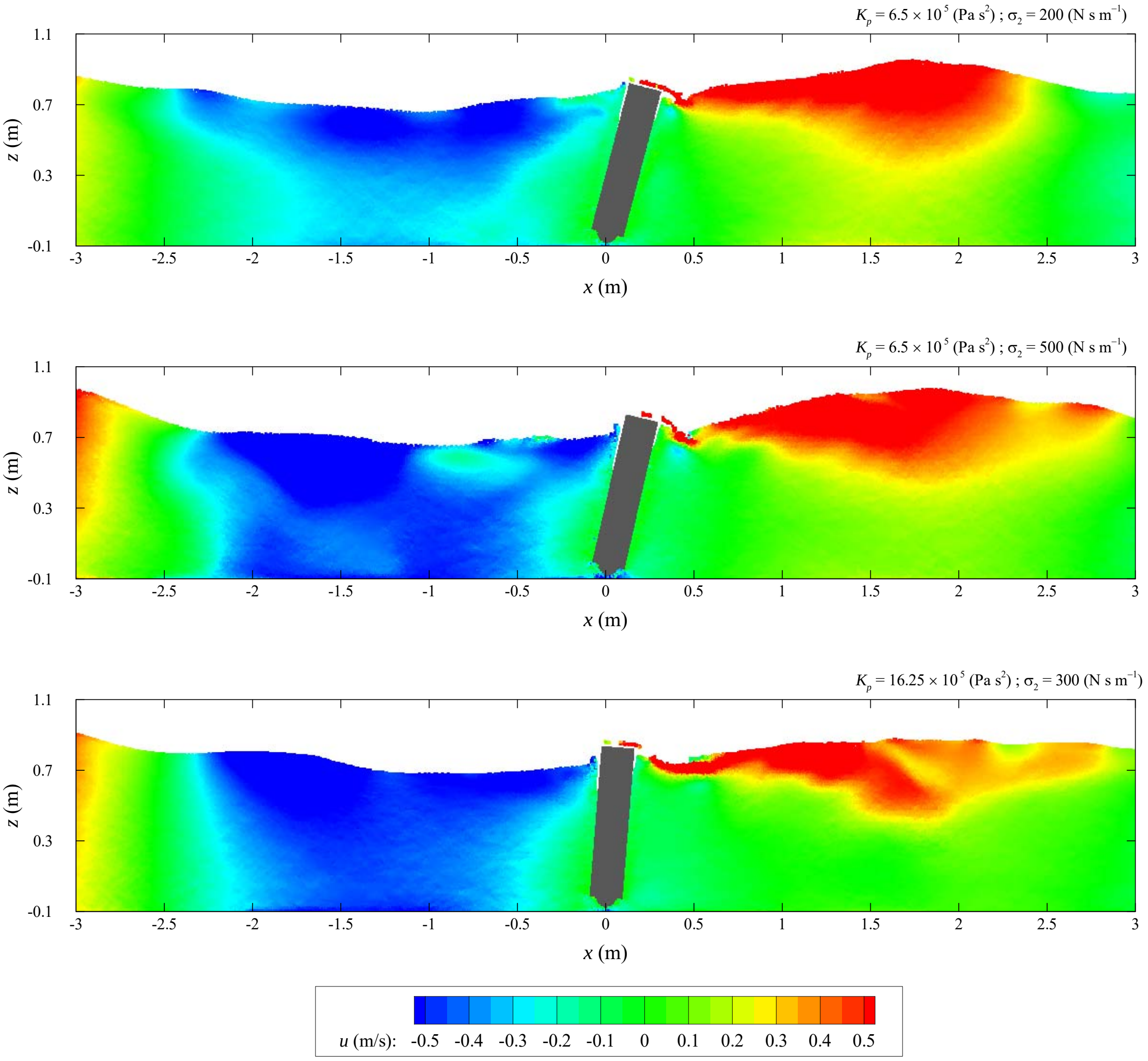

Figure 9.14: Different instants of the velocity field in the vicinity of the flap for different PTO damping coefficients at $t = 53$ s.

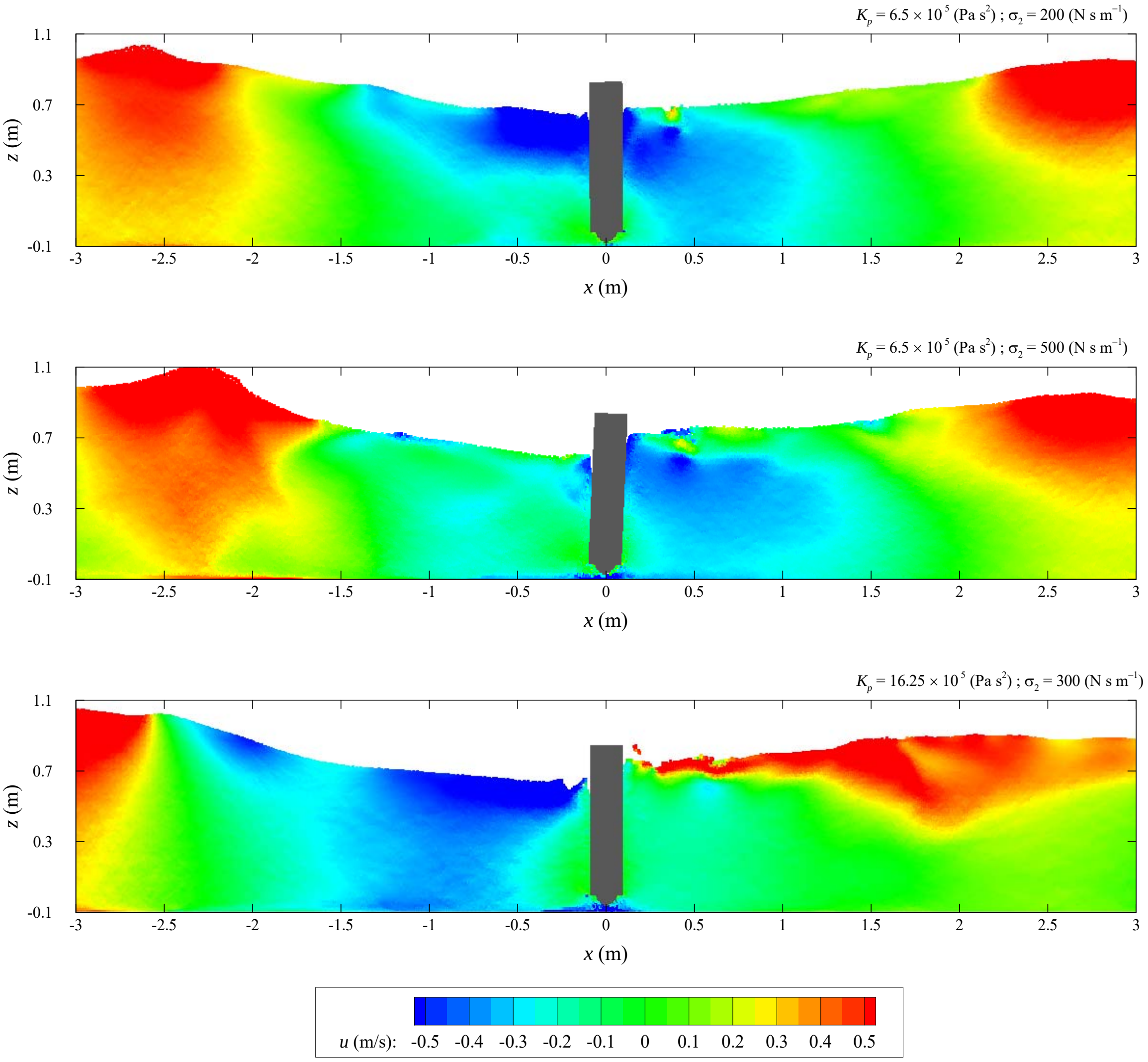

Figure 9.15: Different instants of the velocity field in the vicinity of the flap for different PTO damping coefficients at $t = 53.5$ s.

9.3.2 Influence of flap inertia

The analysis of the flap inertia influence on the hydrodynamics of the OWSC is performed using a similar technique as presented in Gomes et al. (2015), i.e. in two phases. The first is based on the variation of the flap mass, m, and its centre of mass, $\bar{z}$. The second is based on the variation of the flap height, l, and thickness, a. It should be noted that the change of these parameters results in the modification of the flap moment of inertia. The analysis of m effect was performed considering that the mass is uniformly distributed over the flap with a constant $\overline{z} = 0.33$ m. The analysis of $\overline{z}$ effect is done imposing different value of $\overline{z}$ for a constant $m = 72.3$ kg.

The variation of CWR with $\overline{z}$ and m are shown in Figure 9.16. It can be seen that CWR decreases when increasing both m and $\overline{z}$. In general, the $\overline{z}$ has more influence on the CWR than m. The $\overline{z}$ presents a maximum difference of CWR of about 75% for test R1 and 32% for test R2 (Figure 9.16a). For a relatively small $\overline{z}$ the OWSC presents a relatively high CWR. The m presents a maximum difference of the CWR of about 40% and 18% for the test R1 and R2, respectively (Figure 9.16b). It is observed that the effects of $\overline{z}$ is approximately twice of m for the same ratio of variation of $\overline{z}$ and m, respectively.

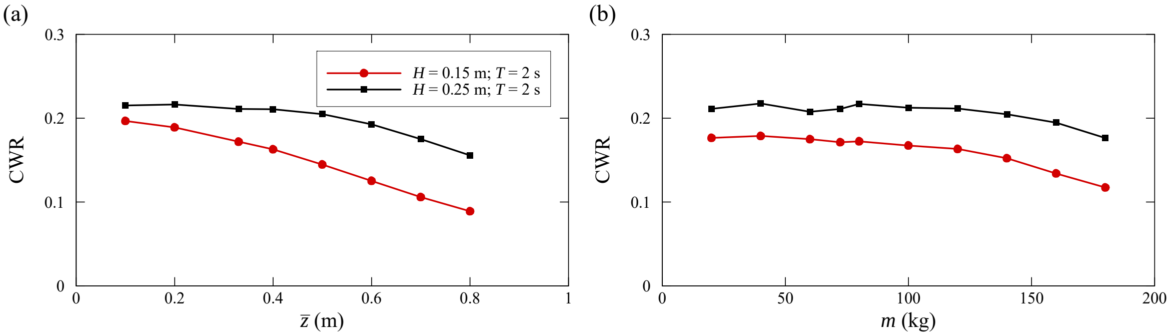

Figure 9.16: Influence, on the CWR, of the flap: (a) centre of mass; (b) mass.

The analysis of a effect was done considering constant $m = 72.3$ kg and $\overline{z} = 0.33$ m. The analysis of l effect was also performed for a constant m but considering different values of $\overline{z}$, equal to approximately $0.4l$. Figure 9.17 shows the variation of CWR with a and l.

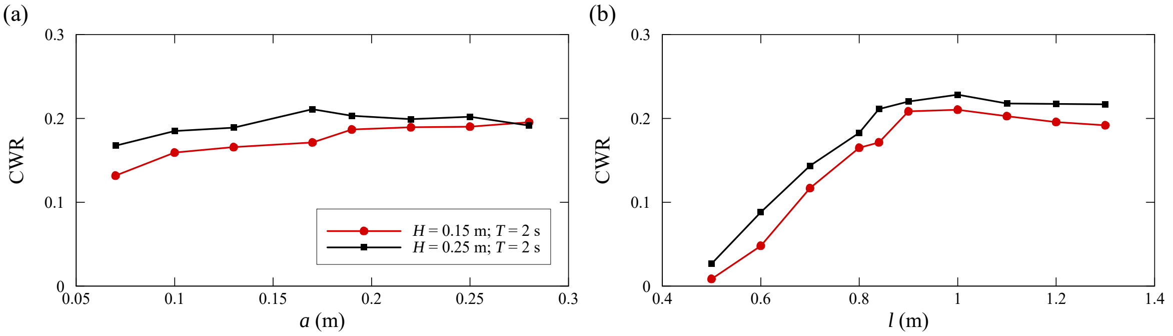

Figure 9.17: Influence, on the CWR, of the flap: (a) thickness; (b) height.

The influence of the a is not seem to be substantial, compared with the influence of the l. In fact, CWR slightly increases when increasing a, with the maximum difference of the CWR of about 36% and 13% for the test R1 and R2, respectively (Figure 9.17a). In contrast, the l causes a large variation of the CWR, with its maximum difference of about 160% for both wave conditions (Figure 9.17b). This behavior is caused by the changing of the flap submergence ratio that results in a large reduction in the wave excitation moment and energy transfer over the flap.

In order to illustrate the influence of these parameters on the flow field, Figures 9.18 to 9.21 show the velocity fields for the three different $l = 0.6$, 0.9 and 1.1 m at $t = 52$, 52.5, 53 and 53.5 s. Similar to Figures 9.12 to 9.15 the velocity fields correspond to wave test condition R2.

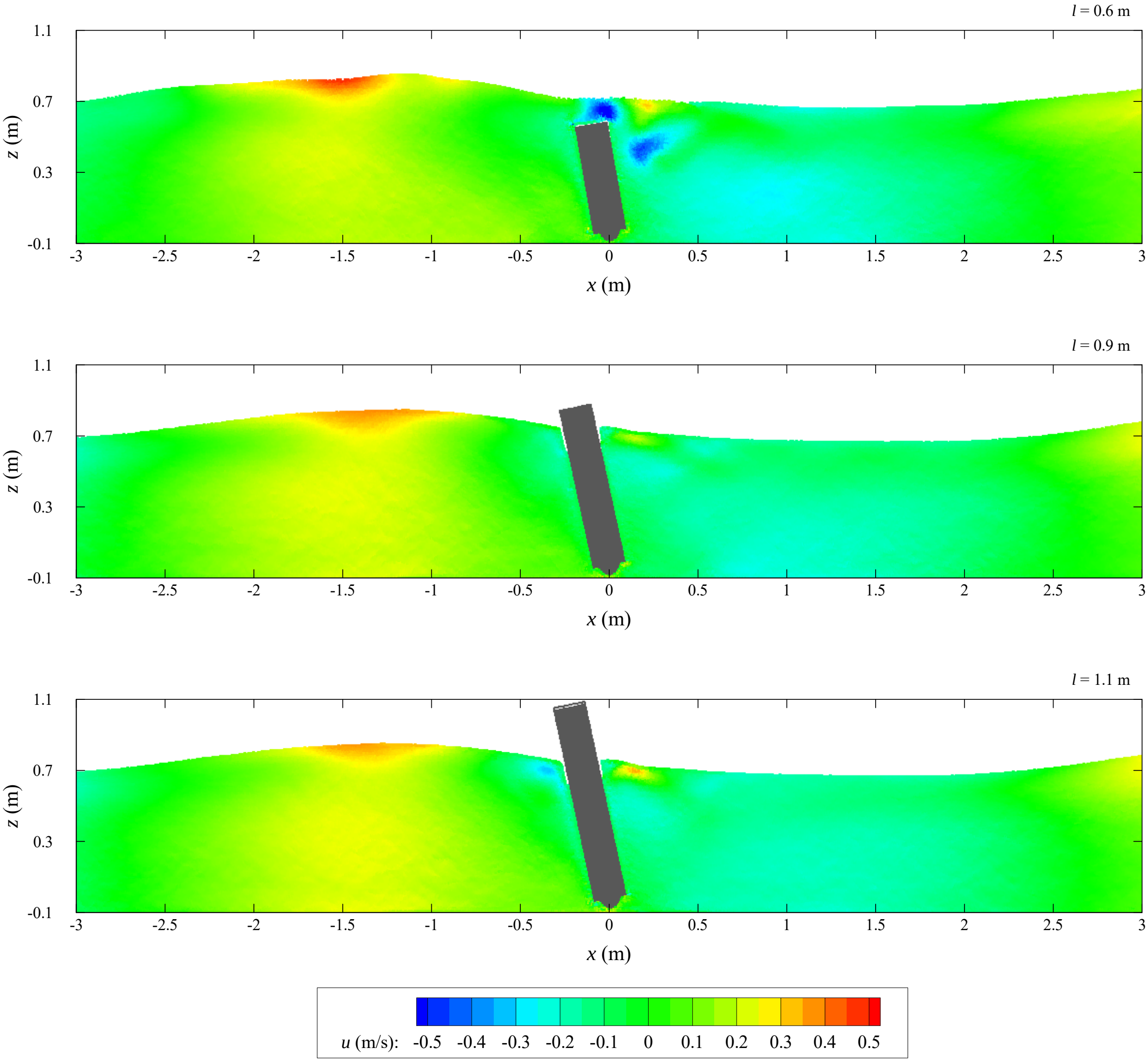

Figure 9.18: Different instants of the velocity field in the vicinity of the flap for different flap height at $t = 52$ s.

The influence of the flap submergence is clearly visible. A very distinct flow features are observed for the fully-submerged ($l = 0.6$ m) and the surface-piercing flap ($l = 0.9$ and 1.1 m). Such difference is caused by the flow separation on the freeboard, that have influence only for fully-submerged flap. For surface-piercing flap the free-surface elevation and u distributions seem very similar, resulting in small difference in the CWR (see Figure 9.17b).

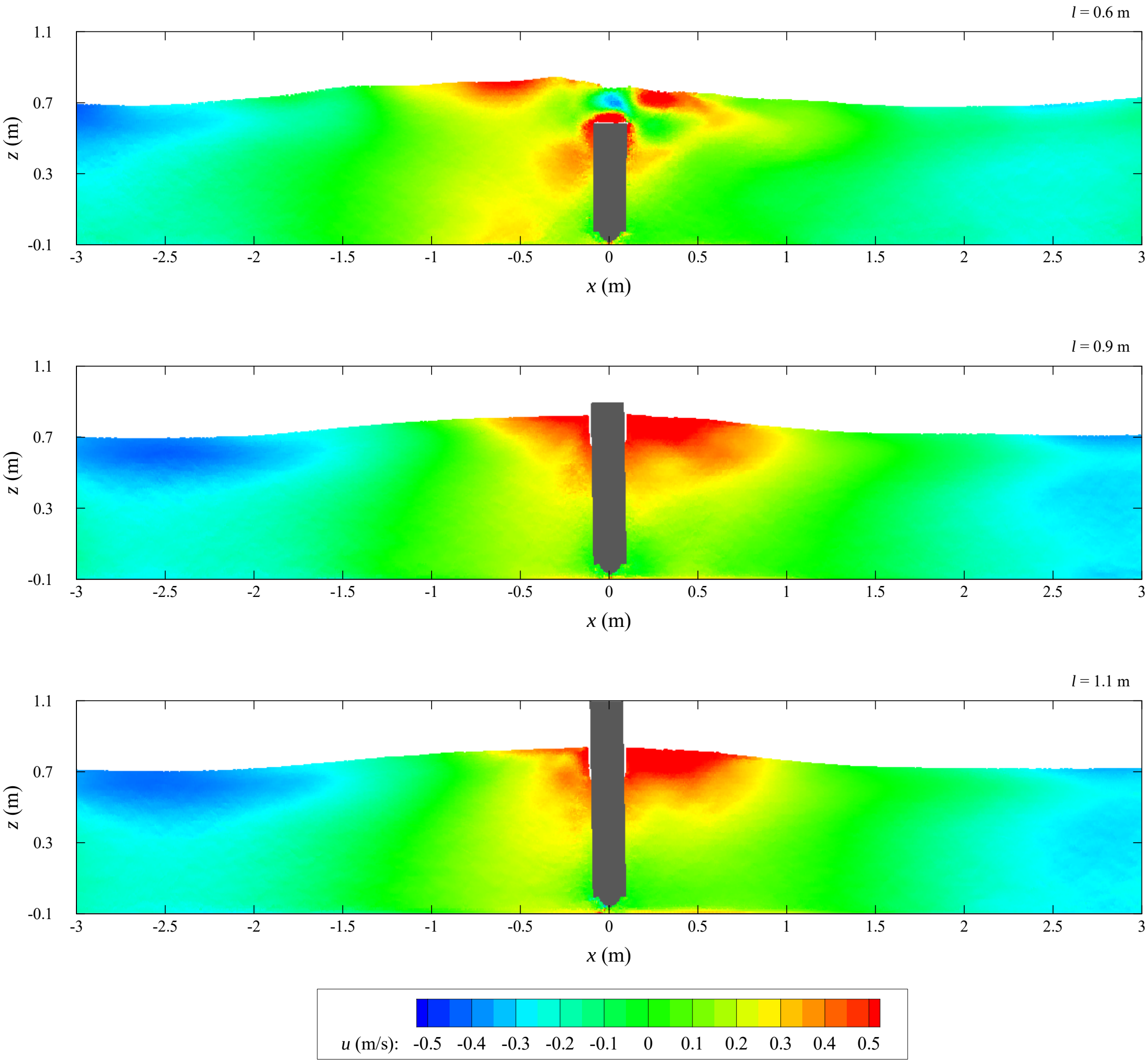

Figure 9.19: Different instants of the velocity field in the vicinity of the flap for different flap height at $t = 52.5$ s.

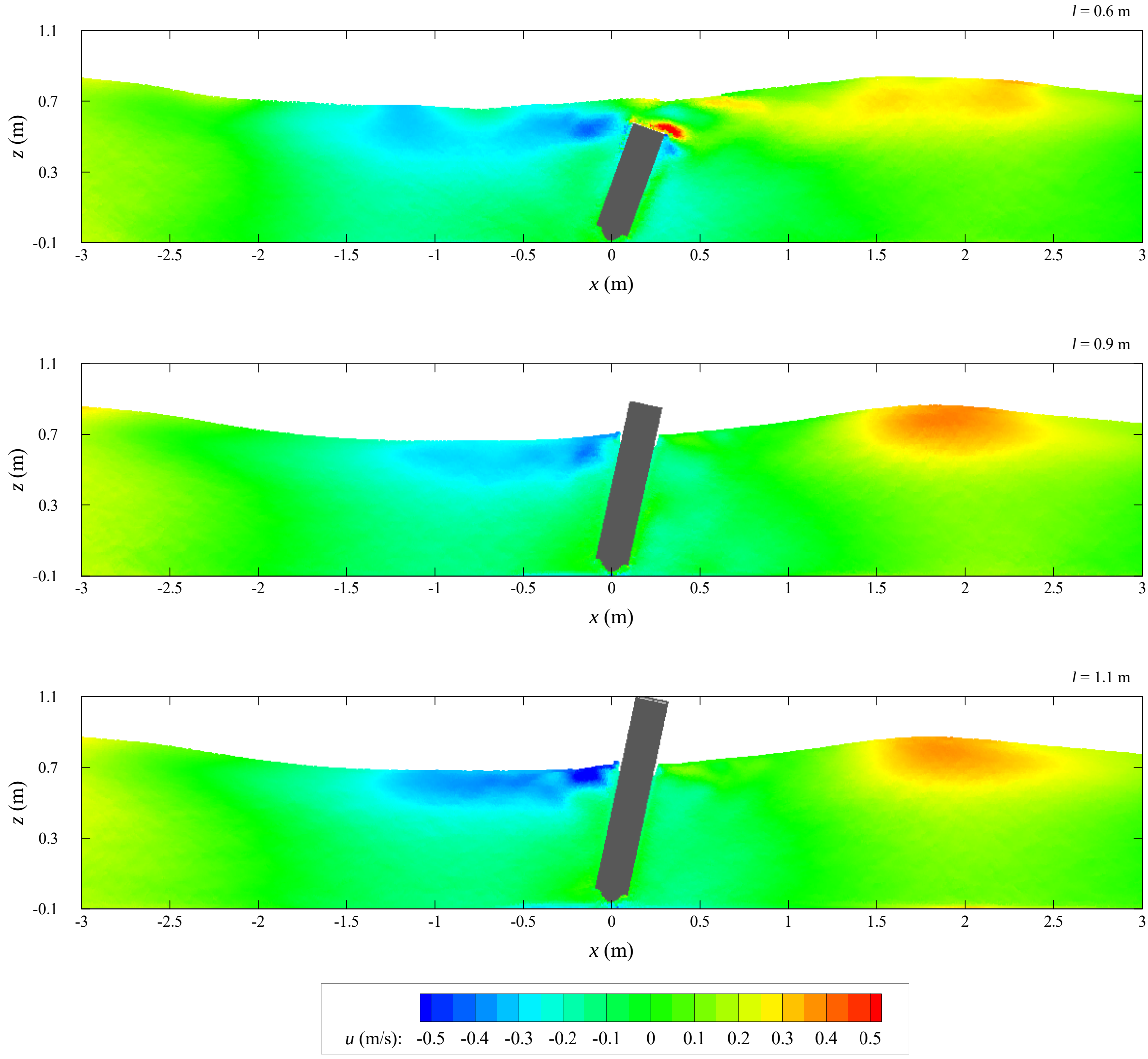

Figure 9.20: Different instants of the velocity field in the vicinity of the flap for different flap height at $t = 53$ s.

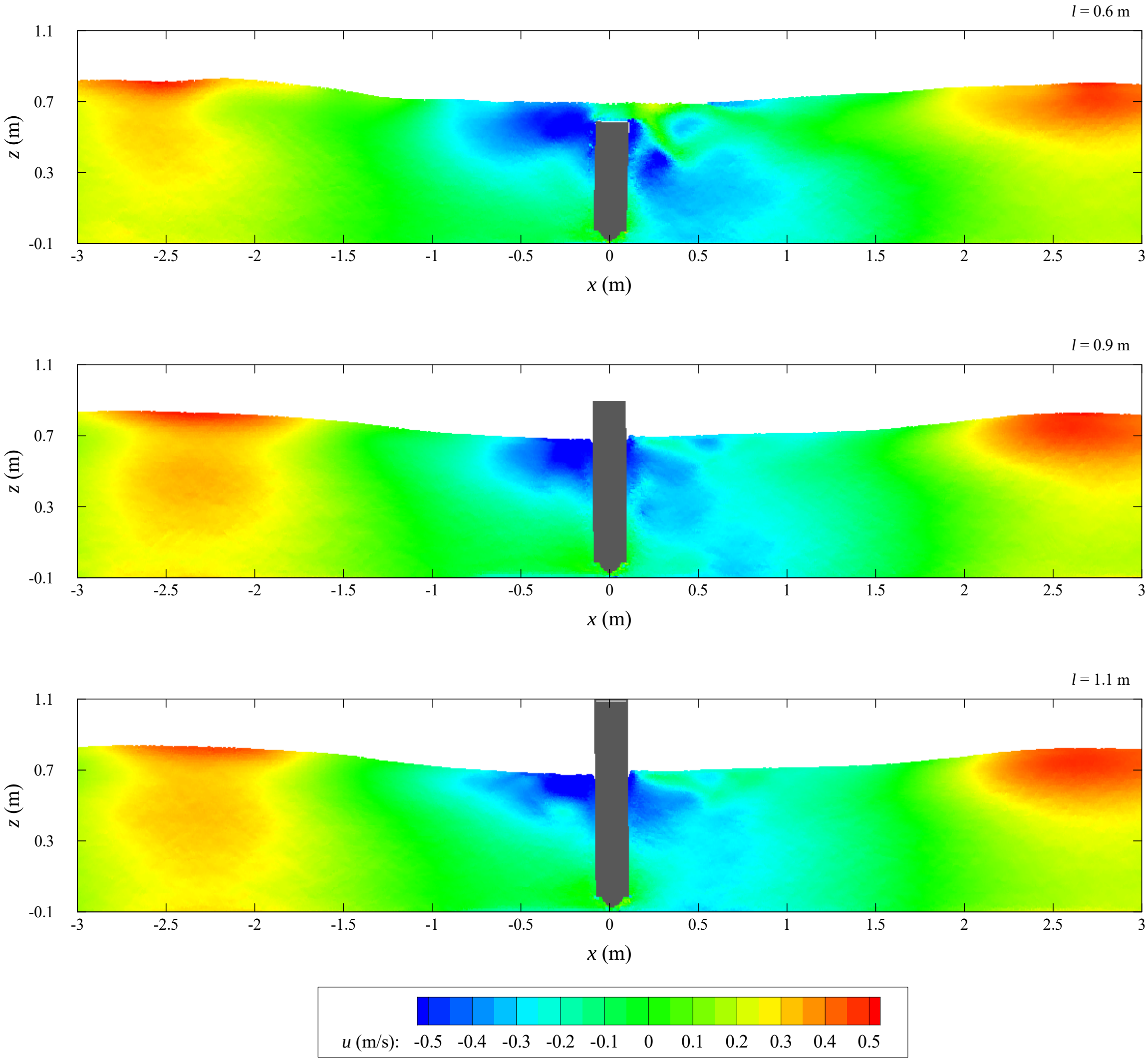

Figure 9.21: Different instants of the velocity field in the vicinity of the flap for different flap height at $t = 53.5$ s.

9.3.3 Influence of flap cross-section configuration

In this section, five different cross-section configurations are considered: FG1, FG2, FG3, FG4 and FG5 in Figure 9.22, to explore the influence of the flap geometry on the hydrodynamics of the OWSCs. These configurations are defined considering different freeboard geometry. The simulation was performed for $K_p = 6.5 \times 10^5$ Pa s^2 and $\sigma_2 = 300$ N s m^{-1}.

The variation of CWR with the five different cross-section configurations are presented in Figure 9.23. As expected, the geometry influence is quite small. The larger differences occur

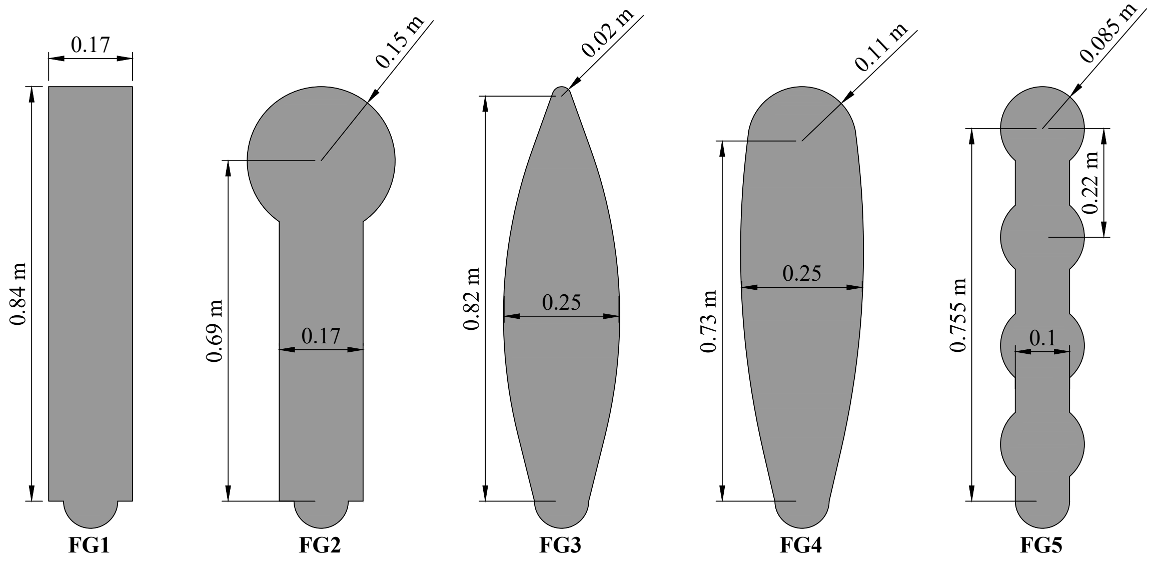

Figure 9.22: Different flap cross-section configuration (FG1, FG2, FG3, FG4 and FG5).

for the small freeboard (FG3), showing a difference of about 20% from the other geometries, that differs of only 5% between them.

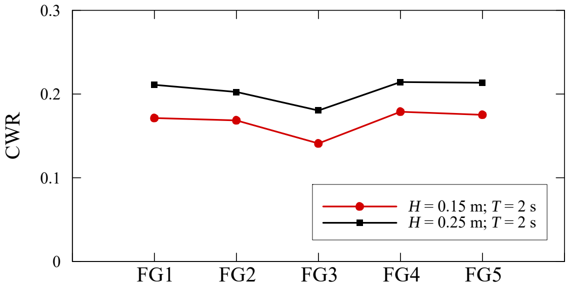

Figure 9.23: Influence of the flap cross-section configuration on the CWR.

In order to illustrate the influence of these parameters on the flow field, Figures 9.24 and 9.25 show the velocity fields in the vicinity of the flap for the five different cross-section configurations considered at $t = 52.5$ and 53 s, respectively. In general, a similar vector orientation are observed in the entire water column, with a small difference in the orientation near the free-surface. The difference is more relevant on the free-surface elevation, caused by the different flap freeboard geometry.

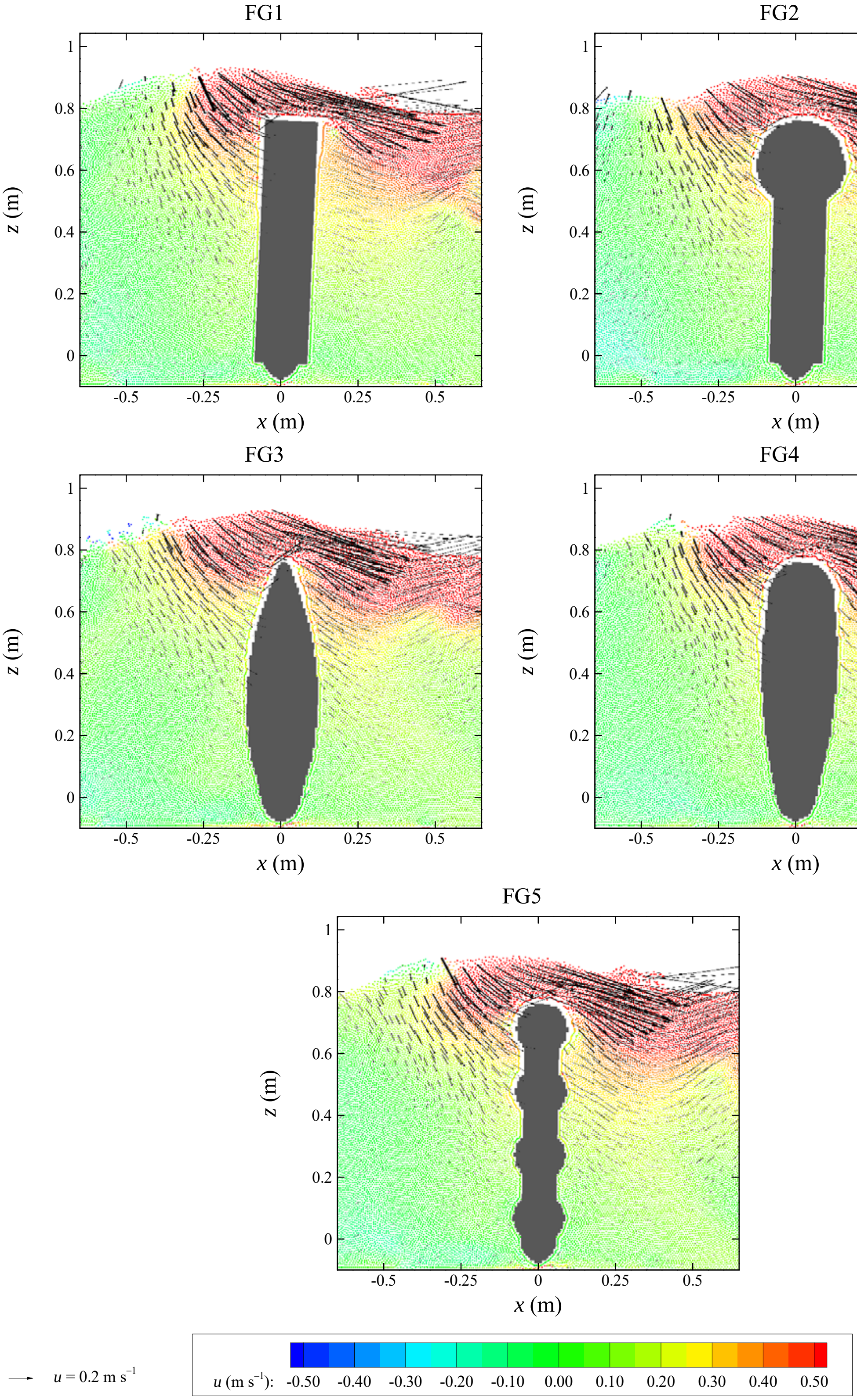

Figure 9.24: Velocity field in the vicinity of the flap for the different geometry at $t = 52.5$ s.

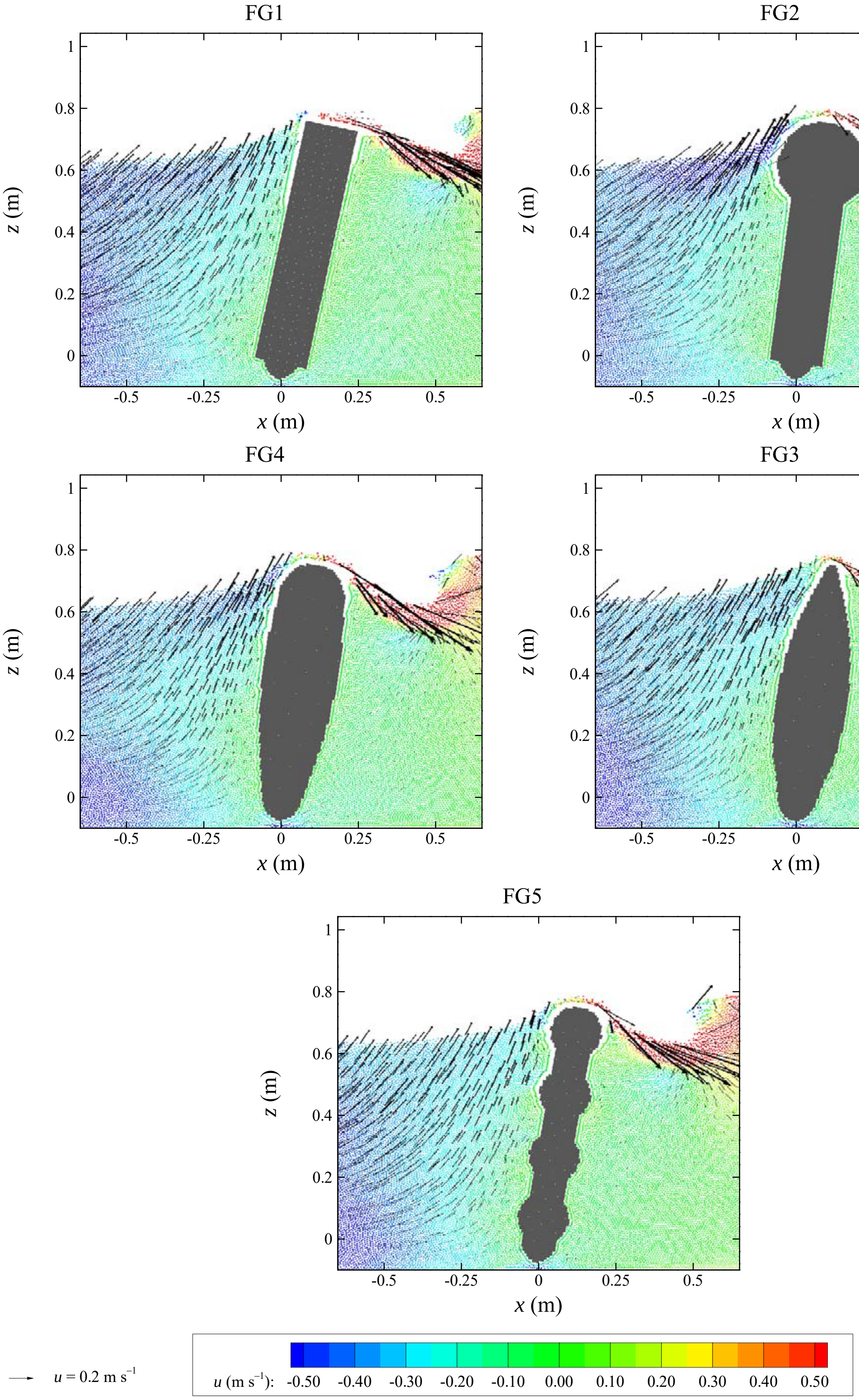

Figure 9.25: Velocity field in the vicinity of the flap for the different geometry at $t = 53$ s.

9.4 Summary and conclusions

In this chapter, the numerical tool was properly validated using the experimental data of an OWSC with mechanical constraints, including the effects of non-linear constraints of hydraulic PTO system and the frictional contacts between flap and bearings. The validation was performed for both unidirectional regular and irregular waves. The comparison between numerical results and experimental data shows that the numerical tool properly predicts the dynamics of the OWSC. Furthermore the computed and observed free-surface elevations and mean flow field show reasonable agreement, with normalized amplitude error of about 1 and normalized phase error less than 0.25. The power spectrum of free-surface elevation and angular velocity of the flap are also accurately predicted with relative error of about 4% and 10%, respectively.

The validated numerical tool was then applied to study the effect of the PTO system, flap inertia and geometry on the hydrodynamics of the OWSC. The PTO system presents an important effect on the CWR. The influence of the friction force shown more relevant than the pressure force on the CWR, since it decreases significantly when increasing viscous friction coefficient with a maximum difference of about 200% and it shows a much reduced response when increasing pressure loss coefficient. This behavior is caused by the large energy dissipation through the friction force and the notable change in the flow field caused by its brake effects. Therefore the designer should be worried with rate-dependent deformation characteristics (viscoelastic nature) of the rubber and not with pipe diameter and roughness as the CWR varies a lot with friction force and not pressure force.

The effect of the flap inertia was analyzed by changing its mass, centre of mass, height and thickness. The variation of these parameters exhibits relevant effects on the hydrodynamics of the OWSC. It was observed that CWR decreases when increasing both flap mass and centre of mass. On the other hand, CWR increases when increasing both flap height and thickness, but with a much higher dependence on the flap height. Distinct flow trends were observed between the fully-submerged and the surface-piercing flap, generated by the flap freeboard effects.

The analysis of several flap cross-section configurations shows that the freeboard geometry influences the CWR. The smallest freeboard geometry presents a difference of the CWR of about 20% from the other geometries tested.

These numerical results demonstrate the usefulness of the developed simulation tool as an aid to design OWSCs. It provides a suitable method for modeling WEC devices with any mechanical constraints, such as revolute joints, frictional contacts, constraints and sliders.

10

Conclusions and future work

Contents

10.1 Main conclusions

The present work has been devoted to fill the main gaps that were found in the numerical modeling and experimental testing of oscillating wave surge converter (OWSC) devices. In this context, the objectives of this thesis was the development of a numerical tool that is able to simulate the complex fluid-structure interactions and hydrodynamic behavior of the OWSC with mechanical constraints; and the validation of the numerical tool with closely controlled laboratory tests. To develop the numerical tool it was necessary to understand the main features of the flow, to understand the dynamic behavior of the hydraulic PTO system, to recognize and validate existing numerical approaches with potential to be combined into the numerical tool. The validation of the numerical tool was performed using independent tests on the dynamic and hydrodynamic behaviors of the OWSC with mechanical constraints.

To achieve this objective, first, a Smoothed Particle Hydrodynamics (SPH) numerical model was adapted for modeling the hydrodynamics of the OWSCs with mechanical constraints. The numerical implementation was carried out by coupling the multi-body solver of Project Chrono library under the SPH model of DualSPHysics code, where the SPH solver resolves the interaction between wave and flap and the multi-body solver resolves the interaction between flap and mechanical constraints. Next, the simulation of wave-flap-mechanical constraints interactions was described and validated with experimental data specially design for that.

Two set of physical model tests of an OWSC with hydraulic PTO system at 1:10 scale model were carried out at the Instituto de Mecánica de los Fluidos e Ingeniería Ambiental (IMFIA), Universidad de la República, Uruguay. In the first set of tests, the hydrodynamics of the OWSC in intermediate water depth under both unidirectional regular and irregular waves with the highest annual frequency in the Uruguayan oceanic coast were investigated. The free-surface elevation, pressure in the PTO system, rotation angle and the longitudinal and vertical velocity components in the vicinity of the flap were measured and analyzed. In the second set of tests, the dynamic behaviors of the hydraulic PTO system were characterized.

The results for regular waves indicated that the PTO system, wave frequency and height have a significant influence on the capture width ratio (CWR) and on the response amplitude operator (RAO). It was observed that RAO decreases when increasing wave height, which may be due to the viscous dissipation caused by vortex shedding and wave non-linearity that increases with wave height. However, the CWR does not seem to vary excessively with wave height, showing a limited variation. Both CWR and RAO shown a strong dependence on wave frequency, however, with a weak correlation between them.

The RAO curve does not present a well-defined peak as from the linear theory, showing a limited variation in a broad wave frequency band and it is strongly affected by the hydraulic PTO system. The time series of free-surface elevation, angular velocity of the flap and pressure in the PTO system are dominated by the linear component. However, the signals also present some important higher-order frequency components. In this context, to predict the variation of CWR, the non-linear output frequency response functions were considered as the extension of the RAO to the non-linear case. These functions also show a limited variation in a broad wave frequency band, presenting values of the same order of magnitude of RAO. The CWR is strongly affected by both significant wave height and peak frequency. CWR greater than 28% was found for higher significant wave height close to the maximum wave steepness and therefore (for best results) the OWSC should be adjusted to match the sea state. The results have shown that the inclusion of the hydraulic PTO system introduces non-linear behaviors that affects the relation between RAO and CWR, namely that the maximum CWR may not be registered at the RAO peak.

The velocity fields have shown that the flow rotation generated by wave-OWSC interaction and mass transfer have an important role on the CWR and, therefore, linear analytical solutions are not accurate to describe the complex hydrodynamics of the OWSC.

The PTO system has shown a strong non-linear behaviors, including hysteretic and stochastic behaviors. To implement these behaviors the modified LuGre model was used for the friction force and a new approach was proposed for the pressure force. To model the stochastic behavior the spectral representation method was used. The systematically comparison between measured and simulated results have been demonstrated that the developed mathematical model can predict, with a satisfactory accuracy, most of dynamic behaviors of PTO force. For large amplitude of the flap motion, the PTO system has also shown the cavitation phenomena. This phenomena has shown to have also an important effect on the hydrodynamics of the OWSC, and thus on the CWR.

The validation of the numerical tool was made considering three stages: (i) the dynamic behaviors of the OWSC with mechanical constraints were validated by describing its motion by a given angular velocity; (ii) the wave generation and propagation were validated for a several wave scenarios in the Uruguayan oceanic coast; (iii) the hydrodynamics of the OWSC with mechanical constraints was validated with experimental data.

The comparison between numerical results and experimental data shows that the numerical tool properly predicts the dynamics of the OWSC. Furthermore the computed and observed free-surface elevation and mean flow field show reasonable agreement. The free-surface elevation and angular velocity were accurately predicted with an normalized amplitude error of about 1 and phase error less than 0.25.

The validated numerical tool was then applied to simulate OWSC with mechanical constraints for several PTO damping and flap configurations. The influence of the PTO damping was performed by changing the friction and pressure forces. The variation of the friction force has shown to be more relevant on the CWR than the variation of pressure force, caused by the large energy dissipation through the friction force and the notable change in the flow field caused by its brake effects on the flap. The variation of the friction force shows a gain of about 200% on the CWR, while the variation of the pressure force shows a gain of about 50%.

The effect of the flap inertia was analyzed by changing its mass, centre of mass, height and thickness. The variation of these parameters exhibits relevant effects on the hydrodynamics of the OWSC. It was observed that CWR decreases when increasing both flap mass and centre of mass. On the other hand, CWR increases with both flap height and thickness, but with a much higher dependence on the flap height. Distinct flow features were observed between the fully-submerged and the surface-piercing flap, generated by the flap freeboard effects. The flap inertia also shows an important effect on the CWR, with maximum gain of about 160%. The analysis of several flap cross-section configurations has shown that the freeboard geometry influences the CWR. The smallest freeboard geometry presents a difference of the CWR of about 20% from the other geometries tested.

These numerical results demonstrate the usefulness of the developed simulation tool as an aid to design OWSCs, and providing a suitable method for modeling wave energy converter (WEC) devices with any mechanical constraints.

10.2 Main contributions and impacts

This research work has yield several contributions to the scientific community with practical implications in the numerical and experimental studies of OWSCs. The main contributions and impacts are summarized as follows:

1) A fully non-linear numerical tool for the design of OSWC with mechanical constraints was developed. This model takes advantage of advanced parallel computing frameworks, allowing to modeling complex fluid-structure interaction and to reproduce complex flows (see two examples of applications in Appendix E). These examples are well defined in Canelas et al. (2018). A large set of dynamic and kinematic restrictions are available and easy to define.

2) The numerical results were validated through comparisons with experimental data. Numerical results demonstrated the usefulness of the developed simulation tool as an aid to design OWSCs.

3) An original experimental investigation on hydrodynamics of an OWSC with hydraulic PTO system was carried out under both unidirectional regular and irregular waves. Hydrodynamic characteristics are presented and analyzed. Linear and non-linear analyses of the OWSC were performed. Flow field in the vicinity of OWSC was measured and analyzed.

4) A comprehensive experimental data was provided.

5) A new approach for predicting the CWR based on the RAO and non-linear output frequency response functions was presented. This approach allows to include the effects of the higher-order frequency components in the estimation of CWR.

6) A mathematical model to describe the dynamic behaviors of the hydraulic PTO system was presented. This model allows to implement and predict accurately the effects of the hydraulic PTO system.

7) Analysis of the influence of the PTO system, flap inertia and cross-section configurations was provided.

10.3 Future Work

This research work has left several unresolved numerical and experimental issues that is identified for future work.

In this work, the hydrodynamics of the OWSC were characterized under unidirectional waves. Therefore, it may be important to determine the effect of the directional waves on the hydrodynamics of the OWSCs. Furthermore, the OWSC model was designed to represent quasi-2D test. Further investigation is needed to analyze the blockage effect of the flap on the CWR. Other effects may also be necessary to study in detail, such as the influence of drift and heave forces and the overtopping, since the flap freeboard has shown some influences on the CWR. An optimal flap freeboard must be found which maximizes CWR while allowing the shedding of load in the more powerful sea states, since the literature is scarce in this subject.

This work was also performed for a single OWSC. However, it should be obvious that OWSC will not be installed as a single device. It is envisaged that the device will be installed as an array of OWSCs to take advantage of economies of scale and produce power. Studies are important to be done to determine the separating distances between flaps and the connections between them.

As this work has shown that the hydraulic PTO system has a large effect on the hydrodynamics of the OWSC, and thus on the CWR, further studies should reveal the optimal damping characteristics. Further studies are required to explore control strategies, such as phase control should be implemented.

The high loads on the flap, foundations and PTO system pose significant design challenges. Perhaps the biggest problem relates to the fatigue of parts as the loads are cycled. The loading tests will form a key part of the future development of the OWSC.

OWSCs cannot be optimized on hydrodynamics alone. Structure, secondary power conversion and transmission, installation and finally maintenance must be considered to develop cost-effective reliable OWSCs. The next step in the development of the OWSC will have to focus on economic viability studies. Those studies would determine the costs of the device, its components and maintenance operations. The optimization model can be updated in order to account for these costs in the design of the OWSC.

More work is needed to investigate the effects of the sand in the water and its deposition around the OWSC. Although the sea bed can be composed of rock there are large loose boulders scattered about the sea bed which may migrate towards and interfere with the OWSC. The effect that the OWSC may have on the sea bed, or vice versa, may become a research topic of its own, forming part of an environmental impact study. There are further effects which have not been studied in this work which include the effects of currents and windage on the flap.

Both numerical and experimental tests were carried out for closely controlled conditions. The assessment of the OWSC survivability under extreme sea states will be other subjects of future work. This will include the simulation of the dynamic instability of the OWSC.

Bibliography

Adami, S., Hu, X. and Adams, N. (2012), 'A generalized wall boundary condition for smoothed particle hydrodynamics', *Journal of Computational Physics* **231**(21), 7057–7075.

Alonso, R., Solari, S. and Teixeira, L. (2015), 'Wave energy resource assessment in Uruguay', *Energy* **93**, 683–696.

Altomare, C., Crespo, A. J., Domínguez, J. M., Gómez-Gesteira, M., Suzuki, T. and Verwaest, T. (2015), 'Applicability of smoothed particle hydrodynamics for estimation of sea wave impact on coastal structures', *Coastal Engineering* **96**, 1–12.

Altomare, C., Crespo, A., Rogers, B., Dominguez, J., Gironella, X. and Gómez-Gesteira, M. (2014), 'Numerical modelling of armour block sea breakwater with smoothed particle hydrodynamics', *Computers & Structures* **130**, 34–45.

Altomare, C., Domínguez, J., Crespo, A., González-Cao, J., Suzuki, T., Gómez-Gesteira, M. and Troch, P. (2017), 'Long-crested wave generation and absorption for SPH-based DualSPHysics model', *Coastal Engineering* **127**, 37–54.

Andersen, T. L. and Frigaard, P. (2014), *Wave Generation in Physical Models: Technical documentation for AwaSys 6*, Department of Civil Engineering, Aalborg University, Denmark.

Andersson, S., Söderberg, A. and Björklund, S. (2007), 'Friction models for sliding dry, boundary and mixed lubricated contacts', *Tribology International* **40**(4), 580–587.

Anitescu, M. (2006), 'Optimization-based simulation of nonsmooth rigid multibody dynamics', *Mathematical Programming* **105**(1), 113–143.

Anitescu, M. and Hart, G. D. (2004), 'A constraint-stabilized time-stepping approach for rigid multibody dynamics with joints, contact and friction', *International Journal for Numerical Methods in Engineering* **60**(14), 2335–2371.

Antuono, M., Colagrossi, A. and Marrone, S. (2012), ‘Numerical diffusive terms in weakly-compressible SPH schemes’, *Computer Physics Communications* **183**(12), 2570–2580.

Antuono, M., Colagrossi, A., Marrone, S. and Molteni, D. (2010), ‘Free-surface flows solved by means of SPH schemes with numerical diffusive terms’, *Computer Physics Communications* **181**(3), 532–549.

Armstrong-Hélouvry, B., Dupont, P. and Wit, C. C. D. (1994), ‘A survey of models, analysis tools and compensation methods for the control of machines with friction’, *Automatica* **30**(7), 1083–1138.

Babarit, A., Duclos, G. and Clément, A. (2004), ‘Comparison of latching control strategies for a heaving wave energy device in random sea’, *Applied Ocean Research* **26**(5), 227–238.

Babarit, A., Guglielmi, M. and Clément, A. H. (2009), ‘Declutching control of a wave energy converter’, *Ocean Engineering* **36**(12-13), 1015–1024.

Babarit, A., Hals, J., Muliawan, M., Kurniawan, A., Moan, T. and Krokstad, J. (2012), ‘Numerical benchmarking study of a selection of wave energy converters’, *Renewable Energy* **41**, 44–63.

Bhinder, M. A., Babarit, A., Gentaz, L. and Ferrant, P. (2012), Effect of viscous forces on the performance of a surging wave energy converter, *in* ‘The Twenty-second International Offshore and Polar Engineering Conference, Rhodes, Greece’.

Bouscasse, B., Colagrossi, A., Marrone, S. and Antuono, M. (2013), ‘Nonlinear water wave interaction with floating bodies in SPH’, *Journal of Fluids and Structures* **42**, 112–129.

Brito, M., Teixeira, L., Canelas, R. B., Ferreira, R. M. L. and Neves, M. G. (2017), ‘Experimental and numerical studies of dynamic behaviors of a hydraulic power take-off cylinder using spectral representation method’, *Journal of Tribology* **140**(2), 021102.

Canelas, R. B., Crespo, A. J., Domínguez, J. M., Ferreira, R. M. and Gómez-Gesteira, M. (2016), ‘SPH–DCDEM model for arbitrary geometries in free surface solid–fluid flows’, *Computer Physics Communications* **202**, 131–140.

Canelas, R. B., Domínguez, J. M., Crespo, A. J., Gómez-Gesteira, M. and Ferreira, R. M. (2015), ‘A smooth particle hydrodynamics discretization for the modelling of free surface flows and rigid body dynamics’, *International Journal for Numerical Methods in Fluids* **78**(9), 581–593.

Canelas, R., Brito, M., Feal, O., Domínguez, J. and Crespo, A. (2018), ‘Extending DualSPHysics with a differential variational inequality: modeling fluid-mechanism interaction’, *Applied Ocean Research* **76**, 88–97.

Cargo, C. (2012), Design and Control of Hydraulic Power Take-Offs for Wave Energy Converters, PhD thesis, University of Bath.

Caska, A. and Finnigan, T. (2008), ‘Hydrodynamic characteristics of a cylindrical bottom-pivoted wave energy absorber’, *Ocean Engineering* **35**(1), 6–16.

Child, B. and Venugopal, V. (2010), ‘Optimal configurations of wave energy device arrays’, *Ocean Engineering* **37**(16), 1402–1417.

Colagrossi, A., Antuono, M. and Touzé, D. L. (2009), ‘Theoretical considerations on the free-surface role in the smoothed-particle-hydrodynamics model’, *Physical Review E* **79**(5).

Colagrossi, A. and Landrini, M. (2003), ‘Numerical simulation of interfacial flows by smoothed particle hydrodynamics’, *Journal of Computational Physics* **191**(2), 448–475.

Count, B. M. and Evans, D. V. (1984), ‘The influence of projecting sidewalls on the hydrodynamic performance of wave-energy devices’, *Journal of Fluid Mechanics* **145**(1), 361–376.

Crespo, A., Altomare, C., Domínguez, J., González-Cao, J. and Gómez-Gesteira, M. (2017), ‘Towards simulating floating offshore oscillating water column converters with smoothed particle hydrodynamics’, *Coastal Engineering* **126**, 11–26.

Crespo, A., Domínguez, J., Rogers, B., Gómez-Gesteira, M., Longshaw, S., Canelas, R., Vacondio, R., Barreiro, A. and García-Feal, O. (2015), ‘DualSPHysics: Open-source parallel CFD solver based on smoothed particle hydrodynamics (SPH)’, *Computer Physics Communications* **187**, 204–216.

Crespo, A. J. C., Gómez-Gesteira, M. and Dalrymple, R. A. (2007), ‘Boundary Conditions Generated by Dynamic Particles in SPH Methods’, *Computers, Materials, & Continua* **5**(3), 173–184.

Crespo, A. J., Gómez-Gesteira, M. and Dalrymple, R. A. (2008), ‘Modeling dam break behavior over a wet bed by a SPH technique’, *Journal of Waterway, Port, Coastal, and Ocean Engineering* **134**(6), 313–320.

Dalrymple, R. A. and Knio, O. (2001), SPH modelling of water waves, *in* ‘Coastal Dynamics’, Vol. 01, American Society of Civil Engineers.

Dalrymple, R. and Rogers, B. (2006), ‘Numerical modeling of water waves with the SPH method’, *Coastal Engineering* **53**(2), 141–147. Coastal Hydrodynamics and Morphodynamics.

Day, A., Babarit, A., Fontaine, A., He, Y.-P., Kraskowski, M., Murai, M., Penesis, I., Salvatore, F. and Shin, H.-K. (2015), ‘Hydrodynamic modelling of marine renewable energy devices: A state of the art review’, *Ocean Engineering* **108**, 46–69.

de Wit, C. C., Olsson, H., Astrom, K. and Lischinsky, P. (1995), ‘A new model for control of systems with friction’, *IEEE Transactions on Automatic Control* **40**(3), 419–425.

Dean, R. and Dalrymple, R. (1991), *Water Wave Mechanics for Enginners and Scientists*, Vol. 2, Advanced Series on Ocean Engineering.

Dias, F., Renzi, E., Gallagher, S., Sarkar, D., Wei, Y., Abadie, T., Cummins, C. and Rafiee, A. (2017), ‘Analytical and computational modelling for wave energy systems: the example of oscillating wave surge converters’, *Acta Mechanica Sinica* **33**(4), 647–662.

Dimas, A. A. and Galani, K. A. (2016), ‘Turbulent flow induced by regular and irregular waves above a steep rock-armored slope’, *Journal of Waterway, Port, Coastal, and Ocean Engineering* **142**(5), 04016004.

Do, N. B., Ferri, A. A. and Bauchau, O. A. (2007), ‘Efficient simulation of a dynamic system with LuGre friction’, *Journal of Computational and Nonlinear Dynamics* **2**(4), 281–289.

Domínguez, J. M., Crespo, A. J. C., Cercós-Pita, J. L., Fourtakas, G. and Neves, B. (2015), Evaluation of reliability and efficiency of different boundary conditions in an SPH code, *in* ‘10th SPHERIC International Workshop, Parma, Italy’.

Domínguez, J. M., Crespo, A. J. and Gómez-Gesteira, M. (2013), ‘Optimization strategies for CPU and GPU implementations of a smoothed particle hydrodynamics method’, *Computer Physics Communications* **184**(3), 617–627.

Evans, D. and Porter, R. (1996), ‘Hydrodynamic characteristics of a thin rolling plate in finite depth of water’, *Applied Ocean Research* **18**(4), 215–228.

Falcão, A. F. (2007), ‘Modelling and control of oscillating-body wave energy converters with hydraulic power take-off and gas accumulator’, *Ocean Engineering* **34**(14-15), 2021–2032.

Falcão, A. F. (2008), ‘Phase control through load control of oscillating-body wave energy converters with hydraulic PTO system’, *Ocean Engineering* **35**(3-4), 358–366.

Falcão, A. F. (2010), 'Wave energy utilization: A review of the technologies', *Renewable and Sustainable Energy Reviews* **14**(3), 899–918.

Falnes, J. (2002), *Ocean Waves and Oscillating Systems: Linear Interactions Including Wave-Energy Extraction*, Cambridge University Press, Pitt Building, Trumpington Street, Cambridge, United Kingdom.

Flocard, F. and Finnigan, T. (2012), 'Increasing power capture of a wave energy device by inertia adjustment', *Applied Ocean Research* **34**, 126–134.

Folley, M. and Whittaker, T. (2009), 'The control of wave energy converters using active bipolar damping', *Proceedings of the Institution of Mechanical Engineers, Part M: Journal of Engineering for the Maritime Environment* **223**(4), 479–487.

Folley, M., Whittaker, T. and Henry, A. (2007), 'The effect of water depth on the performance of a small surging wave energy converter', *Ocean Engineering* **34**(8-9), 1265–1274.

Folley, M., Whittaker, T. and Osterried, M. (2004), The oscillating wave surge converter, *in* 'The Fourteenth International Offshore and Polar Engineering Conference, Toulon, France', International Society of Offshore and Polar Engineers.

Gingold, R. A. and Monaghan, J. J. (1977), 'Smoothed particle hydrodynamics: theory and application to non-spherical stars', *Monthly Notices of the Royal Astronomical Society* **181**(3), 375–389.

Gomes, R., Lopes, M., Henriques, J., Gato, L. and Falcão, A. (2015), 'The dynamics and power extraction of bottom-hinged plate wave energy converters in regular and irregular waves', *Ocean Engineering* **96**, 86–99.

Gómez-Gesteira, M., Cerqueiro, D., Crespo, C. and Dalrymple, R. (2005), 'Green water overtopping analyzed with a SPH model', *Ocean Engineering* **32**(2), 223–238.

Gómez-Gesteira, M. and Dalrymple, R. A. (2004), 'Using a three-dimensional smoothed particle hydrodynamics method for wave impact on a tall structure', *Journal of Waterway, Port, Coastal, and Ocean Engineering* **130**(2), 63–69.

Gómez-Gesteira, M., Rogers, B. D., Dalrymple, R. A. and Crespo, A. J. (2010), 'State-of-the-art of classical SPH for free-surface flows', *Journal of Hydraulic Research* **48**(1), 6–27.

Henry, A. (2009), The hydrodynamics of small seabed mounted bottom hinged wave energy converters in shallow water, PhD thesis, Queen's University Belfast.

Henry, A., Kimmoun, O., Nicholson, J., Dupont, G., Wei, Y. and Dias, F. (2014a), A two dimensional experimental investigation of slamming of an oscillating wave surge converter, *in* 'The Twenty-fourth International Ocean and Polar Engineering Conference, Busan, Korea'.

Henry, A., Rafiee, A., Schmitt, P., Dias, F. and Whittaker, T. (2013), A two dimensional experimental investigation of slamming of an oscillating wave surge converter, *in* 'The Twenty-third International Offshore and Polar Engineering Conference, Anchorage, Alaska, USA'.

Henry, A., Rafiee, A., Schmitt, P., Dias, F. and Whittaker, T. (2014b), 'The characteristics of wave impacts on an oscillating wave surge converter', *Journal of Ocean and Wind Energy* **1**, 101–110.

Hu, B. and Schiehlen, W. (1997), 'On the simulation of stochastic processes by spectral representation', *Probabilistic Engineering Mechanics* **12**(2), 105–113.

Hughes, S. (1993), *Physical Models and Laboratory Techniques in Coastal Engineering*, Advanced series on ocean engineering, World Scientific.

Ismaila, T., Akmeliawati, R. and Salami, M. J. E. (2011), Artificial intelligent based friction modelling and compensation in motion control system, *in* 'Advances in Mechatronics', InTech.

Kamizuru, Y. and Murrenho, H. (2011), Improved control strategy for hydrostatic transmissions in wave power plants, *in* 'Proceedings of the Twelth Scandinavian International Conference on Fluid Power, Tampere, Finland'.

Korde, U. (1999), 'Efficient primary energy conversion in irregular waves', *Ocean Engineering* **26**(7), 625–651.

Lang, Z. Q. and Billings, S. A. (2005), 'Energy transfer properties of non-linear systems in the frequency domain', *International Journal of Control* **78**(5), 345–362.

Leimkuhler, B. J., Reich, S. and Skeel, R. D. (1996), *Integration Methods for Molecular Dynamics*, Springer New York, New York, NY, pp. 161–185.

Lemmin, U. and Rolland, T. (1997), 'Acoustic velocity profiler for laboratory and field studies', *Journal of Hydraulic Engineering* **123**(12), 1089–1098.

Lin, C. C., Chen, J. H., Chow, Y. C., Tzang, S. Y., Hou, S. J. and Wang, F. Y. (2012), The experimental investigation of the influencing parameters of flap type wave energy converters, *in* '4th International Conference on Ocean Energy, Dublin'.

Lind, S., Xu, R., Stansby, P. and Rogers, B. (2012), 'Incompressible smoothed particle hydrodynamics for free-surface flows: A generalised diffusion-based algorithm for stability and validations for impulsive flows and propagating waves', *Journal of Computational Physics* **231**(4), 1499–1523.

Liu, G. R. and Liu, M. B. (2003), *Smoothed Particle Hydrodynamics*, World Scientific.

Lucas, J., Livingstone, M., Vuorinen, N. and Cruz, J. (2012), Development of a wave energy converter (WEC) design tool - application to the waveroller wec including validation of numerical estimates, *in* 'Fourth International Conference on Ocean Energy, Dublin, Ireland'.

Lucy, L. B. (1977), 'A numerical approach to the testing of the fission hypothesis', *The Astronomical Journal* **82**, 1013.

Mansard, E. and Funke, E. (1980), The measurement of incident and reflected spectra using a least squares method, *in* 'Coastal Engineering', American Society of Civil Engineers (ASCE).

Marongiu, J.-C., Leboeuf, F., Caro, J. and Parkinson, E. (2010), 'Free surface flows simulations in pelton turbines using an hybrid SPH-ALE method', *Journal of Hydraulic Research* **48**(sup1), 40–49.

Marrone, S., Antuono, M., Colagrossi, A., Colicchio, G., Touzé, D. L. and Graziani, G. (2011), 'δ-SPH model for simulating violent impact flows', *Computer Methods in Applied Mechanics and Engineering* **200**(13-16), 1526–1542.

Martínez-Ferrer, P. J., Qian, L., Causon, D. M., Mingham, C. G. and Ma, Z. (2018), 'Numerical simulation of wave slamming on a flap-type oscillating wave energy device', *International Journal of Offshore and Polar Engineering* **28**(1), 65–71.

Mazhar, H., Heyn, T., Negrut, D. and Tasora, A. (2015), 'Using nesterov's method to accelerate multibody dynamics with friction and contact', *ACM Trans. Graph.* **34**(3), 32:1–32:14.

Mazhar, H., Heyn, T., Pazouki, A., Melanz, D., Seidl, A., Bartholomew, A., Tasora, A. and Negrut, D. (2013), 'CHRONO: a parallel multi-physics library for rigid-body, flexible-body, and fluid dynamics', *Mechanical Sciences* **4**(1), 49–64.

Mei, C., Stiassnie, M. and Yue, D. (2005), *Theory and applications of ocean surface waves*, World Scientific.

Met-Flow (2002), *UVP Monitor User's Guide*, Met-Flow S.A., Chemin Auguste-Pidou 8, 1007 Lausanne, Switzerland.

Molteni, D. and Colagrossi, A. (2009), ‘A simple procedure to improve the pressure evaluation in hydrodynamic context using the SPH’, *Computer Physics Communications* **180**(6), 861–872.

Monaghan, J. (1994), ‘Simulating free surface flows with SPH’, *Journal of Computational Physics* **110**(2), 399–406.

Monaghan, J. (2012), ‘Smoothed particle hydrodynamics and its diverse applications’, *Annual Review of Fluid Mechanics* **44**(1), 323–346.

Monaghan, J. J. (1992), ‘Smoothed particle hydrodynamics’, *Annual Review of Astronomy and Astrophysics* **30**(1), 543–574.

Monaghan, J. J. (2005), ‘Smoothed particle hydrodynamics’, *Reports on Progress in Physics* **68**(8), 1703–1759.

Monaghan, J. J. and Kos, A. (1999), ‘Solitary waves on a cretan beach’, *Journal of Waterway, Port, Coastal, and Ocean Engineering* **125**(3), 145–155.

Monaghan, J. J., Kos, A. and Issa, N. (2003), ‘Fluid motion generated by impact’, *Journal of Waterway, Port, Coastal, and Ocean Engineering* **129**(6), 250–259.

Monaghan, J. J. and Lattanzio, J. C. (1985), ‘A refined particle method for astrophysical problems’, *Astronomy and Astrophysics* **149**, 135–143.

Monin, A. S. and Yaglom, A. M. (1971), *Statistical Fluid Mechanics: Mechanics of Turbulence.*, Vol. 1, MIT Press, Boston, USA.

Newman, J. (1977), *Marine Hydrodynamics*, MIT Press. Cambridge, Massachussetts.

Ning, D., Liu, C., Zhang, C., Göteman, M., Zhao, H. and Teng, B. (2017), ‘Hydrodynamic performance of an oscillating wave surge converter in regular and irregular waves: an experimental study’, *Journal of Marine Science and Technology* **25**(5), 520–530.

Olsson, H., Åström, K., de Wit, C. C., Gäfvert, M. and Lischinsky, P. (1998), ‘Friction models and friction compensation’, *European Journal of Control* **4**(3), 176–195.

Parsons, N. F. and Martin, P. A. (1992), ‘Scattering of water waves by submerged plates using hypersingular integral equations’, *Applied Ocean Research* **14**(5), 313–321.

Parsons, N. F. and Martin, P. A. (1994), ‘Scattering of water waves by submerged curved plates and by surface-piercing flat plates’, *Applied Ocean Research* **16**(3), 129–139.

Parsons, N. F. and Martin, P. A. (1995), 'Trapping of water waves by submerged plates using hypersingular integral equations', *Journal of Fluid Mechanics* **284**(1), 359.

Patir, N. and Cheng, H. S. (1978), 'An average flow model for determining effects of three-dimensional roughness on partial hydrodynamic lubrication', *Journal of Lubrication Technology* **100**(1), 12.

Pedocchi, F. and García, M. H. (2012), 'Acoustic measurement of suspended sediment concentration profiles in an oscillatory boundary layer', *Continental Shelf Research* **46**, 87–95.

Qian, L., MIingham, C., Causon, D., Ingram, D., Folley, M. and Whittaker, T. (2005), 'Numerical simulation of wave power devices using a two-fluid free surface solver', *Modern Physics Letters B* **19**(28-29), 1479–1482.

Renzi, E. and Dias, F. (2012), 'Resonant behaviour of an oscillating wave energy converter in a channel', *Journal of Fluid Mechanics* **701**, 482–510.

Renzi, E. and Dias, F. (2013*a*), 'Hydrodynamics of the oscillating wave surge converter in the open ocean', *European Journal of Mechanics - B/Fluids* **41**, 1–10.

Renzi, E. and Dias, F. (2013*b*), 'Relations for a periodic array of flap-type wave energy converters', *Applied Ocean Research* **39**, 31–39.

Salter, S. H., Taylor, J. R. M. and Caldwell, N. J. (2002), 'Power conversion mechanisms for wave energy', *Proceedings of the Institution of Mechanical Engineers, Part M: Journal of Engineering for the Maritime Environment* **216**(1), 1–27.

Santo, H., Taylor, P. H., Moreno, E. C., Stansby, P., Taylor, R. E., Sun, L. and Zang, J. (2017), 'Extreme motion and response statistics for survival of the three-float wave energy converter M4 in intermediate water depth', *Journal of Fluid Mechanics* **813**, 175–204.

Sarmento, A. J. N. A. (1992), 'Wave flume experiments on two-dimensional oscillating water column wave energy devices', *Experiments in Fluids* **12**(4-5), 286–292.

Schmitt, P., Asmuth, H. and Elsäßer, B. (2016), 'Optimising power take-off of an oscillating wave surge converter using high fidelity numerical simulations', *International Journal of Marine Energy* **16**, 196–208.

Schmitt, P., Bourdier, S., Sarkar, D., Renzi, E., Dias, F., Doherty, K., Whittaker, T. and van't Hoff, J. (2012), Hydrodynamic loading on a bottom hinged oscillating wave surge converter, *in* 'Twenty-second International Offshore and Polar Engineering Conference, Rhodes, Greece'.

Schmitt, P. and Elsaesser, B. (2015), ‘On the use of OpenFOAM to model oscillating wave surge converters’, *Ocean Engineering* **108**, 98–104.

Shabana, A. A. (2005), *Dynamics of Multibody Systems*, Cambridge University Press.

Sheng, W., Alcorn, R. and Lewis, T. (2014), ‘Physical modelling of wave energy converters’, *Ocean Engineering* **84**, 29–36.

Shinozuka, M. and Deodatis, G. (1991), ‘Simulation of stochastic processes by spectral representation’, *Applied Mechanics Reviews* **44**(4), 191.

Singh, S. K., Debnath, K. and Mazumder, B. S. (2016), ‘Turbulence statistics of wave-current flow over a submerged cube’, *Journal of Waterway, Port, Coastal, and Ocean Engineering* **142**(3), 04015027.

Stewart, D. E. (2000), ‘Rigid-body dynamics with friction and impact’, *SIAM Review* **42**(1), 3–39.

Stribeck, R. (1902), ‘Die wesentlichen eigenschaften der gleitund rollenlager – the key qualities of sliding and roller bearings’, *Zeitschrift des Vereines Deutscher Ingenieure* **46**(38,39), 1342–1348, 1432–1437.

Swevers, J., Al-Bender, F., Ganseman, C. and Projogo, T. (2000), ‘An integrated friction model structure with improved presliding behavior for accurate friction compensation’, *IEEE Transactions on Automatic Control* **45**(4), 675–686.

Tasora, A. and Anitescu, M. (2011), ‘A matrix-free cone complementarity approach for solving large-scale, nonsmooth, rigid body dynamics’, *Computer Methods in Applied Mechanics and Engineering* **200**(5-8), 439–453.

Tasora, A., Serban, R., Mazhar, H., Pazouki, A., Melanz, D., Fleischmann, J., Taylor, M., Sugiyama, H. and Negrut, D. (2016), Chrono: An open source multi-physics dynamics engine, *in* ‘Lecture Notes in Computer Science’, Springer International Publishing, pp. 19–49.

Ting, F. C. (2001), ‘Laboratory study of wave and turbulence velocities in a broad-banded irregular wave surf zone’, *Coastal Engineering* **43**(3-4), 183–208.

Ting, F. C. and Kirby, J. T. (1994), ‘Observation of undertow and turbulence in a laboratory surf zone’, *Coastal Engineering* **24**(1-2), 51–80.

Tran, X. B., Hafizah, N. and Yanada, H. (2012), ‘Modeling of dynamic friction behaviors of hydraulic cylinders’, *Mechatronics* **22**(1), 65–75.

Tran, X. B. and Yanada, H. (2013), ‘Dynamic friction behaviors of pneumatic cylinders’, *ICA* **4**(02), 180–190.

Umeyama, M. (2009), ‘Changes in turbulent flow structure under combined wave-current motions’, *Journal of Waterway, Port, Coastal, and Ocean Engineering* **135**(5), 213–227.

van der A, D. A., O’Donoghue, T., Davies, A. G. and Ribberink, J. S. (2011), ‘Experimental study of the turbulent boundary layer in acceleration-skewed oscillatory flow’, *Journal of Fluid Mechanics* **684**, 251–283.

Verbrugghe, T., Domínguez, J. M., Crespo, A. J., Altomare, C., Stratigaki, V., Troch, P. and Kortenhaus, A. (2018), ‘Coupling methodology for smoothed particle hydrodynamics modelling of non-linear wave-structure interactions’, *Coastal Engineering* **138**, 184–198.

Verlet, L. (1967), ‘Computer "experiments" on classical fluids. I. Thermodynamical properties of Lennard-Jones Molecules’, *Physical Review* **159**(1), 98–103.

Walker, D., Taylor, P. and Taylor, R. E. (2004), ‘The shape of large surface waves on the open sea and the draupner new year wave’, *Applied Ocean Research* **26**(3-4), 73–83.

Wei, Y., Abadie, T. and Dias, F. (2017), ‘A cost-effective method for modelling wave-OWSC interaction’, *International Journal of Offshore and Polar Engineering* **27**(4), 366–373.

Wei, Y., Abadie, T., Henry, A. and Dias, F. (2016), ‘Wave interaction with an oscillating wave surge converter. Part II: Slamming’, *Ocean Engineering* **113**, 319–334.

Wei, Y., Rafiee, A., Henry, A. and Dias, F. (2015), ‘Wave interaction with an oscillating wave surge converter. Part I: Viscous effects’, *Ocean Engineering* **104**, 185–203.

Wendland, H. (1995), ‘Piecewise polynomial, positive definite and compactly supported radial functions of minimal degree’, *Advances in Computational Mathematics* **4**(1), 389–396.

Whittaker, T., Collier, D., Folley, M., Osterried, M., Henry, A. and Crowley, M. (2007), The development of Oyster – a shallow water surging wave energy converter, *in* ‘7th Annual European Wave & Tidal Energy Conference, Porto, Portugal’.

Whittaker, T. and Folley, M. (2012), ‘Nearshore oscillating wave surge converters and the development of oyster’, *Philosophical Transactions of the Royal Society A: Mathematical, Physical and Engineering Sciences* **370**(1959), 345–364.

Wiercigroch, M. and Cheng, A.-D. (1997), ‘Chaotic and stochastic dynamics of orthogonal metal cutting’, *Chaos, Solitons & Fractals* **8**(4), 715–726.

Wiercigroch, M., Sin, V. W. T. and Liew, Z. F. K. (1999), 'Non-reversible dry friction oscillator: Design and measurements', *Proceedings of the Institution of Mechanical Engineers, Part C: Journal of Mechanical Engineering Science* **213**(5), 527–534.

Wojewoda, J., Stefanski, A., Wiercigroch, M. and Kapitaniak, T. (2008), 'Hysteretic effects of dry friction: modelling and experimental studies', *Philosophical Transactions of the Royal Society A: Mathematical, Physical and Engineering Sciences* **366**(1866), 747–765.

Yanada, H. and Sekikawa, Y. (2008), 'Modeling of dynamic behaviors of friction', *Mechatronics* **18**(7), 330–339.

Yanada, H., Takahashi, K. and Matsui, A. (2009), 'Identification of dynamic parameters of modified LuGre model and application to hydraulic actuator', *Transactions of the Japan Fluid Power System Society* **40**(4), 57–64.

Yavuz, H., McCabe, A., Aggidis, G. and Widden, M. B. (2006), 'Calculation of the performance of resonant wave energy converters in real seas', *Proceedings of the Institution of Mechanical Engineers, Part M: Journal of Engineering for the Maritime Environment* **220**(3), 117–128.

Yavuz, H., Mıstıkoğlu, S. and Stallard, T. (2011), 'Processing irregular wave measurements to enhance point absorber power capture performance', *Ocean Engineering* **38**(4), 684–698.

Yeylaghi, S., Moa, B., Oshkai, P., Buckham, B. and Crawford, C. (2016), 'ISPH modelling of an oscillating wave surge converter using an OpenMP-based parallel approach', *Journal of Ocean Engineering and Marine Energy* **2**(3), 301–312.

Zhang, D., Shi, Y., Huang, C., Si, Y., Huang, B. and Li, W. (2018), 'SPH method with applications of oscillating wave surge converter', *Ocean Engineering* **152**, 273–285.

A

An example of XML file

Listing A.1: XML file.

```xml
<?xml version="1.0" encoding="UTF-8" ?>
<case app="GenCase4 v4.0.026 (22-04-2016)" date="09-05-2016 21:57:32">
<casedef>
<constantsdef>
<lattice bound="1" fluid="1" />
<gravity x="0" y="0" z="-9.81" comment="Gravitational acceleration" units_comment="m/s^2" />
<rhop0 value="1000" comment="Reference density of the fluid" units_comment="kg/m^3" />
<hswl value="0" auto="true" comment="Maximum still water level to calculate speedofsound using coefsound" units_comment="metres (m)" />
<gamma value="7" comment="Polytropic constant for water used in the state equation" />
<speedsystem value="0" auto="true" comment="Maximum system speed (by default the dam-break propagation is used)" />
<coefsound value="20" comment="Coefficient to multiply speedsystem" />
<speedsound value="0" auto="true" comment="Speed of sound to use in the simulation (by default speedofsound=coefsound*speedsystem)" />
<coefh value="1.5" comment="Coefficient to calculate the smoothing length (h=coefh*sqrt(3*dp^2) in 3D)" />
<cflnumber value="0.2" comment="Coefficient to multiply dt" />
</constantsdef>
<mkconfig boundcount="230" fluidcount="10">
<mkorientfluid mk="0" orient="Xyz" />
</mkconfig>
<geometry>
<definition dp="0.01" units_comment="metres (m)">
<pointmin x="-40" y="-1.0" z="-0.2" />
<pointmax x="40" y="1.0" z="2.2" />
</definition>
<commands>
<mainlist>
<setshapemode>real | dp | bound</setshapemode>
<setdrawmode mode="full" />
<setmkbound mk="1" />
<drawfilestl file="bed.stl" />
<setmkbound mk="10" />
<drawfilestl file="wavemaker.stl" />
<setmkbound mk="5" />
<drawfilestl file="flap.stl" />
<setmkfluid mk="0" />
<fillbox x="-2" y="0" z="0.5">
<modefill>void</modefill>
<point x="-34" y="-1" z="-0.1" />
<size x="60" y="2" z="0.85" />
</fillbox>
<setmkfluid mk="0" />
<fillbox x="2" y="0" z="0.5">
<modefill>void</modefill>
<point x="-6" y="-1" z="-0.1" />
<size x="60" y="2" z="0.85" />
</fillbox>
<setmkbound mk="5" />
<fillbox x="0" y="0" z="0.5">
<modefill>void</modefill>
<point x="-6" y="-1" z="-0.1" />
<size x="60" y="2" z="1.2" />
```

```
</fillbox>
<shapeout file="" reset="true" />
</mainlist>
</commands>
</geometry>
<floatings>
<floating mkbound="5" relativeweight="0.461">
<center x="0" y="0" z="0.33" />
<inertia x="27.6" y="14.8" z="13.1" />
</floating>
</floatings>
<motion>
<objreal ref="10">
<begin mov="1" start="0.00" finish="300" />
<mvfile id="1" duration="300">
<file name="Reg_H025_T20_movement.dat" fields="2" fieldtime="0" fieldx="1" />
</mvfile>
</objreal>
</motion>
</casedef>
<execution>
<special>
<chrono datadir=".">
<savedata value="0.001" comment="Saves CSV with data exchange for each time interval (0=all steps)" />
<bodyfloating idb="0" name="flap" mkbound="5">
<_objmodel value="flap.obj" />
</bodyfloating>
<link_hinge idbody1="0">
<rotpoint x="0.0" y="0.0" z="0.0" comment="Point for rotation" />
<rotvector x="0.0" y="1.0" z="0.0" comment="Vector direction for rotation" />
<stiffness value="150.0" comment="Torsional stiffness" />
<damping value="1000.0" comment="Torsional damping" />
</link_hinge>
<bodyfixed idb="10" name="domain" mkbound="1">
<_objmodel value="bed.obj" />
</bodyfixed>
</chrono>
</special>
<parameters>
<parameter key="PosDouble" value="1" comment="Precision in particle interaction 0:Simple, 1:Double, 2:Uses and saves double (default=0)" />
<parameter key="StepAlgorithm" value="2" comment="Step Algorithm 1:Verlet, 2:Symplectic (default=1)" />
<parameter key="VerletSteps" value="40" comment="Verlet only: Number of steps to apply Euler timestepping (default=40)" />
<parameter key="Kernel" value="2" comment="Interaction Kernel 1:Cubic Spline, 2:Wendland (default=2)" />
<parameter key="ViscoTreatment" value="1" comment="Viscosity formulation 1:Artificial, 2:Laminar+SPS (default=1)" />
<parameter key="Visco" value="0.01" comment="Viscosity value" />
<parameter key="ViscoBoundFactor" value="0" comment="Multiply viscosity value with boundary (default=1)" />
<parameter key="DeltaSPH" value="0.1" comment="DeltaSPH value, 0.1 is the typical value, with 0 disabled (default=0)" />
<parameter key="#Shifting" value="0" comment="Shifting mode 0:None, 1:Ignore bound, 2:Ignore fixed, 3:Full (default=0)" />
```

```
<parameter key="#ShiftCoef" value="-2" comment="Coefficient for shifting computation (default=-2)" />
<parameter key="#ShiftTFS" value="1.5" comment="Threshold to detect free surface. Typically 1.5 for 2D and 2.75 for 3D (default=0)" />
<parameter key="RigidAlgorithm" value="1" comment="Rigid Algorithm 1:SPH, 2:DEM (default=1)" />
<parameter key="FtPause" value="0.0" comment="Time to freeze the floatings at simulation start (warmup) (default=0)" units_comment="seconds" />
<parameter key="CoefDtMin" value="0.05" comment="Coefficient to calculate minimum time step dtmin=coefdtmin*h/speedsound (default=0.05)" />
<parameter key="#DtIni" value="0.0001" comment="Initial time step (default=h/speedsound)" units_comment="seconds" />
<parameter key="#DtMin" value="0.00001" comment="Minimum time step (default=coefdtmin*h/speedsound)" units_comment="seconds" />
<parameter key="#DtFixed" value="DtFixed.dat" comment="Dt values are loaded from file (default=disabled)" />
<parameter key="DtAllParticles" value="0" comment="Velocity of particles used to calculate DT. 1:All, 0:Only fluid/floating (default=0)" />
<parameter key="TimeMax" value="150" comment="Time of simulation" units_comment="seconds" />
<parameter key="TimeOut" value="0.04" comment="Time out data" units_comment="seconds" />
<parameter key="IncZ" value="0.0" comment="Increase of Z+" units_comment="decimal" />
<parameter key="PartsOutMax" value="1" comment="%/100 of fluid particles allowed to be excluded from domain (default=1)" units_comment="decimal" />
<parameter key="RhopOutMin" value="700" comment="Minimum rhop valid (default=700)" units_comment="kg/m^3" />
<parameter key="RhopOutMax" value="1300" comment="Maximum rhop valid (default=1300)" units_comment="kg/m^3" />
</parameters>
</execution>
</case>
```

B

Source codes for coupling between DualSPHysics and Project Chrono

Listing B.1: Types.h (line 84 to 95).

```
84  typedef struct{
85  word mkbound;      // MkBound of the floating object
86  unsigned begin;    // First particle of the floating object
87  unsigned count;    // Number of floating objects
88  float mass;        // Mass of the floating object
89  float massp;       // Mass of the particle of the floating object
90  float radius;      // Maximum distance between particles and center
91  tdouble3 center;   // Center of the floating object
92  tfloat3 fvel;      // Linear velocity of the floating object
93  tfloat3 fomega;    // Angular velocity of the floating object
94  bool usechrono;    // Activates the use of Project Chrono library
95  }StFloatingData;
```

Listing B.2: JChronoData.h (line 89 to 266).

```
89  // Manages the info of each body
90  class JChBody : public JChObject
91  {
92  public:
93  // Types of body
94  typedef enum{ BD_Floating,BD_External,BD_Fixed }TpBody;
95  static std::string TypeToStr(TpBody type);
96  private:
97  std::vector<JChLink*> LinkRefs;
98  protected:
99  double Mass;
100 tdouble3 Center;
101 tdouble3 Inertia;
102 std::string ObjModel;
103 tfloat3 InpuInertXX;
104 tfloat3 InpuInertXY;
105 // Manages the info of a floating body.
106 class JChBodyFloating : public JChBody
107 {
108 protected:
109 bool InputData;
110 tfloat3 InputFace;
111 tfloat3 InputFomegaAce;
112 tdouble3 OutputCenter;
113 tfloat3 OutputVel;
114 tfloat3 OutputOmega;
115 public:
116 const word MkBound;
117 JChBodyFloating(unsigned idb,std::string name,word mkbound);
118 JChBodyFloating(const JChBodyFloating &src);
119 void Reset();
120 void SetFloatingData(double mass,tdouble3 center,tdouble3 inertia);
121 void ResetInputData(){ InputData=false; }
122 void SetInputData(const tfloat3 &face,const tfloat3 &fomegaace){ InputData=true; InputFace=face; InputFomegaAce=fomegaace; }
123 void SetOutputData(const tdouble3 &center,const tfloat3 &vel,const tfloat3 &omega){ OutputCenter=center; OutputVel=vel; OutputOmega=omega; }
124 bool     GetInputData()      const{ return(InputData);      }
125 tfloat3  GetInputFace()      const{ return(InputFace);      }
126 tfloat3  GetInputFomegaAce()const{ return(InputFomegaAce); }
```

```
tdouble3 GetOutputCenter()  const{ return(OutputCenter);   }
tfloat3  GetOutputVel()     const{ return(OutputVel);      }
tfloat3  GetOutputOmega()   const{ return(OutputOmega);    }
};
// Manages the info of a fixed body.
class JChBodyFixed : public JChBody
{
protected:
bool InputData;
public:
const word MkBound;
JChBodyFixed(unsigned idb, std::string name, word mkbound);
JChBodyFixed(const JChBodyFixed &src);
void Reset();
void ResetInputData(){ InputData = false; }
bool     GetInputData()     const{ return(InputData); }
};
// Manages the info of a floating body
class JChBodyExternal : public JChBody
{
public:
JChBodyExternal(unsigned idb,std::string name,double mass,tdouble3 center, tdouble3 inertia);
JChBodyExternal(const JChBodyExternal &src);
};
// Manages the info of each link between bodies
class JChLink : public JChObject
{
public:
// Types of link
typedef enum{ LK_Hinge, LK_Spheric, LK_PointLine, LK_CustomSpring }TpLink;
static std::string TypeToStr(TpLink type);
private:
std::vector<JChBody*> BodyRefs;
tdouble3 RotPoint;  // Point for rotation
tdouble3 Pointfb0;  // Point from fb0
tdouble3 Pointfb1;  // Point from fb1
tdouble3 RotVector; // Vector for rotation
double Stiffness;   // Stiffness
double Damping;     // Damping
double RestLength; // Rest length for spring
protected:
void CopyFrom(const JChLink &src);
public:
const unsigned IdBody1;
const unsigned IdBody2;
const std::string Name;
const TpLink Type;
JChLink(std::string name,TpLink type,unsigned idbody1,unsigned idbody2);
virtual ~JChLink();
void Reset();
void ResetRefs(){ BodyRefs.clear(); }
void AddBodyRef(const JChBody* body);
unsigned GetBodyRefCount()const{ return(unsigned(BodyRefs.size())); };
const JChBody* GetBodyRef(unsigned ipos)const;
tdouble3 GetRotPoint() const{ return(RotPoint);  }
tdouble3 GetPointfb0() const{ return(Pointfb0); }
tdouble3 GetPointfb1() const{ return(Pointfb1); }
```

```
tdouble3 GetRotVector()const{ return(RotVector); }
double   GetStiffness()const{ return(Stiffness); }
double   GetDamping()   const{ return(Damping);   }
double   GetRestLength()   const{ return(RestLength); }
void SetRotPoint  (tdouble3 v){ RotPoint =v; }
void SetPointfb0  (tdouble3 v){ Pointfb0 =v; }
void SetPointfb1  (tdouble3 v){ Pointfb1 =v; }
void SetRotVector(tdouble3 v){ RotVector=v; }
void SetStiffness(double   v){ Stiffness=v; }
void SetDamping   (double   v){ Damping  =v; }
void SetRestLength(double  v){ RestLength = v; }
};
// Manages the info of a link
class JChLinkHinge : public JChLink
{
public:
JChLinkHinge(std::string name,unsigned idbody1,unsigned idbody2);
JChLinkHinge(const JChLinkHinge &src);
};
// Manages the info of a link
class JChLinkSpheric : public JChLink
{
public:
JChLinkSpheric(std::string name, unsigned idbody1, unsigned idbody2);
JChLinkSpheric(const JChLinkSpheric &src);
};
// Manages the info of a link
class JChLinkPointLine : public JChLink
{
public:
JChLinkPointLine(std::string name, unsigned idbody1, unsigned idbody2);
JChLinkPointLine(const JChLinkPointLine &src);
};
// Manages the info of a link
class JChLinkCustomSpring : public JChLink
{
public:
JChLinkCustomSpring(std::string name, unsigned idbody1, unsigned idbody2);
JChLinkCustomSpring(const JChLinkCustomSpring &src);
};
// Manages the info of Project Chrono from the input XML file
class JChronoData : protected JChBase
{
private:
std::string DataDir;
bool UseDVIChrono;
std::vector<JChBody*> LisBody;
std::vector<JChLink*> LisLink;
double Dp;
public:
JChronoData();
JChronoData(const JChronoData &src);
~JChronoData();
JChronoData& operator=(const JChronoData &src);
void Reset();
void Prepare();
void CheckData();
void SetDataDir(const std::string &datadir){ DataDir=datadir; }
```

```
std::string GetDataDir()const{ return(DataDir); }
void SetUseDVIChrono(bool usedvichrono){ UseDVIChrono=usedvichrono; }
bool GetUseDVIChrono()const{ return(UseDVIChrono); }
void SetDP(double dp){ Dp = dp; }
double GetDp()const{ return(Dp); }
JChBodyFloating* AddBodyFloating(unsigned idb,std::string name,word mkbound);
JChBodyFixed*    AddBodyFixed(unsigned idb, std::string name, word mkbound);
JChBodyExternal* AddBodyExternal(unsigned idb,std::string name,double mass, tdouble3 center,tdouble3 inertia);
JChLinkHinge*    AddLinkHinge(std::string name,unsigned idbody1,unsigned idbody2);
JChLinkSpheric*  AddLinkSpheric(std::string name, unsigned idbody1, unsigned idbody2);
JChLinkPointLine*  AddLinkPointLine(std::string name, unsigned idbody1, unsigned idbody2);
JChLinkCustomSpring*  AddLinkCustomSpring(std::string name, unsigned idbody1, unsigned idbody2);
unsigned GetBodyCount()const{ return(unsigned(LisBody.size())); }
unsigned GetLinkCount()const{ return(unsigned(LisLink.size())); }
unsigned BodyIndexById(unsigned idb)const;
unsigned BodyIndexByMkBound(word mkbound)const;
unsigned BodyIndexByMkBoundFixed(word mkbound)const;
unsigned BodyIndexByName(const std::string &name)const;
unsigned LinkIndexByName(const std::string &name)const;
const JChBody* GetBody(unsigned ipos)const;
const JChBody* GetBodybymk(word mkbound)const;
const JChLink* GetLink(unsigned ipos)const;
const JChBodyFixed* GetBodyFixed(word mkbound)const;
const JChBodyFloating* GetBodyFloating(word mkbound)const;
};
```

Listing B.3: JSph.cpp (line 543 to 563).

```
FtCount=parts.CountBlocks(PT_Floating);
if(FtCount){
AllocMemoryFloating(FtCount);
unsigned cobj=0;
for(unsigned c=0;c<parts.CountBlocks() && cobj<FtCount;c++){
const JSpacePartBlock && block=parts.GetBlock(c);
if(block.Type==PT_Floating){
const JSpacePartBlock_Floating &fblock=(const JSpacePartBlock_Floating &)block;
StFloatingData* fobj=FtObjs+cobj;
fobj->mkbound=fblock.GetMkType();
fobj->begin=fblock.GetBegin();
fobj->count=fblock.GetCount();
fobj->mass=(float)fblock.GetMassbody();
fobj->massp=fobj->mass/fobj->count;
fobj->radius=0;
fobj->center=fblock.GetCenter();
fobj->fvel=ToTFloat3(fblock.GetVelini());
fobj->fomega=ToTFloat3(fblock.GetOmegaini());
// Project Chrono configuration
fobj->usechrono=(ChronoObjects && ChronoObjects->ConfigBodyFloating(fblock.GetMkType(),fblock.GetMassbody(),fblock.GetCenter(),fblock.GetInertia()));
cobj++;}}}
```

Listing B.4: JSph.cpp (line 1205 to 1235).

```
const int ftcount = int(FtCount);
for (int cf = 0; cf<ftcount; cf++){
const StFloatingData fobj = FtObjs[cf];
const unsigned fpini = fobj.begin - CaseNpb;
const unsigned fpfin = fpini + fobj.count;
const tdouble3 fcenter = fobj.center;
const float fmassp = fobj.massp;
tmatrix3f inert = TMatrix3f(0, 0, 0, 0, 0, 0, 0, 0, 0);
// Calculate inertia
for (unsigned fp = fpini; fp<fpfin; fp++){
const unsigned p = ridp[fp];
if (p == UINT_MAX)RunException(met, "Floating particle was not found.");
tfloat3 dist = ToTFloat3(pos[p] - fcenter);
// Inertia tensor
inert.a11 += (float)(dist.y*dist.y + dist.z*dist.z)*fmassp;
inert.a12 += (float)-(dist.x*dist.y)*fmassp;
inert.a13 += (float)-(dist.x*dist.z)*fmassp;
inert.a21 += (float)-(dist.x*dist.y)*fmassp;
inert.a22 += (float)(dist.x*dist.x + dist.z*dist.z)*fmassp;
inert.a23 += (float)-(dist.y*dist.z)*fmassp;
inert.a31 += (float)-(dist.x*dist.z)*fmassp;
inert.a32 += (float)-(dist.y*dist.z)*fmassp;
inert.a33 += (float)(dist.x*dist.x + dist.y*dist.y)*fmassp;
}
// Export inertia tensor to Project Chrono
tfloat3 inertxx; tfloat3 inertxy;
inertxx.x = inert.a11; inertxx.y = inert.a22; inertxx.z = inert.a33;
inertxy.x = inert.a12; inertxy.y = inert.a23; inertxy.z = inert.a13;
if (FtObjs[cf].usechrono)ChronoObjects->SetFtInertia(FtObjs[cf].mkbound,
    inertxx, inertxy);
}
```

Listing B.5: DSPHChronoLib.h (line 5 to 43).

```
#include "JChronoData.h"
#include <string>
#define VNULL ChVector<double>(0., 0., 0.)

// Forward declarations to avoid including chrono classes
namespace chrono{
class ChSystem;
};

class DSPHChronoLib{
public:
// States of execution
typedef enum{ RSTATE_Init,RSTATE_Loading,RSTATE_Results }TpRunState;

const std::string version;
private:
// Chrono physical system
chrono::ChSystem *mphysicalSystem;
std::string dirOut;
JChronoData chData;
TpRunState RunState;
double currentframeforcesgrab = 0.0;
void ConfigLink(const JChLink* link);
public:
DSPHChronoLib();
~DSPHChronoLib();
// Initialize floating body
void Config(std::string dirout,const JChronoData &chdata);
// Initialize floating body
void Config_Inertia();
// Loads inertia tensor to Chrono
bool SetFtInertia(word mkbound, const tfloat3 &inertxx, const tfloat3 &inertxy);
// Loads data to calculate coupling with Chrono
bool SetFtData(word mkbound,const tfloat3 &face,const tfloat3 &fomegaace);
// Obtains data from coupling with Chrono
bool GetFtData(word mkbound,tdouble3 &fcenter,tfloat3 &fvel,tfloat3 &fomega) const;
// Compute a single timestep for each floating body
bool RunChrono(double timestep,double dt);
};
```

Listing B.6: JChronoObjects.h (line 14 to 60).

```
class JLog2;
class JXml;
class TiXmlElement;
class JChronoData;
class JChValues;
class JChBody;
class JChLink;
class DSPHChronoLib;

class JChronoObjects : protected JObject
{
protected:
JLog2 *Log;
std::string DirData;
const double Dp;
const word MkBoundFirst;
const bool UseDEMChrono;

JChronoData *ChronoData; // Chrono data loaded from XML
DSPHChronoLib *ChronoLib; // Object for integration with Project Chrono library

double SaveDataTime;  // Saves CSV with data exchange
double NextTime;
double LastTimeOk;
void LoadXml(JXml *sxml, const std::string &place);
void ReadXml(const JXml *sxml, TiXmlElement* lis);
void ReadXmlValues(const JXml *sxml,TiXmlElement* lis,JChValues* values);
void VisuValues(const JChValues *values)const;
void VisuBody(const JChBody *body)const;
void VisuLink(const JChLink *link)const;
void SaveVtkScheme()const;

public:
JChronoObjects(JLog2* log,const std::string &dirdata,JXml *sxml,const std::
    string &place,double dp,word mkboundfirst,bool usedemchrono);
~JChronoObjects();
void Reset();
bool ConfigBodyFloating(word mkbound,double mass,tdouble3 center,tdouble3
    inertia);
void ConfigBodyDEMFloating(word mkbound, float young, float poisson, float
    kfric, float restitu);
void ConfigBodyDEMFixed(word mkbound, float young, float poisson, float kfric,
    float restitu);
void Init();
void Init_Inertia();
void VisuConfig(std::string txhead, std::string txfoot)const;
void SetFtData(word mkbound,const tfloat3 &face,const tfloat3 &fomegaace);
void GetFtData(word mkbound,tdouble3 &fcenter,tfloat3 &fvel,tfloat3 &fomega)
    const;
void SetFtInertia(word mkbound, tfloat3 &inertxx, tfloat3 &inertxy);
void RunChrono(unsigned nstep,double timestep,double dt,bool predictor);
};
```

Listing B.7: JChronoObjects.cpp.

```
#include "JChronoObjects.h"
#include "DSPHChronoLib.h"
#include "JChronoData.h"
#include "Functions.h"
#include "FunctionsMath.h"
#include "JLog2.h"
#include "JXml.h"
#include "JSpaceParts.h"
#include "JSaveCsv.h"
#include "JShapeVtk.h"
#include <cstring>
#include <cfloat>
#include <climits>
#include <algorithm>
using namespace std;

JChronoObjects::JChronoObjects(JLog2* log,const std::string &dirdata,JXml *sxml
    ,const std::string &place,double dp,word mkboundfirst,bool usedemchrono)
:Log(log),DirData(dirdata),Dp(dp),MkBoundFirst(mkboundfirst),UseDEMChrono(
    usedemchrono)
{
ClassName="JChronoObjects";
ChronoData=NULL;
ChronoLib=NULL;
Reset();
LoadXml(sxml,place);
}
JChronoObjects::~JChronoObjects(){
Reset();
}
void JChronoObjects::Reset(){
delete ChronoData; ChronoData=NULL;
delete ChronoLib; ChronoLib=NULL;
SaveDataTime=NextTime=0;
LastTimeOk=-1;
}
```

```
bool JChronoObjects::ConfigBodyFloating(word mkbound,double mass,tdouble3 center,tdouble3 inertia){
JChBodyFloating* body=(JChBodyFloating*)ChronoData->GetBodyFloating(mkbound);
if(body)body->SetFloatingData(mass,center,inertia);
return(body!=NULL);
}
void JChronoObjects::ConfigBodyDEMFloating(word mkbound, float young, float poisson, float kfric, float restitu){
JChBodyFloating* body = (JChBodyFloating*)ChronoData->GetBodyFloating(mkbound);
if (body) body->SetDEMData(young, poisson, kfric, restitu);
}
void JChronoObjects::ConfigBodyDEMFixed(word mkbound, float young, float poisson, float kfric, float restitu){
JChBodyFixed* body = (JChBodyFixed*)ChronoData->GetBodyFixed(mkbound);
if (body) body->SetDEMData(young, poisson, kfric, restitu);
}
void JChronoObjects::LoadXml(JXml *sxml,const std::string &place){
TiXmlNode* node=sxml->GetNode(place,false);
if(!node)RunException("LoadXml",std::string("Cannot find the element \'")+place+"\'.");
ReadXml(sxml,node->ToElement());
}
void JChronoObjects::ReadXml(const JXml *sxml,TiXmlElement* lis){
const char met[]="ReadXml";
Reset();
ChronoData=new JChronoData;
// Loads directory for data files
string datadir=sxml->GetAttributeStr(lis,"datadir",true,"");
if(datadir==".")datadir="";
if(!datadir.empty())datadir=fun::GetDirWithSlash(datadir);
ChronoData->SetDataDir(datadir);
ChronoData->SetUseDVIChrono(UseDEMChrono);
ChronoData->SetDP(Dp);
// Loads configuration to save CSV file for debug
SaveDataTime=sxml->ReadElementFloat(lis,"savedata","value",true,-1.f);
// Loads elements floating body
TiXmlElement* ele=lis->FirstChildElement("bodyfloating");
while(ele){
unsigned idb=sxml->GetAttributeUnsigned(ele,"idb");
string name=sxml->GetAttributeStr(ele,"name",true,fun::PrintStr("Body_%04u",idb));
word mkbound=sxml->GetAttributeWord(ele,"mkbound");
JChBodyFloating *body=ChronoData->AddBodyFloating(idb,name,mkbound);
body->SetObjModel(sxml->ReadElementStr(ele,"objmodel","value",true));
ReadXmlValues(sxml,ele->FirstChildElement("values"),body->GetValuesPtr());
ele=ele->NextSiblingElement("bodyfloating");
}
// Loads elements bodyfixed
ele = lis->FirstChildElement("bodyfixed");
while (ele){
unsigned idb = sxml->GetAttributeUnsigned(ele, "idb");
string name = sxml->GetAttributeStr(ele, "name", true, fun::PrintStr("Body_%04u", idb));
word mkbound = sxml->GetAttributeWord(ele, "mkbound");
JChBodyFixed *body = ChronoData->AddBodyFixed(idb, name, mkbound);
body->SetObjModel(sxml->ReadElementStr(ele, "objmodel", "value", true));
ReadXmlValues(sxml, ele->FirstChildElement("values"), body->GetValuesPtr());
ele = ele->NextSiblingElement("bodyfixed");
```

```
}
// Loads elements bodyexternal
ele=lis->FirstChildElement("bodyexternal");
while(ele){
unsigned idb=sxml->GetAttributeUnsigned(ele,"idb");
string name=sxml->GetAttributeStr(ele,"name",true,fun::PrintStr("Body_%04u",idb));
double mass=sxml->ReadElementDouble(ele,"massbody","value");
tdouble3 center=sxml->ReadElementDouble3(ele,"center");
tdouble3 inertia=sxml->ReadElementDouble3(ele,"inertia");
JChBodyExternal *body=ChronoData->AddBodyExternal(idb,name,mass,center,inertia);
body->SetObjModel(sxml->ReadElementStr(ele,"objmodel","value",true));
ReadXmlValues(sxml,ele->FirstChildElement("values"),body->GetValuesPtr());
ele=ele->NextSiblingElement("bodyexternal");
}
// Loads elements link_hinge
ele=lis->FirstChildElement("link_hinge");
while(ele){
unsigned idbody1=sxml->GetAttributeUint(ele,"idbody1");
unsigned idbody2=(sxml->ExistsAttribute(ele,"idbody2")? sxml->GetAttributeUint(ele,"idbody2"): UINT_MAX);
string name=sxml->GetAttributeStr(ele,"name",true);
if(name.empty()){
if(idbody2!=UINT_MAX)name=fun::PrintStr("Link_body%04u_body%04u",idbody1,idbody2);
else name=fun::PrintStr("Link_body%04u",idbody1);
}
JChLinkHinge *link=ChronoData->AddLinkHinge(name,idbody1,idbody2);
link->SetRotPoint( sxml->ReadElementDouble3(ele,"rotpoint" ));
link->SetRotVector(sxml->ReadElementDouble3(ele,"rotvector"));
link->SetStiffness(sxml->ReadElementDouble (ele,"stiffness","value"));
link->SetDamping(   sxml->ReadElementDouble (ele,"damping"   ,"value"));
ReadXmlValues(sxml,ele->FirstChildElement("values"),link->GetValuesPtr());
ele=ele->NextSiblingElement("link_hinge");
}
//-Loads elements link_spheric.
ele = lis->FirstChildElement("link_spheric");
while (ele){
unsigned idbody1 = sxml->GetAttributeUint(ele, "idbody1");
unsigned idbody2 = (sxml->ExistsAttribute(ele, "idbody2") ? sxml->GetAttributeUint(ele, "idbody2") : UINT_MAX);
string name = sxml->GetAttributeStr(ele, "name", true);
if (name.empty()){
if (idbody2 != UINT_MAX)name = fun::PrintStr("Link_body%04u_body%04u", idbody1, idbody2);
else name = fun::PrintStr("Link_body%04u", idbody1);
}
JChLinkSpheric *link = ChronoData->AddLinkSpheric(name, idbody1, idbody2);
link->SetRotPoint(sxml->ReadElementDouble3(ele, "rotpoint"));
link->SetStiffness(sxml->ReadElementDouble(ele, "stiffness", "value"));
link->SetDamping(sxml->ReadElementDouble(ele, "damping", "value"));
ReadXmlValues(sxml, ele->FirstChildElement("values"), link->GetValuesPtr());
ele = ele->NextSiblingElement("link_spheric");
}
// Loads elements link_PointLine
ele = lis->FirstChildElement("link_pointline");
while (ele){
```

```
unsigned idbody1 = sxml->GetAttributeUint(ele, "idbody1");
unsigned idbody2 = (sxml->ExistsAttribute(ele, "idbody2") ? sxml->GetAttributeUint(ele, "idbody2") : UINT_MAX);
string name = sxml->GetAttributeStr(ele, "name", true);
if (name.empty()){
if (idbody2 != UINT_MAX)name = fun::PrintStr("Link_body%04u_body%04u", idbody1, idbody2);
else name = fun::PrintStr("Link_body%04u", idbody1);
}
JChLinkPointLine *link = ChronoData->AddLinkPointLine(name, idbody1, idbody2);
link->SetRotPoint(sxml->ReadElementDouble3(ele, "rotpoint"));
link->SetRotVector(sxml->ReadElementDouble3(ele, "rotvector"));
link->SetStiffness(sxml->ReadElementDouble(ele, "stiffness", "value"));
link->SetDamping(sxml->ReadElementDouble(ele, "damping", "value"));
ReadXmlValues(sxml, ele->FirstChildElement("values"), link->GetValuesPtr());
ele = ele->NextSiblingElement("link_pointline");
}
// Loads elements link_CustomSpring
ele = lis->FirstChildElement("link_customspring");
while (ele){
unsigned idbody1 = sxml->GetAttributeUint(ele, "idbody1");
unsigned idbody2 = (sxml->ExistsAttribute(ele, "idbody2") ? sxml->GetAttributeUint(ele, "idbody2") : UINT_MAX);
string name = sxml->GetAttributeStr(ele, "name", true);
if (name.empty()){
if (idbody2 != UINT_MAX)name = fun::PrintStr("Link_body%04u_body%04u", idbody1, idbody2);
else name = fun::PrintStr("Link_body%04u", idbody1);
}
JChLinkCustomSpring *link = ChronoData->AddLinkCustomSpring(name, idbody1, idbody2);
link->SetPointfb0(sxml->ReadElementDouble3(ele, "point_fb1"));
link->SetPointfb1(sxml->ReadElementDouble3(ele, "point_fb2"));
link->SetStiffness(sxml->ReadElementDouble(ele, "stiffness", "value"));
link->SetDamping(sxml->ReadElementDouble(ele, "damping", "value"));
link->SetRestLength(sxml->ReadElementDouble(ele, "rest_length", "value"));
ReadXmlValues(sxml, ele->FirstChildElement("values"), link->GetValuesPtr());
ele = ele->NextSiblingElement("link_customspring");
}
ChronoData->Prepare();
NextTime=(SaveDataTime>=0? 0: DBL_MAX);
LastTimeOk=-1;
}
void JChronoObjects::ReadXmlValues(const JXml *sxml,TiXmlElement* lis,JChValues* values){
const char met[]="ReadXmlValues";
if(lis){
// Loads elements floating body
TiXmlElement* ele=lis->FirstChildElement();
while(ele){
const string cmd=ele->Value();
if(cmd.length()&&cmd[0]!='_'){
const bool triple=(sxml->ExistsAttribute(ele,"x") && sxml->ExistsAttribute(ele,"y") && sxml->ExistsAttribute(ele,"z"));
if(cmd=="vstr")values->AddValueStr(sxml->GetAttributeStr(ele,"name"),sxml->GetAttributeStr(ele,"v"));
else if(cmd=="vint"){
const string name=sxml->GetAttributeStr(ele,"name");
if(triple)values->AddValueInt3(name,sxml->GetAttributeInt3(ele));
else      values->AddValueInt (name,sxml->GetAttributeInt (ele,"v"));
}
else if(cmd=="vuint"){
const string name=sxml->GetAttributeStr(ele,"name");
if(triple)values->AddValueUint3(name,sxml->GetAttributeUint3(ele));
else      values->AddValueUint (name,sxml->GetAttributeUint (ele,"v"));
}
else if(cmd=="vreal"){
const string name=sxml->GetAttributeStr(ele,"name");
if(triple)values->AddValueDouble3(name,sxml->GetAttributeDouble3(ele));
else      values->AddValueDouble (name,sxml->GetAttributeDouble (ele,"v"));
}
else sxml->ErrReadElement(ele,cmd,false);
}
ele=ele->NextSiblingElement();
}
}
}
void JChronoObjects::SaveVtkScheme()const{
JShapeVtk fvtk;
for(unsigned c=0;c<ChronoData->GetBodyCount();c++){
const JChBody* body=ChronoData->GetBody(c);
const word mk=(body->Type==JChBody::BD_Floating? MkBoundFirst+((const JChBodyFloating*)body)->MkBound: 0);
const tdouble3 center=body->GetCenter();
fvtk.AddSphere(center,Dp*2,16,mk);
for(unsigned cl=0;cl<body->GetLinkRefCount();cl++){
const JChLink *link=body->GetLinkRef(cl);
const tdouble3 rotpoint=link->GetRotPoint();
fvtk.AddLine(center,rotpoint,mk);
const tdouble3 rotvector=link->GetRotVector();
// Draw rotation axis
tdouble3 vec=fmath::VecUnitary(TDouble3(rotvector.y,rotvector.x,rotvector.z))*(Dp*3);
tdouble3 p1=rotpoint-vec;
tdouble3 p2=rotpoint+vec;
fvtk.AddLine(p1,p2,mk);
}
}
fvtk.SaveVtkData(Log->GetDirOut()+"ChronoScheme.vtk");
}
void JChronoObjects::Init(){
const char met[] = "Init";
// Checks data in ChronoData
ChronoData->CheckData();
// Creates VTK file with the scheme of Chrono objects
SaveVtkScheme();
// Creates and configures object ChronoLib
ChronoLib=new DSPHChronoLib();
ChronoLib->Config(Log->GetDirOut(),*ChronoData);
}
void JChronoObjects::Init_Inertia(){
ChronoLib->Config_Inertia();
}
void JChronoObjects::VisuValues(const JChValues *values)const{
if(values->GetCount()){
Log->Printf("    Values...: %u",values->GetCount());
```

```
int lenmax=0;
for(byte mode=0;mode<2;mode++){
for(unsigned c=0;c<values->GetCount();c++){
const JChValues::StValue* v=values->GetValue(c);
string vtx;
switch(v->type){
case JChValues::TP_Text:     vtx=v->vtext;                      break;
case JChValues::TP_Int:      vtx=fun::IntStr(v->vint);          break;
case JChValues::TP_Uint:     vtx=fun::UintStr(v->vuint);        break;
case JChValues::TP_Double:   vtx=fun::DoubleStr(v->vdouble);    break;
case JChValues::TP_Int3:     vtx=fun::Int3Str(v->vint3);        break;
case JChValues::TP_Uint3:    vtx=fun::Uint3Str(v->vuint3);      break;
case JChValues::TP_Double3:  vtx=fun::Double3Str(v->vdouble3);  break;
default: RunException("VisuValues","Type of value is invalid.");
}
if(mode==0){
int len=(int)fun::PrintStr("      %s <%s>",v->name.c_str(),JChValues::TypeToStr(v->type).c_str()).size();
lenmax=max(lenmax,len);
}
else{
string tx=fun::PrintStr("      %s <%s>",v->name.c_str(),JChValues::TypeToStr(v->type).c_str());
while(tx.size()<lenmax)tx=tx+".";
Log->Printf("%s: %s",tx.c_str(),vtx.c_str());
}
}
}
}
}
void JChronoObjects::VisuBody(const JChBody *body)const{
Log->Printf("  Body_%04u \"%s\" - type: %s", body->Idb, body->Name.c_str(), body->TypeToStr(body->Type).c_str());
if (body->Type == JChBody::BD_Floating){
Log->Printf("    MkBound..: %u", ((const JChBodyFloating *)body)->MkBound);
Log->Printf("    Mass.....: %g", body->GetMass());
Log->Printf("    Center...: (%s)", fun::Double3gStr(body->GetCenter()).c_str());
Log->Printf("    Inertia..: (%s)", fun::Double3gStr(body->GetInertia()).c_str());
}
if (body->Type == JChBody::BD_Fixed)
Log->Printf("    MkBound..: %u", ((const JChBodyFixed *)body)->MkBound);
if(!body->GetObjModel().empty())
Log->Printf("    ObjModel.: %s",body->GetObjModel().c_str());
VisuValues(body->GetValuesPtr());
if(body->GetLinkRefCount()){
Log->Printf("    Links....: %u",body->GetLinkRefCount());
for(unsigned c=0;c<body->GetLinkRefCount();c++){
Log->Printf("      %s",body->GetLinkRef(c)->Name.c_str());
}
}
}
void JChronoObjects::VisuLink(const JChLink *link)const{
Log->Printf("  Link \"%s\" - type: %s",link->Name.c_str(),link->TypeToStr(link->Type).c_str());
if (link->Type != 3)Log->Printf("    Rotation point......: (%s)", fun::Double3gStr(link->GetRotPoint()).c_str());
```

```
else {
Log->Printf("    Point Body 1........: (%s)", fun::Double3gStr(link->GetPointfb0()).c_str());
Log->Printf("    Point Body 2........: (%s)", fun::Double3gStr(link->GetPointfb1()).c_str());
}
if (link->Type == 0 || link->Type == 2)Log->Printf("    Rotation axis......: (%s)", fun::Double3gStr(link->GetRotVector()).c_str()); //only for links with axis - need to add as more are added
Log->Printf("    Stiffness.......: %g",link->GetStiffness());
Log->Printf("    Damping.........: %g",link->GetDamping());
if (link->Type == 3)Log->Printf("    Rest length.........: %g", link->GetRestLength());
VisuValues(link->GetValuesPtr());
if(link->GetBodyRefCount()){
Log->Printf("    Bodies...: %u",link->GetBodyRefCount());
for(unsigned c=0;c<link->GetBodyRefCount();c++){
Log->Printf("      Body_%04u %s",link->GetBodyRef(c)->Idb,link->GetBodyRef(c)->Name.c_str());
}
}
}
void JChronoObjects::VisuConfig(std::string txhead, std::string txfoot)const{
if(!txhead.empty())Log->Print(txhead);
Log->Printf("  DSPHChrono version: %s",ChronoLib->version.c_str());
Log->Printf("  Data directory.....: [%s]",ChronoData->GetDataDir().c_str());
Log->Printf("  Bodies.............: %d",ChronoData->GetBodyCount());
Log->Printf("  Links..............: %u",ChronoData->GetLinkCount());
for(unsigned c=0;c<ChronoData->GetBodyCount();c++)VisuBody(ChronoData->GetBody(c));
for(unsigned c=0;c<ChronoData->GetLinkCount();c++)VisuLink(ChronoData->GetLink(c));
if(!txfoot.empty())Log->Print(txfoot);
if(0){//Debug.
JChronoData chdata=*ChronoData;
Log->Print("\n*** Copia ***");
Log->Printf("  Bodies.............: %d",chdata.GetBodyCount());
Log->Printf("  Links..............: %u",chdata.GetLinkCount());
for(unsigned c=0;c<chdata.GetBodyCount();c++)VisuBody(chdata.GetBody(c));
for(unsigned c=0;c<chdata.GetLinkCount();c++)VisuLink(chdata.GetLink(c));
ChronoData->Reset();
Log->Print("\n*** Copia2 ***");
Log->Printf("  Bodies.............: %d",chdata.GetBodyCount());
Log->Printf("  Links..............: %u",chdata.GetLinkCount());
for(unsigned c=0;c<chdata.GetBodyCount();c++)VisuBody(chdata.GetBody(c));
for(unsigned c=0;c<chdata.GetLinkCount();c++)VisuLink(chdata.GetLink(c));
}
}
void JChronoObjects::SetFtData(word mkbound,const tfloat3 &face,const tfloat3 &fomegaace){
if(!ChronoLib->SetFtData(mkbound,face,fomegaace))RunException("SetFtData","Error running Chrono library.");
}
void JChronoObjects::GetFtData(word mkbound,tdouble3 &fcenter,tfloat3 &fvel,tfloat3 &fomega)const{
if(!ChronoLib->GetFtData(mkbound,fcenter,fvel,fomega))RunException("GetFtData","Error running Chrono library.");
}
```

```
void JChronoObjects::SetFtInertia(word mkbound, tfloat3 &inertxx, tfloat3 &inertxy){
if (!ChronoLib->SetFtInertia(mkbound, inertxx, inertxy))RunException("SetFtInertia", "Error running Chrono library.");
}
void JChronoObjects::RunChrono(unsigned nstep,double timestep,double dt,bool predictor){
if(!ChronoLib->RunChrono(timestep,dt))RunException("RunChrono","Error running Chrono library.");
// Saves floating body data in CSV files
if((LastTimeOk==timestep || NextTime<=timestep) && (SaveDataTime==0 || !predictor)){
for(unsigned cb=0;cb<ChronoData->GetBodyCount();cb++)if(ChronoData->GetBody(cb)->Type==JChBody::BD_Floating){
const JChBodyFloating *body=(JChBodyFloating*)ChronoData->GetBody(cb);
JSaveCsv sv(Log->GetDirOut()+fun::PrintStr("ChronoExchange_mkbound_%u.csv",body->MkBound),true);
sv.AddHead("nstep;time;dt;predictor;face.x;face.y;face.z;fomegaace.x;fomegaace.y;fomegaace.z;fvel.x;fvel.y;fvel.z;fcenter.x;fcenter.y;fcenter.z;fomega.x;fomega.y;fomega.z");
sv.AddValue(nstep);
sv.AddValue(timestep);
sv.AddValue(dt);
sv.AddValue(predictor? "True": "False");
sv.AddValue(body->GetInputFace());
sv.AddValue(body->GetInputFomegaAce());
sv.AddValue(body->GetOutputVel());
sv.AddValue(body->GetOutputCenter());
sv.AddValue(body->GetOutputOmega());
sv.AddEndl();
sv.SaveData();
// Recalculates NextTime.
if(LastTimeOk!=timestep){
if(SaveDataTime>0)while(NextTime<=timestep)NextTime+=SaveDataTime;
LastTimeOk=timestep;
}
}
}
}
```

Listing B.8: JSphCpuSingle.cpp (line 773 to 834).

```
void JSphCpuSingle::RunFloating(double dt,bool predictor){
const char met[]="RunFloating";
if(TimeStep>=FtPause){// This is used because if FtPause=0 in symplectic-predictor, code would not enter clause
TmcStart(Timers,TMC_SuFloating);
// Calculate forces around floating objects
FtCalcForces(FtoForces);
// Calculate data to update floatings
FtCalcForcesRes(dt,FtoForces,FtoForcesRes);

// Run floating with Project Chrono
if(ChronoObjects){
// Export data
for(unsigned cf=0;cf<FtCount;cf++)if(FtObjs[cf].usechrono)ChronoObjects->SetFtData(FtObjs[cf].mkbound,FtoForces[cf].face,FtoForces[cf].fomegaace);
// Calculate data using Chrono
ChronoObjects->RunChrono(Nstep,TimeStep,dt,predictor);
// Load calculated data by Chrono
for(unsigned cf=0;cf<FtCount;cf++)if(FtObjs[cf].usechrono)ChronoObjects->
    GetFtData(FtObjs[cf].mkbound,FtoForcesRes[cf].fcenterres,FtoForcesRes[cf].
    fvelres,FtoForcesRes[cf].fomegares);
}

// Apply movement around floating objects
const int ftcount=int(FtCount);
#ifdef _WITHOMP
#pragma omp parallel for schedule (guided)
#endif
for(int cf=0;cf<ftcount;cf++){
// Get Floating object values
const StFloatingData fobj=FtObjs[cf];
const tfloat3 fomega=FtoForcesRes[cf].fomegares;
const tfloat3 fvel=FtoForcesRes[cf].fvelres;
const tdouble3 fcenter=FtoForcesRes[cf].fcenterres;
//-Updates floating particles.
const float fradius=fobj.radius;
const unsigned fpini=fobj.begin-CaseNpb;
const unsigned fpfin=fpini+fobj.count;
for(unsigned fp=fpini;fp<fpfin;fp++){
const int p=FtRidp[fp];
if(p!=UINT_MAX){
tfloat4 *velrhop=Velrhopc+p;

// Compute and record position displacement
const double dx=dt*double(velrhop->x);
const double dy=dt*double(velrhop->y);
const double dz=dt*double(velrhop->z);
UpdatePos(Posc[p],dx,dy,dz,false,p,Posc,Dcellc,Codec);
// Compute and record new velocity
tfloat3 dist=(PeriActive? FtPeriodicDist(Posc[p],fcenter,fradius): ToTFloat3(
    Posc[p]-fcenter));
velrhop->x=fvel.x+(fomega.y*dist.z-fomega.z*dist.y);
velrhop->y=fvel.y+(fomega.z*dist.x-fomega.x*dist.z);
velrhop->z=fvel.z+(fomega.x*dist.y-fomega.y*dist.x);
}
}

// Stores floating data
if(!predictor){
FtObjs[cf].center=(PeriActive? UpdatePeriodicPos(fcenter): fcenter);
FtObjs[cf].fvel=fvel;
FtObjs[cf].fomega=fomega;
}
}
TmcStop(Timers,TMC_SuFloating);
}
}
```

Listing B.9: JSphGpuSingle.cpp (line 550 to 587).

```
void JSphGpuSingle::RunFloating(double dt,bool predictor){
const char met[]="RunFloating";
if(TimeStep>=FtPause){// Used because if FtPause is zero we don't enter the predictor
TmgStart(Timers,TMG_SuFloating);

// Calculate forces around floating objects
cusph::FtCalcForces(PeriActive != 0, FtCount, Gravity, FtoDatag, FtoMasspg, FtoCenterg, FtRidpg, Posxyg, Poszg, Aceg, FtoForcesg);

// Calculate data to update floatings
cusph::FtCalcForcesRes(FtCount,Simulate2D,dt,FtoOmegag,FtoVelg,FtoCenterg,FtoForcesg,FtoForcesResg,FtoCenterResg);

// Run floating with Project Chrono library
if(ChronoObjects){

// Export data
cudaMemcpy(FtoAuxForces,FtoForcesg,sizeof(tfloat3)*FtCount*2,cudaMemcpyDeviceToHost);

for(unsigned cf=0;cf<FtCount;cf++)if(FtObjs[cf].usechrono)ChronoObjects->SetFtData(FtObjs[cf].mkbound,FtoAuxForces[cf*2],FtoAuxForces[cf*2+1]);

// Calculate data using Chrono
ChronoObjects->RunChrono(Nstep,TimeStep,dt,predictor);

// Load calculated data by Chrono
cudaMemcpy(FtoAuxCenter,FtoCenterResg,sizeof(tdouble3)*FtCount    ,cudaMemcpyDeviceToHost);
cudaMemcpy(FtoAuxForces,FtoForcesResg,sizeof(tfloat3)  *FtCount*2,cudaMemcpyDeviceToHost);

for(unsigned cf=0;cf<FtCount;cf++)if(FtObjs[cf].usechrono)ChronoObjects->GetFtData(FtObjs[cf].mkbound,FtoAuxCenter[cf],FtoAuxForces[cf*2+1],FtoAuxForces[cf*2]);

cudaMemcpy(FtoCenterResg,FtoAuxCenter,sizeof(tdouble3)*FtCount    ,cudaMemcpyHostToDevice);

cudaMemcpy(FtoForcesResg,FtoAuxForces,sizeof(float3)  *FtCount*2,cudaMemcpyHostToDevice);
}

// Apply movement on floating objects
cusph::FtUpdate(PeriActive!=0,predictor,FtCount,dt,FtoDatag,FtoForcesResg,FtoCenterResg,FtRidpg,FtoCenterg,FtoVelg,FtoOmegag,Posxyg,Poszg,Dcellg,Velrhopg,Codeg);
TmgStop(Timers,TMG_SuFloating);
}
}
```

C

Source code for the implementation and configuration of the mechanical systems

Listing C.1: DSPHChronoLib.cpp.

```cpp
#include "DSPHChronoLib.h"
#include "CustomSpring.h"
#include "chrono/physics/ChSystemNSC.h"
#include "chrono/physics/ChBodyEasy.h"
#include "chrono/physics/ChParticlesClones.h"
#include "chrono/assets/ChTexture.h"
#include "chrono/assets/ChTriangleMeshShape.h"
#include "chrono/geometry/ChTriangleMeshConnected.h"
#include "chrono/physics/ChMaterialSurface.h"
//#include "chrono/physics/ChMaterialSurfaceDEM.h"
//#include "chrono/physics/ChSystemDEM.h"
//#include "chrono/physics/ChContactContainerDEM.h"
//#include "chrono/solver/ChSolverDEM.h"
#include "chrono_fea/ChElementBeamANCF.h"
#include "chrono_fea/ChBuilderBeam.h"
#include "chrono_fea/ChMesh.h"
#include "chrono_fea/ChVisualizationFEAmesh.h"
#include "chrono_fea/ChLinkPointFrame.h"
#include "chrono_fea/ChLinkDirFrame.h"

#include "chrono/core/ChFileutils.h"
#include <string>
#include <fstream>

//Use the namespace of Chrono.
using namespace chrono;
using namespace chrono::fea;
using namespace std;

DSPHChronoLib::DSPHChronoLib():version("v0.15"){
//-Set path to Chrono data directory.
SetChronoDataPath(CHRONO_DATA_DIR);

//-Create a Chrono physical system.
mphysicalSystem = new ChSystemNSC();
mphysicalSystem->Set_G_acc(ChVector<>(0, 0, 0));
//mphysicalSystem->SetTimestepperType(ChTimestepper::Type::HHT);
mphysicalSystem->SetTimestepperType(ChTimestepper::Type::EULER_IMPLICIT_LINEARIZED);
mphysicalSystem->SetSolverType(ChSolver::Type::APGD);
mphysicalSystem->SetMaxItersSolverSpeed(100);
mphysicalSystem->SetMaxItersSolverStab(100);
mphysicalSystem->SetMaxPenetrationRecoverySpeed(0.1);
mphysicalSystem->SetMinBounceSpeed(0.05);
mphysicalSystem->SetSolverWarmStarting(true);
mphysicalSystem->SetTolForce(1e-7);
}

DSPHChronoLib::~DSPHChronoLib(){
delete(mphysicalSystem);
}

const double timeskip = 0.01; //-placeholder for forces aquisisition rate, must come from DSPH

// Loads data for bodies and configures objects.
void DSPHChronoLib::Config(std::string dirout, const JChronoData &chdata){
```

```
const bool DG = false;
dirOut = dirout;
chData = chdata;

collision::ChCollisionModel::SetDefaultSuggestedEnvelope(chData.GetDp());
collision::ChCollisionModel::SetDefaultSuggestedMargin(chData.GetDp());

for (unsigned cb = 0; cb<chData.GetBodyCount(); cb++){
const JChBody* body = chData.GetBody(cb);
if (body->Type == JChBody::BD_Floating){
const double mass = body->GetMass();
const tdouble3 center = body->GetCenter(); //not used as it is read from a .obj
     mesh
ChVector<> COG(center.x, center.y, center.z);
const tfloat3 inertiaxx = body->GetInputInertXX(); //also computed from the
    mesh, but we want it to be coherent with DSPH inertia computation
const tfloat3 inertiaxy = body->GetInputInertXY();
string objname = dirOut + body->GetObjModel();
auto RigBody = std::make_shared< ChBodyEasyMesh >(objname.c_str(), 1000, false,
     chData.GetUseDVIChrono(), chData.GetDp()/2.0);
//if mesh is not read, it still creates a body object
mphysicalSystem->Add(RigBody);  //Added to chrono scene
ChMatrix33<> global_csys(1); //-global coord system
RigBody->SetFrame_COG_to_REF(ChFrame<>(COG, global_csys)); //-seting the COG
    according to DSPH, not by mesh baricenter
if (chData.GetUseDVIChrono()){ //Need to attribute collision parameters
//Might be important to define object families to disregard contacts between
    mechanism parts for example
//Need to define material properties
RigBody->GetMaterialSurfaceNSC()->SetRestitution(body->GetRestitu());
RigBody->GetMaterialSurfaceNSC()->SetFriction(body->GetKfric());
}
RigBody->SetMass(mass);
RigBody->SetInertiaXX(ChVector<>(inertiaxx.x, inertiaxx.y, inertiaxx.z));
RigBody->SetInertiaXY(ChVector<>(inertiaxy.x, inertiaxy.y, inertiaxy.z));
RigBody->SetNameString(body->Name);
RigBody->SetBodyFixed(false);
}
else if (body->Type == JChBody::BD_Fixed){ //Getting fixed boundaries
string objname = dirOut + body->GetObjModel();
auto RigBound = std::make_shared< ChBodyEasyMesh >(objname.c_str(), 1000, false
    , chData.GetUseDVIChrono(), chData.GetDp()/2.0);
//if mesh is not read, it still creates a body object
mphysicalSystem->Add(RigBound);  //Added to chrono scene
RigBound->SetNameString(body->Name);
RigBound->SetBodyFixed(true);
if (chData.GetUseDVIChrono()){ //Need to attribute collision parameters
//Might be important to define object families to disregard contacts between
    mechanism parts for example
//Need to define material properties
RigBound->GetMaterialSurfaceNSC()->SetFriction(body->GetKfric());
RigBound->GetMaterialSurfaceNSC()->SetRestitution(body->GetRestitu());
}
}
else throw "Type of body is invalid.";
} //all bodies are created in chrono

for (unsigned ck = 0; ck<chData.GetLinkCount(); ck++){
```

```
const JChLink* link = chData.GetLink(ck);
if (link->Type != JChLink::LK_Hinge && link->Type != JChLink::LK_Spheric && link->Type != JChLink::LK_PointLine && link->Type != JChLink::LK_CustomSpring)throw "Type of Link is invalid."; //different types must be created
if (DG)printf("++> link types are ok \n");
unsigned nb = link->GetBodyRefCount();
if (DG)printf("++> number of bodies is [%u] \n", nb);
if (nb == 0)throw "At least one body per link is necessary.";
const JChBody* body0 = link->GetBodyRef(0);
const JChBody* body1 = (nb > 1 ? link->GetBodyRef(1) : NULL);

//if (DG)printf("++> body.name:[%s] \n", body0->Name.c_str());
if (DG)printf("++> first body pointers are ok \n");

auto fb0 = mphysicalSystem->SearchBody(body0->Name.c_str());
auto fb1 = (nb > 1 ? mphysicalSystem->SearchBody(body1->Name.c_str()) : std::make_shared<ChBody>()); // - if it exists recover the body from the chrono system, if not create a new one to populate after

if (DG)printf("++> second body pointers are ok \n");

if (nb < 2){ //-Create a virtual hinge body, this is attached to a point in space
//ChVector<> COG_hinge(0, 0, 0); //surprisingly ok...
//fb1->SetPos(COG_hinge);
fb1->SetBodyFixed(true);
fb1->SetName("virtual_body");
mphysicalSystem->Add(fb1);
fb1->SetCollide(false);
if (DG)printf("++> virtual hinge is ok \n");
}
if (DG)printf("++> body.name:[%s] \n", fb0->GetNameString().c_str());
if (DG)printf("++> body.name:[%s] \n", fb1->GetNameString().c_str());

//- create the desired link
if (link->Type == JChLink::LK_Hinge){
if (DG)printf("++> hinge was well selected \n");
auto MyLink = std::make_shared<ChLinkLockRevolute>();
const tdouble3 rotpoint = link->GetRotPoint();
tdouble3 rotvector = link->GetRotVector();
const double rotvector_norm = sqrt(rotvector.x*rotvector.x + rotvector.y*rotvector.y + rotvector.z*rotvector.z); // rotation axis vector
rotvector.x = rotvector.x / rotvector_norm; rotvector.y = rotvector.y / rotvector_norm; rotvector.z = rotvector.z / rotvector_norm;
ChVector<> rev_point(rotpoint.x, rotpoint.y, rotpoint.z); // rotation point
//now we need to build a quaternion that rotates the default z axis to our desired axis
const double ang = acos(rotvector.z);// *180. / 3.14159265; //angle shortcut, since the default is always (0,0,1)
tdouble3 to_q;
to_q.x = rotvector.y; to_q.y = -rotvector.x; to_q.z = 0; //external product shortcut, this is the normal vector to the default z from chrono and our desired rotation vector
ChVector<> rotvec(to_q.x, to_q.y, to_q.z); // rotation vector
rotvec.Normalize();
if (DG)printf("++> link parameters are ok \n");
```

```
MyLink->Initialize(fb0, fb1, ChCoordsys<>(rev_point, Q_from_AngAxis(ang, rotvec)));
MyLink->SetNameString(link->Name);
if (DG)printf("++> link was initialized ok \n");
ChLinkForce *force = new ChLinkForce;
force->Set_active(true);
force->Set_K(link->GetStiffness()); // Torsional stiffness, to set, in [N*m/rad]
force->Set_R(link->GetDamping()); // Torsional damping, to set, in [N*m*s/rad]
MyLink->SetForce_R(force); //-Add a rotational spring damper to the revolute joint
if (DG)printf("++> force was initialized ok \n");
mphysicalSystem->AddLink(MyLink);
}
if (link->Type == JChLink::LK_Spheric){
auto MyLink = std::make_shared<ChLinkLockSpherical>();
const tdouble3 rotpoint = link->GetRotPoint();
ChVector<> rev_point(rotpoint.x, rotpoint.y, rotpoint.z); // rotation point
MyLink->Initialize(fb0, fb1, ChCoordsys<>(rev_point));
MyLink->SetNameString(link->Name);
ChLinkForce *force = new ChLinkForce;
force->Set_active(true);
force->Set_K(link->GetStiffness()); // Torsional stiffness, to set, in [N*m/rad]
force->Set_R(link->GetDamping()); // Torsional damping, to set, in [N*m*s/rad]
MyLink->SetForce_R(force); //-Add a rotational spring damper to the revolute joint
mphysicalSystem->AddLink(MyLink);
}
if (link->Type == JChLink::LK_PointLine){
auto MyLink = std::make_shared<ChLinkLockPointLine>(); //-this stupid thing has the xx axis as default, because of reasons.
const tdouble3 rotpoint = link->GetRotPoint();
tdouble3 rotvector = link->GetRotVector();
const double rotvector_norm = sqrt(rotvector.x*rotvector.x + rotvector.y*rotvector.y + rotvector.z*rotvector.z); // movement axis vector
rotvector.x = rotvector.x / rotvector_norm; rotvector.y = rotvector.y / rotvector_norm; rotvector.z = rotvector.z / rotvector_norm;
if (DG) printf("++> rotvector:[%f %f %f] \n", rotvector.x, rotvector.y, rotvector.z);
ChVector<> rev_point(rotpoint.x, rotpoint.y, rotpoint.z); // rotation point
//now we need to build a quaternion that rotates the default z axis to our desired axis
//const double ang = acos(rotvector.z);
const double ang = acos(rotvector.x);
tdouble3 to_q;
//to_q.x = rotvector.y; to_q.y = -rotvector.x; to_q.z = 0; //external product shortcut
to_q.x = 0; to_q.y = -rotvector.z; to_q.z = -rotvector.y; //external product shortcut
ChVector<> rotvec(to_q.x, to_q.y, to_q.z); // rotation vector
rotvec.Normalize();
if (DG) printf("++> rotvector:[%f %f %f], ang:[%f] \n", to_q.x, to_q.y, to_q.z, ang);
MyLink->Initialize(fb0, fb1, ChCoordsys<>(rev_point, Q_from_AngAxis(ang, rotvec)));
MyLink->SetNameString(link->Name);
ChLinkForce *force = new ChLinkForce;
```

```
force->Set_active(true);
force->Set_K(link->GetStiffness()); // Torsional stiffness, to set, in [N*m/rad]
force->Set_R(link->GetDamping()); // Torsional damping, to set, in [N*m*s/rad]
MyLink->SetForce_R(force); //-Add a rotational spring damper to the lock point joint
mphysicalSystem->AddLink(MyLink);
}

} //all links are created in chrono

if (chData.GetBodyCount()){ //-Creating a file for body reactions to be written on during the run
ChStreamOutAsciiFile mfileo("Body_forces.txt");
mfileo << "Time;  ";
ChSystem::IteratorBodies myiter = mphysicalSystem->IterBeginBodies();
while (myiter != mphysicalSystem->IterEndBodies()){
mfileo << "Body " << (*myiter)->GetName() << "_fx;  fy; fz; mx; my; mz; ";
++myiter;
}
mfileo << "\n";
}

if (chData.GetLinkCount()){ //-Creating a file for link reactions to be written on during the run
ChStreamOutAsciiFile mfileo("link_forces.txt");
mfileo << "Time;  ";
ChSystem::IteratorLinks myiter = mphysicalSystem->IterBeginLinks();
while (myiter != mphysicalSystem->IterEndLinks()){
mfileo << "Link " << (*myiter)->GetName() << "_fx;  fy; fz; mx; my; mz; ";
++myiter;
}
mfileo << "\n";
}
RunState = RSTATE_Init;
}

// Loads inertia for bodies
void DSPHChronoLib::Config_Inertia(){
for (unsigned cb = 0; cb<chData.GetBodyCount(); cb++){
const JChBody* body = chData.GetBody(cb);
if (body->Type == JChBody::BD_Floating){
//throw "Type of body is invalid."; //different types must be created (allow colision, meshes, etc)
const tfloat3 inertiaxx = body->GetInputInertXX();
const tfloat3 inertiaxy = body->GetInputInertXY();
auto fb = mphysicalSystem->SearchBody(body->Name.c_str());
fb->SetInertiaXX(ChVector<>(inertiaxx.x, inertiaxx.y, inertiaxx.z));
fb->SetInertiaXY(ChVector<>(inertiaxy.x, inertiaxy.y, inertiaxy.z));
}
} //all bodies are created in chrono
}

// Loads inertia tensor to Chrono
bool DSPHChronoLib::SetFtInertia(word mkbound, const tfloat3 &inertxx, const tfloat3 &inertxy)
{
JChBody *body = (JChBody*)chData.GetBodybymk(mkbound);
```

```
if (body)body->SetInputInertia(inertxx, inertxy);
return(body != NULL);
}


// Loads data to calculate coupling with Chrono
bool DSPHChronoLib::SetFtData(word mkbound,const tfloat3 &face,const tfloat3 &
    fomegaace)
{
if(RunState!=RSTATE_Loading){
for(unsigned cb=0;cb<chData.GetBodyCount();cb++)if(chData.GetBody(cb)->Type==
    JChBody::BD_Floating){
((JChBodyFloating *)chData.GetBody(cb))->ResetInputData();
}
RunState=RSTATE_Loading;
}
JChBodyFloating *body=(JChBodyFloating*)chData.GetBodyFloating(mkbound);
if(body)body->SetInputData(face,fomegaace);
return(body!=NULL);
}

// Obtains data from coupling with Chrono
bool DSPHChronoLib::GetFtData(word mkbound,tdouble3 &fcenter,tfloat3 &fvel,
    tfloat3 &fomega)const
{
const JChBodyFloating *body=(RunState==RSTATE_Results? chData.GetBodyFloating(
    mkbound): NULL);
if(body){
fcenter=body->GetOutputCenter();
fvel=body->GetOutputVel();
fomega=body->GetOutputOmega();
}
return(body!=NULL);
}

// Compute a given timestep for the full chrono physical system
bool DSPHChronoLib::RunChrono(double timestep,double dt)
{
bool err = false;
for (unsigned cb = 0; cb<chData.GetBodyCount() && !err; cb++)if (chData.GetBody
    (cb)->Type == JChBody::BD_Floating){
JChBodyFloating *body = (JChBodyFloating *)chData.GetBody(cb);
auto fb = mphysicalSystem->SearchBody(body->Name.c_str());

//-Do time step and position, velocity e angular velocity of the floating
    object
if (fb != NULL && body->GetInputData()){
//-Load input data.
const tfloat3 face = body->GetInputFace();
const tfloat3 fomegaace = body->GetInputFomegaAce();
//-Apply forces.
fb->Empty_forces_accumulators();
fb->Accumulate_force(fb->GetMass() * ChVector<>(face.x, face.y, face.z), fb->
    GetPos(), false);
//printf("++> face_body[%u]:[%f %f %f] \n", cb, face.x, face.y, face.z);
ChVector<> torque(fomegaace.x*fb->GetInertiaXX().x() + fomegaace.y*fb->
    GetInertiaXY().x() + fomegaace.z*fb->GetInertiaXY().z(), fomegaace.y*fb->
    GetInertiaXX().y() + fomegaace.x*fb->GetInertiaXY().x() + fomegaace.z*fb->
GetInertiaXY().y(), fomegaace.z*fb->GetInertiaXX().z() + fomegaace.x*fb->GetInertiaXY().z() + fomegaace.y*fb->GetInertiaXY().y());
fb->Accumulate_torque(torque, false);
}
else err = true;
}

// PERFORM SIMULATION UP TO chronoTime
mphysicalSystem->DoFrameDynamics(timestep);

// Writting data back to the bodies in DSPH
for (unsigned cb = 0; cb<chData.GetBodyCount() && !err; cb++)if (chData.GetBody(cb)->Type == JChBody::BD_Floating){
JChBodyFloating *body = (JChBodyFloating *)chData.GetBody(cb);
auto fb = mphysicalSystem->SearchBody(body->Name.c_str());
//-Obtains: center, fvel, fomega.
const tdouble3 center = TDouble3(fb->GetPos().x(), fb->GetPos().y(), fb->GetPos().z());
const tfloat3 fvel = TFloat3(float(fb->GetPos_dt().x()), float(fb->GetPos_dt().y()), float(fb->GetPos_dt().z()));
const tfloat3 fomega = TFloat3(float(fb->GetWvel_par().x()), float(fb->GetWvel_par().y()), float(fb->GetWvel_par().z()));
// Store output data
body->SetOutputData(center, fvel, fomega);
}

if (mphysicalSystem->GetChTime() >= currentframeforcesgrab){

// Writting body forces to file directly
if (chData.GetBodyCount()){
ChStreamOutAsciiFile mfileo("Body_forces.txt", std::ios::app);
mfileo << mphysicalSystem->GetChTime() << ";  ";
ChSystem::IteratorBodies myiter = mphysicalSystem->IterBeginBodies();
while (myiter != mphysicalSystem->IterEndBodies()){
mfileo << (*myiter)->Get_accumulated_force().x() << ";  " << (*myiter)->Get_accumulated_force().y() << "; " << (*myiter)->Get_accumulated_force().z() << "; " << (*myiter)->Get_accumulated_torque().x() << ";  " << (*myiter)->Get_accumulated_torque().y() << ";  " << (*myiter)->Get_accumulated_torque().z() << ";  ";
++myiter;
}
mfileo << "\n";
}

// Writting link forces to file directly
if (chData.GetLinkCount()){
ChStreamOutAsciiFile mfileo("link_forces.txt", std::ios::app);
mfileo << mphysicalSystem->GetChTime() << ";  ";
ChSystem::IteratorLinks myiter = mphysicalSystem->IterBeginLinks();
while (myiter != mphysicalSystem->IterEndLinks()){
mfileo << (*myiter)->Get_react_force().x() << ";  " << (*myiter)->Get_react_force().y() << "; " << (*myiter)->Get_react_force().z() << "; " << (*myiter)->Get_react_torque().x() << ";  " << (*myiter)->Get_react_torque().y() << ";  " << (*myiter)->Get_react_torque().z() << ";  ";
++myiter;
}
mfileo << "\n";
}
```

```
currentframeforcesgrab = currentframeforcesgrab + timeskip;
}

if(!err)RunState=RSTATE_Results;
return(!err);
}
```

D

Arduino code

Listing D.1: Arduino code used to measure the hydrodynamics of the OWSC.

```
//#define SERIAL_TX_BUFFER_SIZE 1023
//#define SERIAL_RX_BUFFER_SIZE 1023
#define SERIAL_BUFFER_SIZE 1023

#include <math.h>
#include <Wire.h>

long accelX, accelY, accelZ;
float gForceX, gForceY, gForceZ;

long gyroX, gyroY, gyroZ;
float rotX, rotY, rotZ;

float volt_p, volt_p_ref;
float dt, pressure;
float sensitivity = 0.33; // convert voltage to force g (for instance gravity: 9.81 m/s^2)
float z = 1.65;
unsigned long timer;
unsigned long timep = 0;
volatile long count = 0;
float rot = 0;
boolean A, B;
volatile byte state, statep, index;
volatile int QEM[16] = {0,-1,0,1,1,0,-1,0,0,1,0,-1,-1,0,1,0};

void setup(){
Serial.begin(9600);
Wire.begin();

setupMPU();
pinMode(2, INPUT); // Channel A
pinMode(3, INPUT); // Channel B
attachInterrupt(0,Achange,CHANGE);
attachInterrupt(1,Bchange,CHANGE);
timep = micros(); // set the initial time

// read the initial value of A and B
A = digitalRead(2); // white
B = digitalRead(3); // green

// set initial state value
if ((A==HIGH)&&(B==HIGH)) statep = 1;
if ((A==HIGH)&&(B==LOW)) statep = 2;
if ((A==LOW)&&(B==LOW)) statep = 3;
if ((A==LOW)&&(B==HIGH)) statep = 4;

}

void loop(){
// ------------------------------------------------------------------------
// data accelerometer
// ------------------------------------------------------------------------
recordAccelRegisters();
recordGyroRegisters();

// ------------------------------------------------------------------------
// data pressure sensor
// ----------------------------------------------------------------------
volt_p = analogRead(A0);
volt_p_ref = 311.37;  // set the origin to Zero-g voltage level
pressure = volt_p - volt_p_ref;
pressure = pressure/124.55; // scaled to bar
pressure = pressure*10.2*9.81*1000; // scaled to Pa

// ----------------------------------------------------------------------
// delay
// ----------------------------------------------------------------------
timer = micros();
dt=timer-timep; //calculate delta time in us
rot = 0.05*PI*count/2400; // 600 PPR, r = 0.05 m radius of the encoder

if (dt >= 10000)
{
// ----------------------------------------------------------------------
// write
// ----------------------------------------------------------------------
Serial.print(dt);Serial.print(", ");
Serial.print(gForceX,3);Serial.print(", ");
Serial.print(gForceY,3);Serial.print(", ");
Serial.print(gForceZ,3);Serial.print(", ");
Serial.print(rotX,3);Serial.print(", ");
Serial.print(rotY,3);Serial.print(", ");
Serial.print(rotZ,3);Serial.print(", ");
Serial.print(pressure,1);Serial.print(", ");
Serial.print(rot,5);
Serial.println();

timep=timer;

}

}

void Achange()
{
A = digitalRead(2);
B = digitalRead(3);
// determine state value
if ((A==HIGH)&&(B==HIGH)) state = 0;
if ((A==HIGH)&&(B==LOW)) state = 1;
if ((A==LOW)&&(B==LOW)) state = 2;
if ((A==LOW)&&(B==HIGH)) state = 3;
index = 4 * state + statep;
count = count + QEM[index];
statep = state;
}

void Bchange()
{
A = digitalRead(2);
B = digitalRead(3);
// determine state value
if ((A==HIGH)&&(B==HIGH)) state = 0;
if ((A==HIGH)&&(B==LOW)) state = 1;
if ((A==LOW)&&(B==LOW)) state = 2;
if ((A==LOW)&&(B==HIGH)) state = 3;
index = 4*state + statep;
count = count + QEM[index];
statep = state;
}

void setupMPU(){
Wire.beginTransmission(0b1101000); //This is the I2C address of the MPU (b1101000/b1101001 for AC0 low/high datasheet sec. 9.2)
Wire.write(0x6B); //Accessing the register 6B - Power Management (Sec. 4.28)
Wire.write(0b00000000); //Setting SLEEP register to 0. (Required; see Note on p. 9)
Wire.endTransmission();
Wire.beginTransmission(0b1101000); //I2C address of the MPU
Wire.write(0x1B); //Accessing the register 1B - Gyroscope Configuration (Sec. 4.4)
Wire.write(0x00000000); //Setting the gyro to full scale +/- 250deg./s
Wire.endTransmission();
Wire.beginTransmission(0b1101000); //I2C address of the MPU
Wire.write(0x1C); //Accessing the register 1C - Acccelerometer Configuration (Sec. 4.5)
Wire.write(0b00000000); //Setting the accel to +/- 2g
Wire.endTransmission();
}

void recordAccelRegisters() {
Wire.beginTransmission(0b1101000); //I2C address of the MPU
Wire.write(0x3B); //Starting register for Accel Readings
Wire.endTransmission();
Wire.requestFrom(0b1101000,6); //Request Accel Registers (3B - 40)
while(Wire.available() < 6);
accelX = Wire.read()<<8|Wire.read(); //Store first two bytes into accelX
accelY = Wire.read()<<8|Wire.read(); //Store middle two bytes into accelY
accelZ = Wire.read()<<8|Wire.read(); //Store last two bytes into accelZ
processAccelData();
}

void processAccelData(){
gForceX = accelX / 16384.0;
gForceY = accelY / 16384.0;
gForceZ = accelZ / 16384.0;
}

void recordGyroRegisters() {
Wire.beginTransmission(0b1101000); //I2C address of the MPU
Wire.write(0x43); //Starting register for Gyro Readings
Wire.endTransmission();
Wire.requestFrom(0b1101000,6); //Request Gyro Registers (43 - 48)
while(Wire.available() < 6);
gyroX = Wire.read()<<8|Wire.read(); //Store first two bytes into accelX
gyroY = Wire.read()<<8|Wire.read(); //Store middle two bytes into accelY
gyroZ = Wire.read()<<8|Wire.read(); //Store last two bytes into accelZ
processGyroData();
}

void processGyroData() {
rotX = gyroX / 131.0;
```

```
rotY = gyroY / 131.0;
rotZ = gyroZ / 131.0;
}
```

Listing D.2: Arduino code used to measure the dynamics of the hydraulic PTO system.

```
#include <math.h>

float volt_axx, volt_ayy, volt_azz, volt_f, volt_f_ref, volt_p, volt_p_ref;
float volt_ax, volt_ay, volt_az, dt, gx, gy, gz, force, pressure;
float sensitivity = 0.33; // convert voltage to force g (for instance gravity: 9.81 m/s^2)
float z = 1.65;
unsigned long timer;
unsigned long timep = 0;
volatile long count = 0;
float vel = 0;
boolean A, B;
volatile byte state, statep, index;
volatile int QEM[16] = {0,-1,0,1,1,0,-1,0,0,1,0,-1,-1,0,1,0};

void setup(){
Serial.begin(230400);
pinMode(2, INPUT); // Channel A
pinMode(3, INPUT); // Channel B
attachInterrupt(0,Achange,CHANGE);
attachInterrupt(1,Bchange,CHANGE);
timep = micros(); // set the initial time

// read the initial value of A and B
A = digitalRead(2);
B = digitalRead(3);

// set initial state value
if ((A==HIGH)&&(B==HIGH)) statep = 1;
if ((A==HIGH)&&(B==LOW)) statep = 2;
if ((A==LOW)&&(B==LOW)) statep = 3;
if ((A==LOW)&&(B==HIGH)) statep = 4;

}

void loop(){
// ---------------------------------------------------------------------
// data accelerometer
// ---------------------------------------------------------------------

// read accelerometer output
volt_ax=analogRead(A0);
volt_ay=analogRead(A1);
volt_az=analogRead(A2);

// arduino analog maps 0v-5v into 0-1023 (accelerometers work at 3.3 v)
float volt_axx=volt_ax*5/1023;
float volt_ayy=volt_ay*5/1023;
float volt_azz=volt_az*5/1023;

volt_axx-=z;
volt_ayy-=z;
volt_azz-=z;

// now we can apply the formula to our readings and get force (g)
gx = volt_axx*9.81/sensitivity; // scaled to m/s^2
gy = volt_ayy*9.81/sensitivity; // scaled to m/s^2
gz = volt_azz*9.81/sensitivity; // scaled to m/s^2

// -----------------------------------------------------------------------
// data load cell
// -----------------------------------------------------------------------
volt_f = analogRead(A3);
volt_f_ref = 346;  // set the origin to Zero-g voltage level
force = volt_f - volt_f_ref;
force = force/28; // scaled to kg

// -----------------------------------------------------------------------
// data pressure sensor
// -----------------------------------------------------------------------
volt_p = analogRead(A4);
volt_p_ref = 254;  // set the origin to Zero-g voltage level
pressure = volt_p - volt_p_ref;
pressure = pressure/312.42; // scaled to bar
pressure = pressure*10.2; // scaled to m.c.a.

// -----------------------------------------------------------------------
// delay
// -----------------------------------------------------------------------
timer = micros();
dt=timer-timep; //calculate delta time in us
vel = 0.05* (2*PI*count*1000000/(600*dt)); // 600 PPR, r = 0.05 m radius of the encoder

if (dt >= 1000)
{
// -----------------------------------------------------------------------
// write
// -----------------------------------------------------------------------
Serial.print(dt);Serial.print(" ,     ");
Serial.print(gx,4);Serial.print(" , ");
Serial.print(gy,4);Serial.print(" , ");
Serial.print(gz,4);Serial.print(" ,    ");
Serial.print(force,4);Serial.print(" ,    ");
Serial.print(pressure,6);Serial.print(" ,    ");
Serial.print(vel,6);Serial.print(" ,         ");
Serial.print(volt_ax);Serial.print(" , ");
Serial.print(volt_ay);Serial.print(" , ");
Serial.print(volt_az);Serial.print(" , ");
Serial.print(volt_f);Serial.print(" , ");
Serial.print(volt_p);Serial.print(" , ");
Serial.print(count);Serial.print(" , ");
Serial.println();

timep=timer;

}

}
```

```

void Achange()
{
A = digitalRead(2);
B = digitalRead(3);
// determine state value
if ((A==HIGH)&&(B==HIGH)) state = 0;
if ((A==HIGH)&&(B==LOW)) state = 1;
if ((A==LOW)&&(B==LOW)) state = 2;
if ((A==LOW)&&(B==HIGH)) state = 3;
index = 4 * state + statep;
count = count + QEM[index];
statep = state;
}

void Bchange()
{
A = digitalRead(2);
B = digitalRead(3);
// determine state value
if ((A==HIGH)&&(B==HIGH)) state = 0;
if ((A==HIGH)&&(B==LOW)) state = 1;
if ((A==LOW)&&(B==LOW)) state = 2;
if ((A==LOW)&&(B==HIGH)) state = 3;
index = 4*state + statep;
count = count + QEM[index];
statep = state;
}
```

E

Applications to the complex fluid-structure interaction

E.1 WaveStar

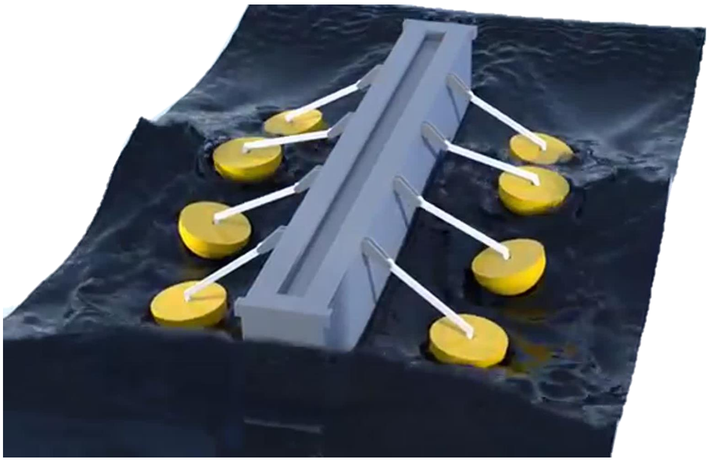

Figure E.1: WaveStar implemented (Canelas et al., 2018).

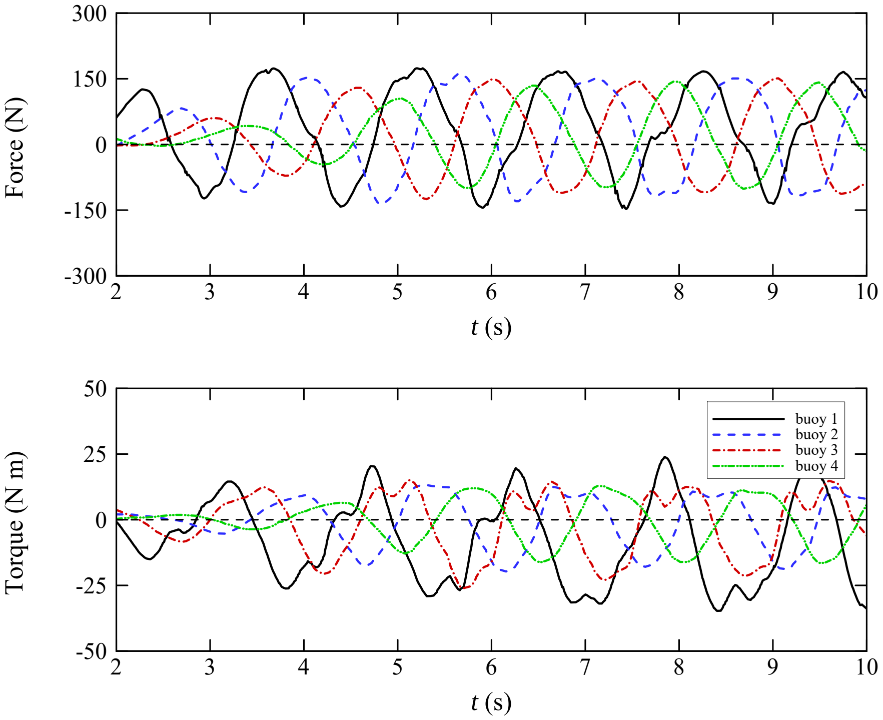

Figure E.2: Example of WaveStar buoy force and torque response.

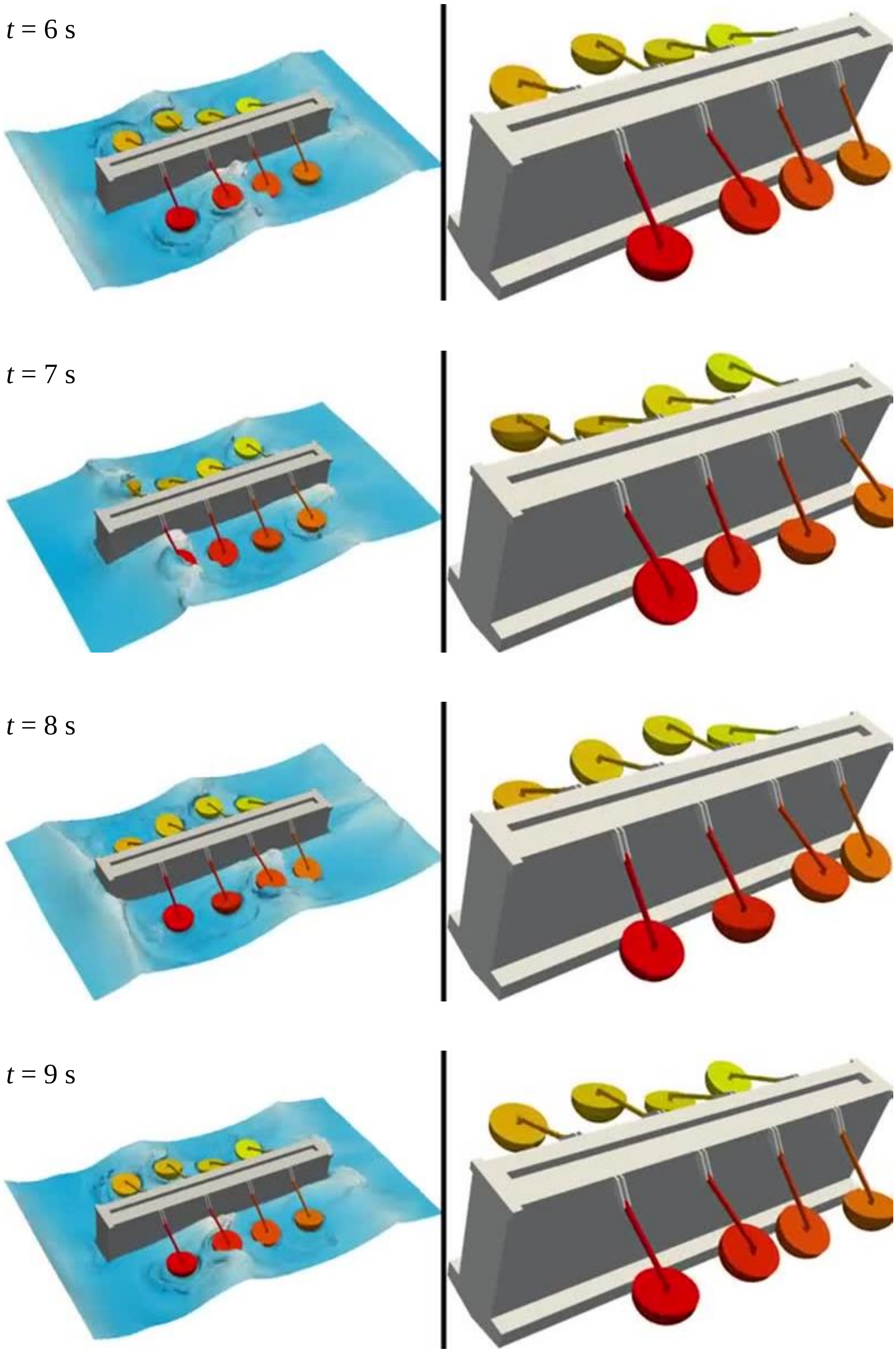

Figure E.3: Sequential instants of the WaveStar simulation.

E.2 Tidal turbine

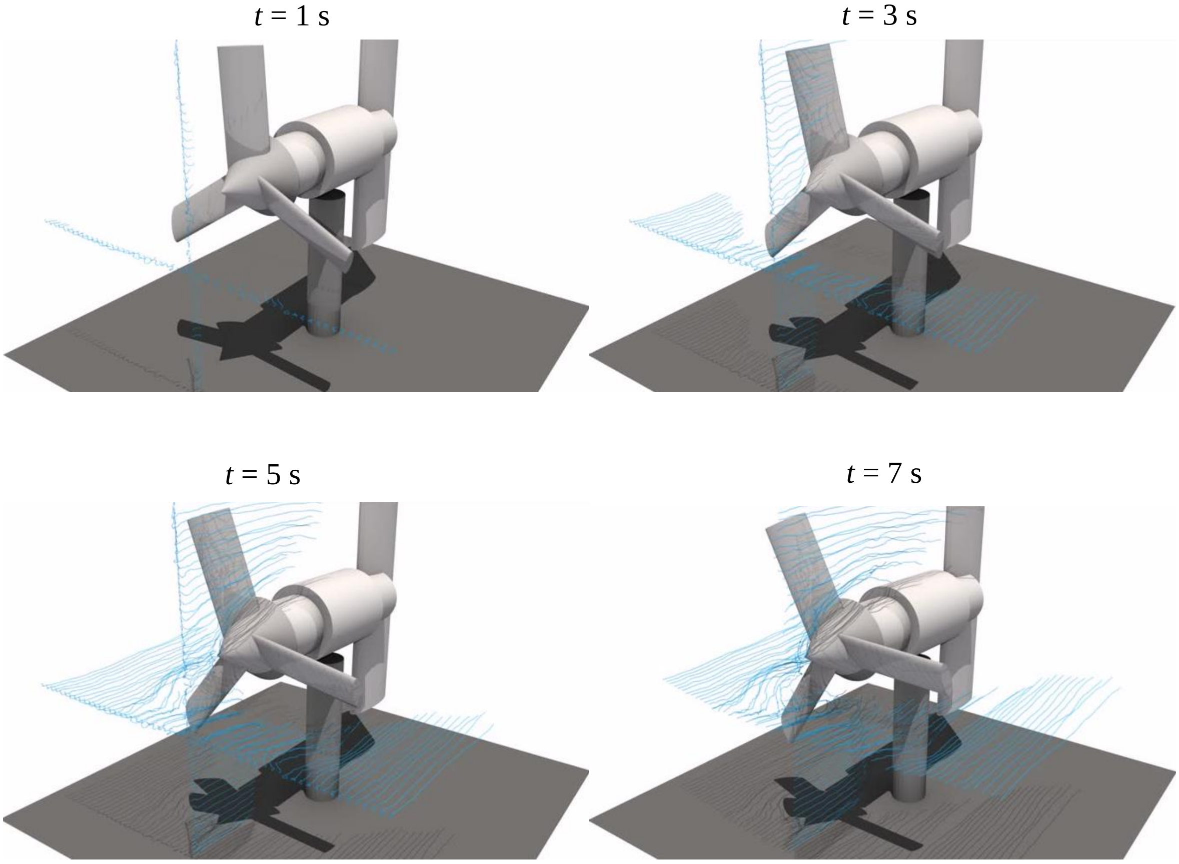

t = 1 s

t = 3 s

t = 5 s

t = 7 s

Figure E.4: Sequential instants of the passive tidal turbine simulation (Canelas et al., 2018).